Direct solar air heating in linear concentrating collectors assisted by a turbocharger for industrial processes: theoretical analysis and experimental characterization

by

Antonio Famiglietti

A dissertation submitted by in partial fulfillment of the requirements for the degree of Doctor of Philosophy in

Mechanical Engineering and Industrial Organization

Universidad Carlos III de Madrid

Advisor:

Prof. Dr. Antonio Lecuona Neumann

November 2021

ACKNOWLEDGEMENTS

I would like to express my gratitude to the supervisor of this work Prof. Antonio Lecuona Neumann for his continuous guidance throughout the academic research and his invaluable support, advice and encouragement during all the stages of my Ph.D study. I extend the acknowledgement to the whole Research Group of Thermal Engineering, Energy and Atmosphere (ITEA) of Carlos III University of Madrid. I dedicate a special mention to Prof. José Nogueira Goriba and Prof. Pedro Rodríguez Aumente, for their insightful suggestions and support during the development of this work. I would like to thank Mohammad Rahjoo who gave me invaluable help with the experimental work. I extend my thanks to the colleagues Dr. Ricardo Lopez Silva, Dr. Roberto Jiménez Sánchez and Dr. Berat Celik for the excellent collaboration. I want to acknowledge Prof. Mathieu Legrand and Dr. Ruben Ventas Garzòn for their precious advice during the first steps of my doctoral studies. My gratitude also goes to the technicians Israel Pina García, Manuel Santos Rodríguez and David Díaz González for their essential contribution to construction and maintenance of the experimental setup, and for the continuous assistance during the laboratory activities. I'm deeply grateful to Javier Roa Fresno and the whole team of DEMEDE Engineering and Research Company which supported the industrial Ph.D project, and assisted my work during these years. My acknowledgement goes to Dr. Mercedes Ibarra and the team of the Center for Solar Energy Technologies for the wonderful collaboration during my research visit to Fraunhofer Chile Research. I'm grateful to my family and friends for their encouragement and support all through my studies.

This research was supported by the Industrial Ph.D. project "Producción directa de aire a alta temperatura y a presión turboalimentada en colectores solares de concentración" (BOCM Reference IND2017/AMB7769) funded by "Comunidad de Madrid", Spain (Orden 3779/2017 of October 17th 2017, by "Consejero de Educación e Investigación", pubblished on "BOCM. 252, of October 23th 2017.)

PUBLISHED AND SUBMITTED CONTENT

The following publications form the basis of this thesis:

- “Direct solar production of medium temperature hot air for industrial applications in linear concentrating solar collectors using an open Brayton cycle. Viability analysis.” (Famiglietti, A., Lecuona-Neumann, A., Nogueira, J. I., & Rahjoo, M.) Applied Thermal Engineering, 169, (2020). DOI:10.1016/j.applthermaleng.2020.114914, [1].

- “Direct solar air heating inside small-scale linear Fresnel collector assisted by a turbocharger: experimental characterization” (Famiglietti, A. and Lecuona, A.) Applied Thermal Engineering, 196, (2021). DOI:10.1016/j.applthermaleng.2021.117323, [2].

- "Small-scale linear Fresnel collector using air as heat transfer fluid: Experimental characterization." (Famiglietti, A. and Lecuona A.), Renewable Energy, 176 (2021). DOI:10.1016/j.renene.2021.05.048, [3].

- “Turbo-assisted direct solar air heater for medium temperature industrial processes using Linear Fresnel Collectors. Assessment on daily and yearly basis.” (Famiglietti, A., Lecuona, A., Ibarra, M., & Roa, J.) Energy, 223, (2021) . DOI:10.1016/j.energy.2021.120011, [4].

The journal article [1] has been partially included in Chapter 1 and Chapter 2 of this thesis. The journal articles [2] and [3] have been partially included in Chapter 5. The journal article [4] has been partially included in Chapter 6. The author has contributed significantly to conceptualization, methodology, software, validation, experimental data acquisition and processing, investigation, writing, review & editing to the mentioned publications. The material from these sources included in this thesis is not singled out with typographic means and references.

OTHER RESEARCH MERITS

During the research leading to the present work, the author of this thesis has been involved in other publications with some relation to the topic, which are listed as follows. Although they are not reported in this thesis, they contributed to the investigation of concentrating solar systems for heating and cooling applications.

- Modeling of the direct vapor generation for energy integrated solar absorption machines, (Lecuona, A.; Famiglietti, A.; Legrand, M.) Renewable Energy, 135, (2019). DOI:10.1016/j.renene.2018.09.056.

- Advanced cycles based on ammonia/salt. (Antonio Lecuona-Neumann, Pedro A. Rodríguez-Aumente, Mathieu Legrand, Antonio Famiglietti). Sustainable Energy Technology, Chapter 40, Taylor and Francis Catalogue, Editor: Eduardo Rincón Mejía, Prof. Universidad Autónoma de la Ciudad de México.

The following articles have been published as contribution to scientific congresses:

- "Industrial Turbo-Assisted Direct Solar Air Heater Using Linear Fresnel Concentrating Collectors" (Famiglietti, A., Lecuona, A., Rahjoo M, J. Nogueira), EuroSun 2020 13th International Conference on Solar Energy for Buildings and Industry, Virtual Conference. DOI: 10.18086/eurosun.2020.03.06.

- "Producción directa de aire caliente en colectores solares Fresnel para la industria minera: estudio de prefactibilidad." (Famiglietti, A., Lecuona, A., Rahjoo M., Ibarra, M., & Roa J.), CIES 2020 Conference Proceedings, DOI:10.34637/cies2020.2.4146.

- "Solar Hot Air for Industrial Applications Using Linear Fresnel Concentrating Collectors and Open Brayton Cycle Layout." (Famiglietti, A., Lecuona-Neumann, A., Rahjoo, M., & Nogueira-Goriba, J.) (2021). In E3S Web of Conferences (Vol. 238, p. 01003). EDP Sciences. DOI:10.1051/e3sconf/202123801003.

- "Preliminary Study of Direct High-Temperature Air Generation Inside Linear Fresnel Concentrating Solar Collectors" (Famiglietti, A., Lecuona-Neumann, A., Nogueira, J. I., & Rahjoo, M), ISES Solar World Conference 2019, Santiago de Chile, November 2019. DOI: 10.18086/swc.2019.12.04.

- "Direct high temperature solar air production for industry" (Famiglietti, A., Lecuona-Neumann, A., Legrand, M., Nogueira-Goriba, J), CNIT11- XI Congreso Nacional y II Internacional de Ingeniería Termodinámica (11-CNIT), June 2019.

- "Use of Parabolic Trough Collector as Direct Vapor Generator for an Absorption Machine: Experimental Study" (Famiglietti, A., Celik, B., Lecuona-Neumann, A., López, R., Nogueira-Goriba, J.), ISES Solar World Conference 2019, Santiago de Chile, November 2019. DOI:10.18086/swc.2019.55.04.

- “Modeling of an Absorption Cycle with a Direct Ammonia Vapor Generator Inside a Concentrating Parabolic Trough Solar Collector” (Celik, B., Lecuona-Neumann, A., Rodriguez-Aumente, P., Famiglietti, A.) ISES EuroSun 2018 Conference – 12th International Conference on Solar Energy for Buildings and Industry, September 2018. DOI: 10.18086/eurosun2018.04.19.

- “Direct vapor ammonia generation inside a concentrating parabolic trough solar collector for an ammonia/lithium nitrate absorption machine. Theoretical study.” (Famiglietti, A., Lecuona, A., Nogueira, J., Celik, B.) 13th IIR-GUSTAV LORENTZEN CONFERENCE ON NATURAL REFRIGERANTS, June 2018, DOIi:10.18462/IIR.GL.2018.1371

ABSTRACT

Energy demand of industry has a relevant share of global energy consumption. The larger portion of industrial demand is heating, mainly provided from fossil fuels. The concerns about pollutant and greenhouse gas emissions, together with the fossil fuels scarcity encourage the research efforts toward environmentally sustainable energy sources and among them, solar energy is widely available. Among solar thermal technologies, linear concentrating collectors represent a suitable solution for providing industrial process heat in the medium temperature range. A heat transfer fluid, as thermal oil, or water, is generally adopted to evacuate heat from the solar receivers and to deliver it to thermal processes, contributing to complexity, cost, and even environmental impact.

In this thesis the direct air heating inside concentrating solar collector is investigated as a promising solution for industrial processes requiring hot air in the medium temperature range, aiming at low installation and maintenance costs. Although uncommon, the theoretical analysis carried out revealed the feasibility of direct air heating at atmospheric pressure either in a parabolic trough and linear Fresnel collectors within a limited range of design and operating conditions. The high pumping power required to blow air through the receivers arises as one of the main constraints, becoming unsustainable at medium and large scale. To overcome this limitation, an innovative layout is proposed using an automotive turbocharger to configure an original open-to-atmosphere solar Brayton cycle with null power efficiency. The compressor increases the air pressure before solar heating inside the receivers, minimizing the pumping power consumption. The turbine placed at the receiver outlet recovers the compressing and the pumping power, releasing hot air at between 300 °C and 400 °C for its usage in the thermal process. The maximum allowable temperature of evacuated standard receivers, indicated as 600 °C by most of the manufacturers, limits the inlet turbine temperature. No substantial mechanical excess of power at the common turbine and compressor shaft is expected. Instead, turbocharger freewheeling enables to blow air through the solar receivers without auxiliary energy consumption, eventually delivering the hot air with an overpressure for pumping to the user.

To support the proposal, a first small-scale experimental prototype of the turbo-assisted solar air heater is designed and installed, using Linear Fresnel collectors and a low-capacity turbocharger. The experimental results allow the thermal and mechanical characterization of the solar collector and the turbocharger, besides tuning and validating the numerical model implemented. They corroborate the practical viability of the concept and indicates relevant features and critical aspects for scaling up to industrial size. A detailed quasi-steady numerical model is developed, including technical features of commercial linear Fresnel collectors and off-the-shelf turbochargers. Daily and yearly assessments of several medium-scale facilities are obtained considering the typical meteorological year of the selected location. The results allow identifying the relevant design and operating parameters and their effect on the performances of the turbo-assisted solar air heater. By combining theoretical and experimental approaches this thesis establishes the framework for the development, design, optimization, and operation of the innovative technology proposed, opening the possibility to its application to several industrial sectors.

RESUMEN

La demanda energética de la industria tiene una participación relevante en el consumo energético mundial. La mayor parte de la demanda industrial es calor, principalmente obtenido a partir de combustibles fósiles. Las preocupaciones sobre las emisiones de gases contaminantes y de efecto invernadero, junto con la escasez de combustibles fósiles, fomentan los esfuerzos de investigación hacia fuentes de energía ambientalmente sostenibles, entre las cuales, la energía solar se encuentra ampliamente disponible. Entre las tecnologías solares térmicas, los colectores de concentración lineal representan una solución adecuada para proporcionar calor de proceso industrial en el rango de media temperatura. Generalmente se adopta un fluido caloportador, como aceite térmico o agua, para evacuar el calor de los receptores solares y entregarlo al proceso térmico, contribuyendo a la complejidad, costo, e incluso impacto ambiental.

En esta tesis se investiga el calentamiento directo de aire en colectores solares de concentración como una solución prometedora para procesos industriales que requieran aire caliente en el rango de media temperatura, con el objetivo de reducir los costos de instalación y mantenimiento. Aunque poco común, el análisis teórico realizado revela la viabilidad del calentamiento directo del aire a presión atmosférica tanto en colectores cilindro-parabólicos como en colectores Fresnel lineales dentro de un rango limitado de condiciones de diseño y operación. La alta potencia de bombeo necesaria para soplar aire a través de los receptores es una de las principales limitaciones, volviéndose insostenible a mediana y gran escala. Para superar esta limitación, se propone un diseño innovador que utiliza un turbocompresor de automóvil para configurar un ciclo Brayton solar abierto a la atmósfera con una eficiencia energética nula. El compresor aumenta la presión del aire antes del calentamiento solar en los receptores, minimizando el consumo de energía de bombeo. La turbina, colocada en la salida del receptor, recupera la potencia de compresión y bombeo, liberando aire caliente entre 300 °C y 400 °C para su uso en el proceso térmico. La temperatura máxima permitida de los receptores estándar evacuados, indicada como 600 °C por la mayoría de los fabricantes, limita la temperatura de entrada de la turbina, por lo que no se espera un exceso mecánico de potencia sustancial en la turbina común y el eje del compresor. En cambio, el turbocompresor permite soplar aire a través de los receptores solares sin consumo de energía auxiliar de bombeo. Si existiera un exceso, estará disponible para el bombeo hasta el usuario.

Para apoyar la propuesta, se diseña e instala un primer prototipo experimental de pequeña escala del calentador de aire solar turbo-asistido, utilizando colectores lineales Fresnel y un turbocompresor de baja capacidad. Los resultados experimentales permiten la caracterización térmica y mecánica del colector solar y el turbocompresor, además de ajustar y validar los modelos numéricos implementados. Los ensayos corroboran la viabilidad práctica del concepto e indican características relevantes y aspectos críticos para escalar al tamaño industrial. Se desarrolla un modelo numérico cuasi-estacionario detallado, que incluye las características técnicas de los colectores Fresnel lineales comerciales y los turbocompresores estándar. Se obtienen evaluaciones diarias y anuales de varias instalaciones de mediana escala considerando el año meteorológico típico de la ubicación seleccionada. Los resultados permiten identificar los parámetros de diseño y funcionamiento relevantes y su efecto sobre el rendimiento del calentador de aire solar turbo-asistido. Combinando enfoques teóricos y experimentales, esta

tesis establece el marco para el desarrollo, diseño y operación de la tecnología innovadora propuesta, abriendo la posibilidad de su aplicación a varios sectores industriales, apuntando a la descarbonización y transición industrial sustentable.

CONTENTS

LIST OF FIGURES

LIST OF TABLES

NOMENCLATURE

Latin

A	Flow cross-section [m^2], Aperture surface area [m^2]
A_{tot}	Overall solar field area [m^2]
A_{bra}	Minimum cross section bracket [m^2]
A_m	Active LFC area [m^2]
ac	Auxiliary compressor
B	Parameter equation of time [rad]
b	blower
c	Compressor
C	Solar geometrical concentration factor [-]
c_e	Turbine mass flow fitting function coefficient [kg s^{-1}]
c_{ec1}	Fitting function coefficient [W °C^{-1}]
c_{ec2}	Fitting function coefficient [-]
c_{eamb}	Fitting function coefficient [-]
COP	Coefficient of performance [-]
c_p	Air constant p specific heat capacity [J $kg^{-}1$ $°C^{-1}$]
c_{tr},c_{tr1}	Coefficient tracking efficiency [rad^{-1}]
c_{tr2}	Coefficient tracking efficiency [-]
$c_{U,i}$	Coefficient for polynomial fitting of U_L [W m^{-2} k^{-5+i}]
D	Inner diameter of the receiver tube [m]
D_g	Glass cover internal diameter [m]
D_h	Hydraulic diameter [m]
e	Turbine
E	Correction equation of time [s]
e_g	Glass cover thickness [m]
e_w	Tube wall thickness [m]
f	Darcy friction coefficient [-]
F'	Collector efficiency factor [-]
f_{end}	Optical end losses factor [-]
$f_{n,I}$, $f_{n,II}$	Fitting functions [-]
FQ	Frequency [Hz]
F_R	Collector heat removal factor [-]

g	Gravitational acceleration [m s^{-2}]
G_{bn}	Normal beam irradiance [W m^{-2}]
G_{bT}	Normal to aperture area beam irradiance [W m^{-2}]
G_d	Diffuse irradiance [W m^{-2}]
G_{glo}	Global irradiance on horizontal surface [W m^{-2}]
h_a	Air heat transfer coefficient [W m^{-2} °C^{-1}]
h_{bra}	Bracket heat transfer coefficient [W m^{-2} °C^{-1}]
h_c^{con}	Convection heat transfer coefficient [W m^{-2} °C^{-1}]
h_c^{rad}	Radiation heat transfer coefficient [W m^{-2} °C^{-1}]
h_{co}	Convection heat transfer coefficient [W m^{-2} °C^{-1}]
h_{ir}	Radiation heat transfer coefficient [W m^{-2} °C^{-1}]
H_m	LFC receiver height [m]
IAM	Incidence angle modifier [-]
i	Specific enthalpy [J kg^{-1}]
IR	Interpolation ratio [-]
J_T	Turbocharger polar inertia [kg m^2]
K	Concentrated pressure losses coefficient [-]
k	Thermal conductivity [W m^{-1} °C^{-1}]
k_e	Turbine mass flow fitting function coefficient [-]
k_i	Compressor mass flow fitting function parameters [-]
L	Length of the receiver tube [m]
L^*	Receiver generic length [m]
L_c	Length of the collector mirrors [m]
L_{exi}	Extra lengths [m]
L_h	Characteristic heating length in the receiver tube [m]
L_j	Junction length [m]
L_m	LFC length [m]
L_n	Connection pipe length [m]
L_{nc}	Length of the connection piping [m]
L_r	Receiver overall length [m]
LF	Load factor $\dot{q}_s/\dot{q}_{s,peak}$
LST	Local standard time [hr]
$\dot{m}$	Air mass flow rate [kg s^{-1}]
$\dot{m}_{T_{ou}}$	Air mass flow rate for the specified T_{ou} [kg s^{-1}]

Ma	Mach number [-]
n	Supply tube
n_d	Day of the year
n_e	Number of elements in one tube [-]
n_m	Number of mirrors
n_p	Number parallel U-loops
n_s	LFC in series [-]
n_t	Number of tubes [-]
n_T	Turbocharger speed [rpm]
n_1, n_2, n_3	Connection tubes
P	Receiver tube cross-section perimeter [m]
P_{bra}	Bracket perimeter [m]
ph	Post-heating
Pr	Prandtl number [-]
p	Pressure [Pa]
Q	Thermal energy [J]
$\dot{Q}$	Thermal power [W]
$\dot{q}_s$	Incident concentrated solar irradiance [W m^{-2}]
$\dot{q}_u$	Useful thermal power flux [W m^{-2}]
r	Receiver
Ra	Rayleigh number [-]
Re	Reynolds number [-]
R_g	Gas constant $= R/M_g$ [m2 s^{-2} °C^{-1}]
R_p	Pumping ratio [-]
SR	Blade speed ratio [-]
T	Temperature [K]
TST	True solar time [hr]
U	Tip balde speed [m/s]
U_C	Capacitive equivalent heat transfer coefficient [W m^{-2} K^{-1}]
U_L	Thermal losses overall coefficient [W m^{-2} K^{-1}]
U_{Ln}	Thermal losses coefficient of insulated tubes [W m^{-2} K^{-1}]
UTC	Standard time zone of Universal Coordinate Time [s]
v	Average airflow velocity [m s^{-1}]
$\dot{W}$	Power [W]

W_a	Rectangular aperture total width [m]
w_m	Aperture width of a single reflector of LFC [m]
z	Longitudinal coordinate for receiver [m]

Greek

α_s	Solar elevation [rad]
α_{abs}	Solar absorbance [-]
γ	Isentropic exponent [-]
γ_s	Solar azimuth [rad]
γ_r	LFC azimuth [rad]
Δp_t	Stagnation pressure drop [bar]
δ	Sun declination [rad]
ε	Emissivity [-]
η	Isentropic efficiency [-]
η_a	Global air heating efficiency [-]
η_{op}	Optical efficiency [-]
η_{op0}	LFC normal optical efficiency [-]
η_{opg}	Global optical efficiency [-]
$\eta_{r,SAH}$	Receiver efficiency of SAH [-]
$\eta_{r,TSAH}$	Receiver efficiency of T-SAH [-]
η^*_{SAH}	Efficiency of SAH [-]
η_{eg}	Averaged electricity generation efficiency [-]
η_{em}	Global turbine efficiency [-]
η_m	Mechanical efficiency turbocharger coupling shaft [-]
η_{st}	Static correction for efficiency [-]
η_{th}	Thermal efficiency [-]
η_{tr}	Tracking efficiency [-]
η^*_{TSAH}	Efficiency of T-SAH [-]
η_{tt}	Total to total isoentropic efficiency [-]
η_{TC}	Turbocharger global efficiency [-]
θ	Non-dimensional temperature [-]
θ_L	Longitudinal angle [rad]
θ_s	Half-angle of solar beam cone [rad]
θ_T	Transversal angle [rad]
θ_z	Solar zenith angle [rad]

κ	273°C
λ_{st}	Local time zone standard meridian longitude west [deg]
λ_{loc}	Collector location longitude west [deg]
μ	Dynamic viscosity [$kg \cdot m^{-1} \cdot s^{-1}$]
ν	Kinematic viscosity [$m^2\ s^{-1}$]
π	Pressure ratio [-]
ρ	Density [$kg\ m^{-3}$]
σ	Stefan-Boltzmann constant [$W\ m^{-2}\ K^{-4}$)]
σ_{tr}	Tracking error [rad]
σ_{tr}^{*}	Tracking error threshold [rad]
τ	Time [s]
Φ_{loc}	Latitude north [deg]
ϕ_c	Non-dimensional flow rate parameter [-]
φ	Extended surface coefficient [-]
ψ_c	Head parameter [-]
ω	Angular speed [$rad\ s^{-1}$]
ω_s	Hour angle [rad] (negative in the morning)

Subscripts

a	Air
ac	Auxiliary compressor
af	After
amb	Ambient
atm	Atmospheric
b	Blower
be	Before
c	Compression
cor	Corrected
$c \rightarrow amb$	Compressor to ambient
d	Delivery to user, Direct
e	Expansion, Turbine
$e \rightarrow amb$	Turbine to ambient
$e \rightarrow c$	Turbine to compressor
em	Electro-mechanical
ex	Receiver tube external surface, extra

f	Friction
i	Discretization element
in	Receiver inlet
ins	Insulation
j	Tube junction
L	Thermal losses to ambient
loc	Location
k	Kinetic energy component
m	Average along the receiver, LFC module, mirror
max	Maximum
min	Minimum
n	Outlet of supply tube to receiver
net	Net
$norm$	Normalized
ON	T-SAH operative
OFF	T-SAH shut off
op	Optical
opt	Optimum
ou	Receiver outlet
p	Polytropic, pumping
ph	Post-heating
R	Recirculation, over-pressure
r	Receiver
ref	Reference turbomachine
row	LFC series row
s	Isoentropic, solar
t	Total or stagnation variable
T	Turbocharger
Tou	At outlet temperature
tot	Total
tr	Tracking
ts	Total to static
u	Useful
w	Wall

$\dot{W}=0$	Mechanical balanced operation
0	Inlet from atmosphere
1	Compressor inlet
2	Compressor outlet
$2n$	Receiver entrance TSAH
3	Turbine inlet
4	Turbine outlet

Superscripts

adi	Adiabatic
cal	Calculated value
$choke$	Choke limit
dia	Diabatic
dy	Dynamic
exp	Experimental value
min	Minimum
max	Maximum
pt	Potential
$surge$	Surge limit
st	Steady-state, static
th	Threshold
$*$	Corrected with parasitic pressure losses

Acronyms

AC	Air Collector
ETC	Evacuated Tube Collector
EU	European Union
HTF	Heat transfer fluid
HX	Heat exchanger
H&C	Heating and cooling
IAM	Incident Angle Modifier
LFC	Linear Fresnel collector
OAC	Open-air circuit
PTC	Parabolic Trough collector
PV	Photovoltaic
SAH	Solar air heater
SCADA	Supervisory Control and Data Acquisition

SHC	Solar heating and cooling
SHIP	Solar heat for industrial processes
T-SAH	Turbo-assisted solar air heater
T-SAH*	Turbo-assisted solar air heater integrated with SAH
TMY	Typical Meteorological Year

Others

⟨ ⟩	Functional dependence
$\bar{\ }$	Average value

1 INTRODUCTION

1.1 Solar energy for heating and cooling

The simultaneous increase in world population, development and the enhancement in living standards have driven a growing energy demand and it is projected to increase in the coming years, according to the International Energy Agency [5]. On the other hand, fossil fuel consumption, such as oil, natural gas, and coal, leads to greenhouse-effect and air pollutant emissions in the atmosphere that have raised concerns about climate change [6] and local health hazards. At the same time, the increased consumption of fossil fuels leads to shortages and also can lead to price instabilities and geopolitical conflicts. The adverse environmental effects and safety issues of fossil fuel consumption strengthen the suitability of renewable energy sources and give them a unique opportunity to develop and grow. Among renewable energies, solar energy, the most abundant source of renewable energy on the planet, attracts the most attention. Many studies have been accomplished on methods of using Solar energy for Heating and Cooling (SHC) [7] in a program by the International Energy Agency, and on a review by [8], among others. Solar Electricity production and in particular by Photovoltaic means (PV) is also investigated, [9] as well as thermo-solar solutions. As one of the most significant energy consumptions in developed countries corresponds to heat demand, both in buildings and industries, solar energy for obtaining heat is one of the priorities in research policies for its high efficiency among other advantages, either from the European Commission, by Solar Heat Europe and the European Technology Platform on Renewable Heating and Cooling. Obtaining heat from solar energy can be performed by using technologies that spread from very simple, even using local expertise and local materials, up to high tech setups, some of them now in development.

According to the European Commission [10], Heating and Cooling (H&C) represent 46 % of the European Union's (EU) energy needs. The EU industry uses 70.6 % of its energy consumption (193.6 Mtoe) for space and industrial process heating, and still, 84 % of H&C is generated from fossil fuels, while renewable energy generates only the remaining 16 %. The European Strategy plan for H&C states that 45 % of energy for heating and cooling in the EU is used in the residential sector, 37 % in industry, and 18 % in services.

1.2 Solar heat for industrial processes

Industry consumes around one-third of energy worldwide [11]. The larger part of industrial energy demand is process heat, followed by electricity. Heat is required at different temperature levels which are generally classified as low-temperature heat ($T < 150$ °C), medium-temperature heat (150 °C $< T < 400$ °C), and high-temperature heat ($T > 400$ °C). According to [12] and [13], Fig. 1.1, heat has a 74 % share of industrial world energy demand, almost totally provided by fossil fuel. 30 % of heat demand is in the low-temperature range, 22 % in the medium temperature range, and 48 % in the high-temperature range.

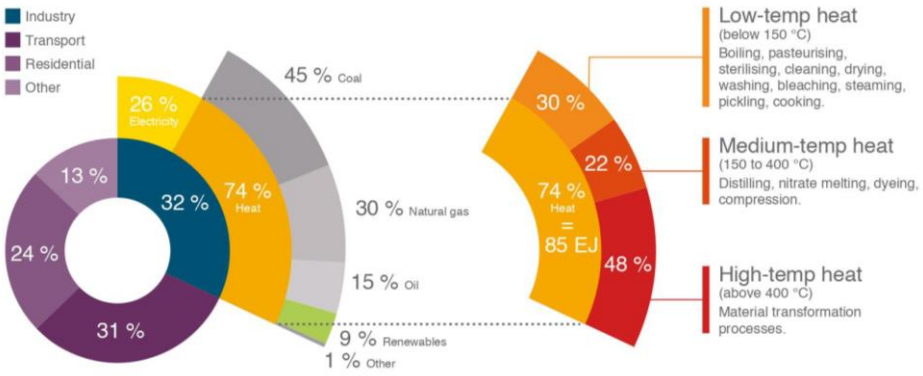

Fig. 1.1. Global industrial heat demand, based on IEA statistics and calculations by IRENA, [12], [13]

Similar information is reported by [14] about industrial energy demand in Europe. Heat demand is for the 42 % above 500 °C, 9 % between 200 - 500 °C, 21 % between 100-200 °C and 9 % below 100 °C, Fig. 1.2.

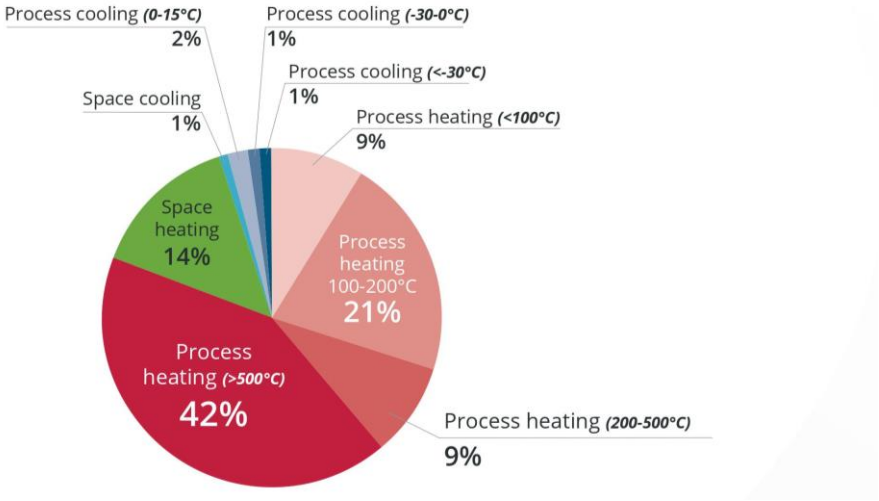

Fig. 1.2. Industrial energy demand in Europe (2015), [14]**.**

Solar energy has a great potential for replacing fossil fuel consumption in industry, aiming at GHG and pollutant emission reduction and environmental sustainability. Sharma et al. [15] reviewed solar potential in industrial heating for several countries. Mainly low to medium temperature processes are reported for several industrial sectors: food and beverage, textile, pulp and paper, chemical, casting industry, cement, rubber, and plastic manufacturing. Farjana et al. [16] and [17] reviewed the Solar Heat for Industrial Processes (SHIP) state of art and potential. They analysed the industrial heat demand by sectors, identifying the processes requiring low and medium-temperature heat.

A few technologies are available for solar industrial heating [18]. Flat Plate Collectors (FPCs) and Evacuated Tube collectors (ETCs) are suitable solutions for low-temperature applications (below 100 - 150 °C). Solar Air collectors can be used for direct air heating in the low-temperature range.

Higher temperature up to 500 - 550 °C can be achieved by using concentrating linear technologies as Parabolic Trough Collectors (PTCs) and Linear Fresnel Collectors (LFCs). Parabolic

dish reflector and central receiver are promising technologies allowing temperatures above 1,000 °C.

According to [19], 635 SHIP plants are in operation around the world. The industrial sector with more installed SHIP is food and beverage, followed by textile and pharmaceutical. The majority use FPCs followed by ETCs. 88 % of the plants use non-concentrating technologies. Existing SHIP plants are reported in the SHIP database [20] developed by AEE INTEC and PSE within the IEA SHC Task 49/SolarPACES, as well as by [16] and [15].

1.3 Concentrating solar heat

In the past decades, PTC and LFC have been developed as concentrating solar power technology (CSP) for large-scale plants aiming at electricity generation, [21]. PTC has a parabolic-shaped reflector able to focus on the focal point the incoming direct component of solar irradiance impacting on the aperture with normal direction. The tubular receiver is located in the focal point as in Fig.1.3(a). According to the current state-of-art of the technology, [22] the receiver is an evacuated tube with high thermal performances: an internal stainless-steel tube coated with a spectrally selective coating is embedded into a coaxial high transparency glass tube, with vacuum annulus. A Heat Transfer Fluid (HTF) with suitable thermal properties flows inside the receiver to evacuate heat and deliver it where required. A one-axis tracking system continuously adjusts the collector inclination and keeps the aperture normal to incident irradiance.

Linear Fresnel collector has a segmented (primary) reflector, obtained a series of flat or slightly curved mirrors [23]. The tracking system adjusts the inclination of each mirror to concentrate the incoming direct solar irradiance on the receiver, Fig. 1.3(b). Several types of receivers have been studied and applied. The use of an evacuated tube as a receiver for LFC gives better performances with respect to other solutions (multiple tubes, non-evacuated single tube, cavity receiver, etc.), [24]. In most applications based on a single tube, a secondary reflector is used for redirecting to the receiver the concentrated irradiance missing it, due to unperfect focusing.

Linear concentrating collectors, either PTC or LFC have a great potential for SHIP applications. Due to their modularity, they can be adapted to small and medium-scale facilities, suitable for installation in industries. According to their technical features, PTCs and LFCs can work in the medium temperature range, up to 500 – 550 °C. Both Linear Fresnel Collectors (LFCs) and Parabolic Trough Collectors (PTCs) for SHIP application are commercially available.

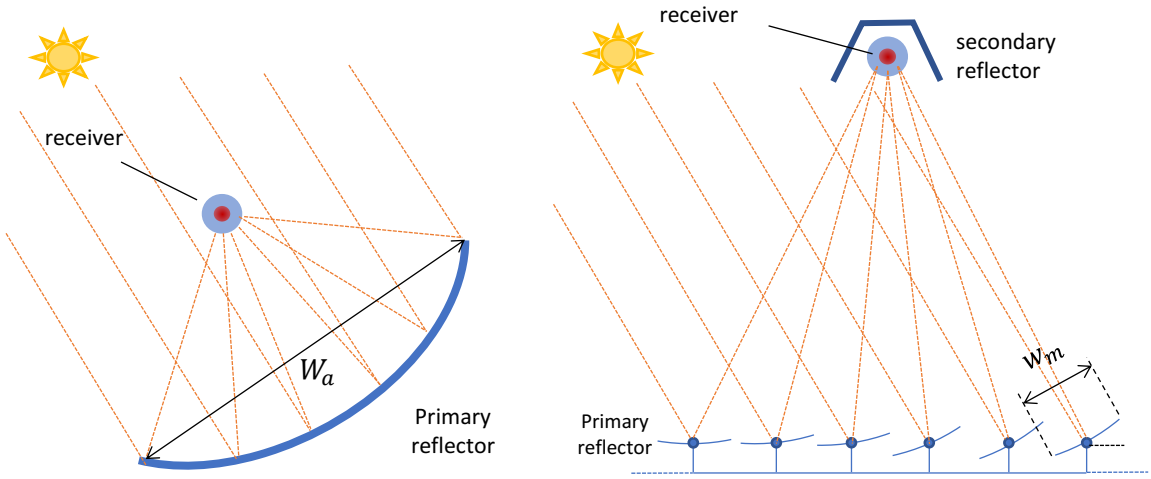

(a) (b)

(c) (d)

Fig. 1.3. Linear concentrating solar collectors. Parabolic trough collector PTC working principle (a), example (c). Linear Fresnel collector working principle, with an evacuated receiver and secondary reflector (b) and example (d).

Among the existing SHIP applications, according to [19] only 12 % use linear concentrating collectors. Among them the 79 % use PTCs. The SHIP database [20] reports 58 projects using PTCs, with solar field areas ranging from 34 m^2 to 5060 m^2, except for the large Miraah Oman project for steam generation. From the same source, 13 existing plants use LFCs for SHIP, from 123 m^2 of aperture surface up to 2000 m^2.

Farjana et al. [16] detail the existing Concentrating Solar Heat (CSH) applications for several industrial sectors, as reported in Tab. 1.1. The usage of CSH goes from water heating (95 °C), drying (50 - 160°C) preheating process (95 °C), steam-driven processes (130 - 240 °C), pasteurization (80 - 95 °C), drying and cooking (40 – 95 °C), food processing (150 °C), and space heating (95 °C). Pressurized water, oil, or steam are used as primary heat transfer fluid (HTF).

Table 1.1. Concentrating solar heat applications

Sector	Operation	Collector type	Operating temperature
Breweries	Absorption cooling	LFC	110-160 °C
Food	Heating water	PTC	95 °C
	Process heat	PTC	80-100 °C
	Pasteurization	PTC	80-95 °C
	Boiler preheating	PTC	20-95 °C
	Cooking	PTC	40-95 °C
	Milk processing	PTC	150 °C
	Steam generation	PTC	140-240 °C
	Process heating	LFC	200 °C
Pharmaceutical	Process heating	PTC	173 °C
Textile	Process heating	PTC	140 °C
Chemical	Steam generation	PTC	130 °C
Agricultural	Space heating	PTC	95 °C
Metal	Steam generation	PTC	143 °C
	During finished product	PTC	50-160 °C
	Water heating	PTC	95 °C
Manufacturing	Chemical baths	PTC	160 °C

1.4 Hot air for industrial processes

Sharma et al. [15] reported as conventional heating techniques in industries can be combustion-based or electricity-based. Heat can be directly applied to the material, through contact with combustion gas, or by ohmic dissipation of electricity through the material. In many applications heating occurs indirectly, using a Heat Transfer Fluid (HTF), going from thermal oil to saturated steam, superheated steam, pressurized hot water, and air.

Industrial processes using air as a heat transfer medium are widespread and operate in several sectors, as reported in Tab. 1.2. They are more common below 250 °C and rarely up to 1,500 °C. Tab. 1.3 reports the operative temperature of several thermal processes.

A widespread application of hot air is drying. Drying is common to different industrial sectors and is one of the high energy-demanding processes [25]. Hot air convective drying is much used, among a variety of techniques. The different drying methods and equipment are reviewed by [26] among others. Drying in industrial processes and agriculture is reviewed by [27]. Wu et al. [28] reviewed the drying techniques in the mineral processing industry. [29] analyzed the effects of the drying process on food quality. [30] analyzed the freezing drying technique comparing with hot air drying in the food industry. Due to the large energy consumption the temperature

required, the application of solar thermal energy has a great potential for drying decarbonization [31].

Table 1.2. Some examples of industrial process heat with hot moderate pressure air.

Process	Application
Distillation and evaporation	Drying, e.g., paper, seeds and grains, leaves, ceramics, mining products, timber. Biomass. Foods drying/ processing/ cooking e.g., dry milk/coffee production
Thermal processing	Preheating of combustion air. Preheating before expansion in CAES. Fabric clothes ironing/dying/scouring. Torrefaction
Curing/backing	Painted products, pharmaceutical drugs. Wood superficial treatment
Residues processing	Waste sludge drying, e.g., Blackwater sediments, olive oil residues. Brine spray evaporation. Ash dewatering. Anaerobic digester water heating by bubbling
Plastics and rubber processing	Separation, drying, melting, and soldering of plastics. Shrinking of plastic sleeves. Vacuum plastic sheet forming

Table 1.3. Thermal processes using air as HTF. * own research, air temperature.

Sector	Process	Temperature [°C]	Source
Food & Beverage	Drying, dehydration	40 - 100	[15]
"	Washing, cleaning	40 - 80	[15]
"	Pasteurization, sterilization	70 - 100	[32]
"	Concentration	70 - 150*	[32]
Pulp and paper	Drying	90 - 200	[15]
Chemical and pharmaceutical	Drying	120 - 170	[15]
Rubber	Drying	50 - 130	[15]
Glass	Drying	150 - 175	[15]
Manufacturing	Laminating	100 - 180	[15]
Casting	Hardening, annealing, tempering, forging, rolling	200 - 700	[15]
Cement	Lime calcining	600 - 1200	[15]
Automobile	Paint drying and curing	200 - 300	[16]
Water treatment	Desalination	200 - 300*	[32]
Blackwater purification	Sludge drying	200 - 300*	Own research

Hot air consumed by industrial processes is commonly provided from fossil fuel or electricity. The direct use of combustion fumes instead of atmospheric air is also widespread [15]. Due to the partial renewable source share of current electricity generation, hot air production is associated with GHG and pollutant emission, therefore hot air production from solar energy has an enormous potential aiming at the sustainable industry.

1.5 Hot air from solar energy

Hot air production from solar thermal energy can be carried out by direct heating inside the collector, in an open to atmosphere OA circuit, or indirectly, by means a primary HTF circulating in a closed loop delivering heat to process air through an HTF/air heat exchanger HX.

In current practice, solar direct air heating is performed using air collectors (ACs), also referred to as solar air heater (SAH), and is limited to low-temperature applications (T < 100 °C), [33]. Saxena et al [34] and Kumar et al. in [35] indicate the nowadays progress of SAHs. [16] reported several industrial applications of air collectors, mainly for food drying.

Indirect solar air heating in the low-temperature range can be implemented using FPCs, or ETCs. For higher temperature requirements linear concentrating collectors can be used, although the existing applications are rare. Thermal oil, steam, or pressurized water are generally used as HTF, as in Fig.1.4.

One example is reported by [20], where an LFCs solar field of 132 m^2 is used to heat water up to 180 °C, in a car paint shop in Germany. Process air is heated through a water/air heat exchanger integrated with a natural gas boiler. Another installation in Portugal is reported in the SHIP database [20], using PTCs. A solar field of 105 m^2 heats thermal oil to 160 °C. Hot air for processing finished products is obtained using an oil/air HX. Rehman et al. [36] describe and analyse the performances of an LFC system of 102 kW rated thermal capacity for indirect evaporative cooling. Thermal oil is used as primary HTF, heating an airflow through an oil/air HX up to 180 °C. The effectiveness of oil/air HX was estimated between 0.8 and 0.9. Pietruschka et al. [37] discussed the design, installation, and commissioning of a large-scale plant for indirect air heating for brick drying in Italy. An LFCs solar field is divided into two plants, one (1702 m^2 area) operates with thermal oil for indirect steam generation, the other (1608 m^2 area) operates with direct steam generation. Steam, at 180°C and 12 bar, heats process air through a steam/air HX.

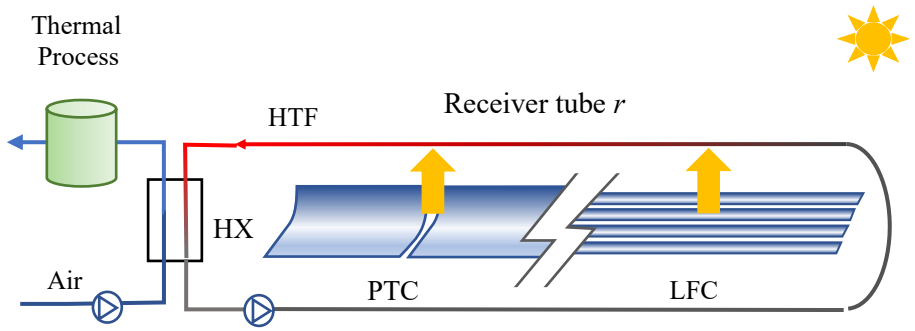

Fig. 1.4. Indirect air heating using linear concentrating collectors

1.6 Direct solar air heating in concentrating solar collectors

All the mentioned examples of PTCs and LFCs for hot air production use a primary liquid Heat Transfer Fluid HTF (thermal oil or water) to evacuate heat from the collectors and HTF/air Heat eXchanger HX to heat process air as a secondary HTF. Using thermal oil implies non-negligible

installation, replacement, and disposal costs, present degradation at high temperature, leakages problems related to environmental pollution, and fire risk. Water implies the drawbacks of boiling and two-phase flow unless pressurization is achieved, increasing risks related to leakages, besides freezing during the night, and corrosion. A primary pump is needed for circulating the HTF. Besides its relevant installation cost, the use of an HTF/air heat exchanger introduces an exergy loss, needs an additional blower for the airflow, and requires space availability.

Although still uncommon, the direct solar air heating inside concentrating collectors, either with PTCs or LFCs, would reduce the complexity and the cost of a solar facility, avoiding the need for a primary HTF as well as an HTF/air HX. As for a non-concentrating solar air heater, an Open-to-Atmosphere (OA) circuit, Fig. 1.5, could be implemented for industrial solar hot air generation, aiming at lower costs, maintenance requirement, safety, and environmental concerns, with the advantage of higher delivery temperature, achievable thanks to the high thermal efficiency of linear concentrating collectors.

Despite the expected advantages, the thermophysical properties of air do not encourage its direct use as HTF for the following main reasons.

The low specific heat capacity c_p (half of steam and one-quarter of liquid water) implies that the mass flow rate $\dot{m}$ must be higher compared to a convectional HTF, to limit the outlet temperature at the collector end for a concentrated given solar irradiance $\dot{q}_s$.

Due to low density ρ the flow velocity reached using the required mass flow increases, leading to higher stagnation pressure drops across the receiver tube. As consequence, the pumping power required for blowing air through the facility can be not anymore negligible and, especially for long collector rows with high aperture, it can be in the same order of magnitude of solar power gain.

The low thermal conductivity reduces the heat transfer coefficient h_a between the receiver wall and the airflow. In addition, the low density and high viscosity μ of air implies a high kinematic viscosity $\nu = \mu\rho^{-1}$, two orders of magnitude greater than water. For a given diameter D, the Reynolds number of the flow Re is modest, leading to a potentially low turbulent heat transfer coefficient $h_a \propto Re^{0.8}$. As a consequence, the wall overtemperature $\Delta T_w = T_w - T$, between the flow and the receiver tube wall, increases. This increases the mean receiver temperature for a given flow temperature, leading to higher heat losses to ambient. Moreover, the risk of receiver overheating arises. Although commercial stainless-steel tubing can easily withstand receiver tube temperatures above 600 °C, the external optically selective coating degrades with excessive temperatures. Zu et al., [38], indicates that the selective coating is typically limited to 450 to 550 ℃ assuming a 20 to 30 years lifetime. [39] indicate a maximum temperature of 600 °C and a limiting operating temperature of 580 °C.

Further concerns affect the receiver tube lifetime. The inhomogeneous peripherical distribution of solar concentrated irradiance across the tube induces non-uniform wall temperature, which causes tube bending [21]. Due to thermal and mechanical properties differences between the receiver and the glass envelope, thermal deformation can cause the glass cover rupture. This is one of the main failure cause of PTC receiver observed in CSP plants. The methods to minimize the thermal deformation range from optical optimization of solar flux distribution, heat transfer enhancement, structural improvement of the metal tube. Peripherical temperature

inhomogeneities are supposed to grow using gaseous HTF due to the low internal heat transfer rate [40].

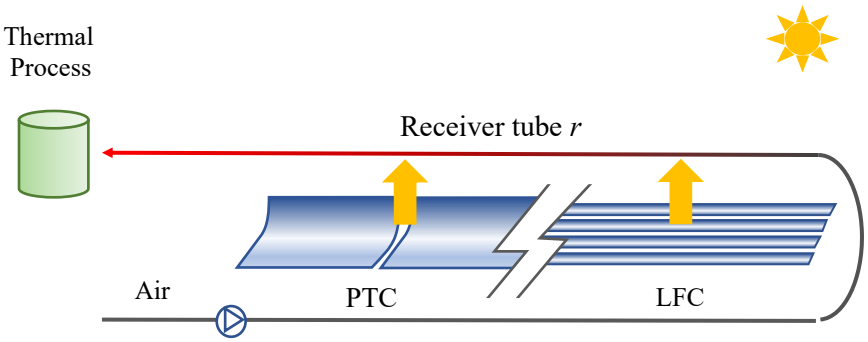

Fig. 1.5. Direct air heating layout using concentrating collectors.

The use of air as HTF, as well as other gases, has been considered by many studies in literature, which highlighted different critical aspects, per the mentioned concerns.

Direct air heating inside concentrating collector is uncommon although an original example is presented in [41] using PTCs delivering air at 280 ℃ at 2 bar. Still, 330 ℃ seemed optimal from CFD simulations. Hot pressurized air is used to evaporate brine from the desalination process, in a spray evaporation tower.

Bellos et al. [42] compared various liquid and gaseous HTFs for their usage inside a PTC, including air. They highlighted as gaseous HTF can withstand higher temperatures than liquid HTF, but the pressure losses represent an important drawback, limiting the exergetic collector efficiency. In a further study, [43], air, nitrogen, carbon dioxide, helium, and argon were analyzed to determine the best working conditions for each gas. Muñoz et al. [40] performed a theoretical and experimental investigation of high temperature and high-pressure gas solar heating using linear concentrating solar collectors. They mainly analysed carbon dioxide, helium, and nitrogen. They indicate that the latest developments on receiver tubes and selective coating provide tubes with a wall temperature limit of 550 ℃, while the pressure can be kept up to 100 bar. They stated that operating with high pressure can reduce significantly the pressure drop across the circuit and the related pumping power. Receiver overheating risks have been studied for PTC operating with superheated steam in [44]. Supercritical CO_2 was theoretically explored by Bellos et al. [45], as HTF inside a PTC, being more favorable than air for direct solar heating.

To overcome the receiver temperature limit drawbacks, several studies have been proposed, aiming at maximum temperature reduction or alternative receiver designs.

The use of extended internal surface has been investigated aiming at wall overtemperature reductions. A PTC operating with gas using longitudinal internal fins has been studied by [46]. Air, helium, and carbon dioxide heating were analysed as HTF. The results indicated that internal fins improve thermal efficiency although they introduce higher stagnation pressure drops. In addition, the authors highlighted as an increase in mass flow rate is beneficial on h_a, although

higher stagnation pressure drops and pumping power consumption are induced by the increased velocities.

Kasperski et al. [47] proposed concentrating solar air heater, which uses a PTC for direct air heating. They analysed different types of internal longitudinal fins for enhancing receiver-to-flow heat transfer. To account for the increased thermal losses as well as for increased pressure drops, they defined a thermo-hydraulic collector efficiency, which includes pumping power consumption. The internal multiple-fins array arrangement proposed resulted in a higher thermohydraulic efficiency compared to a smooth pipe, either considering a double glass envelope with receiver external black painting and a single glass envelope with selective coating. The extra cost of finning internally the tubes is not considered.

Good et al. [48] stated that conventional tubular receivers are not suitable for direct air heating. Instead, an original cavity receiver is proposed for operating air temperature above 600 °C. According to [49], cavity receivers are an optimal solution for direct air heating in PTC, allowing a larger diameter for increased heat transfer area, but they avoid the increase of radiation surface. They developed an innovative cavity receiver for usage with a large-span PTC with 9 m of aperture. They found a pumping power varying from 2.5 kW to 47 kW according to the air mass flow rate for a 200 m long PTC. Heat losses vary between 1533 and 2450 W m^{-1} with air at 500 °C.

1.7 Solar Brayton cycle

The use of air as HTF inside linear concentrating collectors has been also studied in the framework of the solar Brayton cycle for power production. They are Brayton cycles which include solar energy as the heat source, integrating or replacing conventional fuels. To reach competitive efficiency, this cycle needs high air temperature, in the range of 600 ℃ to 1.000 ℃, normally achieved inside the combustion chamber.

Linear concentrating collectors, with the current technology, do not allow this temperature, but they can be still used in combination with a combustion chamber to power a Brayton cycle in solar-assisted gas turbines. Air exiting the compressor is preheated using concentrating solar energy before entering the combustion chamber in a Brayton cycle, as well as in a combined Brayton-Rankine cycle. Ahmadi et al. [50] reviewed the solar-assisted gas turbine researches, [51] analysed possible configurations. Compressed air can be directly preheated flowing inside the solar collectors or indirectly through a heat exchanger, using a conventional HTF. Either in open circuit or closed-circuit layout.

Amelio et al. [52] studied an open direct solar-assisted combined Brayton cycle (Integrated Solar Combined Cycle Systems ISCCS) using PTC. Compressed air at 13.8 bar is sent to PTC solar field and heated for 400 °C up to 580 °C before entering the combustion chamber. Air at 1200 °C expands across the turbine than it fed a Rankine cycle downstream.

One example of a solar-assisted gas turbine is studied by [53]. Compressed air is heated inside a PTC solar field before reaching the combustion chamber. A parametric analysis is carried out to optimize the solar field size and configuration, as well as pressure ratio, turbine inlet temperature, fuel savings. The authors highlight the importance of pressure drop across the

solar field on the system performances. Moreover, the evacuated tube thermal limit seems not considered explicitly.

The use of linear concentrating collector as the unique heat source in the Brayton cycle has been studied with less extend, aiming at lower maximum temperature and modest efficiency. The first direct open solar Bryton cycle was proposed and studied by [54], using PTC solar field as the unique power source. The combustion chamber is avoided. The inlet turbine temperature does not exceed 550 °C according to the evacuated tube thermal limit. Two configurations were discussed, one simple and one with intercooling and regeneration. Although complicating the layout, intercooling increases the compression efficiency but also the required heating power, so that outlet turbine air is used to preheat compressed air. Using a pressure ratio of 9 they obtained a conversion efficiency (useful power over thermal solar power absorbed) of 0.24 and 0.3 respectively for the two configurations.

Cinocca et al. [55] studied a complex direct solar Brayton cycle for electricity production in an open-loop scheme. They use PTC as the heat source, integrated with biomass combustors only for compensating sun variability. The maximum cycle temperature is 580 °C with high pressure of 30 bar. They approached a discrete steps Ericsson cycle by means of implementing four-stage compression intercooled and two-stage reheated expansion. Preheating compressed air using the turbine outlet air, the conversion efficiency of 0.2 is reached.

1.8 Turbo-assisted concentrating solar air heater

According to the open literature, implementing a Brayton cycle for power production using linear concentrating collectors is challenging. The limited maximum air temperature achievable inside the solar receivers with current evacuated tube technology, 500 - 550 °C, limits the mechanical efficiency of the cycle to very low values when very high mechanical efficiency is enabled by compressor and turbine. On the other hand, the cycle could not be self-sustainable as turbomachines decreases and/or pressure drops inside the receiver increases.

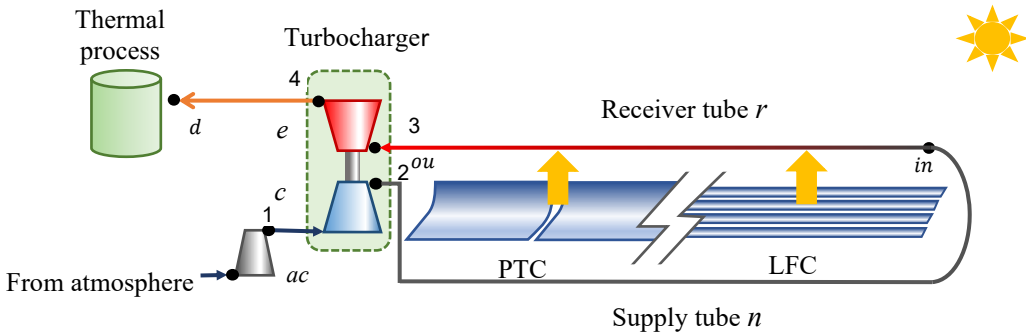

Fig. 1.6. Layout of Turbo-assisted Solar Air Heater (T-SAH) using concentrating linear collectors, shown as an OAC Brayton cycle configuration. The solar receiver tube is *r*, the turbine is *e*, the compressor is *c*, the auxiliary compressor is *ac*, and the supply tube is *n*. Black dots indicate the cycle point.

Moreover, an Open-to-Air (OA) solar Brayton cycle with null mechanical (power) efficiency can still be convenient if the technology aims to provide heat instead of mechanical power (and/or electricity). Compressing ambient air before solar heating increases its density at the receiver inlet and its average value across the receiver length. For a given mass flow rate, the mean

velocity drops reducing the stagnation pressure drops and the pumping power requirements. A turbine placed at the receiver outlet expands the airflow down to ambient pressure, releasing a hot air stream at its outlet and providing both the compressing and pumping power. Since no power is extracted at the turbine and compressor common shaft, a turbocharger can be used for the scope. In a well-designed system, using a compressing ratio from 1.5 to 3.5, typical of turbochargers, and considering the evacuated tube thermal limit, hot airflow at 300-400 °C can be provided at the turbine outlet, available for the industrial usage, with no external power consumption for pumping.

A turbocharger is a compact device that joins a centrifugal compressor and a radial turbine by a common solid shaft. It has been developed for improving the performance of internal combustion engines. The compressor increases the inlet air density at the intake manifold of the engine so that a greater mass of air enters the cylinder at each intake stroke, resulting in higher power output than naturally aspirated engines. The compressor is driven by the expansion of exhaust gases through the turbine, increasing the overall engine efficiency, [56]. The increased output power and efficiency achieved, enable to downsize the engine, matching the pollutant emission reduction and fuel-saving requirements, which arose in the past decades because of more strict regulation and environmental concerns. Nowadays turbocharging is largely applied to passenger cars, trucks, trains, and aircraft, besides to industrial engines. Thanks to the extensive research carried out and its widespread usage, the turbocharger is a reliable and low-cost device, manufactured at a large scale all around the world in a wide range of sizes and models.

Moreover, its application to solar air heaters is innovative. The concept of Turbo-assisted or Turbocharged Solar Air Heater (T-SAH), Fig. 1.6, has been proposed and patented by the ITEA Research Group of Carlos III University of Madrid and has been extensively developed in the present Ph.D. dissertation.

1.9 Objectives and Methodology

The review of the technical literature presented above highlights the relevance of hot air needs in industry and the great potential of the use of solar thermal energy as an alternative source to fossil fuel, aiming at decarbonization. Linear concentrating solar collectors enable to provide heat up to medium temperature range (400 °C), and their application to industrial processes is receiving growing attention, although it is still in its early stage of development. The possibility of direct air heating inside concentrating collector for the industrial processes is not well addressed in the open literature.

This Ph.D. dissertation has several main objectives, which can be summarized as follows:

- To establish the theoretical framework for the viability analysis of direct air heating inside linear concentrating collectors in an Open-to-Atmosphere layout.
- To analyse the physical features of the Turbo-assisted Concentrating Solar Air Heater (T-SAH) establishing the critical aspects and main design and operating parameters that determine its technical feasibility.
- To design, construct and test an original T-SAH prototype of small-scale.
- To identify and face the main technical challenges related to its implementation in a real environment using commercial components.

- To carry out an extensive experimental investigation on the small-scale T-SAH prototype aiming at the characterization of the system behaviour and performances, the required know-how for scaling up to industrial size facilities.
- To develop and validate a numerical model of T-SAH with several levels of accuracy as a tool for experimental analysis, design, and assessment.
- To carry out an extensive feasibility analysis of direct air heating for industrial applications

The thesis is based on combining theoretical and experimental approaches.

Chapter 1 sets the motivation. The state of the art of direct solar air heating for industrial processes has been established throughout the review of technical and scientific literature.

Chapter 2 carries out a theoretical analysis on concentrating solar air heating SAH inside concentrating collectors, using a 1D basic numerical model. Despite its simplicity, it allows one to carry out a full assessment of the technology. The analysis holds general validity and covers both PTCs and LFCs as solar collector types. The innovation of Turbo-assisted solar air heater T-SAH based on a null efficiency solar Brayton cycle is presented. The 1D model developed for SAH is extended, including the basic process of compression and expansion occurring across the turbocharger. The performance of T-SAH is obtained in a wide spectrum of design parameters and operating (collector length, aperture, turbocharger efficiencies, compressing ratio, …).

In Chapter 3, the design, installation, and calibration of the original T-SAH prototype are described in detail. Linear Fresnel collector type is chosen as concentrating technology, configuring a solar field of 79.2 m^2. The design process includes several tasks devoted to face original technical challenges. The high receiver temperature expected and the use of air as heat transfer fluid require carefully consider the thermal dilatation of the receiver tube. Ad-hoc supporting flanges have been developed accordingly. The air circuit has been designed aiming at the minimization of pressure drops and parasitic thermal losses. The blowing unit including the auxiliary compressor, the turbocharger, and auxiliary equipment is designed. The implementation of the control and data acquisition systems is detailed. Two additional components have been designed to be coupled with the basic T-SAH prototype: a post-heating (PH) unit and a thermal energy storage unit (TES).

Chapter 4 reports detailed numerical modelling of the prototype. The solar field model incorporates the optical efficiency and the incident angle modifiers provided by the manufacturer, according to current practice in thermal engineering. The evacuated receiver tube model used for the general prediction of Chapter 2 is improved. Spatial axial discretization allows considering a proper thermal losses coefficient for each length interval, increasing the accuracy. Moreover, the temperature-dependent thermal losses coefficient is inter-extrapolated from experimental data in the open literature. Besides a static (steady-state) receiver model, an original dynamic model has been developed, aiming at increased accuracy on transient heating and cooling prediction.

A turbocharger model has been obtained as an extension of the basic model proposed in Chapter 1. It incorporates the performance of a real turbocharger device, according to its 'maps'. For the compressor, both pressure ratio-mass flow rate relation and the efficiency-mass flow

rate relation for any rotating speed have been obtained from “compressor maps” provided by the manufacturer.

The turbine mass flow rate/pressure ratio relation is also extrapolated from the manufacturer’s map. Moreover, the manufacturer only provides the turbine maximum efficiency, so that the efficiency-pressure ratio relation has been modelled following a theoretical approach.

According to several authors, the turbocharger maps are provided by ‘cold’ test benches, so that their application at real operating temperature should be corrected to account for the heat transfer phenomena occurring between the hot turbine and the colder compressor, as well as to the ambient. Moreover, a critical analysis of the ‘diabatic’ turbocharger behaviour is carried out in Chapter 4 and completed with experimental data obtained in the following Chapter 5.

In Chapter 5 the more relevant results obtained from the experimental campaign on the installed T-SAH prototype are presented and discussed. Several tests are devised to investigate the individual components or the global behaviour of the prototype. Being one of the main technical challenges of this thesis, the feasibility of direct air heating inside the evacuated receiver has been scrutinized. High temperatures are reached under continuous operation, up to 500 °C for the air at the receiver outlet, and close to 600 °C for the tube without tube damage. Either static and dynamic receiver numerical models are validated against experimental data from transient heating and cooling tests devised for this purpose. Linear Fresnel collector operation is analysed, obtaining an experimental estimation of optical efficiency. Experimental correction factors are proposed for improving the accuracy of the optical performance prediction of the specific LFC employed, although the methodology implemented holds general validity. A deep analysis of turbocharger performance is presented. It includes both the adiabatic and diabatic behaviors of the turbocharger under the operating conditions achieved within the proposed T-SAH layout. The experimental post-heating unit is used to increase the heating power of the system and extending the range of turbocharger testing conditions in terms of maximum temperature and pressure. Experimental ‘hot’ test performances obtained have been contrasted with the ‘cold’ performances predicted using extrapolation of the manufacturer’s maps, allowing to quantify the parasitic heat transfer phenomena according to their simplified modeling proposed in Chapter 4.

Globally, the experimental campaign shows the behavior of a small-scale T-SAH allowing its characterization under real ambient conditions, underpinning critical aspects and possible improvements. The experimental data acquired allows the numerical model validation and tuning, preparing the scaling-up studies carried out in the following Chapter 6.

Based on the previous achievements, Chapter 6 presents a feasibility study of T-SAH at an industrial scale, considering solar field size 500 -1.500 m^2. Commercial Linear Fresnel collectors and large-size automotive turbochargers are considered for the scope. A numerical procedure for obtaining a good matching between the solar field and the turbocharger is implemented and applied to several cases of interest. Once the solar field configuration and turbocharger are defined, using the typical meteorological year of the selected location, the behavior of the system is predicted for each hour of the year under quasi-steady-state conditions. The combination of T-SAH layout and simpler SAH layout is investigated. An optimization process

was carried out comparing results from several simulated cases, obtained varying some of the solar field design and operating parameters.

The investigation of possible solutions for thermal energy storage has been considered as a complementary task of this Ph.D. thesis. Solar intermittency and variability can preclude matching the solar heat supply with industrial demand, representing an important obstacle to solar thermal system implementation at a large scale. Thermal Energy Storage TES represents a key technology for mitigating the mismatch between the solar heat supply and industrial demand, increasing the reliability of solar thermal systems. Extensive research has been carried out during the last decades on TES applications for low-temperature domestic heating systems as well as for large-scale and high-temperature concentrated solar power CSP. Medium temperature TES, especially suitable for solar heat for industrial process SHIP applications, has received limited attention, despite its high potential. [57] offers an extensive review on TES systems, analysing the state of the art of technology and materials. They highlight the potential of latent heat storage for industrial applications in the range of temperature 150 – 400 °C. An experimental medium-temperature latent heat storage unit, integrated into the existing T-SAH prototype, has been designed, built, and tested as reported in Chapters 3 and 5.

A Conclusions chapter summarizes the main achievements of this Thesis and highlight possible further works.

2 THEORETICAL BASIS OF DIRECT SOLAR AIR HEATING IN LINEAR CONCENTRATING COLLECTORS

In this chapter, a comprehensive theoretical analysis is carried out on concentrating solar air heater SAH to highlight the relevant technical aspects that characterize its feasibility and performance. A simplified 1D numerical model is presented, as required for capturing the main physical features of concentrating solar collector, the receiver tube, and heat transfer phenomena taking place. The concept of turbo-assisted concentrating solar air heater T-SAH is introduced as a promising solution for effective direct air heating. Compression and expansion processes and their balanced operation as in a turbocharger, are incorporated into the model, obtaining a reliable tool for the first screening of T-SAH behavior, aiming at a first assessment of the technology.

2.1 Linear concentrating collector

Linear concentrating collectors, either parabolic trough PTC or linear Fresnel LFC type can reflect the direct component of solar irradiance G_{bn} impacting on the primary reflector area $A_c = W_a L_c$ toward the receiver tube with a certain optical efficiency η_{op}.The heat flux $\dot{q}_s$ on the receiver external surface $A_r = L_c P_{ex}$ can be expressed as in Eq. (2.1).

$$\dot{q}_s = \frac{G_{bn}\eta_{op}A_c}{A_r} = \frac{G_{bn}\eta_{op}W_a}{P_{ex}} = G_{bn}\eta_{op}C \tag{2.1}$$

$P_{ex} = D_{ex}\pi$ is the external perimeter of the receiver tube with an external diameter D_{ex}. The concentration ratio $C = \frac{W_a}{P_{ex}}$ is a relevant parameter for collector characterization.

Although Eq.(2.1) holds general validity, the parameters which characterize the collector vary remarkably from PTC to LFC, besides to differ for any specific commercial or not commercial example.

Since modularity is a common feature, collector length L_c can be adjusted to any desired value. In CSP installation very long rows $L_c \sim 100$ to $1{,}000$ m are the standard practice. Smaller-scale $L_c \sim 10$ to 100 m are typically considered for SHIP applications. Besides space availability and economic reasons, from a thermodynamic point of view optimal collector row length is related to HTF used as well as operating mass flow rate and concentrating ratio, to meet the output temperature requirements. It is worth mentioning that part of optical losses, referred to as 'optical end losses', are a length-dependent feature, decreasing in relative terms with length [58].

Primary reflector aperture W_a varies according to collector model, from ~ 1 m for small size PTC up to ~ 8 m for the largest example in CSP. For Linear Fresnel collectors W_a is the sum of the aperture w_m of n_m mirrors constituting the discretized primary reflector, Fig.1.3. Both w_m and

n_m vary significantly from one example to another, since an optimum standard design for LFC has not been reached yet. For LFC $W_a \sim 4$ m to 12 m can be considered as a range.

The receiver can have different configurations, including multiple-tube or cavity receiver types. For the present analysis, only a single tube receiver is considered, being also the most used type. Moreover, if not mentioned differently, an evacuated tube with a selective coating is considered. It refers to a stainless-steel tube covered with a special external layer, having low infrared emissivity and high absorptance of the solar radiation spectrum, thus able to reduce the radiation losses to ambient and maximize the sunlight absorption. Besides, it is concentric to a high transparency glass tube, with very low pressure in the annulus aiming at convection losses minimization. Developed for CSP applications, primary for their use with PTC and further extended to LFC, it is commercially available with a tube external diameter D_{ex} between 0.03 m and 0.08 m, with a thickness $e_w \cong 2$ to 5 mm according to plant requirements. Examples on the market are provided by [39], [59].

It follows that concentration ratios $C \sim$10 to 30 are reasonable values for PTC, going up to $C \sim$50 for LFC, although even higher values are possible [60]. The high thermal efficiency of concentrating technologies lays on the fact that concentration ratios $C \gg 1$ allows large primary reflector surface for collecting great amounts solar energy against the small receiver surface, which is instead responsible for thermal losses.

Nevertheless, reaching high optical efficiency is not an easy task, involving design optimization, high-quality constructive material, and a reliable and precise sun tracking system. With current technology maximum optical efficiency range between $\eta_{op,max} \sim 0.5$ to 0.8 varying from PTCs to LFCs. Its off-design value can be lower according to incident solar angle, for which an Incidence Angle Modifier $IAM \sim$0 to 1 is used as correcting factor for $\eta_{op,max}$. For PTCs, the IAM includes the 'cosine effect' produced by the non-null incident angle of sun rays with the reflecting surface normal, the anisotropic optical properties variations as well as 'optical end losses', due to concentrated irradiance impacting away from the tube end [58]. In the case of LFC, the IAM accounts for more complex effects which include, beyond the mentioned ones, also blocking and mutual shadowing, among others [23]. η_{op} is generally expressed as $\eta_{op} = \eta_{op,max}\ IAM$.

As a consequence of optical concentration, the heat flux circumferential distribution across the receiver tube perimeter can be non-uniform, as documented in the open literature, [60] among others. Both for PTC and LFC, the primary reflector focuses the concentrated sunlight mainly on the bottom region of the receiver cross-section. The non-uniform heat flux distribution induces a circumferential temperature gradient on the receiver tube which is especially critical when operating with a low internal heat transfer rate, typical of gaseous HTF or steam. The non-uniform thermal dilatation can cause tube bending with the risk of cover glass breaking, as well as an efficiency loss due to tube displacement from the focal line. Besides this, increased thermal losses and selective coating degradation concerns due to hot spots have oriented the research toward heat flux homogenization. Secondary reflectors based on non-imaging concentration have been optimized for this scope with good results [61]. Based on these considerations, for the present analysis, an uniform heat flux distribution is assumed as a reasonable hypothesis.

According to these considerations, the following analysis assumes the concentrated heat flux $\dot{q}_s$ as the most relevant parameter characterizing the solar input to the receiver, in the same cases

considered, an independent variable for the sensitivity studies of SAH. This way the screening holds general validity, regardless of the collector type, aperture, optical efficiency, and solar irradiance which determine its value. The value considered goes up $\dot{q}_s$~30,000 W m^{-2}.

2.2 Receiver thermal model

Although the evacuated tube receiver has high thermal efficiency, part of the incident energy on the receiver is lost due to heat transfer to the ambient. Several heat transfer mechanisms are involved: radiation occurs between the receiver external surface and the glass cover, as well as from the glass cover to the ambient. Convection is almost null across the vacuum annulus while is not negligible from the glass cover to ambient. Additional parasitic thermal losses can take place from the supporting bracket and bellows. Some detailed numerical models of thermal losses have been developed by many authors, with different levels of accuracy, [62] among others. Experimental thermal losses quantification is also provided, [63], [64], [65] among others.

A uniform tube wall temperature T_w is assumed at each cross-section, as a consequence of the hypothesis of homogeneous circumferential solar heat flux mentioned above.

A global heat losses coefficient can be used to account for heat losses from the receiver tube external wall, at a temperature T_w, toward the ambient at a temperature T_{amb}, expressing heat flux balance on the external tube surface as in Eq.(2.2).

$$\dot{q}_s - U_L(T_w - T_{amb}) = \dot{q}_u \tag{2.2}$$

$\dot{q}_u$ is then the "useful" heat flux transferred to the internal flow. Heat losses coefficient U_L depends on the geometry of the coaxial tubes and the material thermal properties, like thermal conductivity and emissivity, ambient conditions. In general terms, it mainly depends on T_w.

The PTCs and LFCs used for medium and high-temperature liquid HTFs show a relatively small value of the non-dimensional losses' parameter, such that $U_L(T_w - T_{amb})/\dot{q}_s \ll 1$.

In the following chapters of this work, an expression of U_L as a function of wall temperature will be provided. Here, as the first approximation, U_L is considered constant, following typical values in the technical literature $U_L = 3$ to 6 W m^{-2} °C^{-1}, [66] . Since a detailed thermal losses model of the solar tube is not needed for the first screening on Concentrating Solar Air Heater (CSAH), $U_L = 5$ W m^{-2} °C^{-1} will be used here as a reasonable value.

Concerning internal heat transfer, it can be expressed through the coefficient h_a, across the internal perimeter $P = D\pi\varphi$, according to Eq.(2.3). Notice that the factor φ accounts for extended surfaces (finned tube) and its is $\varphi = 1$ for smooth tubes.

$$\dot{q}_u = \frac{h_a P(T_w - T)}{P_{ex}} \tag{2.3}$$

Wall-to-flow h_a can be expressed as a first approximation, using the well known Dittus-Boelter correlation [67], with Re_{D_h} and Pr the Reynolds and Prandlt numbers respectively, $D_h = D\varphi$ the hydraulic diameter, and mass flow $\dot{m}$, Eqs (2.4)-(2.5).

$$h_a = \frac{k}{D_h} 0.023 Re_{D_h}^{0.8} Pr^{0.4} \tag{2.4}$$

$$Re_{D_h} = \frac{4\dot{m}}{\mu \pi D \varphi} \qquad Pr = \frac{\mu c_p}{k} \tag{2.5}$$

The total solar heat power delivered to the flow is $\dot{Q}_u$, according to Eq. (2.6).

$$\dot{Q}_u = P_{ex} \int_0^L \dot{q}_u \mathrm{d}x \tag{2.6}$$

[66] provides a useful formulation for $\dot{Q}_u$ that is widely used in thermal engineering, which is based on the use of the collector efficiency factor F' and heat dissipation factor F_R. This methodology allows express $\dot{Q}_u$ in terms of inlet collector temperature T_{in} and T_{amb}, avoiding T_w evaluation. It lays on constant values of h_a, U_L and $\dot{q}_s$, besides fluid properties, Eq. (2.7). $_t$ indicates stagnation properties.

$$\dot{Q}_u = F_R L P_{ex} [\dot{q}_s - U_L (T_{in} - T_{amb})] = \dot{m}(i_{out} - i_{int}) = \dot{m}\left(c_{p,ou} T_{out} - c_{p,in} T_{int}\right) \tag{2.7}$$

The collector efficiency factor F' relates the wall and flow temperature, Eq.(2.8).

$$F'\langle \dot{m} \rangle = \frac{\dot{q}_s - U_L (T_w - T_{amb})}{\dot{q}_s - U_L (T - T_{amb})} = \left[1 + \frac{U_L P_{ex}}{h_a \langle \dot{m} \rangle P}\right]^{-1} \tag{2.8}$$

An analytical expression of F_R can be obtained by integrating the temperature from the tube inlet $z = 0$ where $T = T_{in}$ to the outlet $z = L$ where $T = T_{ou}$, using an average specific heat $c_{p,m}$, Eq. (2.9).

$$F' P_{ex} \mathrm{d}x = \frac{\dot{m} c_{p,m} \mathrm{d}T_t}{[\dot{q}_s - U_L (T - T_{amb})]} \Longrightarrow F_R = \frac{\dot{m} c_{p,m}}{L P_{ex} U_L} \left[1 - \exp\left(-\frac{L F' P_{ex} U_L}{\dot{m} c_{p,m}}\right)\right] \tag{2.9}$$

Using Eqs. (2.7) to (2.9) an expression for the thermal efficiency of the receiver tube η_r can be formulated Eq. (2.10).

$$\eta_r = \frac{\dot{Q}_u}{\dot{Q}_s} = \frac{\dot{Q}_u}{\dot{q}_s P_{ex} L} = F_R \langle \dot{m} \rangle \left[1 - \frac{U_L (T_{in} - T_{amb})}{\dot{q}_s}\right] \tag{2.10}$$

2.3 Concentrating Solar Air Heater

The above presented 1D steady-state model allows a first assessment of direct solar air heater inside concentrating collector. Fig.2.1 shows the reference layout.

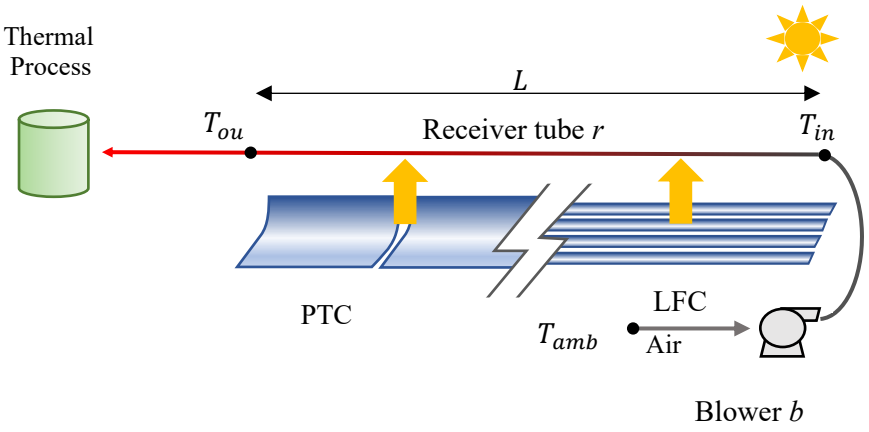

Fig. 2.1. Layout for direct SAH using concentrating linear collectors, in open circuit configuration. The solar receiver tube is r; the blowing fan is b. PTC or LFC type collectors are possible.

The outlet collector temperature is the delivery temperature to the user's thermal process, neglecting thermal losses in the delivery pipe. Inlet receiver temperature T_{in} is affected by the blower. The blower imposes a total overpressure Δp_{pt} which must equal the total pressure drop across the SAH circuit Δp_t. Considering a compressible process air total temperature after compression results from Eq. (2.11), being η_{ptt} the isoentropic total to total compressor efficiency, Following typical values, here assumed $\eta_{ptt} = 0.5$.

$$T_{int} = T_{amb} + \frac{T_{atm}}{\eta_{ptt}}\left[\left(1 + \frac{\Delta p_t}{p_{atm}}\right)^{\frac{\gamma-1}{\gamma}} - 1\right] \tag{2.11}$$

Stagnation pressure drop $\Delta p_t = p_{int} - p_{out}$ are estimated as in Eq. (2.12), considering both its kinetic and frictional components, respectively Δp_{kt} and Δp_{ft}. K_n takes into account localized pressure losses, as bends, connection, section variations, and the Darcy friction factor f characterize the distributed losses on the internal tube surface. The last can be evaluated following Blasius correlation for smooth tubes, Eq. (2.13).

$$\begin{aligned}\Delta p_t &= \overbrace{\frac{1}{2}\left(\rho_{ou} v_{ou}^2 - \rho_{in} v_{in}^2\right)}^{\Delta p_{kt}} + \overbrace{\frac{1}{2}\rho_m v^2 \left(f\frac{L\varphi + L_{nc}}{D} + K_n\right)}^{\Delta p_{ft}} \\ &= \frac{1}{2}\left(\frac{4\dot{m}}{\pi D^2}\right)^2 \left(\frac{1}{\rho_{ou}} - \frac{1}{\rho_{in}} + f\frac{L\varphi + L_{nc}}{\rho_m D} + \frac{K_n}{\rho_m}\right)\end{aligned} \tag{2.12}$$

$$f = 0.316 Re_{D_h}^{-\frac{1}{4}} \tag{2.13}$$

It is worth mentioning that the overall air circuit length can be greater than just collector length L, due to connection length with the blower or/and with the delivery point so that a corresponding L_{nc} is included in Eq. (2.12), with the same diameter D for simplicity.

Two aspects are investigated to establish their influence on the design and operating parameters:

- The thermal limit of the receiver tube
- The pumping power consumption by the blower *b*

2.3.1 Receiver thermal limit

Combining Eqs. (2.3) and (2.4) an expression of receiver wall over-temperature $\Delta T_w = T_w - T$ can be obtained, Eq. (2.14), highlighting its dependency on h_a. As mentioned h_a for air and gases, in general, is low compared to liquid substances commonly used as HTF and mainly function of Reynolds number, thus related to mass flow rate $\dot{m}$. For a given $\dot{q}_s$ and $\dot{q}_u$, ΔT_w decreases for a growing mass flow rate. Moreover, the use of extended internal surface (finned tubes) with $\varphi > 1$ is beneficial for reducing ΔT_w.

$$\Delta T_w = T_w - T = \frac{\dot{q}_u}{h_a}\frac{P_{ex}}{P} = \frac{\dot{q}_u}{0.023\varphi^2 \frac{k}{D\varphi} {Re_{D_h}}^{0.8} Pr^{0.4}}\frac{D_{ex}}{D\varphi} \quad \propto\approx \frac{\dot{q}_s}{\underbrace{\left(\frac{\dot{m}^{0.8}}{D^{1.8}}\right)}_{\approx(\rho v)^{0.8}} \varphi^{1.2}} \tag{2.14}$$

A drawback related to increased ΔT_w is the high length-average wall temperature $T_{w,m} = (T_{w,in} + T_{w,ou})/2$, which reduces the collector efficiency. In addition to that, an excess of thermal dilatation of the tube material will occur, which causes mechanical stress on receiver tube, the glass cover and the junctions.

Considering a maximum wall temperature limited to $T_{w,max} \leq 450$ °C to 600 °C with current technologies, an high value of ΔT_w reduces the maximum fluid temperature achievable inside the receiver $T_{max} = T_{w,max} - \Delta T_w$.

It follows that for a given desired outlet temperature T_{ou}, Eq. (2.15) defines the minimum mass flow rate which can be employed without overcoming $T_{w,max}$. In fact, when using exactly $\dot{m}_{min}$, the maximum wall temperature reached at the collector outlet section is $T_{w,ou} = T_{w,max}$.

$$\dot{m}_{min} = \frac{\mu\pi D\varphi}{4}\left(\frac{\dot{q}_s - U_L\left(T_{w,max} - T_{amb}\right)}{0.023\left(T_{w,max} - T_{ou}\right)\varphi^2 \frac{k}{D} Pr^{0.4}}\right)^{1.25} \tag{2.15}$$

Besides affecting ΔT_w, the mass flow rate $\dot{m}$ determine the temperature at the collector outlet T_{ou} for a given length L and $\dot{q}_s$. Rewriting Eq. (2.7) including Eq. (2.9) it can be seen as T_{ou} depends on the operating parameters $\dot{m}$ and $\dot{q}_s$ besides on the design parameter L.

$$\frac{\dot{q}_s c_{p,m}}{U_L}\left[1 - \exp\left(-\frac{L\, P_{ex} U_L}{\left(1 + \frac{U_L D_{ex}}{h_a D}\right)\dot{m} c_{p,m}}\right)\right]\left(1 - \frac{U_L(T_{in} - T_{amb})}{\dot{q}_s}\right) = c_{p,ou} T_{out} - c_{p,in} T_{int} \tag{2.16}$$

Solving iteratively Eq (2.16) with T_{int} from Eq (2.11), the mass flow rate $\dot{m} = \dot{m}_{Tou}$ which ensures a given output temperature T_{ou} can be found.

Introducing $\dot{m}_{min}$ of Eq. (2.15) into Eq. (2.16), $T_{w,max}$ and T_{ou} give a compact condition, which determines a minimum allowable collector length L_{min} for any $\dot{q}_s$, Eq. (2.17).

$$\frac{\dot{q}_s c_{p,m}}{U_L}\left[1-\exp\left(-\frac{L_{min}\,P_{ex}U_L}{\left(1+\frac{U_L D_{ex}}{h_a D}\right)\dot{m}_{min}c_{p,m}}\right)\right]\left(1-\frac{U_L(T_{in}-T_{amb})}{\dot{q}_s}\right)=c_{p,ou}T_{out}-c_{p,in}T_{int} \qquad (2.17)$$

According to the above equations, using the parameter in Tab.2.1, the wall overtemperature ΔT_w can be computed for any length L, concentrated irradiance $\dot{q}_s$ and the corresponding mass flow rate $\dot{m}_{Tou}$ which gives the desired output temperature $T_{ou} = 350°C$. They are reported in Fig. 2.2 for relatively small L and several $\dot{q}_s$. It can be observed as for high $\dot{q}_s$, a short collector with low mass flow rate $\dot{m}_{Tou}$ have a modest h_a and a high ΔT_w which can also overcome $T_{w,max} - T_{ou.}$

Table 2.1. Common parameters to the different simulation cases.

$T_{amb} = T_{atm}$	p_{atm}	D	D_{ex}	U_L	φ	K_n	L_{nc}
10 °C	1.013 bar	0.066 m	0.07 m	5 W m^{-2} °C^{-1}	1.0	2.0	6 m

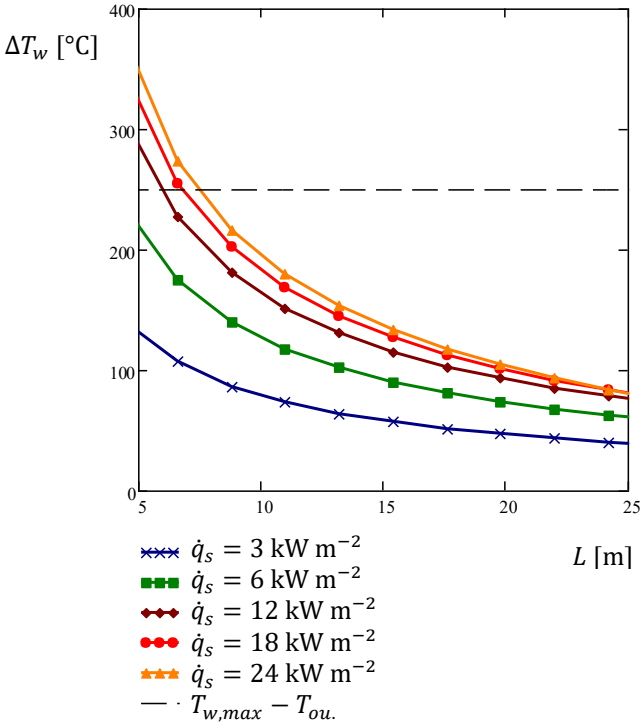

Fig. 2.2. Wall overtemperature versus length for several concentrated irradiances, with $T_{ou} = 350$ °C and $T_{w,max} = 600$ °C

The minimum length L_{min} admitted according to the thermal limit $T_{w,max}$ and the desired outlet temperature T_{ou} is computed and reported in Fig. 2.3, against $\dot{q}_s$ for several T_{ou} and $T_{w,max}$ of interest. Considering the highest thermal limits $T_{w,max} = 600$ °C, L_{min} is very small, but it grows for a lower thermal limit of $T_{w,max} = 500$ °C, turning into a severe constraint to the feasibility of SAH for a less performing receiver tube, with medium temperature $T_{ou} = 300$ °C and $T_{ou} = 400$ °C.

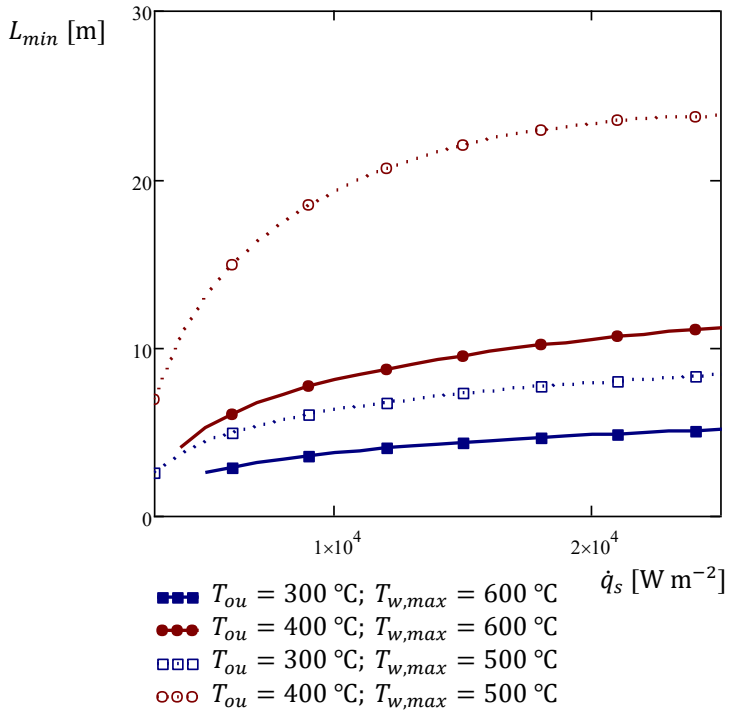

Fig. 2.3. Minimum length L_{min} allowed by thermal limit $T_{w,max}$ versus concentrated solar irradiance $\dot{q}_s$ for different T_{ou} and $T_{w,max}$, according to parameters in Tab.2.1.

2.3.2 Pumping power

The low volumetric heat capacity of air as other gases, compared with a liquid HTF implies that for a given mass flow rate necessary to obtain the desired outlet temperature as in Eq. (2.16), higher velocities v are reached inside the receiver tube. This leads to not negligible stagnation pressure drop across the receiver length and increased pumping power $\dot{W}_p$ consumed by the blower.

The pumping power can be evaluated considering a blower isentropic efficiency, total to total η_{ptt} and the exit kinetic energy valuable, according to Eq. (2.18). It also explicates the incompressible approximation. $O\langle\ \ \rangle$ indicates an infinitesimal of the order indicated, in a Taylor series expansion for $\Delta p_t / p_{atm} < 1.0$.

$$\dot{W}_p = \dot{m} c_{p,p} (T_{int} - T_{atm}) = \dot{m} \frac{c_{p,p} T_{atm}}{\eta_{ptt}} \left[\left(1 + \frac{\Delta p_t}{p_{atm}} \right)^{\frac{\gamma-1}{\gamma}} - 1 \right] = \dot{m} \frac{c_{p,p} T_{atm}}{\eta_{ptt}} \left[\frac{\Delta p_t}{p_{atm}} + O\left\langle \left(\frac{\Delta p_t}{p_{atm}} \right)^2 \right\rangle \right] \tag{2.18}$$

Using Eq. (2.16) to compute the required mass flow rate for a given T_{ou}, the obtained value $\dot{m}_{Tou}$ can be introduced in Eq. (2.12) to estimate Δp_t for several $\dot{q}_s$, varying L. Results for a delivery temperature of $T_{ou} = 350$ °C are reported in Fig. 2.4, showing both Δp_t and $\dot{m}_{Tou}$.

High $\dot{q}_s$ require high $\dot{m}_{Tou}$ to limit T_{ou} to the specified value, inducing high Δp_t, as a consequence of the high v, even for relatively small L. For modest $\dot{q}_s$, lower $\dot{m}_{T_{ou}}$ would be used, with lower velocities and pressure drops also for long collector rows.

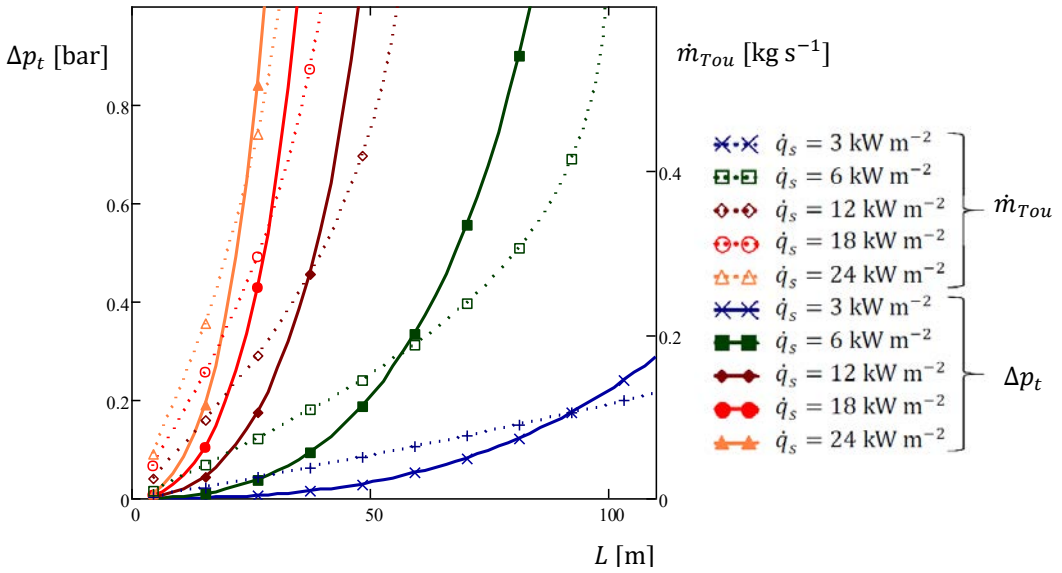

Fig. 2.4. Total pressure drop Δp_t and mass flow rate $\dot{m}_{Tou}$ versus L for $T_{ou} = 350$ ℃.

The pumping power consumption follows the same trends as Δp_t. To obtain a reasonable quantification, it has been compared with the useful solar thermal power absorbed by the airflow in the same conditions $\dot{Q}_u$. Thus the pumping ratio $R_p = \frac{\dot{W}_p}{\dot{Q}_u}$ can be defined to estimate the amount of external power needed to pump air inside the receiver tube in relative terms. An expression for R_p is obtained combining Eqs. (2.12), (2.16) and (2.18).

$$R_p = \left[\left(1 + \frac{8\dot{m}_{Tou}^2}{p_{atm}\pi^2 D^4} \left(\frac{1}{\rho_{ou}} - \frac{1}{\rho_{in}} + 0.316 \frac{L\varphi + L_{nc}}{\rho_m D} \left(\frac{4\dot{m}_{Tou}}{\mu\pi D\varphi} \right)^{-\frac{1}{4}} + \frac{K_n}{\rho_m} \right) \right)^{\frac{\gamma_p - 1}{\gamma_p}} - 1 \right] \cdot \frac{c_{p,p} T_{atm}}{(c_{p,ou} T_{out} - c_{p,in} T_{int})\eta_{ptt}} \tag{2.19}$$

The variation of R_p as a function of L is shown in Fig. 2.5 for several values of concentrated solar irradiance $\dot{q}_s$.

Highly concentrating collectors having high $\dot{q}_s$ operates with high $\dot{m}$ to limit T_{ou}. As consequence, they require great pumping powers, $\dot{W}_p \propto \dot{m}^{(2\text{ to }3)}$, which can be in the same order of magnitude of the solar gain $\dot{Q}_u$.

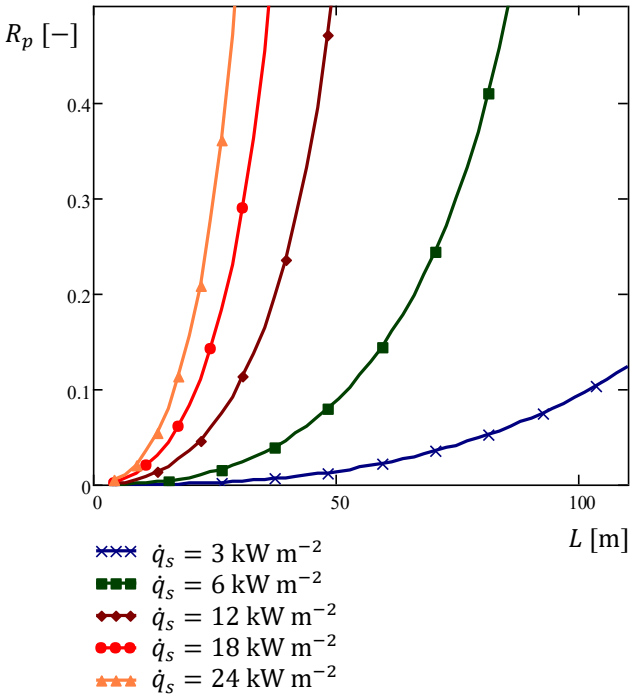

Fig. 2.5. Pumping ratio R_p versus L for several concentrated solar irradiances $\dot{q}_s$. $T_{ou} = 350$ ℃.

Due to its importance for the viability of direct concentrating solar air heating the pumping power is detailed in Eq. (2.20), showing the dependency on basics parameters, assuming incompressible evolution in the blower and splitting it into two components, kinetic $\dot{W}_{pk}$ and frictional $\dot{W}_{pf}$, as done for the stagnation pressure drop.

$$\dot{W}_{pk} \approx \dot{m}\frac{\Delta p_{kt}}{\rho_m \eta_{ptt}} \propto \dot{m}^3 D^{-4} \rho_m^{-2}; \quad \dot{W}_{pf} = \dot{m}\frac{\Delta p_{ft}}{\rho_m \eta_{ptt}} \propto \dot{m}^{2.75} L \rho_m^{-2} \mu^{0.25} D^{-4.75} \varphi^{1.25} \qquad (2.20)$$

Either looking at $\dot{W}_{pk}$ than $\dot{W}_{pf}$ their strong dependency on inner diameter D can be noticed. It follows that enlarging the tube diameter D is highly beneficial for decreasing $\dot{W}_p$. Tubes of larger D could be commercially available in the future as solar thermal power plants increase the PTC mirror width W_a from 6 to 8 or even to 10 m. A larger D would have a negative impact on thermal losses, thus deteriorating the thermal efficiency. Using internal fins, although desirable for reducing ΔT_w, has the drawback of increasing pumping power. The effect of the high pumping power is remarkable on the inlet receiver temperature T_{in}, according to Eq. (2.11), as shown in Fig. 2.6.

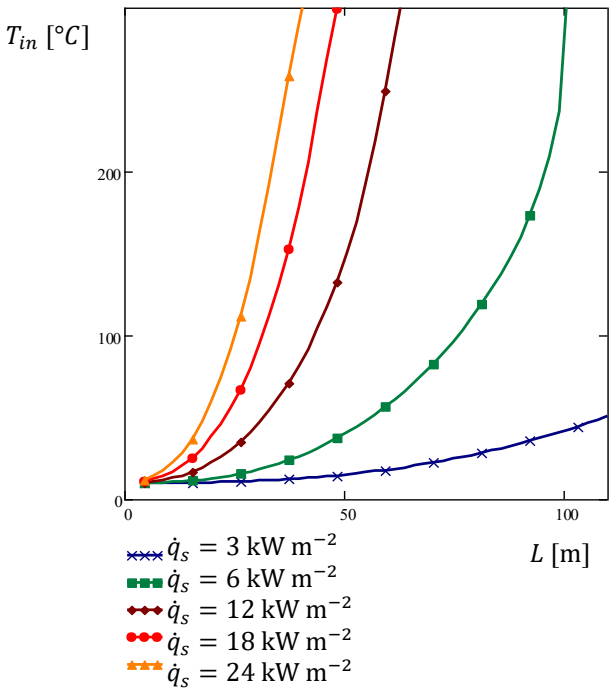

Fig. 2.6. Inlet receiver temperature versus L for several concentrated solar irradiances $\dot{q}_s$. T_{ou} = 350 ℃.

2.3.3 Thermal and global efficiency

The thermal efficiency of the receiver has been defined in Eq. (2.10) and can be rewritten as using $\dot{m}_{Tou}$ which ensures a desired T_{ou}.

$$\eta_r = \frac{\dot{m}_{Tou} c_{p,r}}{L P_{ex} U_L}\left[1 - \exp\left(-\frac{L P_{ex} U_L}{\dot{m}_{Tou} c_{p,r}\left(1 + \frac{U_L P_{ex}}{h_a P}\right)}\right)\right]\left[1 - \frac{U_L (T_{in} - T_{amb})}{\dot{q}_s}\right] \qquad (2.21)$$

An air heating efficiency parameter η_{SAH} can be defined to further characterize the SAH, including as primary source the pumping power consumed by the blower, Eq (2.22). Moreover, the global output energy delivered to the user $\dot{Q}_a = \dot{m}_{Tou}\left(c_{p,ou} T_{out} - c_{p,atm} T_{amb}\right)$ come from solar energy absorbed $\dot{Q}_u$ and also from the blower $\dot{W}_p$, being $\dot{Q}_a = \dot{Q}_u + \dot{W}_p = \dot{Q}_u\left(1 + R_p\right)$.

Since electricity is needed to run the blower with a total-to-total isentropic efficiency η_{ptt}, the electrical pumping consumption is accounted for in terms of primary energy considering an average electricity efficiency, from primary energy to plug, of $\eta_{eg} \approx 0.15$ to 0.5. Here, an average value $\eta_{eg} = 0.42$ and an electro-mechanical pumping efficiency $\eta_{emp} = 0.95$ are chosen. It is worth mentioning that η_r and η_{SAH} are defined consider as a primary source the concentrated solar power $\dot{Q}_s = W_a L G_{bn} \eta_{op}$ instead of gross solar energy impacting on the

primary reflector $\dot{Q}_{bn} = W_a L G_{bn}$. In other words, they do not include optical efficiency $\eta_{op} = \frac{\dot{Q}_s}{\dot{Q}_{bn}}$.

$$\eta_{SAH} = \frac{\dot{Q}_a}{\dot{Q}_s + \frac{\dot{W}_p}{\eta_{emp}\eta_{eg}}} = \frac{\dot{m}_{Tou}\left(c_{p,ou}T_{out} - c_{p,atm}T_{amb}\right)}{LP_{ex}\dot{q}_s + \frac{\dot{W}_p}{\eta_{emp}\eta_{eg}}}; \tag{2.22}$$

η_r and η_{SAH} coincide for $\dot{W}_p = 0$ and they are close at the very small scale where $\dot{W}_p$ is negligible as can be observed in Fig.2.7. It shows efficiencies against L for an outlet temperature of $T_{ou} = 350°C$ and corresponding $\dot{m}_{Tou}$, for different $\dot{q}_s$. η_{SAH} diverges from η_r toward lower values for increasing length because of greater $\dot{W}_p$ requirement either due to higher $\dot{m}_{Tou}$ and to a larger frictional surface. The drop of η_{SAH} is deeper as higher is heat flux, besides to take place at smaller L. This is coherent with Fig .2.4 and Fig. 2.5 and reflects the higher $\dot{m}_{Tou}$ required for greater input power. According to the R_p, as L and $\dot{q}_s$ increase, a higher portion of final energy delivered $\dot{Q}_a$ comes from $\dot{W}_p$, hence from electricity.

A further important feature can be noticed. The curves in Fig. 2.6 stops at a certain length. This is because a further increase in length would lead to overcoming the wall thermal limit, due to excessive receiver inlet temperature caused by compression.

The thermal efficiency η_r does not change remarkably with length. Instead, it is much more affected by heat flux $\dot{q}_s$. According to the principles of concentrating technology, collectors with a higher concentration ratio C, thus larger $\dot{q}_s$, yield better thermal performances for having a smaller ratio $U_L(T_w - T_{amb})/\dot{q}_s$.

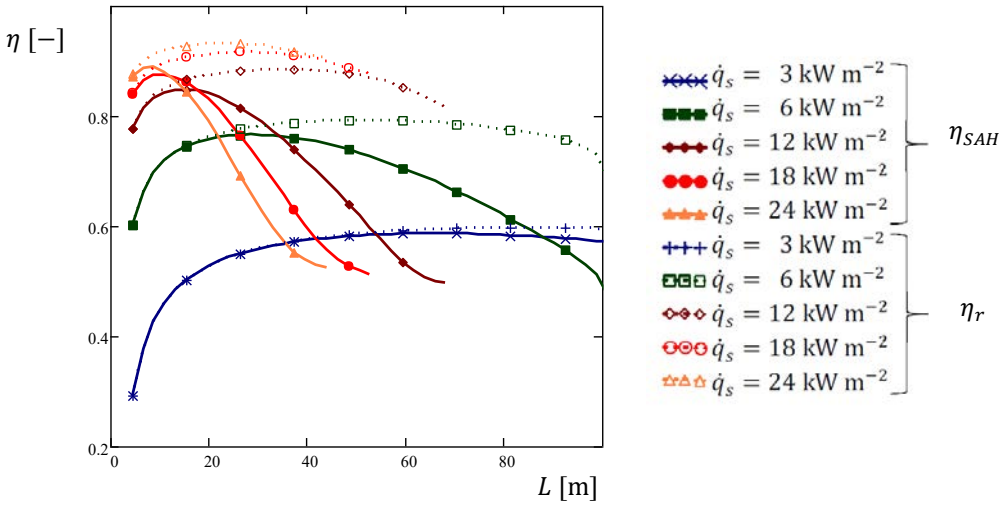

Fig. 2.7. Direct solar air heating efficiency η_{SAH} (solid line) and receiver efficiency η_r (dashed line) versus L for different $\dot{q}_s$. $T_{ou} = 350$ ℃.

Consequently, a concentrating SAH system designed for small $\dot{q}_s$, thus small apertures, needs a small pumping power, Fig. 2.5, even for large L but it carries the drawback of lower thermal

efficiency η_r, leading to modest η_{SAH}, which account for both effects. Collector with large aperture must be necessarily short, otherwise, the pumping power is too high, as well as R_p.

2.4 Turbo-assisted concentrating solar air heater

According to the previous analysis, the minimization of pumping power is of great importance for the technical feasibility of SAH, especially aiming at medium-scale installation and acceptable thermal efficiency, besides low electricity demand.

Looking at Eq. (2.20) in the previous section, it is evident as both frictional and kinetic components of pumping power decrease quadratically with mean air density, for a given diameter and mass flow rate used. Even a moderate increase of density would induce a remarkable pumping power reduction. From this point of view compressing ambient air at the receiver inlet is beneficial for reducing mean velocities, pressure drop, and hence $\dot{W}_p$ across the receiver, but compressing power is required. Moreover, installing a turbine a the collector outlet would allow recovering compressing power from the expansion process. This way an open circuit Brayton cycle is configured, according to the concept patented [68]. If the turbine can provide the compressing power as well as the pumping power required, then the external pumping power required is canceled. As previously mentioned in the introduction chapter, the solar Brayton cycle obtained aims at null mechanical efficiency, ensuring a hot air stream at medium temperature as output for its usage in thermal air-based industrial processes. A turbocharger joins in a compact device a centrifugal compressor and a radial turbine sharing a common shaft. As they have been developed by the automotive industry to enhance the performance of the internal engine, they are reliable and low-cost devices. Fig. 2.8 shows the layout of the Turbo-assisted solar air heater.

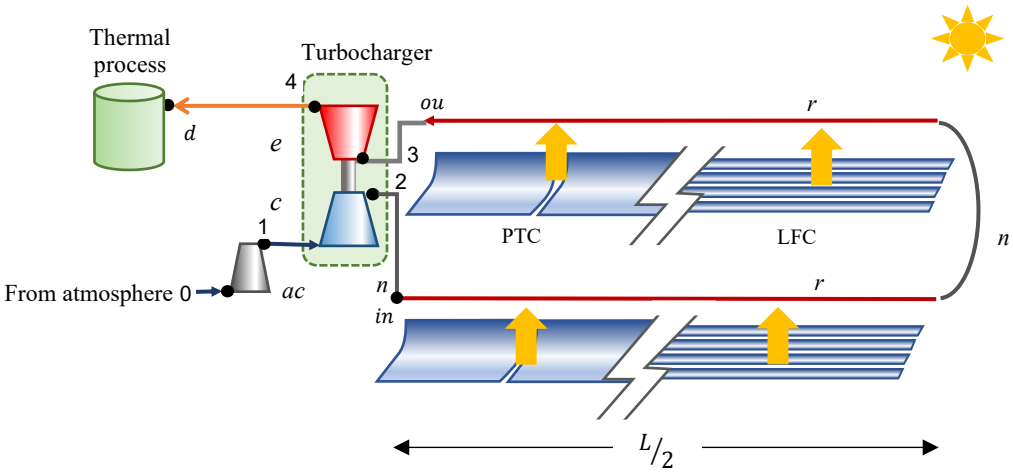

Fig. 2.8. Layout of T-SAH using concentrating linear collectors, shown as an OAC Brayton cycle configuration. The solar receiver tube is *r*, the turbine is *e*, the compressor is *c*, the auxiliary compressor is *ac*, and the supply tube is *n*. Black dots indicate the cycle point.

An auxiliary compressor, electrically driven, is foreseen for transient operation only or control purposes. During normal operation turbocharger is *freewheeling* with the turbine power, extracted from heated air enthalpy, compensating the compressing and pumping power consumption. Under this condition, a direct solar air heater would be possible without any external energy consumption for pumping. The modest compression ratio typical in

turbochargers goes from 1.5 to 4, implying a modest density increase with a remarkable effect on pumping power reduction. Compression also implies an inlet receiver temperature increase up to 100 - 150°C. Due to the receiver's thermal limit, outlet temperature does not overcome 500-550 °C as a maximum, which limits the turbine power. Nevertheless, the moderate expansion ratio allows an outlet turbine temperature of 300-400 °C, suitable for driving medium temperature industrial thermal processes.

In the following sections, general screening of the proposed T-SAH is carried out to identify the critical aspects and most relevant design and operating parameters. For that, a basic numerical model is implemented, as an extension of concentrating SAH numerical model presented above, using the introduction of air compression and expansion processes.

2.4.1 T-SAH basic model

Considering the layout of Fig.2.8, air pressure and temperature in the main point of the cycle can be estimated according to the following equations. Since the auxiliary compressor is bypassed under steady-state operation $p_{1t} = p_{amb}$, and $T_{1t} = T_{amb}$. Total pressure at compressor outlet (2) results from the compression ratio $\pi_c = \frac{p_{2t}}{p_{1t}}$, while the temperature comes from Eq.(2.23).

$$T_2 = T_{1t}\left[1 + \left(\pi_c^{\frac{\gamma_c - 1}{\gamma_c}} - 1\right)\eta_{ctt}^{-1}\right] - \frac{{v_2}^2}{2c_{p,2}} \tag{2.23}$$

η_{ttc} is the isentropic total to total efficiency. It allows also to express the compression power consumed for a given π_c as in Eq. (2.24).

$$\dot{W}_c = \dot{m} c_{p,c} T_{atm}\left(\pi_c^{\frac{\gamma_c - 1}{\gamma_c}} - 1\right)\eta_{ctt}^{-1} \tag{2.24}$$

The configuration of the solar field admits several configurations. Due to the presence of the turbocharger the inlet and outlet of the heating circuit must be located on the same side of the solar field. This means having a straight collector row of length L, as shown in Fig. 1.6, where a thermally insulated pipe with the same length $L_n \sim L$ is needed to supply air compressed air to the receiver inlet. Another possibility is to have a U-loop configuration, made of two straight collector rows of length $\frac{L}{2}$ each, as shown in Fig.2.8. This way the supply tube length is reduced to the connection between receivers and with the turbocharger. Selecting the best option between straight or U-loop configuration can be the object of an optimization process, which will be discussed in the following chapters of this thesis. Inlet air conditions can differ from outlet compressor (2) due to supply tube n, when present. In general terms, assuming a not negligible supply tube length L_n imply frictional pressure drops Δp_{fnt} Eq. (2.25), while the thermal losses can be neglected for thermally insulated tubes. It follows that inlet receiver air conditions are $T_{in} \approx T_2$ and $p_{in} = p_{2t} - \Delta p_{fnt} - \rho_{in}{v_{in}}^2/2$.

$$\Delta p_{fnt} = \frac{1}{2}\rho_2 v_{in}^2\left(f\frac{L_n}{D_n} + K_n\right) \tag{2.24}$$

K_n is used for concentrated pressure drops due to bends, connections, or cross-section variation elements.

Between points (2) and (3) air heating takes place absorbing thermal power $\dot{Q}_u$, according to Eq. (2.7). Air exits the receiver tube at $T_3 = T_{ou}$, corresponding to inlet turbine total temperature $T_{3t} = T_{ou} + {v_3}^2/2c_{p,3}$. Total pressure p_{3t} is reduced by pressure drop, Eq (2.25), inside the receiver both caused by friction and acceleration $p_{3t} = p_{in} + \rho_{in}{v_{in}}^2/2 - \Delta p_{frt}$.

$$\Delta p_{rt} = \frac{1}{2}\left(\frac{4\dot{m}}{\pi D^2}\right)^2 \left(\frac{1}{\rho_3} - \frac{1}{\rho_2} + f\frac{L\varphi}{\rho_m D}\right) \tag{2.25}$$

The expansion provides mechanical power $\dot{W}_e$, expressed in Eq. (2.26) using isoentropic total to total efficiency η_{ett} and the total to total pressure ratio $\pi_e = \frac{p_{3t}}{p_{4t}}$. The outlet turbine temperature Eq. (2.27) coincides with the delivery temperature $T_d = T_4 = T_{4t} - \frac{{v_4}^2}{2c_{p,4}}$ neglecting thermal losses across the delivery pipe.

$$\dot{W}_e = \dot{m}c_{p,e}T_{3t}\left[1 - \pi_e^{-\frac{\gamma_e - 1}{\gamma_e}}\right]\eta_{ett} \tag{2.26}$$

$$T_{4t} = T_{3t}\left[1 - \eta_{ett}\left(1 - \pi_e^{-\frac{\gamma_e - 1}{\gamma_e}}\right)\right] \tag{2.27}$$

The output turbine pressure p_{4t} is in general terms the ambient pressure. Nevertheless, having $p_{4t} > p_{amb}$ can be useful for the user, as for compensating the pressure drop in the delivery pipe or in the thermal process. It holds $p_{4t} = \pi_R p_{amb}$, with $\pi_R = 1$ is considered if it is not otherwise specified.

2.4.2 Freewheeling and the thermal limit

In steady-state operation, the condition for T-SAH avoiding the auxiliary compressor consumption lays on the mechanical balance on the turbocharger shaft. Newton's second law of rotating systems Eq. (2.28), with J_T being the turbocharger polar inertia, η_m the mechanical efficiency, and n_T the speed, it results in Eq. (2.29) under steady-state operation.

$$\left(\frac{\dot{W}_e\eta_m}{n_T} - \frac{\dot{W}_c}{n_T}\right)\frac{1}{J_T} = 2\pi\frac{\mathrm{d}n_T}{\mathrm{d}\tau} \tag{2.28}$$

$$\dot{W} = \dot{W}_e\eta_m - \dot{W}_c = 0 \tag{2.29}$$

Introducing Eqs. (2.24) and (2.26) into Eq (2.29), an expression of mechanical equilibrium under turbocharger freewheeling is obtained, Eq. (2.30).

$$c_{p,c}T_{atm}\left(\pi_c^{\frac{\gamma_c - 1}{\gamma_c}} - 1\right) = \underbrace{\eta_{ctt}\eta_{ett}\eta_m}_{\eta_T} c_{p,e}T_{3t}\left[1 - \left(\frac{\pi_c\left(1 - \frac{\Delta p_{nrt}}{p_{2t}}\right)}{\pi_R}\right)^{-\frac{\gamma_e - 1}{\gamma_e}}\right] \tag{2.30}$$

The main parameters affecting mechanical balance can be noticed, as compression ratio π_c inlet turbine temperature T_{3t}, the pressure drop across the air circuit $\Delta p_{nrt} = \Delta p_{nt} + \Delta p_{rt}$. Besides them, turbocharger efficiency $\eta_T = \eta_{ctt}\eta_{ett}\eta_m$ play an important role. Even though not explicitly shown by Eq. (2.30), turbocharger freewheeling depends on mass flow rate. Both

pressure drops Δp_{nrt} and T_{3t} are a function of operating mass flow rate, Eqs (2.31) and (2.32). It is worth mentioning that also π_c as well as η_{ctt} and η_{ett} could vary with mass flow rate, according to the performance of the specific turbocharger considered. Nevertheless, in the present general analysis π_c as well as and η_{ctt} and η_{ett} are considered as independent variables.

$$\Delta p_{nrt} = \overbrace{\frac{1}{2}\left(\frac{4\dot{m}_{\dot{W}=0}}{D_n^2\pi}\right)^2\left(\frac{K_n}{\rho_2}+f\frac{Sl\,P_{ex}+L_{nc}}{\rho_2 D_n}\right)}^{\Delta p_{nt}} + \overbrace{\frac{1}{2}\left(\frac{4\dot{m}_{\dot{W}=0}}{D^2\pi}\right)^2\left(\frac{1}{\rho_3}-\frac{1}{\rho_2}+f\frac{Sl\,P_{ex}\,\varphi}{\rho_m D}\right)}^{\Delta p_{rt}} \tag{2.31}$$

$$c_{p,3}T_{3t} = \frac{c_{p,m}}{U_L}\left[1-\exp\left(-\frac{LF'P_{ex}U_L}{\dot{m}_{\dot{W}=0}c_{p,m}}\right)\right][\dot{q}_s - U_L(T_2-T_{amb})] + c_{p,2}T_{2t} \tag{2.32}$$

Solving Eqs (2.30) to (2.32) allows finding the mass flow rate $\dot{m}_{\dot{W}=0}$ which ensures turbocharger freewheeling, given the turbocharger parameters π_c, η_T and collector parameters $\dot{q}_s$ and L.

Once $\dot{m}_{\dot{W}=0}$ is defined to fulfill the mechanical constraint, then the receiver thermal limit constraint must be verified. The highest receiver wall temperature reached at the collector outlet section, $T_{w,ou}$, must be below the maximum allowed value $T_{w,max}$. As shown in Eq. (2.33), $T_{w,ou}$ depends on the mass flow rate, besides $\dot{q}_s$ and T_{ou}.

$$T_{w,ou} = \frac{\dot{q}_s + T_{ou}h_a\langle\dot{m}_{\dot{W}=0}\rangle\frac{D}{D_{ex}\varphi} + T_{amb}U_L}{h_a\langle\dot{m}_{\dot{W}=0}\rangle\frac{D}{D_{ex}\varphi} + U_L} \tag{2.33}$$

The values of π_c , η_{ctt} and η_{ett} considered in the present analysis, Tab.2.2, are chosen following recommendations in open technical literature. For compressors, [69] estimated a maximum achievable total to static polytropic efficiency of $\eta_{cpts} = 0.8$, very near the total to total isentropic efficiency η_{ctt} owing to the moderate π_c, and the low exit Mach numbers. For turbines, the maximum achievable polytropic efficiency estimated by [69] is $\eta_{epts} = 0.9$, very near the isentropic efficiency η_{ett} for the same reasons. An optimum choice for this application would be one-stage radial types owing to the moderate $\dot{m}$ envisaged. In the range of $1.5 < \pi_c < 3$, this type of turbomachines show a wide area of efficiencies near the maximum. The present analysis assumes commercial values of such efficiencies, following guidelines in an ample selection of open literature, such as [70] as a classical text, [71] and [72] for turbochargers of the size adequate for internal combustion engines,[73] for a wider view of mixed flow radial turbines, and [69] for general efficiency correlations for turbomachines.

It is well-known that the reachable maximum efficiencies, at the design point, are higher when the size of the turbomachine is larger, characterized by $\dot{m}$, and more generally for the Reynolds number of its rotor tip speed at the design point Re^* using density and viscosity at the inlet section. Weigel and Bal [74] coincide with other authors to estimate the size effect of centrifugal compressors found in typical turbochargers (axial inlet, radial outlet, no stator guide vanes) with formulae like Eqn. (2.34), where $_{ref}$ indicates reference values. According to real data, the exponent seems to decrease with Re^* down to near 0 for $Re^* > \sim 10^6$. Capata and Sciuba in their publications [75] and [76] offer some comparisons among the different correction variants.

$$\frac{1-\eta_{ctt}}{1-\eta_{ctt,ref}} = \left(\frac{Re^*}{Re^*_{ref}}\right)^{0.1 \text{ to } 0.25} \tag{2.34}$$

Concerning the mechanical efficiency of the shaft η_m, at the nominal operating point of the turbocharger, there is not much difference in its values either for plain, ball, and foil bearings, or magnetic levitation. At low speeds, plain bearings dissipate more relative power than the other two alternatives because of external power. For that, they need a higher oil circulation than ball bearings, but in any case, the power consumed is minute compared with $\dot{Q}_u$. The above-described analysis on design point efficiencies supports the values taken in this chapter, Tab. 2.2, and characterizes them as conservative and representative for the smallest facility sizes, below a gross value of 50 kW of heat power.

2.4.3 Efficiency

As done for the simple SAH, efficiency parameters can be defined to evaluate the performance of T-SAH. Receiver thermal efficiency Eq. (2.10) can be rewritten as in Eq. (2.35). Moreover, heating efficiency is defined as in Eq. (2.36).

$$\eta_{r,TSAH} = \frac{\dot{m}_{\dot{W}=0} c_{p,m}}{LP_{ex}U_L}\left[1-\exp\left(-\frac{LP_{ex}U_L}{\dot{m}_{\dot{W}=0}c_{p,m}\left(1+\frac{U_L P_{ex}}{h_a P}\right)}\right)\right]\left[1-\frac{U_L(T_2-T_{amb})}{\dot{q}_s}\right] \tag{2.35}$$

$$\eta_{TSAH} = \frac{\dot{m}_{W=0}\left(c_{p,4}T_{4t} - c_{p,atm}T_{atm}\right)}{LP_{ex}\dot{q}_s}; \tag{2.36}$$

2.4.4 T-SAH assessment

As stated in Section 2.3, considering constant values of η_{TC}, π_c and π_R, Eqs. (2.30) to (2.32) can be solved to determine the mass flow rates $\dot{m}_{\dot{W}=0}$ corresponding to the freewheeling condition $\dot{W}=0$. Using the parameters resumed in Tab., $\dot{m}_{\dot{W}=0}$ has been computed for several $\dot{q}_s$ in the range of interest, varying the collector length L, as Fig. 2.9 reports.

Tab.2.2 T-SAH parameters used for the simulation.

T_{amb}	p_{atm}	D	D_{ex}	U_L	φ	K_n	L_n	π_c	π_R	η_{ctt}	η_{ett}	η_m	η_T
ºC	bar	m	m	$\frac{\text{W}}{\text{m °C}}$	-	-	m	-	-	-	-	-	-
10	1.013	0.066	0.07	5	1.0	2.0	6	2.5	1	0.71	0.75	0.95	0.51

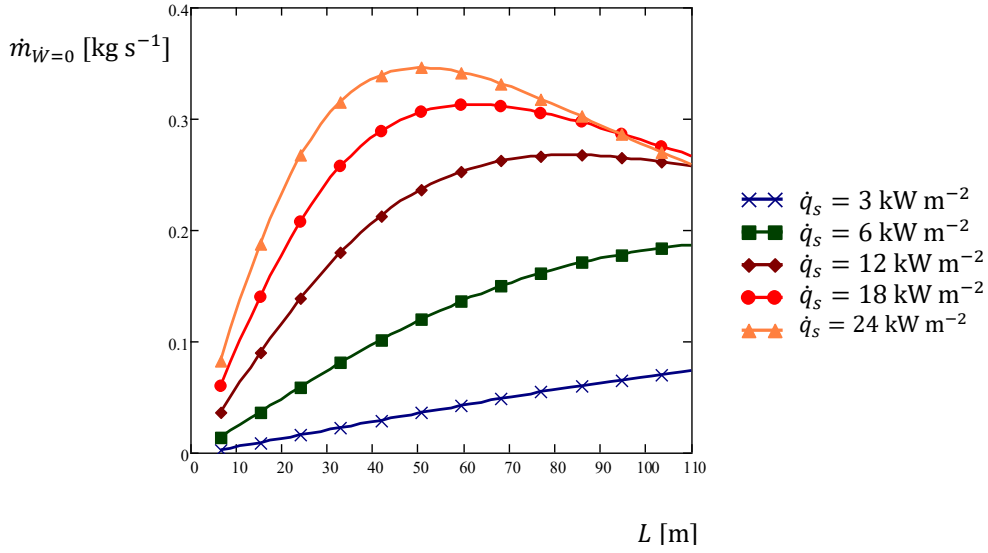

Fig. 2.9. T-SAH mass flow rate at the freewheeling condition, $\dot{m}_{\dot{W}=0}$ versus L for several $\dot{q}_s$ and parameters in Tab.2.2.

The mass flow rate established according to mechanical balance constraint $\dot{m}_{\dot{W}=0}$, determines receiver outlet temperature T_{ou}, as well as the corresponding receiver wall temperature $T_{w,ou}$, according to Eqs. (2.32) and (2.33). They are reported in Fig. 2.10 to verify the fulfillment of thermal constraint and further investigate -T-SAH behavior. Pressure drops and receiver efficiency are reported in Fig. 2.11.

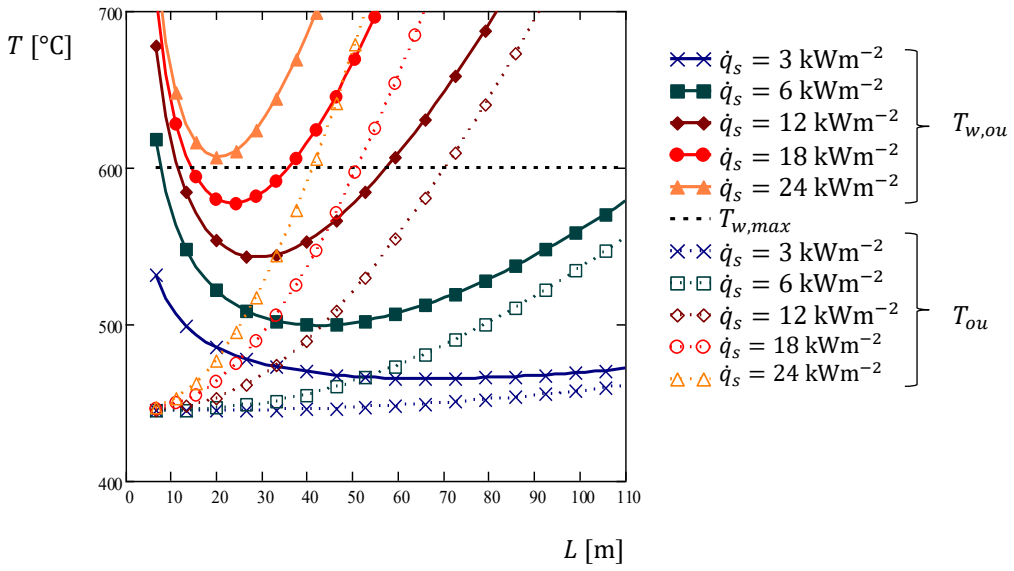

Fig. 2.10. T-SAH wall temperature versus L for several $\dot{q}_s$ under the freewheeling condition $\dot{W} = 0$ and parameters in Tab.2.2.

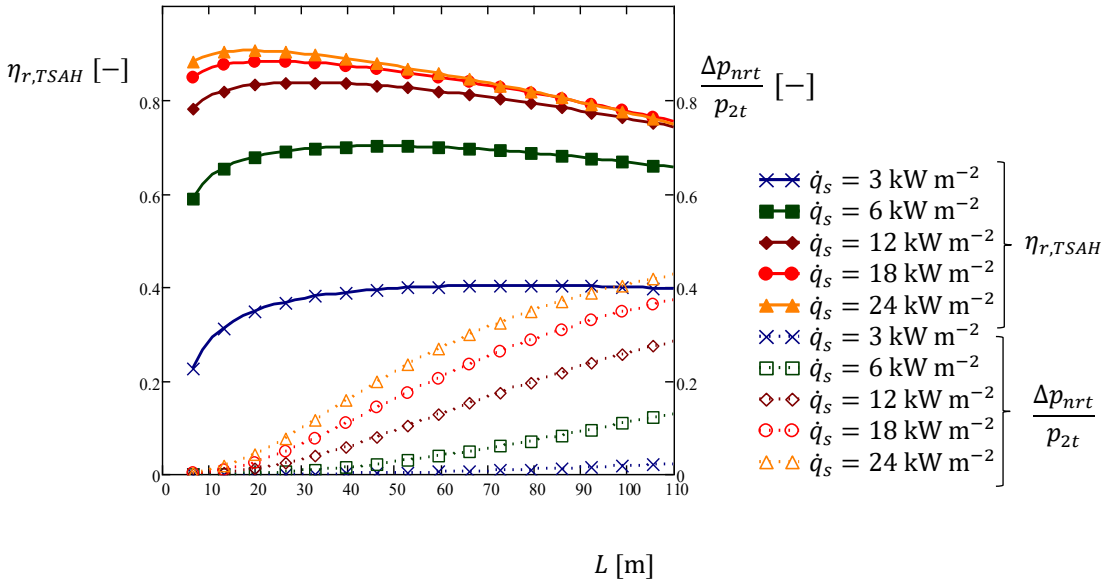

Fig. 2.11. T-SAH receiver thermal efficiency $\eta_{r,TSAH}$ and relative total pressure drop $\frac{\Delta p_{nrt}}{p_{2t}}$ versus L for several $\dot{q}_s$, corresponding to the freewheeling conditions and parameters in Tab.2.2.

For a comprehensive analysis of T-SAH behavior, results shown in Fig.2.9- 2.9-2.11 must be jointly considered. Any changes in length L and heat flux $\dot{q}_s$ modify the T-SAH operating conditions, in terms of $\dot{m}_{\dot{W}=0}$ as well as pressure drops and T_{ou} with a consequence on the maximum wall temperature $T_{w,ou}$.

For a given heat flux $\dot{q}_s$, some features can be noticed:

- Small collector rows collect a modest solar power $\dot{Q}_u$, thus operate with a relatively low mass flow rate, to reach the required inlet turbine temperature needed for mechanical balance. The pressure drops are moderate due to small $\dot{m}_{\dot{W}=0}$, which is beneficial for mechanical balance, reached at a lower T_{ou}.
- Long collector row, with higher $\dot{Q}_u$ requires greater mass flow rate to limit the outlet temperature T_{ou}. Pressure drops increase and a higher turbine inlet temperature is required T_{ou} for reaching mechanical balance.
- The maximum wall receiver temperature $T_{w,ou}$ shows a different trend from T_{ou}. In fact, low heat transfer coefficient h_a established due to low mass flow rate for short collector length induces large wall overtemperature ΔT_w. Hence, even though T_{ou} is moderate, the corresponding $T_{w,ou}$ overcome the receiver thermal limit $T_{w,max} = 600$ °C. $T_{w,ou}$ decreases with length reaching admitted values before to increase again following the T_{ou} trend, although ΔT_w keeps decreasing.
- The rise of $T_{w,ou}$, shown in Fig. 2.10 reveals an increase in the medium wall temperature, which translates into higher thermal losses. For the same $\dot{q}_s$, useful solar power is reduced as long as $T_{w,ou}$ grows. Accordingly, the mass flow rate begins to stabilize or drop at a certain length, especially for high $\dot{q}_s$.
- Besides decreasing with $T_{w,ou}$, receiver efficiency also drops for low $\dot{q}_s$, as seen for SAH.

The delivery temperature, obtained at the turbine outlet is a remarkable output value, together with the mass flow rate. $T_d = T_4$ follows the trend of T_{ou}, as shown in Fig. 2.12.

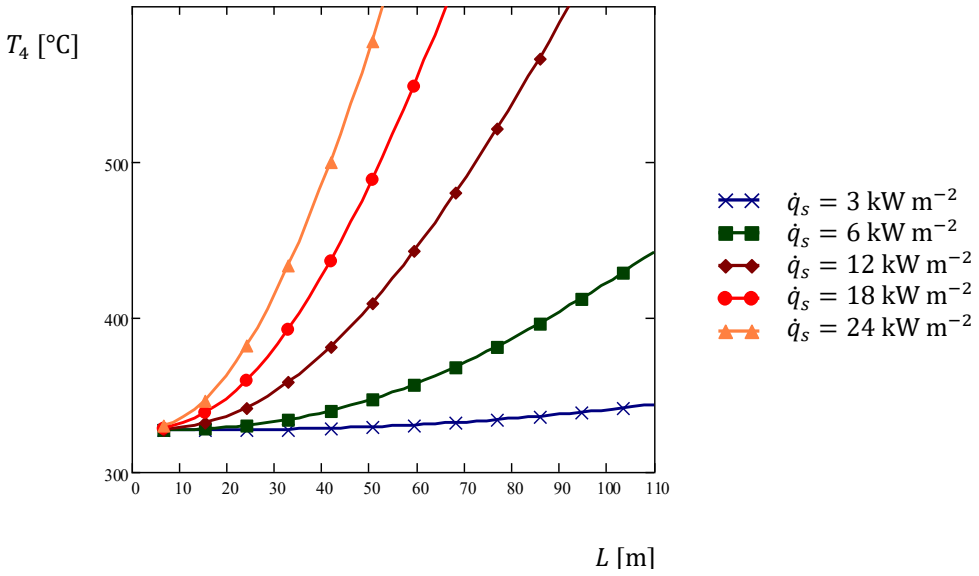

Fig. 2.12. T-SAH delivery temperature versus L for several $\dot{q}_s$, corresponding to the freewheeling conditions and parameters in Tab.2.2.

According to Fig. 2.10, under turbocharger freewheeling condition, the thermal constraint $T_{w,ou} < T_{w,max}$ is not fulfilled for very small length as well as for long collector. The range of allowed length reduces for medium and high heat fluxes. Very small heat fluxes allow long collector length with the drawback of low efficiency.

Varying the collector length, $T_{w,ou}$ increases with $\dot{q}_s$. A maximum heat flux $\dot{q}_{s,max}$ can be defined as the $\dot{q}_s$ at which temperature limit is reached $T_{w,ou} = T_{w,max}$, as in Eq (2.37).

$$\dot{q}_{s,max} = \frac{h_a \langle \dot{m}_{W=0} \rangle (T_{w,max} - T_{ou}) D}{D_{ex}} + U_L (T_{w,max} - T_{amb}) \qquad (2.37)$$

The maximum heat flux $\dot{q}_{s,max}$ is estimated varying the collector length L for several values of π_c and η_{TC}. Fig. 2.13 reports the results for $\pi_c = 2$ to 3 and $\eta_{TC} = 0.47$ to 0.55. For each of the curves obtained, an optimal length range maximizes the allowed heat flux. Moreover, higher turbocharger efficiency improves the T-SAH performance, extending the range of admissible length and increasing the maximum heat flux. An improved η_T allows reaching the mechanical balance at a lower T_{ou} and $T_{w,ou}$, hence reaching the thermal limit at higher $\dot{q}_s$.

The change in π_c, within the typical turbocharger range, is either favorable or unfavorable, depending on the combination of opposite effects. For one hand, higher π_c leads to an increased inlet receiver temperature T_{in}, inducing for the same $\Delta T = T_{ou} - T_{in}$ a higher T_{ou}, thus higher $T_{w,ou}$, meeting thermal limits at lower $\dot{q}_s$. On the other hand, the increased pressure reduces the pressure drops, the T_{ou} required at the turbine, and $T_{w,ou}$. As a result, an increase of π_c seems more favorable for long collectors than for short ones.

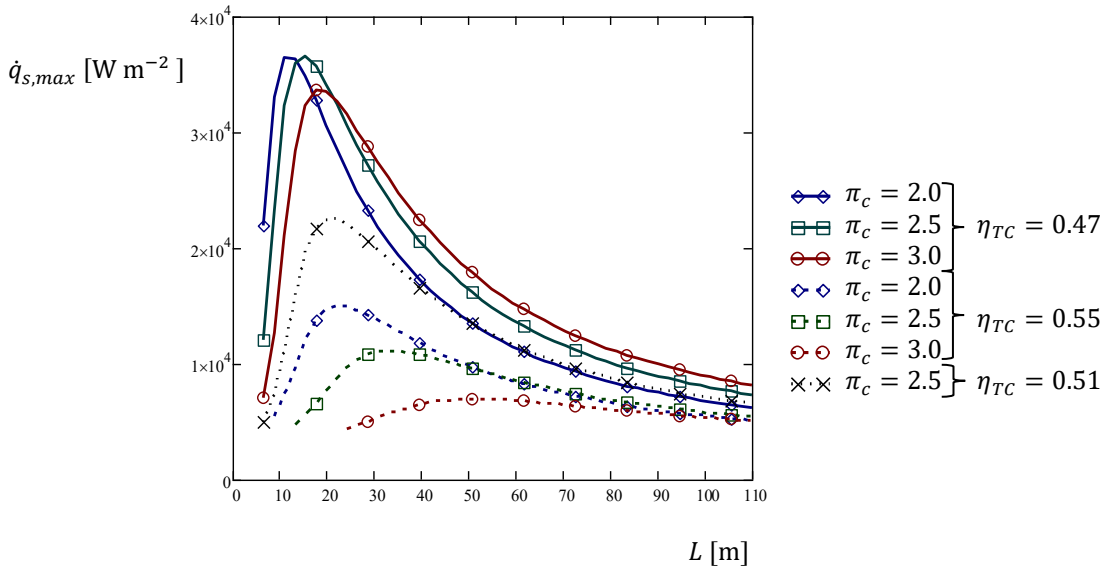

Fig. 2.13. T-SAH allowed $\dot{q}_{s,max}$ under freewheeling condition $\dot{W} = 0$, versus L, for $\pi_c = 2, 2.5$, and 3, for three efficiency cases: 1) low efficiency $\eta_{TC} = 0.47, \eta_{ett} = 0.72$, and $\eta_{ctt} = 0.69$ with dashed lines, 2) high efficiency $\eta_{TC} = 0.55, \eta_{ett} = 0.78, \eta_{ctt} = 0.74$ with continuous lines, and 3) intermediate $\eta_{TC} = 0.51, \eta_{ett} = 0.75, \eta_{ctt} = 0.71, \eta_m = 0.95$ with dot line.

2.5 SAH and T-SAH comparison

In the previous sections both SAH and T-SAH configurations have been scrutinized, revealing the main features and critical aspects of the technologies. A direct comparison between them can induce further considerations. A comparison between the technologies can be carried out assuming the operating condition of T-SAH under its maximum heat flux, as seen in Fig. 2.13 and the parameters of Tab.2.2, and setting the SAH to provide the same delivery temperature $T_d = T_4$, which occurs using the proper mass flow rate $\dot{m}_{SAH}$ from Eq. (2.38).

$$\frac{\dot{q}_s c_{p,m}}{U_L}\left[1-\exp\left(-\frac{LP_{ex}U_L}{\dot{m}_{SAH}c_{p,m}\left(1+\frac{U_L P_{ex}}{h_a P}\right)}\right)\right]\left(1-\frac{U_L(T_{in}-T_{amb})}{\dot{q}_s}\right)=\left(c_{p,d}T_{dt}-c_{p,int}T_{int}\right) \qquad (2.38)$$

Hence the SAH global efficiency η_{SAH} , receiver efficiency $\eta_{r,SAH}$, and pumping ratio $R_{p,SAH}$ are evaluated using Eqs. (2.19), (2.21) and (2.22) with $\dot{m}_{Tou} = \dot{m}_{SAH}$, $T_{ou} = T_d = T_4$.

In addition, as for SAH, a pumping ratio $R_{p,TSAH}$ can be estimated for T-SAH using Eq. (2.39).

$$R_{p,TSAH} \approx \frac{\Delta p_{nrt}\dot{m}_{TSAH}}{\rho_m \dot{Q}_u} = \frac{\Delta p_{nrt} R_g (T_2+T_3)/2}{p_2 \pi_c \left(c_{p,3}T_{3t} - c_{p,2}T_{2t}\right)} \qquad (2.39)$$

A performance comparison is shown in Fig. 2.14, reporting the receiver and heating efficiencies as well as the pumping ratio for both systems. They operate with the same $\dot{q}_s$ corresponding to the maximum allowed for T-SAH at that length. The mass flow rate used ensures the same outlet temperature $T_d = T_4$. It can be noticed that the SAH system requires a high pumping power to

provide the same outlet temperature, reaching almost 40% of the solar power gain. The pumping power in T-SAH is below 5% of the solar power gain and it is not provided by an external source, but taken from solar energy. This highlights the great advantage of using T-SAH configuration, especially when high heat flux and a long collector are used. Even though the receiver efficiency $\eta_{r,TSAH}$ is slightly lower than $\eta_{r,SAH}$ due to the higher mean wall temperature, the overall heating efficiency is greater in T-SAH than SAH, since the latter would need external electrical power for pumping.

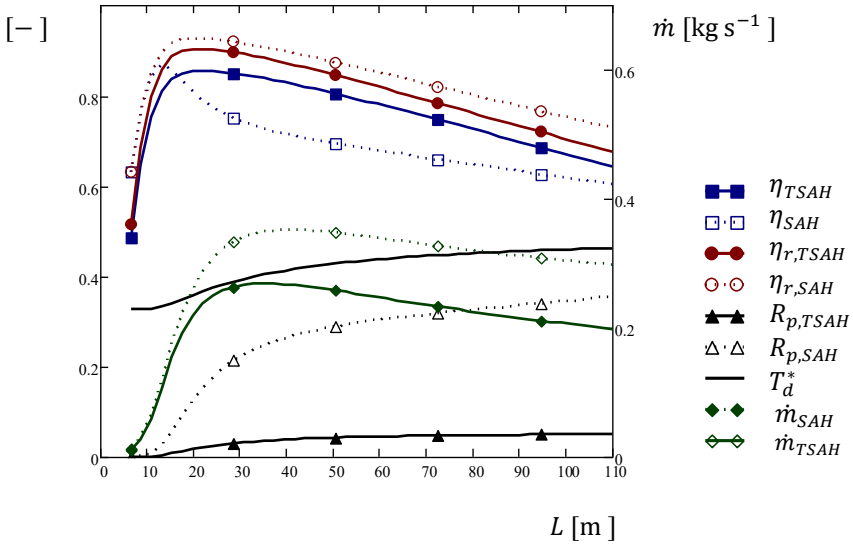

Fig. 2.14. Performances at $\dot{q}_{s,max}$ versus L under the freewheeling condition $\dot{W} = 0$. T-SAH (solid lines), $\pi_c = 2.5$, $\eta_{TC} = 0.51, \eta_{ett} = 0.75, \eta_{ctt} = 0.71$. Comparison with SAH (dashed lines) producing air at the same outlet temperature. $T_d^* = T_4/1,000$ °C. Left axis for non-dimensional parameters.

2.6 Selected example

Previous analysis establishes a framework for the T-SAH feasibility. Further information concerning T-SAH operating characteristics can be obtained from the above numerical model, restricting the simulation to a certain collector length, here chosen as $L = 50$ m, varying the concentrated irradiance below $\dot{q}_s \leq \dot{q}_{s,max} = 13.8$ kWm^2. This approach aims to simulate the operating conditions of a given plant under the variability of solar irradiance.

Temperature and pressure in the main points of the cycle are computed and plotted in Fig. 2.15.

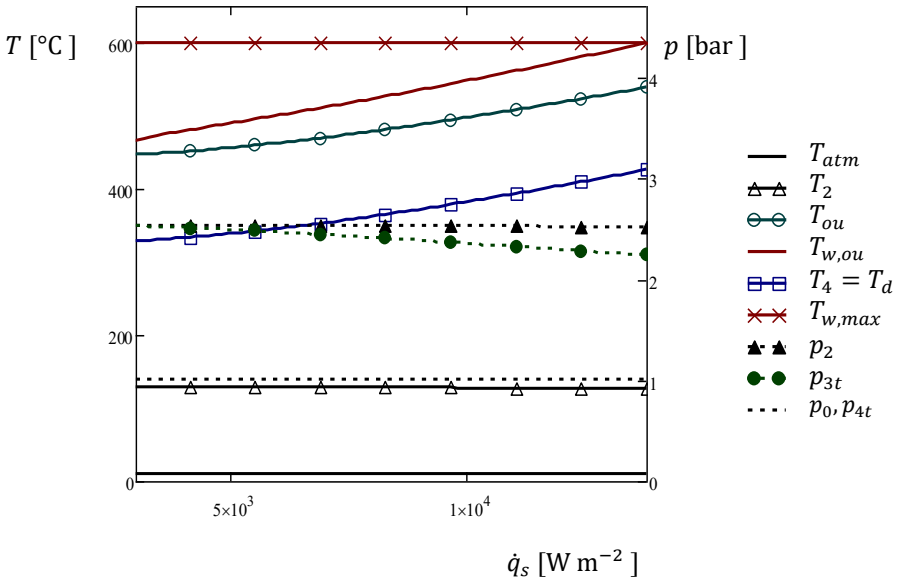

Fig. 2.15. Temperatures and pressures versus concentrated solar irradiance $\dot{q}_s$ for $L = 50$m under the freewheeling condition $\dot{W} = 0$. $\pi_c = 2.5, \eta_{TC} = 0.51, \eta_{ett} = 0.75, \eta_{ctt} = 0.71$.

In this example, the compression ratio is constant $\pi_c = 2.5$ as well as $\eta_{ctt} = 0.71$, giving a steady compression outlet temperature $T_2 \cong 120$ °C. Although the input power varies remarkably, the outlet receiver temperature grows slightly with $\dot{q}_s$, being compensated by the augmented mass flow rate as can be seen in Fig. 2.16. Outlet turbine temperature (delivery temperature) $T_4 = T_d$ follows the same trend, indicating a quite steady output profile despite sun variability. It can be noticed as the maximum receiver wall temperature grows with concentrated irradiance, reaching the limiting value at the maximum allowed irradiance. On the right axis, pressure is reported. The effect of pressure drops across the circuit is not negligible, although mitigated by increased density. Consequently, inlet turbine pressure slightly decreases for high $\dot{q}_s$ and mass flow rate, demanding higher inlet temperature for providing the required power $\dot{W}_e$. Fig. 2.16 reports the T-SAH efficiency. It grows with $\dot{q}_s$ as the ratio $U_L(T_{w,m} - T_{amb})/\dot{q}_s$ decreases.

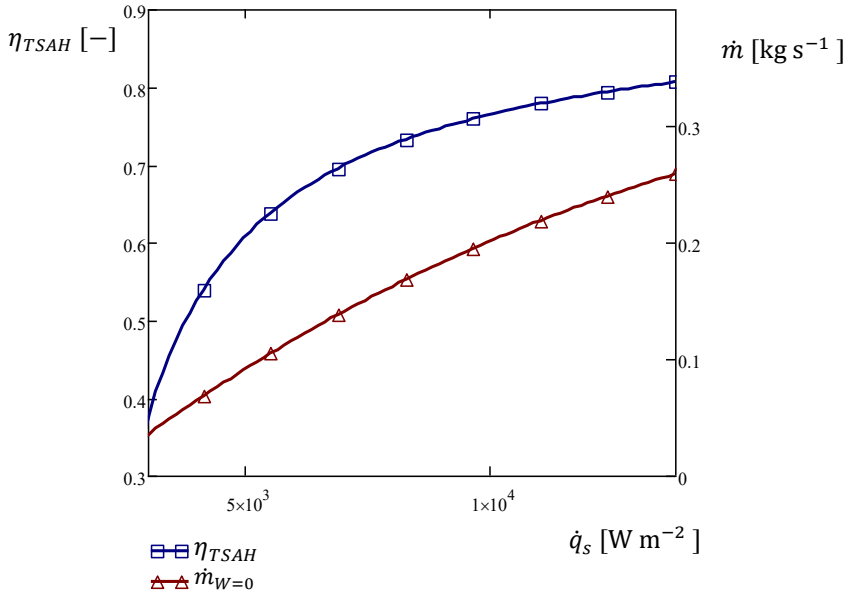

Fig. 2.16. Efficiency and mass flow rate versus concentrated solar irradiance $\dot{q}_s$ for $L = 50$m, under the freewheeling condition $\dot{W} = 0$. $\pi_c = 2.5, \eta_{TC} = 0.51, \eta_{ett} = 0.75, \eta_{ctt} = 0.71$.

The influence of compression ratio π_c on the T-SAH behavior is now investigated. The results are shown in Fig. 2.17. Main temperatures and efficiency are reported against $\dot{q}_s$ for different $\pi_c = 2$ to 3. The compressor outlet temperature varies according to π_c. The effect on outlet receiver temperature is appreciable at low $\dot{q}_s$. A higher π_c is beneficial on mechanical balance, resulting in lower pressure drop Δp_{nrt}, thus allowing freewheeling at a lower temperature T_{ou}. The efficiency slightly decreases with π_c increasing, due to the higher average wall temperature $T_{w,m}$. The turbine outlet temperature drop varies slightly with π_c, as result of a greater expansion ratio $\pi_e \sim \pi_c$. The variation of π_c in the range 2 to 3 does not affect remarkably the T-SAH operating conditions, indicating the flexibility of operating with variable π_c, as is expected using a real turbocharger.

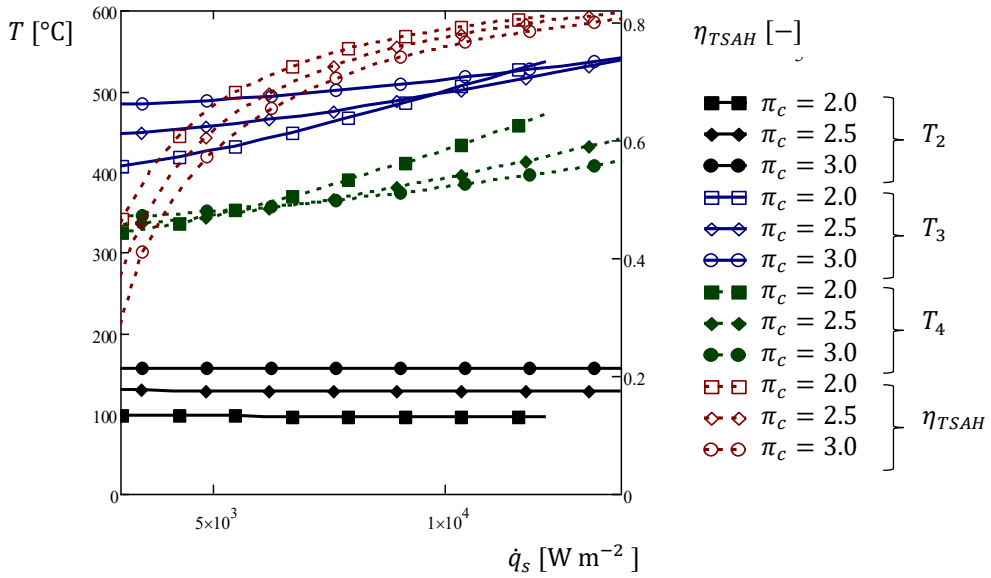

Fig. 2.17. T-SAH main temperatures and efficiency versus concentrated solar irradiance $\dot{q}_s$ for several π_c, under the freewheeling condition $\dot{W} = 0, L = 50\text{m}, \pi_R = 1.0, T_{w,max} = 600$ °C.

As can be observed in Fig. 2.15, for $\dot{q}_s \leq \dot{q}_{s,max}$ the maximum wall temperature reached $T_{w,ou}$ is smaller than $T_{w,max} = 600$ °C. This opens the possibility to operate with a higher outlet temperature T_{ou} than t required by the mechanical balance (freewheeling). A higher T_{ou} would increase the turbine power if the pressure ratio is the same. Instead, the expansion pressure ratio can be reduced to obtain and overpressure at the outlet as a secondary output, besides heat. A delivery pressure $p_d = p_{4t} = \pi_R p_{atm} > p_{atm}$ can be useful for the user to compensate for the pressure drop in the delivery pipe or in the thermal process itself. An estimation of the overpressure achievable within the operating constraints of T-SAH is formulated solving Eq. (2.30) with $\pi_R > 1$. It would result in a higher inlet turbine temperature needed to compensate for the reduction of π_e. Again the thermal constraint indicates the maximum π_R achievable, according to Eq.(2.40), obtained introducing in Eq. (2.30) the maximum T_{3t} allowed.

$$\eta_T c_{p,e}\left(T_{w,max} - \frac{D_{ex}(\dot{q}_s - U_L(T_{w,max} - T_{amb})}{h_a D\varphi} + \frac{{v_3}^2}{2c_{p,3}}\right)\left[1 - \left(\frac{\pi_c\left(1 - \frac{\Delta p_{nrt}}{p_{2t}}\right)}{\pi_R}\right)^{-\frac{\gamma_e - 1}{\gamma_e}}\right] = c_{p,c}T_{atm}\left(\pi_c^{\frac{\gamma_c - 1}{\gamma_c}} - 1\right) \quad (2.40)$$

Fig. 2.18 shows the results considering three different turbocharger efficiencies η_T, for a collector length $L = 50$ m, in a wide range of $\dot{q}_s$, either for $\dot{q}_s < \dot{q}_{s,max}$ and $\dot{q}_s > \dot{q}_{s,max}$. As expected, $\pi_R > 1$ are possible for $\dot{q}_s < \dot{q}_{s,max}$. The beneficial effect of increasing turbocharger efficiency on the over-pressure ratio achievable is noticeable.

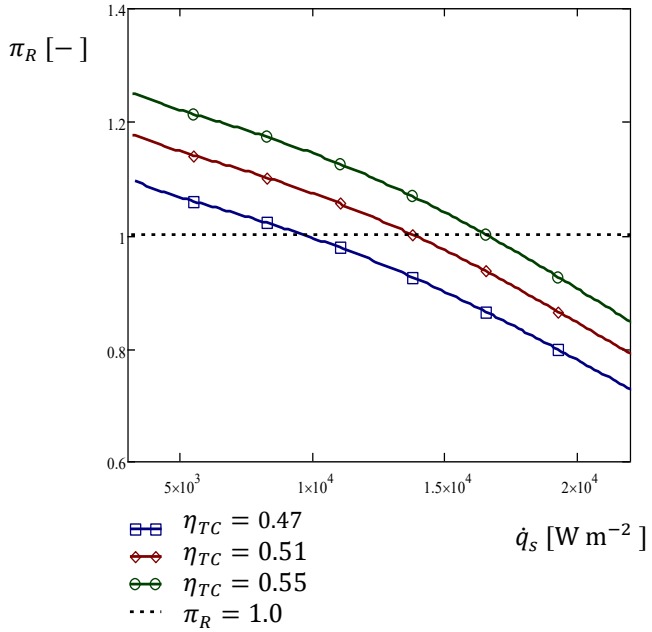

Fig. 2.18. Over-pressure ratio π_R versus concentrated solar irradiance $\dot{q}_s$ for $\eta_{TC} = 0.47, 0.51,$ and 0.55, under the freewheeling condition $\dot{W} = 0$. $L = 50$m, $\pi_c = 2.5$, $T_{w,max} = 600$ ℃.

2.7 Remarks on theoretical analysis

The assessment carried out on the SAH configuration highlights the limited feasibility range of direct air heating inside linear concentrating collectors. The numerical model enables evaluating the effect of low internal heat transfer rate which determines a non-negligible receiver wall overtemperature, which is in the same order of magnitude of the air temperature difference across the collector. This makes that the minimum length arises as a limiting parameter L_{min}~3 to 20 m, according to heat flux expected the outlet air temperature desired, and receiver thermal limit. On the other hand, the pumping power required limits the length of the collector row. A wider aperture also reduces the collector length allowed at reasonably low pumping power, which has, as a drawback, a modest thermal efficiency.

The analysis carried out on the proposed T-SAH using a simplified 1D model indicates the feasibility of the novel layout within a certain domain of design and operating parameters. The collector row length L is one of the most relevant ones, together with the concentrated irradiance, which indirectly counts for the aperture and concentration ratio. T-SAH can operate properly for $20\ \mathrm{m} < L < 100\ \mathrm{m}$ when a proper aperture is considered for not overcoming the maximum $\dot{q}_{s,max}$, derived from the thermal constraint. Intermediate length admits higher heat flux.

The operating pressure ratio can vary in the typical range of turbochargers, whereas an increase in compressor and turbine efficiencies is always beneficial for the design and operating flexibility. The turbocharger efficiency resulted to be of high importance for the T-SAH feasibility.

Considering an intermediate length, $L = 50$ m, the simulation carried out indicates that T-SAH can operate under sun variability with a stable outlet temperature between 300 – 400 °C, as well

as under pressure ratio variation in the range typical of turbochargers. Besides operating without any external energy consumption, under defined conditions, the system can provide hot air with a small overpressure at the delivery point, useful for the user's thermal process.

Comparing TSAH with the simpler SAH working with the same delivery temperature and $\dot{q}_s$, T-SAH shows better performances being $\eta_{TSAH} > \eta_{SAH}$ in the range of $L > \sim 15$ m. Besides the efficiency comparison, TSAH is preferable to SAH since it does not require any additional pumping power consumption, pointing out to lower operating costs, besides being a wholly renewable and greenhouse gases-free application.

Receiver tube diameters that are larger than conventional, eventually incorporating internal fins, would be beneficial for both the SAH and T-SAH concepts, although the proposed TSAH concept is valid with the usual 70 mm O. D. commercial evacuated tubes. These wider receiver tubes were discarded as they are not commercial.

The positive results recommend further theoretical studies to characterize the partial load operation, production profiles, full costs breakdown, and either the convenience of heat storage or a complementary source of reheating to fill solar gaps.

To keep general validity the above analysis wasn't restricted to PTC or LFC respectively, but the usage of concentrating heat flux as an independent variable includes both of them. More detailed results would be obtained considering specific collector features, as from commercial examples. Besides an estimation of heat flux, this approach would include the length-dependent optical losses, which can be relevant due to relatively short collector row investigated either for SAH and T-SAH layouts. Moreover, an increase in accuracy can be obtained through a spatial discretization of the receiver model. Further analysis would include parallel and series combinations of collectors coupled with a single turbocharger/blower.

For the T-SAH assessment, a more detailed analysis would consider the variation in the overall turbocharger performances with the working conditions, according to the performance maps of each commercial device considered. The compressor and turbine efficiencies depend on the respective inlet corrected mass flow rates through both turbomachines and respectively on π_c and π_e, indicated by the respective performance maps, [77], [56], and [78] among others. Solving the system of simultaneous equations taking into account this dependency is a classical turbomachine matching problem. Outputs of this matching process would be the shaft turning speed and the size and even the best type of both turbomachines, compressor, and turbine. Another issue is the time profile of η_{TC}, π_c, and π_e along one day when $\dot{m}, p, \text{and } T$ change as a response to a variable $\dot{q}_s$, and the resulting production profile. All these concerns are addressed in the following section of this thesis.

3 T-SAH PROTOTYPE: DESIGN, INSTALLATION AND CALIBRATION

3.1 Design

The concept of T-SAH is applied to design the earliest prototype. It is intended to be installed on the rooftop of Carlos III University of Madrid (Leganés, Spain). In the following sections, the main technical tasks accomplished are discussed. The main elements of the system are the concentrating solar collectors, the turbocharger, the auxiliary compressor, auxiliary equipment, and piping. They have been selected after a critical screening of the commercial options so that the industrial application is better achieved. Despite that, several original minor mechanical components had to be designed and produced. 2D and 3D CAD have been used for individual component design and for sizing and positioning the whole system. Auxiliary post-heating and thermal storage units were designed to be integrated into the T-SAH prototype. The proper instrumentation and sensors required have been selected. The implementation of Supervisory Control and Data Acquisition (SCADA) is described in this section.

3.1.1 Solar field

Linear concentrating collectors, both parabolic trough PTC and linear Fresnel LFC type, are suitable for implementing a T-SAH, although some differences between them are relevant for the project.

The LFC type uses a fixed receiver that allows a stable connection with the piping system, avoiding the need for a flexible connection and their associate frictional pressure drops and temperature limitations. Their segmented primary reflector offers two main advantages: each mirror rotates around its longitudinal axis close to the ground, hence requires a simpler tracking system. On the other hand, the smaller individual aperture of mirrors with respect to a PTC aperture presents lower wind loads. This is especially important for installation on rooftops, where heavy anchoring systems are not allowed. LFCs generally offer lower optical efficiency than PTCs. Due to larger focal distances, the optical deviation due to tracking errors can easily lead the concentrated irradiance out of the receiver surface. A secondary reflector is often installed for recovering the irradiance missing the receiver. Besides avoiding a drop in optical efficiency, secondary optics can improve the homogenization of the circumferential distribution of concentrated heat flux across the receiver external perimeter. This feature is particularly interesting in the present project since heat flux and temperature inhomogeneities are causes of receiver tube mechanical stress, bending, and damage.

These features make LFC more suitable for the T-SAH prototype. Among the models commercially available for small-scale installation, the collector manufactured by Solatom™ company is chosen, Fig.3.1.

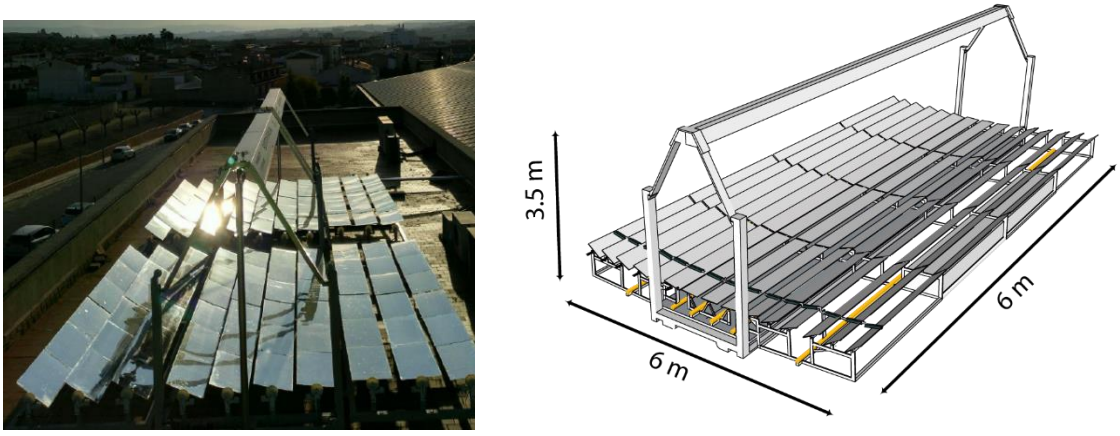

(a) (b)

Fig. 3.1. Linear Fresnel Collector by Solatom™. (a) Installed example of 2 modules, (b) One module 3D drawn.

The collector has a primary reflector made with 10 mirror axes, each of them having 6 aligned mirrors with an aperture of 0.5 m and individual length 0.88 m. An overall number of mirrors of 60 gives a reflective surface of $26.40\ \mathrm{m}^2$. Each mirror has a curvature optimized for its focal distance with the receiver, to improve optical efficiency. The geometrical features are reported in Tab.3.1.

The collector is designed for a single tube receiver, whose characteristics are discussed in the following paragraph. The secondary reflector has a trapezoidal shape.

An original feature of the collector is foldability. The primary reflector structure is made of two foldable wings. In addition, the secondary receiver includes a mechanism for sliding it up and down. When folded and closed, the collector is containerized into a rectangular-shaped box and can be easily transported. The module is pre-assembled in the factory and transported to the installation place already calibrated and tuned. A system of wheels allows adjusting position and orientation in the place of installation without the need for machinery. Feet with adjustable height allow levelling it in-situ. The possibility to simply raise and lower the receiver makes it is accessible for maintenance, cleaning, instrumentation replacement, and inspection.

The collector is equipped with a 1-axis tracking system. Each mirror axis is motorized, and its angular position is revealed by an inclinometer. The control system is implemented on an open-source electronic microcontroller (based on Arduino®). Each axis has independent control and tracking, allowing good solar power control and optimization. The tracking algorithm is based on an astronomical calculation of sun position and tracking angle.

The modules can be assembled in series or parallel layouts, adapting to the power and mass flow rate required. According to preliminary calculation and space availability, only three solar collector modules in series were possible for the prototype.

Table 3.1. LFC technical features for each module.

Primary reflector length L_m	5.28 m
Primary reflector width W_a	5.00 m
Primary reflector area A_m	26.40 m^2
Number of mirror axes n_m	10
Mirror width w_m	0.50 m
Mirror length	0.88 m
Mirrors per axis	6
Number of mirrors	60
Height receiver from mirrors H_m	2.72 m
Overall length	6 m
Overall width	6 m
Area on the ground	36 m^2
Overall height from ground	3.5 m
Containerized size	6m x 6m x 2m
Normal optical efficiency η_{op0}	0.632

3.1.2 Receiver

The solar field is equipped with a receiver tube manufactured by ARCHIMEDE SOLAR ENERGY (Italy) model HCEOI-12, Fig.3.2. It is developed for concentrating solar power plants (CSP) operating with thermal oil as HTF. The stainless-steel absorber tube is covered by a selective coating to reduce thermal radiation to the ambient. The selective coating has high absorptance in the solar wavelength and low infrared emissivity at the operating receiver temperature. It is manufactured according to the multilayer structure developed by ENEA. Italy. It is formed by an internal layer of metal that reflects the infrared radiation and an external antireflective ceramic layer. In the middle, lays a graded ceramic-metal material (CERMET). The selective coating has a maximum operating temperature of 580 °C and a maximum allowable temperature of 600 °C. The absorber is embedded into a concentric cover of borosilicate glass coated with an anti-reflective layer (developed by CIEMAT). Vacuum in the annulus minimizes convective thermal losses. Thermal longitudinal expansion of the stainless-steel tube is compensated by extensible bellows, which are welded on the absorber tube and on the glass jacked to keep a vacuum inside the annulus. The pills getter absorbs residual gases in the annulus and hydrogen molecules which can permeate from the absorber tube.

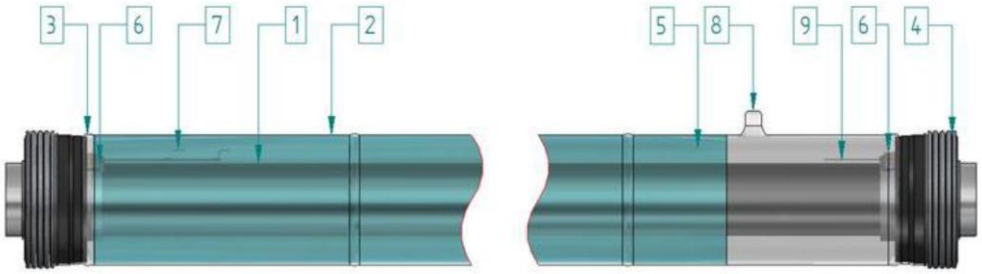

Fig. 3.2. Receiver tube (HCEOI-12 by Archimede Solar Energy). 1. stainless steel absorber tube with a spectrally selective coating; 2. glass jacket with Anti Reflective (AR) coating; 3. glass to metal seals; 4. thermal expansion compensators; 5. vacuum annulus; 6. Not Evaporable Getter (NEG) pills; 7. Barium getter; 8. pump nipple; 9. serial number.

Main receiver technical information taken from the manufacturer datasheet is reported in Tab. 3.2.

Table 3.2. Receiver tube details.

Overall length	4.06 m
Active length (20°C)	3.90 m
Tube external diameter	0.07 m
Tube thickness	0.002 m
Tube material	*Stainless steel AISI 321*
Maximum allowable pressure (400°C)	< 42 bar
Maximum allowable circumferential temperature difference (400 °C)	< 30 °C
Selective coating solar absorbance	95.8 %
Selective coating thermal emissivity (400 °C)	8.2 %
Selective coating maximum operating temperature	580 °C
Selective coating maximum allowable temperature	600 °C
Glass cover external diameter	0.125 m
Glass cover thickness	0.003 m
Glass cover length	3.9 m
Glass cover material	*Borosilicate glass*
Average solar transmittance	96.4 %
Annulus pressure	10^{-4} mbar
Thermal losses (300 °C)	116 W m^{-1}
Thermal losses (400 °C)	273 W m^{-1}

3.1.3 Turbocharger

The turbocharger currently used for boosting internal engine performance in the automotive application joins a radial turbine and a centrifugal compressor, mechanically coupled via a common shaft.

Constructive aspects and the main components of a typical turbocharger can be observed in Fig.3.3. Compressor and turbine wheels are fixed on the rotating shaft. Compressor and turbine housing are fixed on the cast-iron center housing, which hosts the rotating shaft, minimizing the rotational friction through ball bearing or journal bearing, depending on the models. It hosts inlet and outlet connections for lubrication oil.

Compressor housing is cast in aluminum, as well as the compressor wheel. The turbine housing is cast in steel or iron. High-nickel material (Inconel) is used for the investment cast turbine wheel. Compressor inlet and turbine outlet are coaxial to the shaft, while compressor outlet and turbine inlet are perpendicular to the shaft axis. They have an adjustable angular position on the plane normal to the shaft.

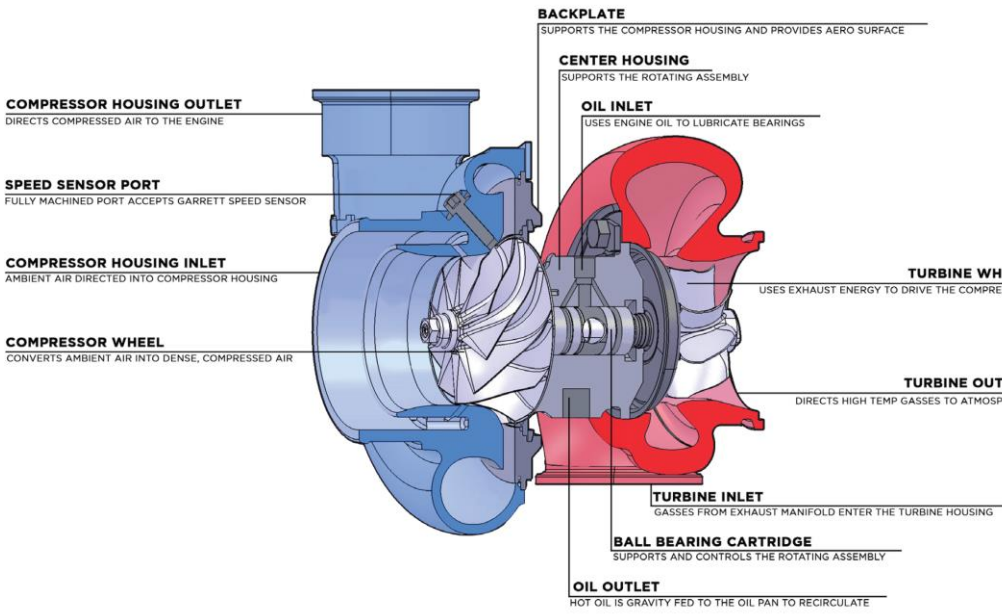

Fig. 3.3. Turbocharger schematic by [79]**.**

According to the preliminary calculation, for the mass flow and compression ratio considered in the present application, commercial turbochargers designed for small vehicles are applicable.

To achieve correct operation and expected performance, the characteristics of the compressor and the turbine must match with the air circuit and solar collectors, in the same way as they match with an internal engine in the automotive application. The automotive turbocharger model GT1544 by [79] is chosen among the small-size models available on the market. Garrett™ is one of the leading companies around the world in turbocharger manufacturing and provides models in a wide range of sizes. The compressor and the turbine of GT1544 have respectively outer wheels diameters $D_c = 43.9$ mm (exducer) and $D_e = 41$ mm (inducer); TRIM (the ratio

between smallest and highest turbine wheel area times 100) 56 and 58; an A/R (ratio between the interior area of the compressor/turbine and the corresponding housing radio) of 0.33 and 0.34. The turbine is originally equipped with a wastegate valve, used for turbocharger control in automotive applications, which has been closed permanently. Turbine and compressor performance are described through their maps provided by the manufacturer and reported in Fig. 3.4.

Shaft standard plain bearing lubrication is ensured by a continuous supply of pressurized oil via a dedicated pump. A dedicated lubricator central SureFire II by Bijur Delimon is selected for the application from the available models on the market. It ensures continuous oil supply to the turbocharger through a self-contained electric motor-driven gear pump with an oil deposit of 3 L capacity. A small heat exchanger for cooling oil is considered.

(a) (b)

Fig. 3.4. Turbocharger GT1544 maps. (a) compressor; (b) turbine.

3.1.4 Auxiliary compressor

An auxiliary compressor in series with the turbocompressor at the inlet side is required for starting and transients, as well as for providing an auxiliary overpressure when the mechanical power provided by the turbine is not enough for driving the compressor alone.

The selected device is a couple of air side-channel blowers, electric motor-driven, connected in parallel. Each blower (SD22FU-FUK model by Elektror) has an asynchronous squirrel-cage electrical motor (rated power 1.1 kW at 50 Hz), controlled by a frequency converter (LENSE 8200 vector). The map showing the relation between volumetric mass flow rate and overpressure for an individual blower, provided by the manufacturer, is reported in Fig. 3.5. The frequency for control ranges between 20 and 80 Hz.

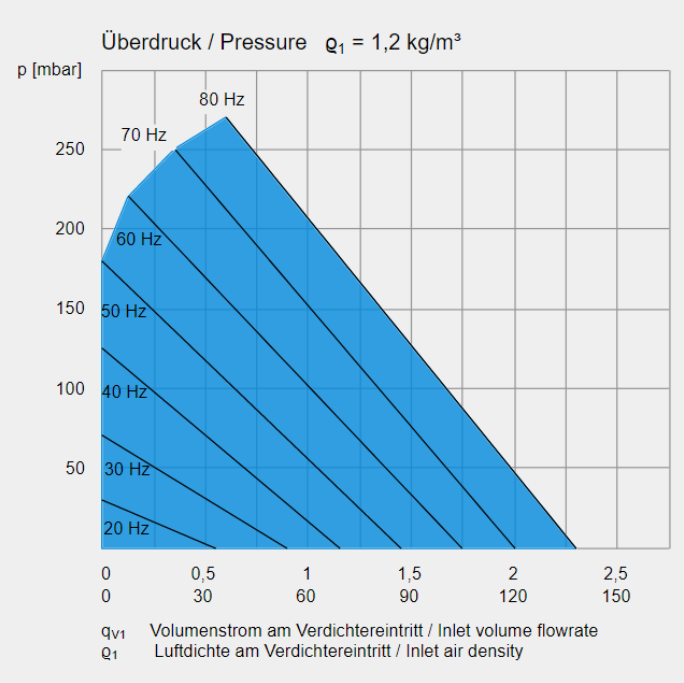

Fig. 3.5. Individual air blower map.

3.1.5 Solar receiver adaptation

Ad-hoc solution for receiver tube support and connection has been developed. Considering three linear Fresnel collectors arranged in series, an overall length of 18 to 20 m is reached, for what five receiver tubes must be connected in series. Although welding consecutive tubes between them is a good solution to avoid the risk of air leakages, it makes difficult tube inspection, maintenance, and replacement. A flanged connection is then preferred. A typical round flange design has been modified to allow hanging the receiver tube to the collector structure, besides connecting two consecutive tubes.

The required air temperatures inside the receiver induce a high receiver temperature, inducing a non-negligible thermal dilatation. Considering the thermal linear expansion coefficient of stainless steel of $0.016 \frac{\text{mm}}{\text{m K}}$, dilatation over the total tube length $L_t = 20\ \text{m}$ is estimated between $100\ \text{mm}$ and $200\ \text{mm}$. Ad hoc support brackets for solar receivers have been designed considering the thermal dilation.

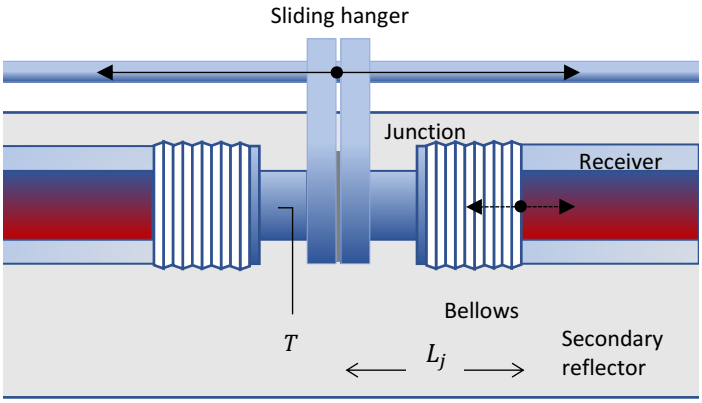

Fig. 3.6. Schematic of junction

They allow to hang the receiver tubes to the secondary optics structure maintaining them in the optical focal point, giving freedom to slides in the axial direction. The dilatation of the receiver with respect to the glass cover evacuated tube is compensated by bellows, according to the manufacturer's design, Fig. 3.6. The bracket design has been joined with an ad hoc flange design for connecting consecutive tubes, resulting in an original solution with the following function:

- Hanging tube to the secondary optic structure
- Placing the tube in the optical focal point
- Allowing thermal expansion and longitudinal tube sliding
- Connecting consecutive tubes without welding
- Allowing easy tube disassembly and assembly for maintenance
- Allowing sensor installation
- Adjusting the lateral tube position for optimum axial alignment
- Increasing the installation speed

Fig. 3.7 reports mechanical drawing of developed sliding flange/brackets in 2D view alone (a) and positioned into secondary optics (b). A supporting plate has been designed to be installed on the secondary optics structure, using a stainless-steel round bar passing through the flange hole, Fig. 3.7 (c) and (d).

The receiver tube outlet has been chosen as a fixed point in the axial direction. Going towards the receiver inlet, each tube extremity, hence each flange, will displace according to its dilatation length and the dilatation of the previous tube. The inlet flange will experience the overall axial displacement during heating. The connection of the receiver inlet with the rest of the air circuit must be flexible, allowing the required axial displacement.

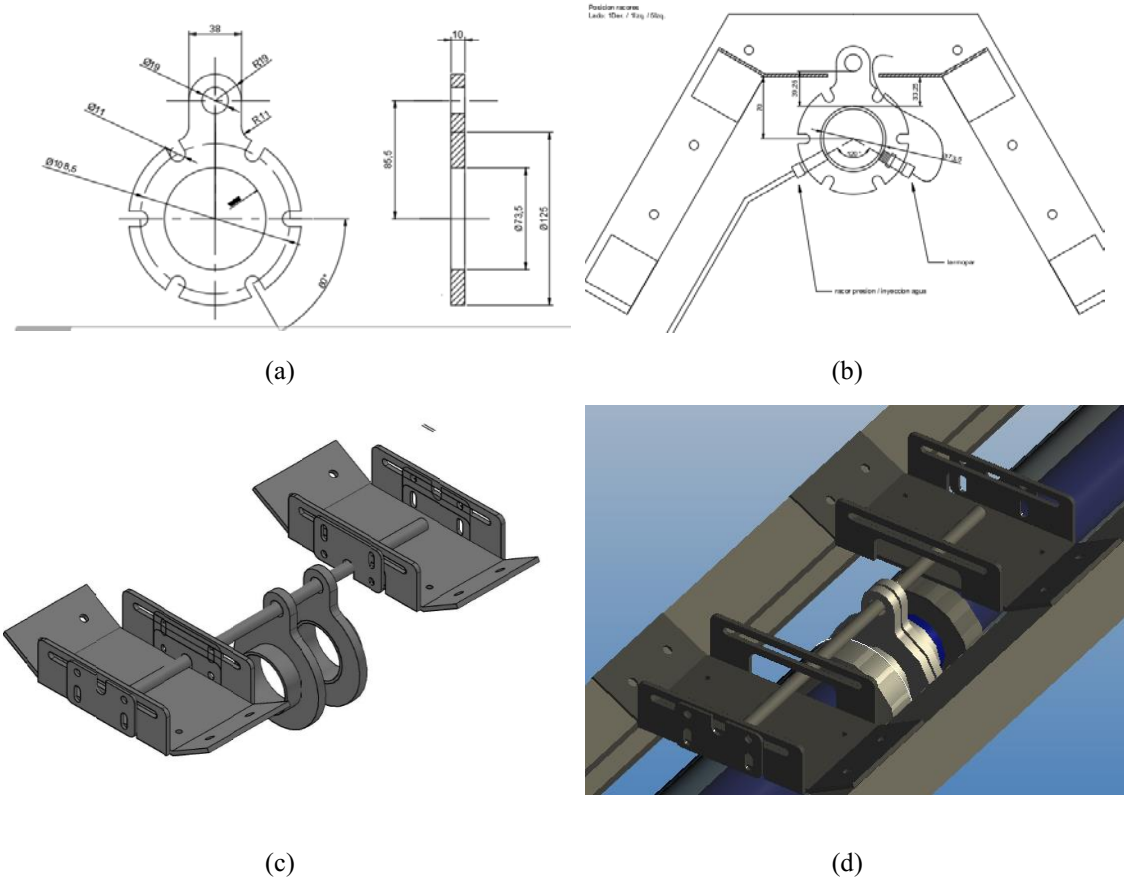

(a) (b)

(c) (d)

Fig. 3.7. Flange/brackets. 2D drawings (a); 2D drawings including secondary optics; 3D views including supporting plates and hanging bar (c) and (d).

3.1.6 Air piping

Air piping has been designed according to preliminary estimations of mass flow rate, flow velocities, pressures, temperatures, and pressure losses minimization were considered. Detailed 3D modeling of the whole piping has been developed using AutoCAD™. A 3D view of the air circuit and solar collectors is shown in Fig 3.8.

Commercial stainless-steel tubes with an internal diameter of 80 mm and wall thickness of 2 mm are used for straight segments, diameter reductions and diffusers have been designed for the connection with the turbocharger and the receiver. Connection flanges have been designed to allow easy installation of prefabricated elements.

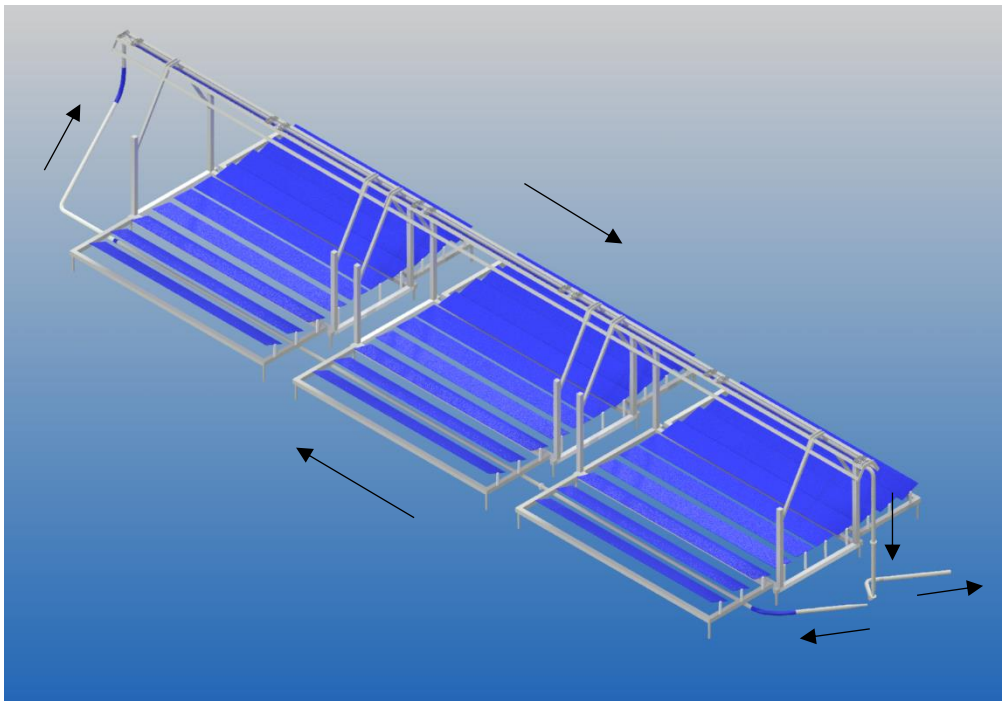

Fig. 3.8. 3D view of the prototype.

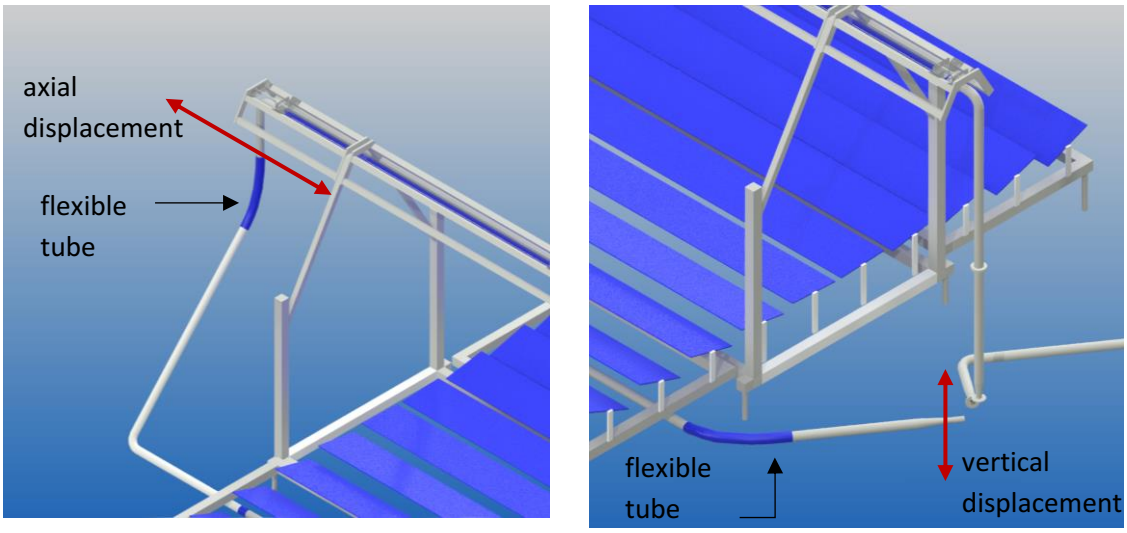

(a) (b)

Fig. 3.9. Flexible tube inserts for horizontal (a) and vertical (b) thermal dilatation.

Two circuit segments have been designed as a flexible connection to compensate for thermal dilatation and to allow manageable installation. The receiver tube inlet requires a flexible junction to compensate axial displacement, which can be obtained by inserting an extensible tube, like the one used in automotive applications. Their corrugated surface would introduce additional pressure drops. Instead, a flexible tube (Venair SIL 700/V RA:) of 1 m length is chosen, having an internal smooth surface, Fig.3.9(a). It is manufactured with two polyester fabric reinforcements and encapsulated stainless steel spring wire. Its continuous operating temperature ranges from -50 °C to +180 °C and it may reach up to 200 °C (392 °F) during short

periods, higher than the expected air temperature at the receiver inlet, which is below 150 °C. A similar flexible tube is needed at the compressor outlet, this way allowing vertical displacement of the turbocharger, consequent to thermal dilatation of the vertical inlet turbine tube (2 - 4 cm), Fig. 3.9(b). It can be noticed that the turbocharger is hanged to the inlet turbine tube.

Special attention has been paid to the air piping connection to the turbocharger. Compressor and turbine inlet and outlet specifications are given by the manufacturer, as reported in Fig. 3.10. Coupling flanges have been designed for turbine inlet and outlet, while the compressor connection is obtained through a silicon hose and clamp. A diffuser is designed at compressor and turbine outlet, Fig. 3.11, ensuring low flow diffusion angle to minimize pressure drops. A converging nozzle is designed for the turbine inlet.

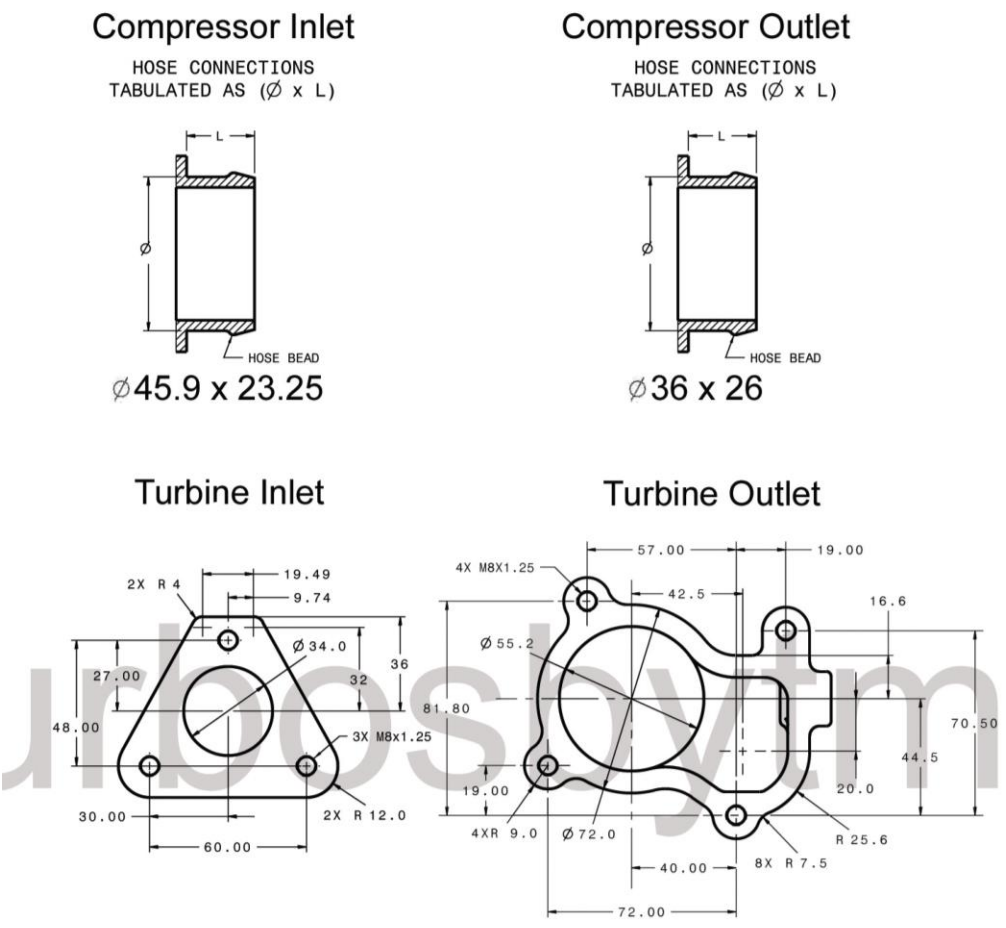

Fig. 3.10. Connection compressor and turbine GT1544.

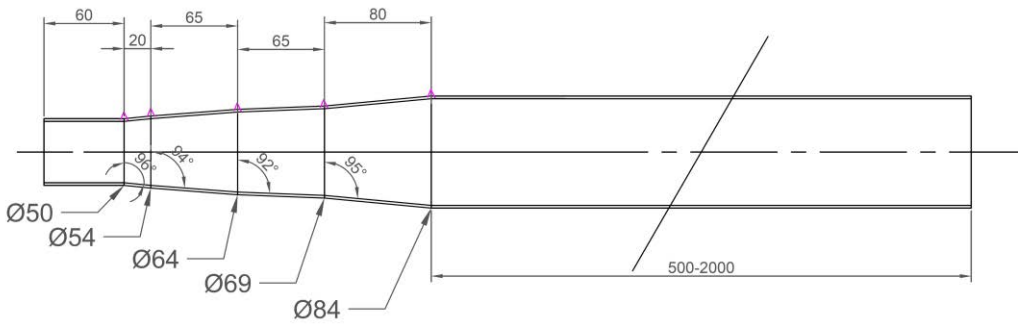

(a)

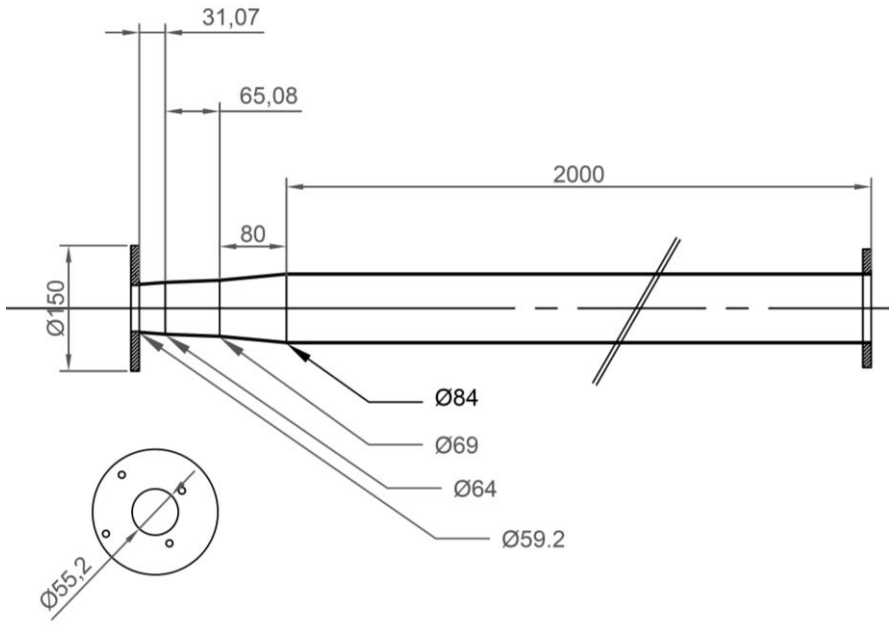

(b)

Fig. 3.11. Diverging duct compressor (a) and turbine (b) outlet (mm).

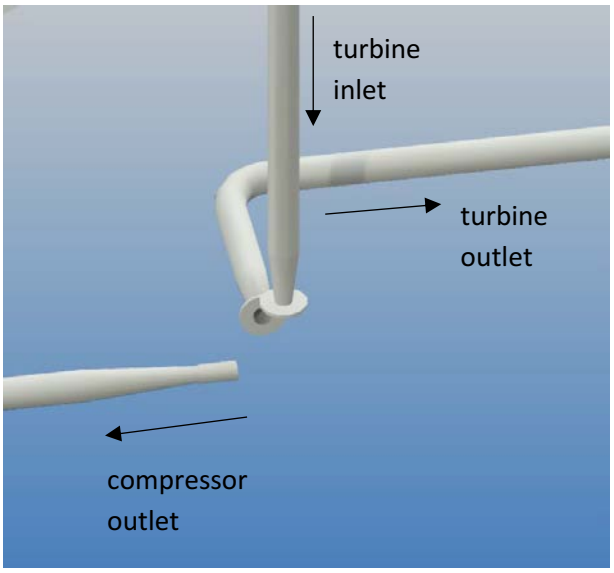

Fig. 3.12. 3D view of turbocharger connection with air circuit.

3.1.7 Post-heating unit

An air post-heating unit has been added to the setup to increase the inlet turbine temperature. It is used only for experimental purposes and would not be implemented in an industrial scale plant, where the use of electricity for air heating is not convenient. In the experimental setup, the post-heating unit goal is to provide additional thermal power as would be done by an extra collector row length in series with the installed collectors. The advantage of using an electrical heater for experimental purposes is the lower cost compared with an extra collector length and the possibility of easy and precise control of power delivery and temperature. Moreover, the post-heating unit allows increasing the air temperature above the thermal limit of the receiver tubes without risk of their damage. This way the post-heating power allows to test the turbocharger behavior under a wider range of operating conditions for the operation with solar collector only. It enables increasing the overall thermal power supplied to the air by adding up to 8 kW to the net solar power input, which ranges between 15 to 20 kW.

The post-heating unit is equipped with 9 electrical resistances, capable of supplying heat to the fluid up to ~650 °C. They are made of a shielded heating wire of 2.0 m length having an electrical resistance of 50.0 Ω, embedded into a metallic enclosure with a rectangular section of 2 mm x 4 mm, insulated by magnesium oxide. To improve heat transfer to the airflow and protecting the resistances from the risk of overheating, a high-temperature resistant steel structure is designed. As shown in Fig. 3.13, square cross-section steel tubes are used to pack the 9 resistances, Fig. 3.13(a). The tubes are joined between them with passing bolds which also play the role of separating the resistance between them, thus avoiding their direct contact with the risk of hot spot formation, and consequent damage. At the same time, this structure minimizes the additional pressure drop introduced. The post-heating block is introduced inside the vertical tube connecting the receiver outlet with the turbine. This tube is soldered with a tee element on the upper edge, Fig 3.13 (c) allowing to introduce the post-heating block from the upper aperture and sealing the circuit with a flange. The upper flange, Fig. 3.13 (b), also allows the

installation of the resistances connectors. The post-heating unit is equipped with a suitable power supply and its control is implemented into the general control panel.

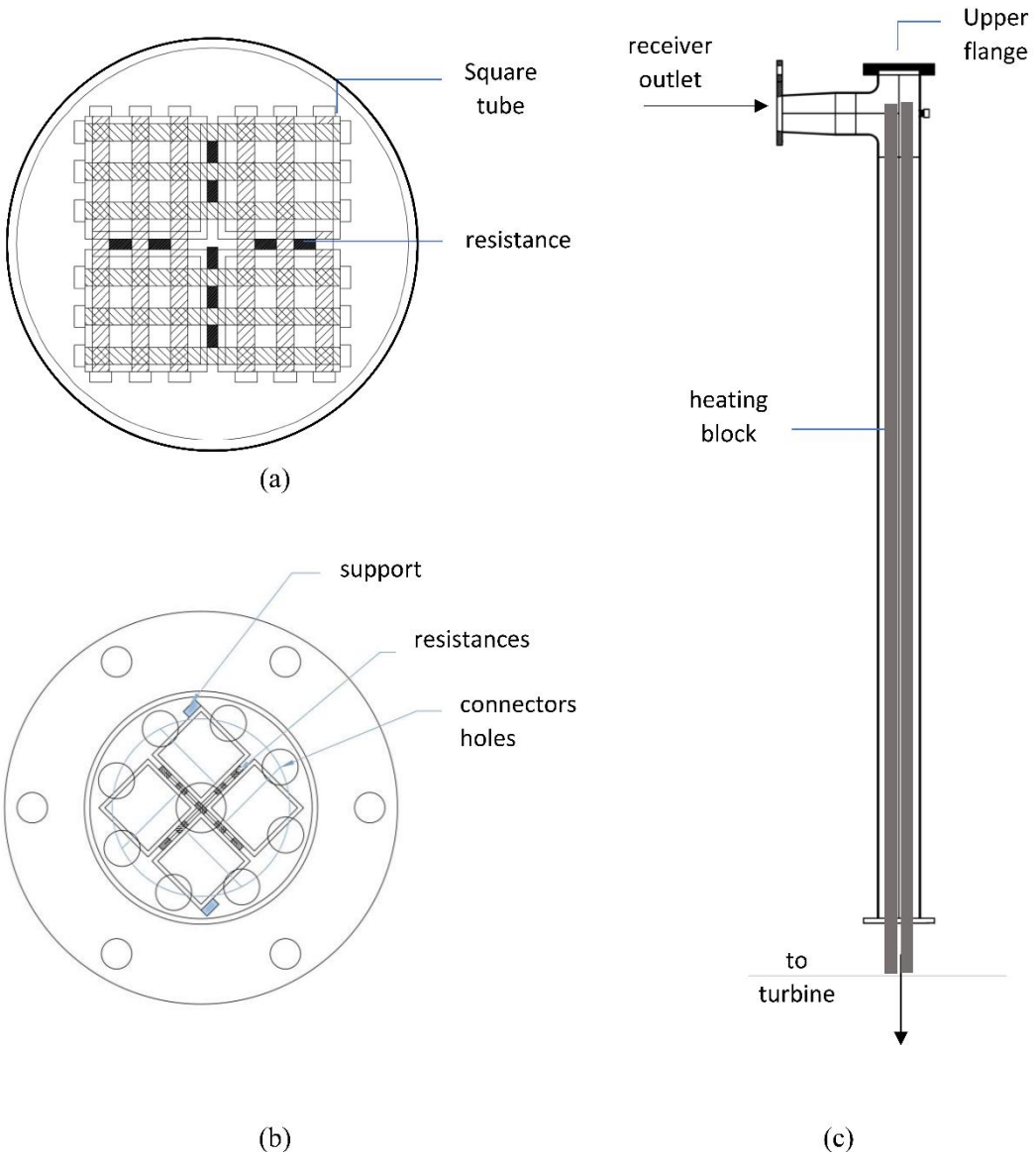

Fig. 3.13. Post-heating drawings. (a) Cross-section; (b) Upper flange with resistances hoses; (c) lateral drawing of heating block inside the vertical tube.

3.1.8 Location

The prototype is installed on the rooftop of the Agustín de Betancourt building at the Universidad Carlos III de Madrid in Leganés (Spain). The limited surface of the rooftop already hosts solar installations for investigation purposes, for which a study of the space availability is required. The main objects and obstacles on the rooftop are reported in AutoCAD 3D as Fig. 3.14 shows, including a wooden log cabin, which hosts the control unit, electric power input, and necessary instruments.

Shadowing analysis has been carried out to select the best emplacement orientation. The 3D model has been used for evaluating the effect of surrounding objects and facilities over the solar

field, through the AutoCAD sky simulation tool. Simulations have been obtained in representative days at different times, some examples are shown below. The selected orientation is 54.1° to EAST from North-South direction.

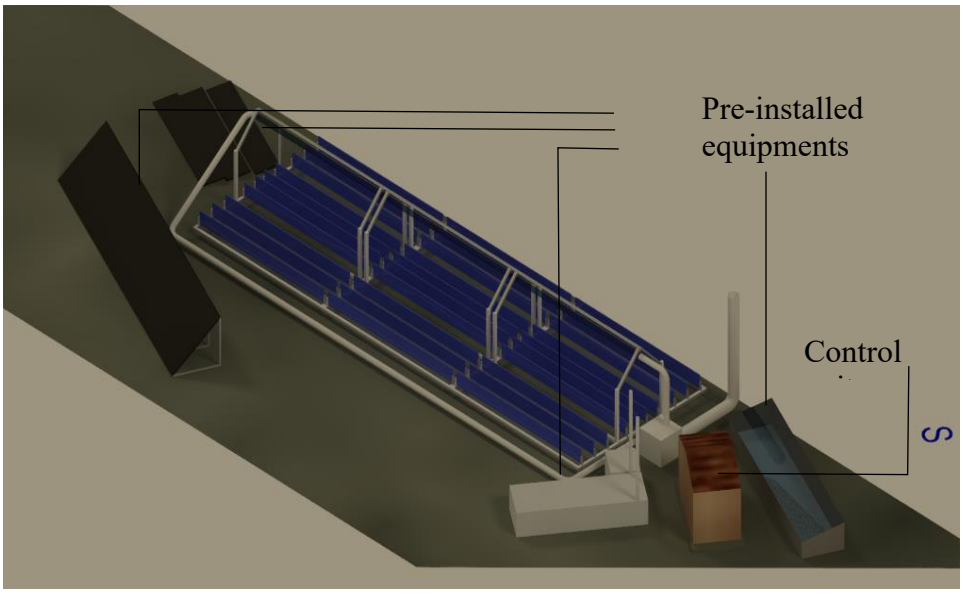

Fig. 3.14. 3D view of Betancourt building rooftop, Universidad Carlos III de Madrid in Leganés (Spain), with pre-installed equipment and T-SAH prototype

According to the shadowing analysis, the selected location and orientation ensure no shadowing on the solar field during spring, autumn, and summer seasons, when the testing campaigns will be carried out. Only during winter days does the solar field receive partial shadowing, which is a minor issue, being the prototype operative during the whole year.

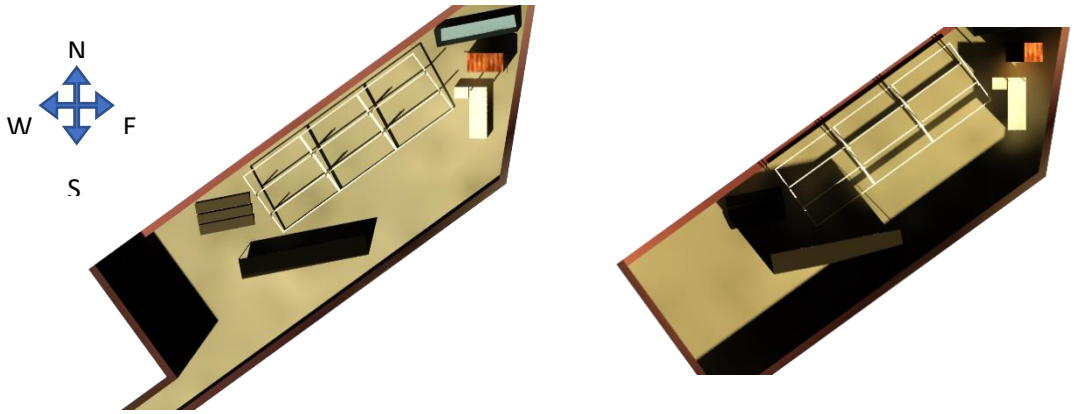

(a) (b)

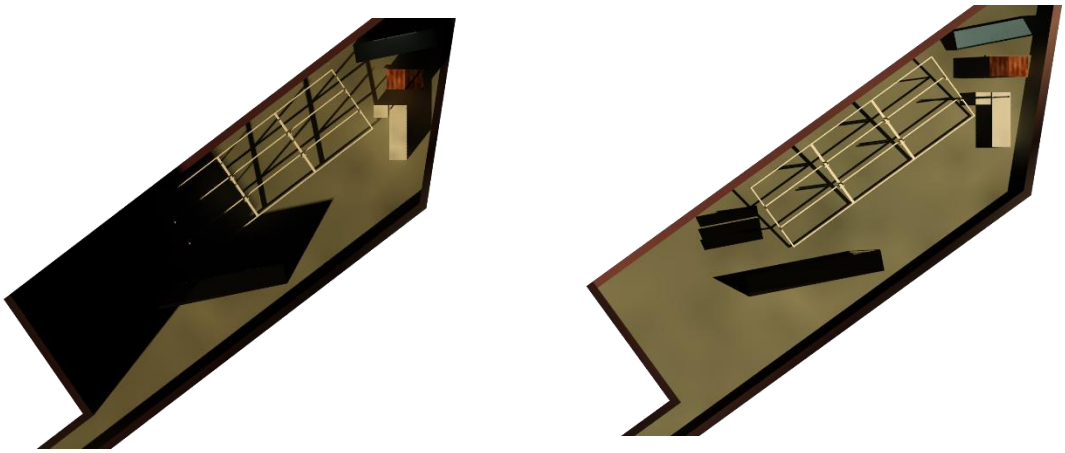

(c) (d)

Fig. 3.15. Shadowing simulation at representative days and times of the year. (a) March 21th 15:00 h; (b) December 21th 13:00 h; (c) December 21th 16:00 h; (d) June 21th 9:00 h.

3.1.9 Process flow diagram and instrumentation

A process flow diagram has been developed to define the relevant measurements, the sensors selection, and the location on the circuit. The system is over-instrumented according to experimental purposes. The redundancy has been increased by utilizing additional instruments for security and protection reasons.

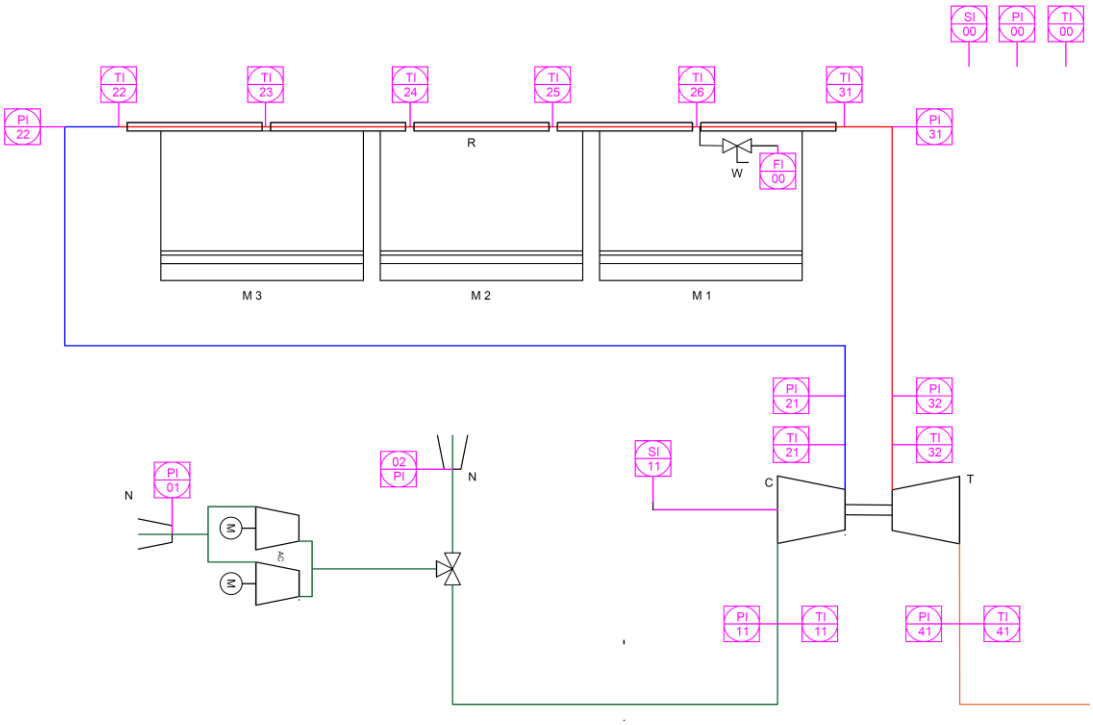

Fig. 3.16. Prototype schematic flow diagram and sensors. Compressor C, Turbine T, Nozzle N, receiver tube R, Solar modules M1, M2, M3, Auxiliary Compressors AC. Green Line: Low pressure/low-temperature flow. Blue Line: Pressurized/ intermediate temperature flow. Red Line: Pressurized/high-temperature flow. Brown Line: Ambient pressure/ high-temperature flow.

The main components are reported in the flow diagram: compressor C, turbine T, receiver tubes R, the three solar modules M1, M2, M3, auxiliary compressors AC. Two air inlets are implemented: one is the direct inlet to the turbocompressor, and the other is the indirect inlet to the auxiliary compressor. A manual switching valve allows switching from one to another inlet. It is worth mentioning that direct inlet only can be used when the turbocharger is accelerated and can operate in steady-state conditions without the auxiliary compressor aid.

Temperature and pressure sensors are required in the main reachable points of the air circuit, according to Fig. 3.16. Type K thermocouples class A are suitable for TI 00, TI 11, TI 21, TI 22, TI 23, TI 24, TI 25, TI 26, TI 31, TI 32, TI 41. They are calibrated inside a humid stabilized bath well against a reference thermocouple. They showed a total expanded uncertainty of ±1.2 °C, for which a total maximum measurement uncertainty can be estimated as an expanded uncertainty ±2.0 °C in worst cases when installed. Relative pressure transmitters (Wika A-10) are suitable for air pressure measurements PI 11, PI 21, PI 22, PI 31, PI 32, PI 41. Absolute ambient pressure measured value PI00 is added to the relative pressure measurements to achieve absolute values for all the pressure variables. Pressure measurements yield an installed total expanded uncertainty of ±25 mbar after calibration. Volume flow is measured at the atmospheric inlet by an airflow sensor (Schmidt 30.015 MPM) with a declared uncertainty of ±3%. Moreover, a redundant mass flow measurement is obtained from purposely devised inlet nozzles and a differential pressure sensor (First-Sensor BTEM5P070 -70...+70 mbar) connected to points PI 01 and PI02 in Fig.3.15. Mass flow rate can be obtained from Eq. (3.1), with $C_D = 0.97$, $R_g = 287.1 \frac{\mathrm{J}}{\mathrm{K\,Kg}}$, p_{amb} in bar, T_{amb} in K. Δp is the differential pressure between ambient and static pressure at inner nozzle diameter (bar). $D_{in} = 0.034$ m for the indirect inlet and $D_{in} = 0.044$ m for the direct inlet.

$$\dot{m} = \frac{\pi D_{in}^2}{4} C_D \sqrt{\frac{2}{R_g}} \sqrt{\Delta p \frac{p_{amb}}{T_{amb}}} \tag{3.1}$$

Measuring the pressure difference between the inner nozzle diameters of the two nozzles gives Δp either using the direct or the indirect entrance. In fact, they never are used at the same time, so that when operating, the pressure on the other nuzzle is the ambient pressure.

A rotating speed sensor SI 11 provided by the turbocharger manufacturer is used for turbocharger rotating speed measurement with +/-0.05% uncertainty, installed on the compressor housing. Wind speed SI 00 is monitored for safety reasons. The injection of water into the last receiver tube is considered as a possibility for fast cooling down in case of accidental overheating and eventually monitored (FI 00).

The existing meteorological station, Fig. 3.17, provides global solar irradiance G_{glo} on the horizontal plane and diffuse irradiance G_d using two pyranometers (Kipp&Zonen) with ±3% total uncertainty, and a shadow band.

(a) (b)

Fig. 3.17. Meteorological station at Carlos III University of Madrid (Betancourt building roof). (a) pyranometer with shadow band for diffusive irradiance measurement; (b) pyranometer for global horizontal irradiance measurement.

3.1.10 SCADA

A Supervisory Control And Data Acquisition (SCADA) system was implemented using a Programmable Logic Controller PLC (Unitronics USP-104-B10). The SCADA must enable the following functions:

- Control of solar field.
- Monitoring the measured values and allowing continuous data logging.
- Emergency and safety routines and alarms.

Solar field control is implemented according to the proprietary control system already integrated into the solar field by the manufacturer. The overall control architecture is shown in Fig. 3.18.

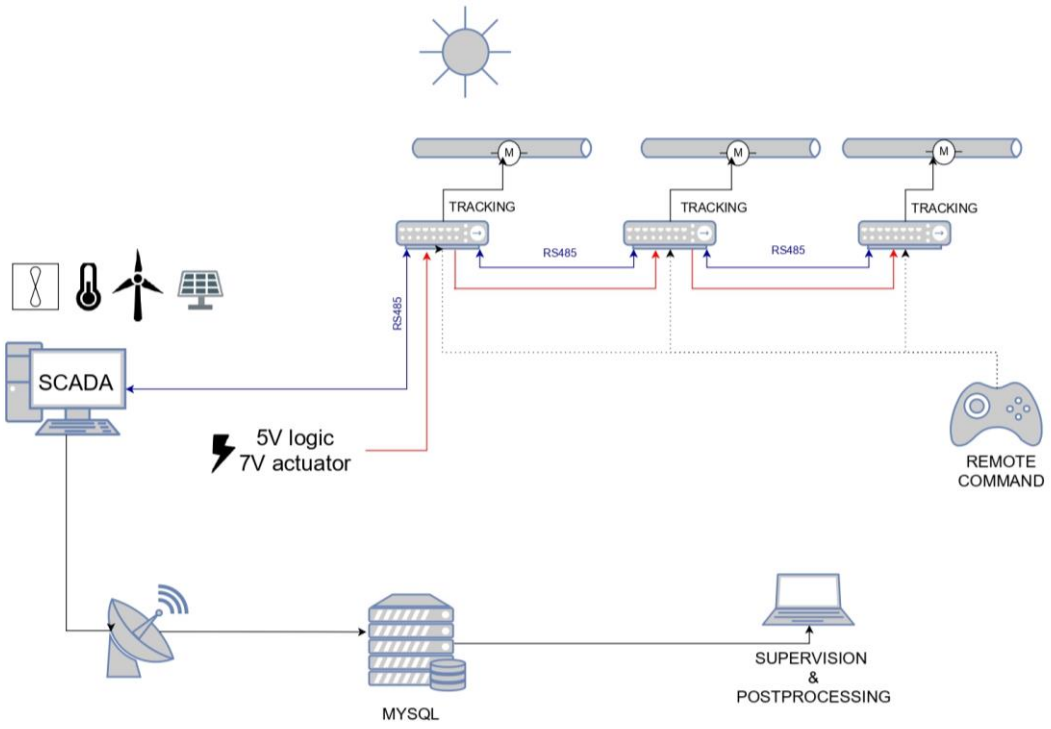

Fig. 3.18. Schematic diagram of solar field control by Solatom™ [80]**.**

Each solar module is equipped with an ATMEGA2560 microcontroller. The controller has a serial interface to fully manage the module in automatic and remote monitoring modes. It is integrated into the module within a dedicated box, Fig. 3.19(a).

(a) (b)

Fig. 3.19. Solar module control equipment. (a) Integrated microcontroller; (b) Manual command

The microcontroller receives a 5 V logic input from PLC and a 7 V voltage for the actuators (axis motors). Using very small voltage and power for the actuator is possible since only one motor per module operates simultaneously. The three microcontrollers are connected between them and to the PLC. One of them is equipped with Global Positioning System (GPS). A manual command can be connected to each microcontroller for maintenance and calibration operations Fig. 3.19(b).

Remote control acts on the overall solar field, a single module, or a single axis, according to the given command. Control commands acting on a single module are implemented on the main PLC window and allow:

- Activate/deactivate module tracking (TRACKING)
- Set module to the vertical rest position (MAINTAIN)
- Fast emergency mirrors defocusing (DEPOWER)

Simultaneous emergency defocusing of all modules is also implemented (EMERGENCY DEPOWER).

A dedicated window is programmed for single-axis control. Each reflector axis can be independently set on tracking mode or depower mode. Depower mode defocus the selected reflector, allowing a detailed solar power control. The number of depowered axes is visualized and counted.

(a) (b)

(c) (d)

Fig. 3.20. SCADA visual interface implemented on PLC. (a) Solar field control commands; (b) Individual axis control interface; (c) alarm and warning setting interface; (d) expert direct commands tool.

Security alerts have been programmed paying attention to the receiver tube over-temperature risk and reflectors protection from wind load. Warning messages advise when critical conditions

are reached (WARNING settings). As soon as safety operation limits (ALARM settings) are violated, emergency reflectors defusing is taken as an automatic action. An adjustable threshold is set as WARNING and ALARM conditions for each monitored parameter (temperature, pressure, and wind speed).

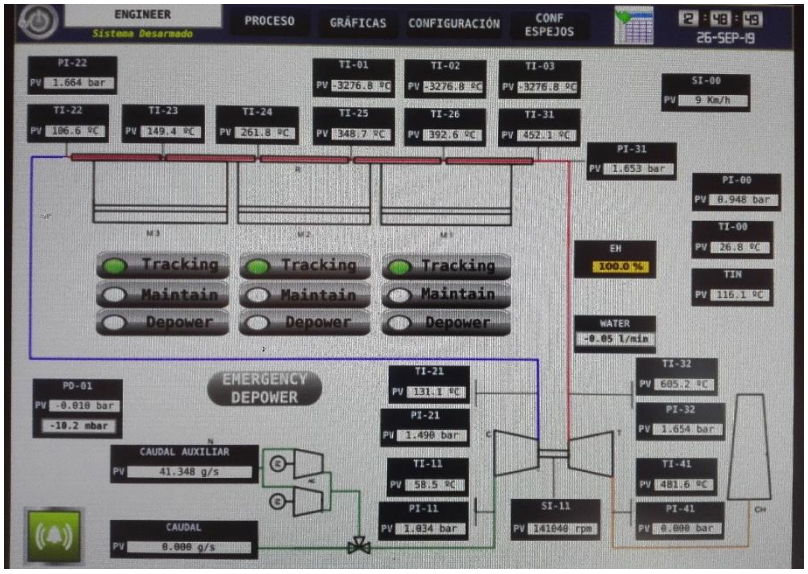

(a)

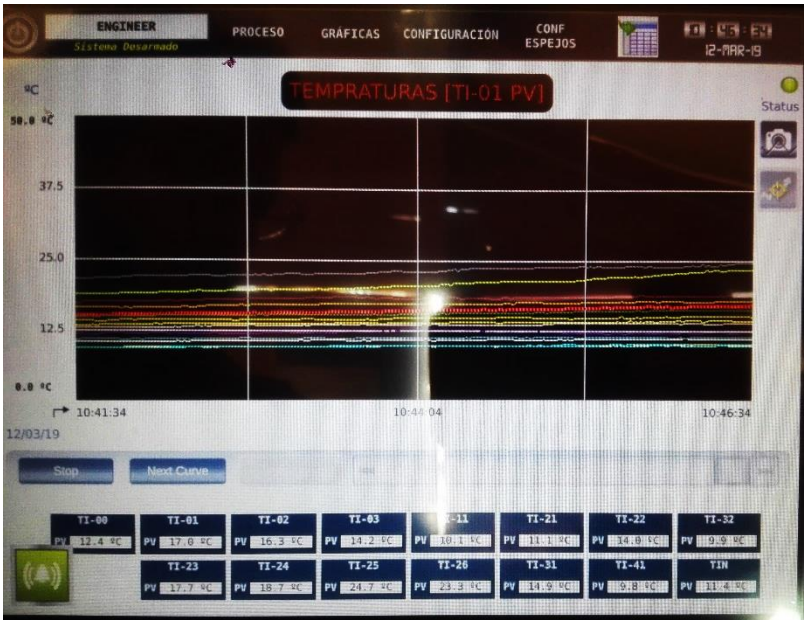

(b)

Fig. 3.21. SCADA visual interface implemented on PLC. (a) Process diagram with monitored variables (b) Example of the on-screen graphical time evolution of one variable.

Besides the commands mentioned above, expert direct communication tools have been implemented on PLC for configuration and settings, calibration and tuning process, as well as a

maintenance operation. It allows to directly send commands to the microcontroller according to the manufacturer's logic. Among other commands, the tool enables to set the geographical coordinates and the orientation of the solar field, needed for the astronomical tracking algorithm.

Data acquisition is programmed according to the process flow diagram shown above and the instrumentation features. On the PLC unit, continuous online monitoring is implemented with an adjustable interval of time, set on $\Delta\tau = 30$ s. Graphical evolution over time of main monitoring variables is provided online.

3.1.11 Wind load analysis

Wind loads are considered a potential risk for prototype structure stability and protection. Following the CTE SE-AE wind loads regulation, an analysis has been carried out to establish the counterweight proper distribution. Due to the structure weight of 900 kg and wind maximum horizontal load estimated as 6,048 kN (616,5 kg), the distribution of 28 concrete counterweights each one of 150 kg is needed for balancing, as indicated in Fig. 3.20. Distribution results in an average roof loading of $64\,\frac{\mathrm{kg}}{\mathrm{m}^2}$, which is less than the critical load of the roof ($400\ \mathrm{kg}\frac{}{\mathrm{m}^2}$).

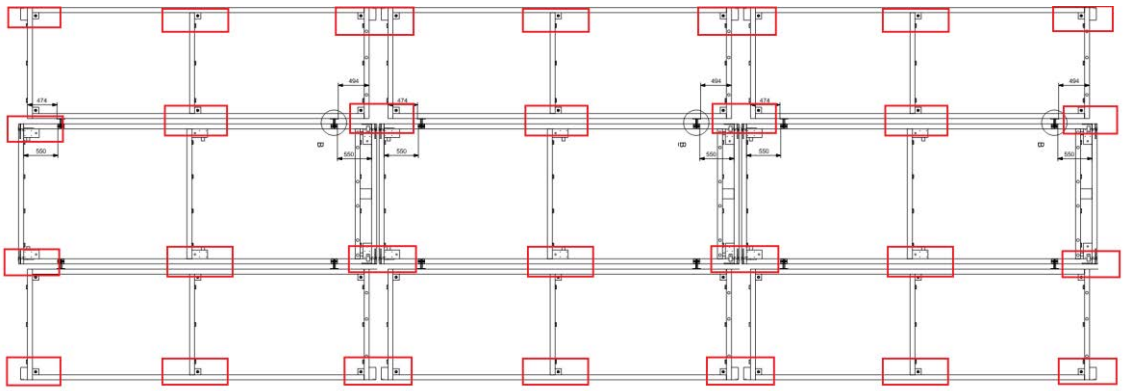

Fig. 3.22. Schematic of concrete counterweights distribution according to wind load risk prevention.

3.2 Prototype installation

The following section describes the main tasks accomplished for the successful installation of the prototype. The SCADA calibration procedure, and the preliminary operation, carried out before the testing campaign are reported.

3.2.1 Solar field

The three solar modules were delivered by the manufacturer in containerized form, with the "wings" and the upper portion of the structure closed for easier transportation, Fig. 3.23 (a)-(b). They were located on the rooftop (Agustín de Betancourt building at Carlos III University) and oriented according to the design. Precise longitudinal alignment and horizontal levelling have been obtained Fig. 3.23 (b)-(c) before installing the concrete counterweights, fixed to the structure as indicated in the wind load study, Fig. 3.23(d). Subsequently, the secondary optic structure has been assembled introducing the extension length between two modules and at the extremities. The supports for the receiver tube were installed on the structure as in Fig. 3.24.

(a) (b)

(c) (d)

Fig. 3.23. Solar field installation. (a) Containerized module; (b) Aligned modules; (c) Module with open wings, leveled; (d) Concrete counterweights.

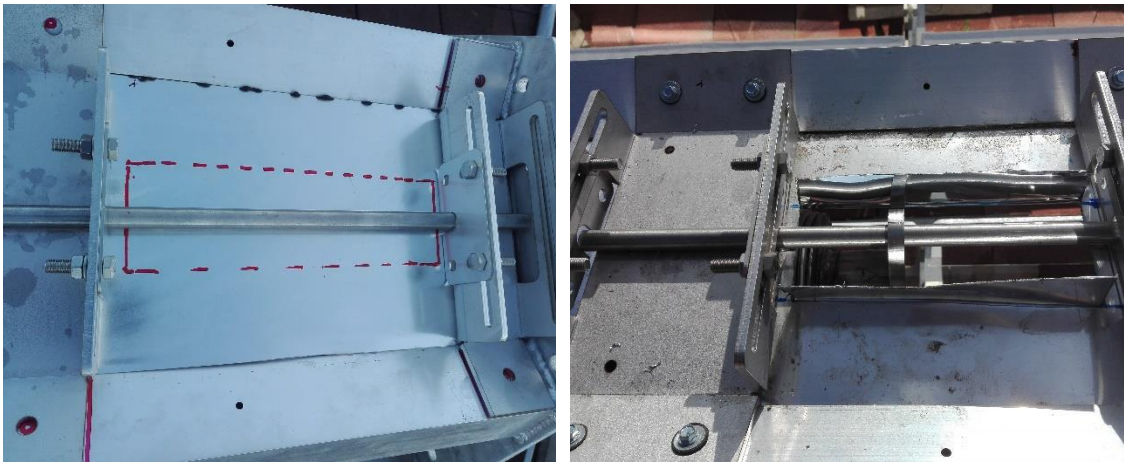

(a) (b)

Fig. 3.24. Support for the receiver tubes mounted on the secondary optics structure

3.2.2 Receiver tubes

Receiver tubes have been adapted to the prototype requirements. An extension of 30 mm of stainless-steel tube of the same diameter has been welded at each extreme cross-section to allow flange welding as well as sensors installation, Fig. 3.25 (a)-(b). Thermocouples for internal air temperature measurement have been installed as shown in Fig. 3.25 (c). Subsequently, receivers have been installed and aligned within the optics on the proper brackets, joint using prefabricated high-temperature resistant gaskets, Fig. 3.25(d).

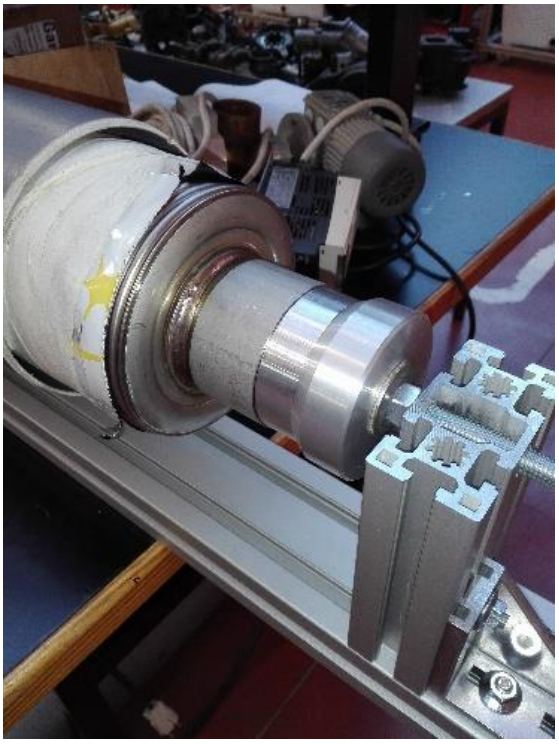

(a)

(b)

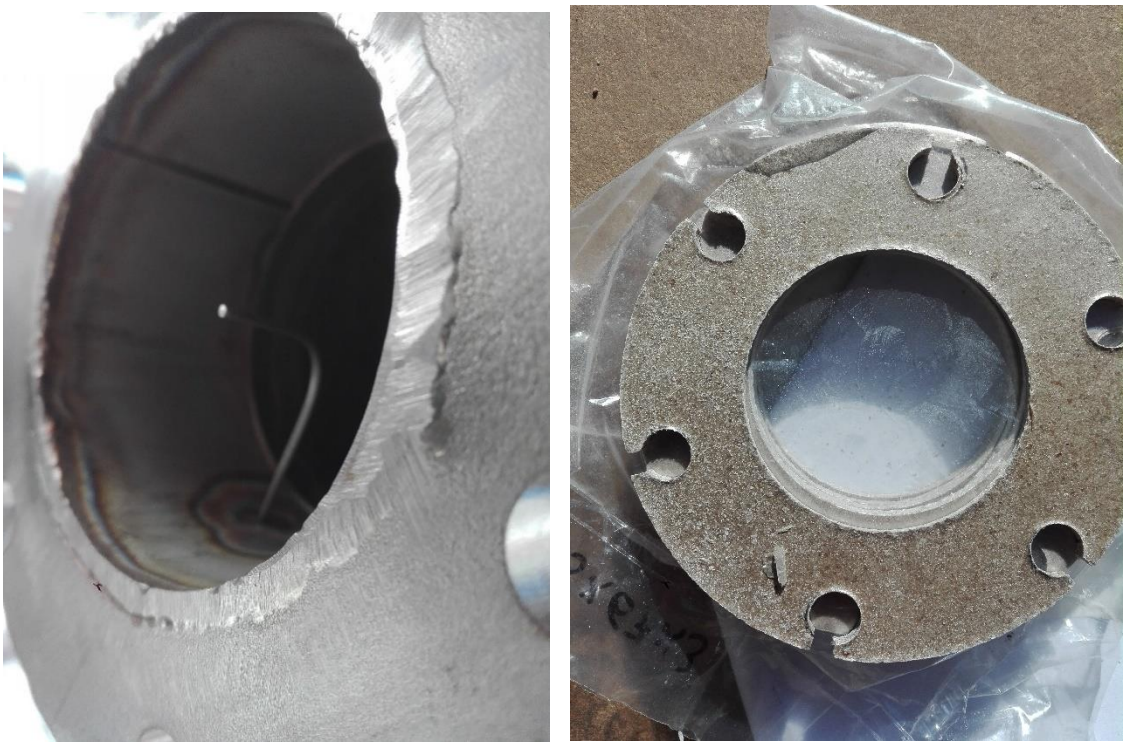

(c) (d)

Fig. 3.25. Receiver tubes connection. (a) welded extension and (b) flange; (c) thermocouple; (d) High-temperature resistant gasket made of Mica with a thickness of 3 mm.

3.2.3 Piping

Air piping has been built after manufacturing the single components, like the diffuser, diameter reductions, and bends, equipped with proper mounting flanges. Fig. 3.26(a) shows the installed receiver tubes (still covered by protective plastic) and the flanged connection at the outlet. Receiver inlet, Fig. 3.26(b)-(c), is mounted between straight rails, allowing the axial displacement of the inlet receiver extremity. The turbocharger connection to piping can be seen in Fig. 3.26(d), where outlet compressor and turbine diffuser are shown (still without insulation), as well as the inlet turbine converging nozzle and compressor flexible clamped connection hoses.

(a)

(b)

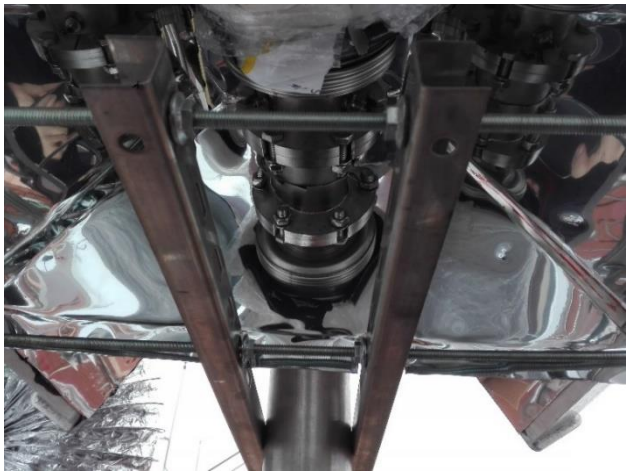

(c)

(d)

Fig. 3.26. Piping details. (a) receiver tubes installed; (b) receiver inlet; (c) Flanged receiver inlet; (d) turbocharger connections.

The moderate temperature inlet side (below 150 °C) has been thermally isolated using fiberglass material, with an average thickness of 80 mm and external aluminum protection against water and sun rays. The high-temperature outlet side (300 - 500°C) has been isolated using fiber wool rock material of 150 – 200 mm thickness and aluminum cladding. Additional flexible aluminum covers are also used throughout the piping to prevent any unintentional and potentially injuries such as concentrated radiation or rain. Fig. 3.27(a) shows the insulated low-temperature side air pipe. The flexible connection required to compensate the receiver thermal dilatation is shown

in Fig. 3.27(b). It can be noticed as the secondary structure has been raised to the operating design height. Connection clamps and flanges are shown in Fig. 3.27(c)-(d).

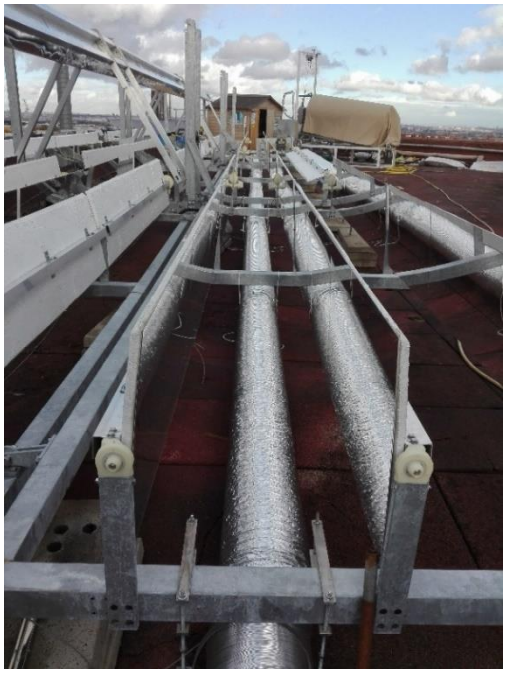

(a)

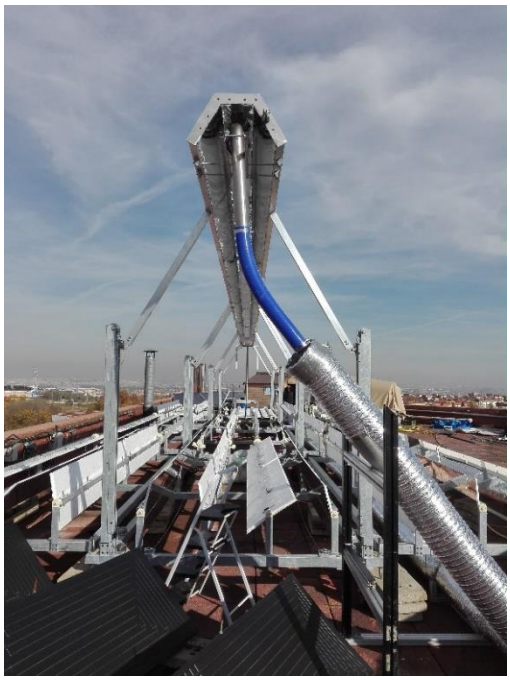

(b)

(c)

(d)

Fig. 3.27. Insulated piping. (a) Low temperature insulated air pipe; (b) Flexible tube; (c) Clamps; (d) Flanges.

3.2.4 Turbocharger unit and auxiliary devices

A dedicated box has been built for hosting the turbocharger and auxiliary devices, Fig. 3.28(a). The two electrical side channel blowers were installed in a parallel configuration, Fig. 3.28(c). They are equipped with a frequency converter for mass flow rate control, Fig. 3.28 (d). Two manual valves enable switching from 'boosted' operation including auxiliary electrical compressors and 'direct operation' with turbocharger only. Direct access to valves, electrical compressor switch, and frequency converter controller is ensured. An electric oil lubricator pump is installed for turbocharger shaft continuous lubrication. The turbocharger with inlet and outlet oil duct is shown in Fig. 3.28(b).

(a)

(b)

(c)

(d)

Fig. 3.28. Blowing unit. (a) Box; (b) Turbocharger with lubrication oil ducts; (c) Electrical blowers, oil pump, and inlet air piping; (d) Frequency converters, inlet nozzle.

3.3 Post-heating unit

The post-heating unit is assembled according to the design. First, the resistances are mounted on the four steel tubes of square cross-section, forming a robust block, Fig. 3.29(a).

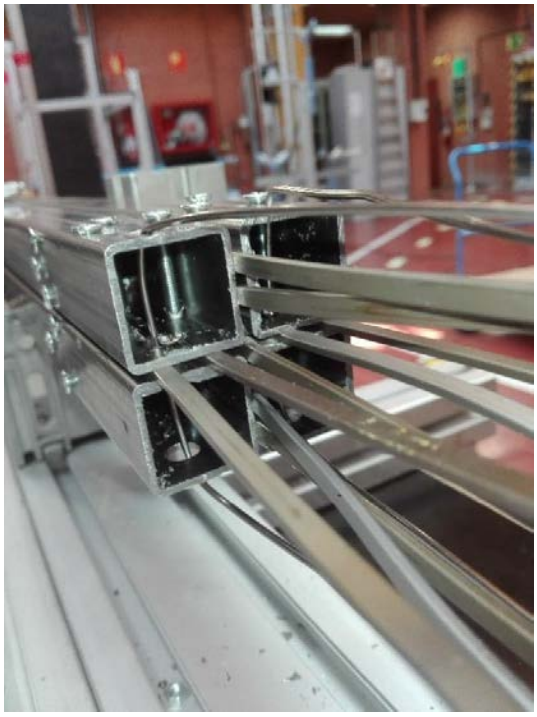

(a)

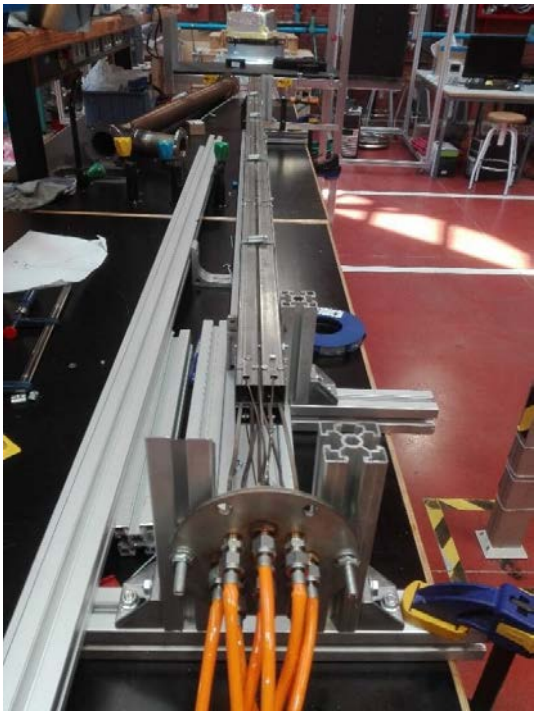

(b)

(c)

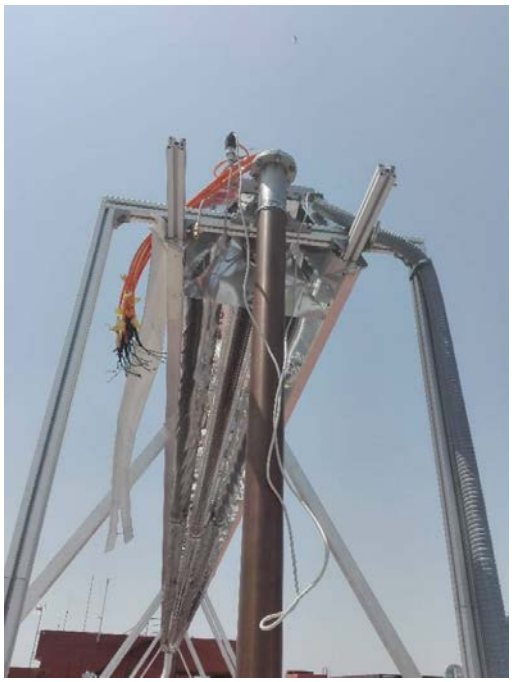

(d)

Fig. 3.29. Post-heating unit. (a) heating block; (b) upper flange; (c) vertical tube with tee connection; (d) installation.

The resistance extremities are fixed on the upper flange through welded connectors Fig. 3.29(b). The heating block is inserted inside the vertical tube having a tee connection to be flanged with the receiver outlet, Fig. 3.29(c). Lastly, the tube is installed on the prototype, Fig. 3.29(d), and covered with mineral rock wool insulation of 200 mm thickness. Resistances were electrically connected to their power controller.

3.3.1 Instrumentation and cabling

The thermocouples and pressure sensors have been calibrated and then connected to the SCADA unit located inside the wooden house, Fig. 3.30.

(a) (b)

(c) (d)

Fig. 3.30. Instrumentation and cabling. (a)-(b) Cabling; (c)-(d) PLC and electrical cabinet.

Cabling of sensors, solar modules controller, and auxiliary devices has been executed avoiding electrical noise, protection from heat, solar radiation, and rain. Thermocouples are installed on the receiver tubes for measuring airflow temperature. Pressure sensors are installed at the receiver extremities. The turbocharger has been equipped with an optic speed sensor (Garett speed sensor kit) and an external additional gauge, besides its connection to SCADA. Pressure and temperature sensors are placed at the inlet and outlet of the compressor and turbine. Two nozzles have been installed at the two air entrances and equipped with a differential pressure sensor to measure the mass flow rate.

3.4 Calibration and tuning

Preliminary tests proceeding the experimental campaign have been executed in several stages.

First, a set of “dark” tests have been run without any solar power input. Such tests aimed to verify the operation of all the installed sensors, as well as the proper data logging by the SCADA. The operation of the auxiliary compressors has been evaluated and tested as well as real circuit pressure drops.

As a second step, solar modules have been tested. The serial controller implemented on the PLC has been verified and tuned. The programmed alerts for excess temperature and dangerous wind load have been checked, the real response delay of the system to emergency commands has been evaluated. Focusing and continuous sun tracking have been tried under different mass flow rates.

Calibration procedures have been iteratively executed on the mirror axes. A first calibration routine implemented by the manufacturer can adjust the angular sensor of the reflectors by recording iteratively horizontal and vertical reference positions.

The second calibration has been done on the parabolic mirrors using lasers, to verify and adjusts their orientation to the gearing. For that purpose, either serial communication from PLC or the portable controller provided by manufacturers have been used.

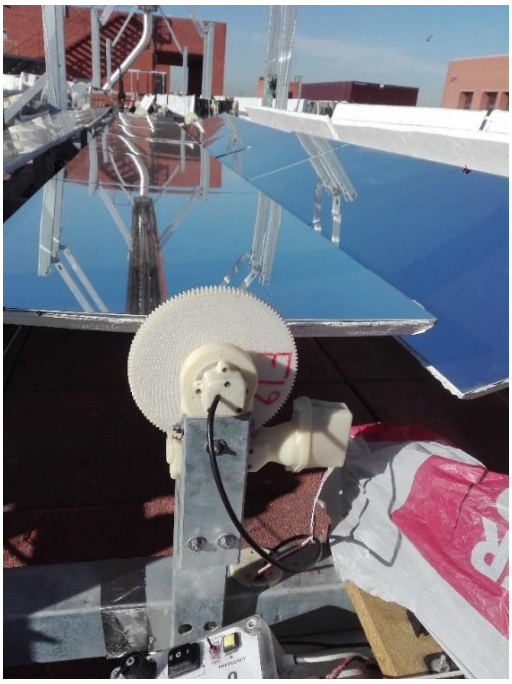

(a)

(b)

(c)

(d)

Fig. 3.31. Solar field calibration. (a) Axes angular position sensor; (b) gear and motor; (c) solar field in tracking mode; (d) solar field in rest mode.

The third calibration step has been made during continuous sun tracking operation mode. This procedure allows setting an offset angle for each axis, respect to the astronomical tracking angle. In fact, due to manufacturing imperfections, mirrors, and structure bendings, the tracking angle could give unprecise focusing, which can be corrected with the offset angle. In addition, in some cases, tube bending can lead to contact with the glass envelope, increasing the risk of rupture, as documented in the technical literature. The offset angle can be modified to deviate the concentrated irradiance of one or more axis on the secondary optics instead of the receiver

directly. This can lead to the more homogeneous circumferential distribution of concentrated irradiance on the receiver perimeter, reducing the bending effect, although a loss of optical efficiency is expected.

(a) (b)

Fig. 3.32. Upstream view of the solar field in full tracking mode (a) and partial tracking (individual axis control) (b).

3.5 Thermal Energy Storage

An experimental Thermal Energy Storage TES unit was designed and implemented for its integration into the T-SAH prototype. Latent heat storage represents a promising solution for industrial applications [57], for which it has been preferred to sensible heat storage. The Lithium Nitrate salt ($LiNO_3$) has been selected as a storage material due to its suitable melting temperature of 254 °C and high specific latent heat of 360 kJ/kg (higher than ice), about three times higher than other alternatives. Its higher cost should not be a problem for the low amount required. It can be recycled after its use. It is non-toxic neither corrosive nor seems to last for many cycles.

A “shell and tube” design is chosen for the heat exchanger configuration, where the air flows inside a straight channel across a series of vertical tubes filled with the phase change material ($LiNO_3$). Commercial tubes with round transversal fins appeared as the best solution for improving the heat transfer rate in the airflow side, keeping the low-cost and easy manufacturing. For the air channel, some air conditioning ducts are considered due to the low cost and their widespread availability on the market as they are used for air conditioning.

Fig. 3.33 (a) reports a 3D drawing of the TES core. An air channel with a square cross-section of 600 mm and a length of 500 mm is chosen. The lithium nitrate salt is filled inside four externally finned cylinders made of stainless steel, having an internal diameter of 76.1 mm, 2.9 mm

thickness, an overall height of 570 mm, and a finned height of 490 mm. The cylinders are externally finned with welded helicoidal corrugated fins of carbon steel, with a height of 35 mm and thickness of 0.7 mm. The distance between fins is 6mm. The upper and lower apertures are closed with removable flanges. The cylinders are placed vertically and adjacent one to another, in parallel to the perpendicular airflow, Fig. 3.33.

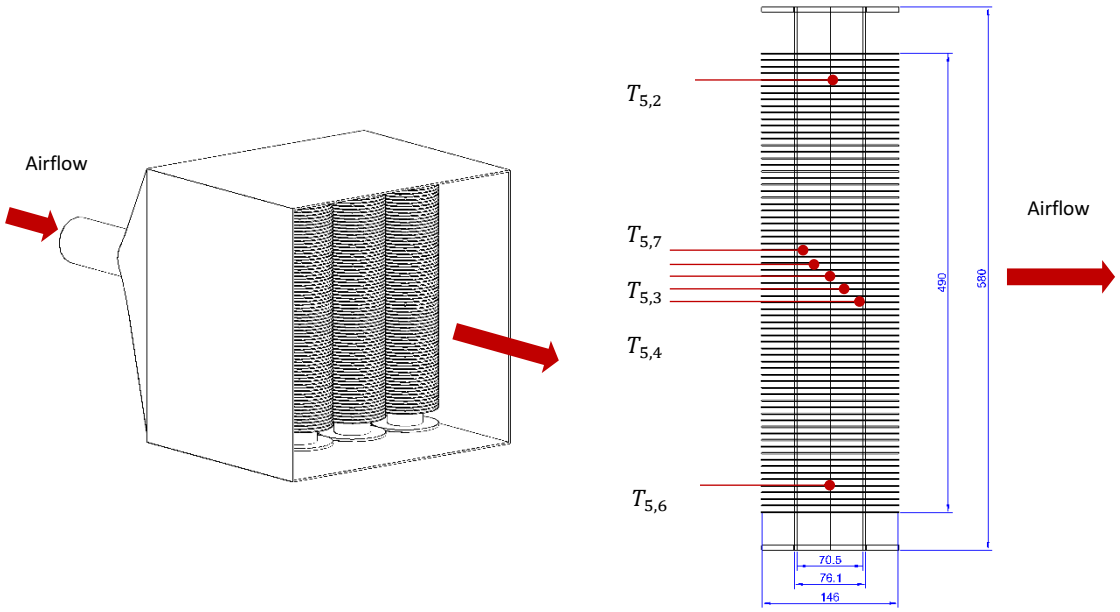

Fig. 3.33. TES layout and finned cylinder. (a) Finned cylinders inside insulated the air channel. (b) Finned cylinder instrumented.

In order to fix the finned cylinders inside the duct and covering their non-finned extremities, steel plates have been designed and sized, as in Fig.3.34.

Fig. 3.35 depicts the whole air channel. A 100 mm diameter round duct connects the TES core with the T-SAH outlet (turbine exit).

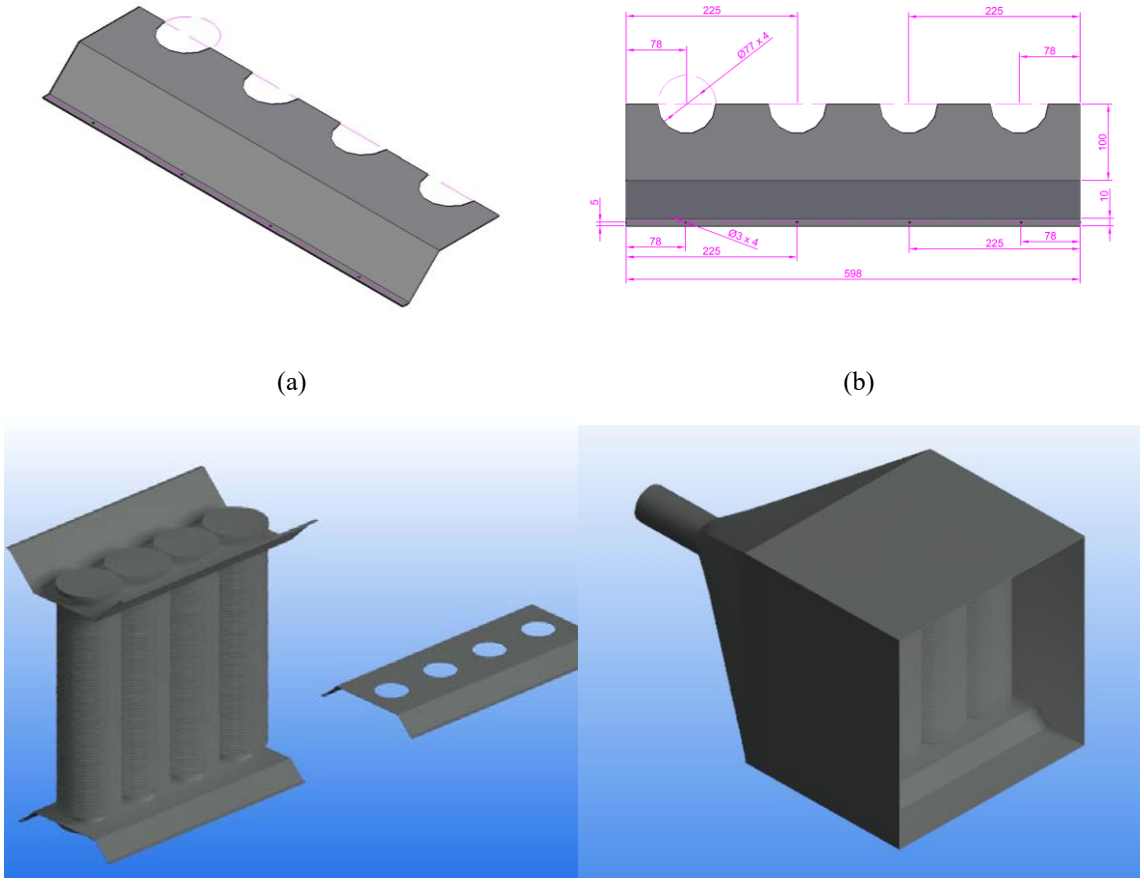

(a) (b)

(c) (d)

Fig. 3.34. Cylinder separator plate. (a) 3d view; (b) 2D technical drawing, (c) mounting scheme, (d) final aspect.

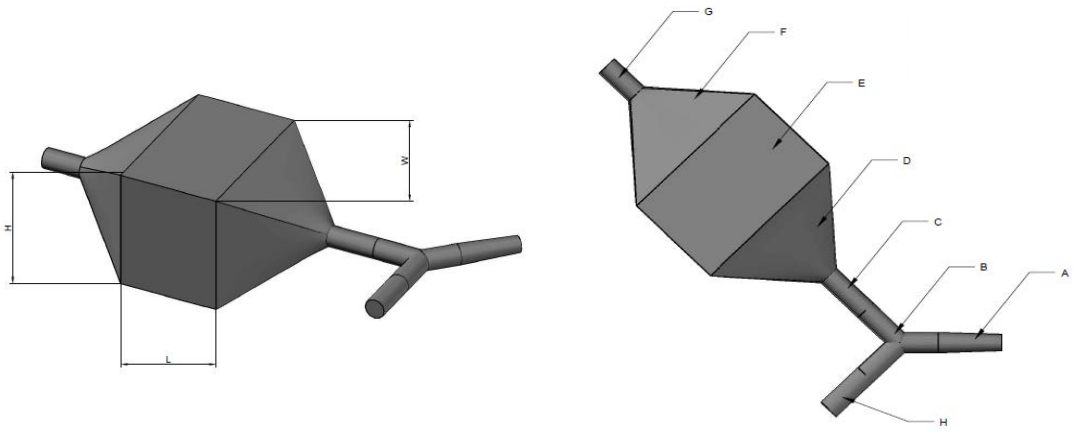

(a) (b)

Fig. 3.35. TES air channel. (a) 3D view. (b) 2D drawing: A diameter reduction; B simple derivation; C-G-H throttle valves, F-D square to round hoppers, E square duct.

One of the four cylinders is instrumented with type K thermocouples, Fig. 3.36(b). They are placed in the central vertical axis, at the upper as well as at the lower part and in the middle. Additional thermocouples were placed in the horizontal plane at the medium height cross-section to detect temperature gradients in the horizontal axial direction, Fig. 3.36 (b). To correctly position the thermocouples inside the tube a thin structure is needed as shown in Fig. 3.36(a). They are fixed on the upper flange and positioned with the aid of three separators made of stainless steel and 1 mm thickness, then aligned using two vertical threaded rods, Fig.3.36(b). Two thermocouples measure air temperature at the inlet and outlet of the TES channel.

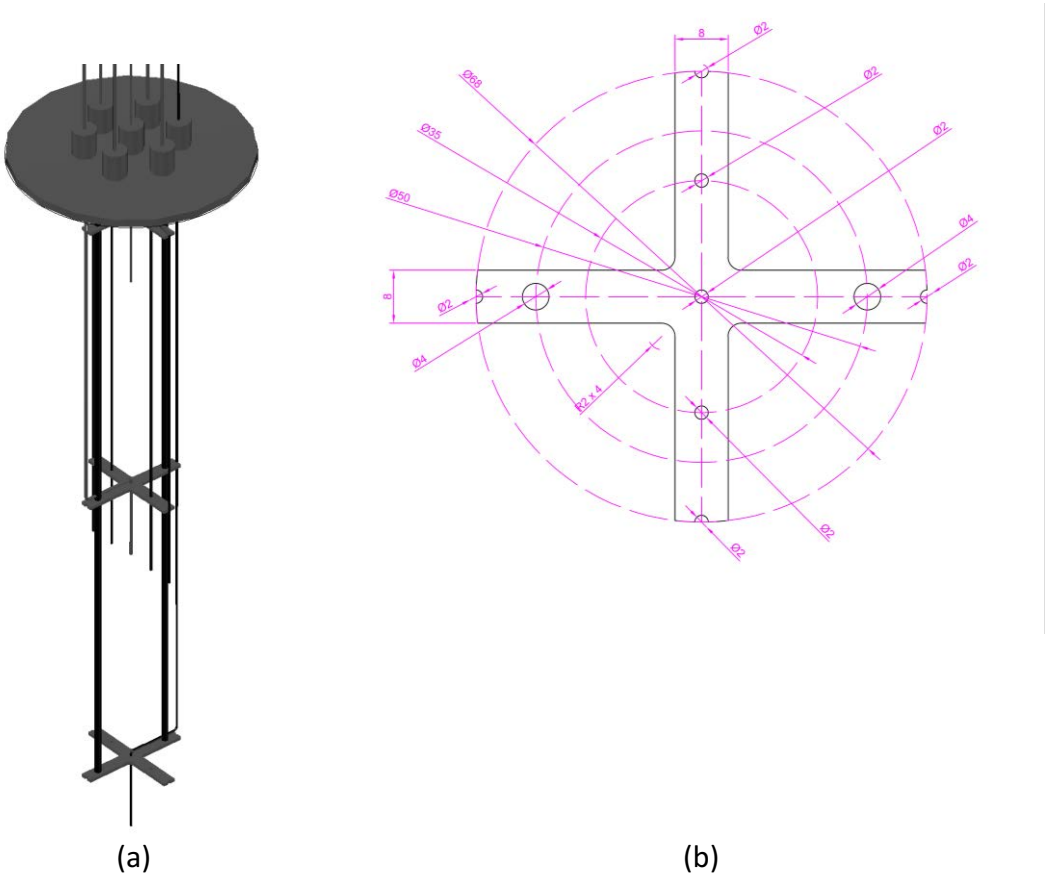

(a) (b)

Fig. 3.36. Cylinder instrumentation (a) thermocouples supporting structure; (b) thermocouple positioning plate.

The TES unit is assembled according to its design, and it is integrated into the T-SAH prototype. The unit is mounted downstream of the turbine. The finned cylinders are filled with $LiNO_3$ as a granular state. Once molten for the first time, it solidifies forming a compact block, with a smaller volume than the initial granular form. For this reason, a second filling operation was devised after the first melt. Fig. 3.37 (a) shows a single finned cylinder partially filled with $LiNO_3$.

The thermocouples assembly is prepared as in Fig. 3.37, to be inserted into the instrumented cylinder before filling it with salt.

(a) (b)

Fig. 3.37. TES preparation. (a) Finned cylinder; (b) Thermocouples and supporting structure.

Then the four cylinders sealed with their flanges are assembled inside the square duct as in Fig. 3.38(a). The air channel before assembly and insulation is shown in Fig. 3.38(b).

The square air channel has been cut to allow the thermocouples connection on the bottom side Fig. 3.39 (a). On the upper side, it has been modified as in Fig. 3.39(b), enabling the inspection of the cylinders.

Once the TES core was assembled, it has been covered with a mineral wool insulation of 150 mm thickness and covered with aluminum foil, Fig. 3.40. The connection duct with the turbine exit is installed and insulated.

(a) (b)

Fig. 3.38. TES components. (a) Cylinders and inside the square duct, (b) air channel before installation.

(a) (b)

Fig. 3.39. Air channel detail. (a) instrumented cylinder flange; (b) upper aperture for inspection.

(a) (b)

Fig. 3.40. Assembled TES. (a) TES core insulated with mineral wool sheets and covered with aluminum foil. (b) tubular duct before insulation.

4 NUMERICAL MODEL OF T-SAH PROTOTYPE

This chapter describes the development of a detailed numerical model of the installed T-SAH prototype, which is described in Chapter 3 and Fig. 4.1. It includes the model of a Linear Fresnel collector, its receiver tube, the turbocharger, and the piping, in addition to a sky model for the solar irradiance.

More specifically, two receiver models have been developed in two forms, either static or steady-state, or dynamic. The receiver static thermal model has been implemented using well-known methodologies based on collector efficiency factor F' and heat removal factor F_R [26], besides applying spatial discretization for increasing the accuracy. An original dynamic model has been obtained modifying F' and F_R for including the receiver thermal inertia, aiming at better accuracy against transient data with low computation cost. Applying spatial discretization of the receiver tube allows increasing the accuracy of predictions, taking into account the non-uniform heat flux in the axial direction generated by the solar field complexity, as well as the discontinuous receiver thermal properties, due to the presence of junctions between consecutive receivers tubes, besides to variation of airflow conditions.

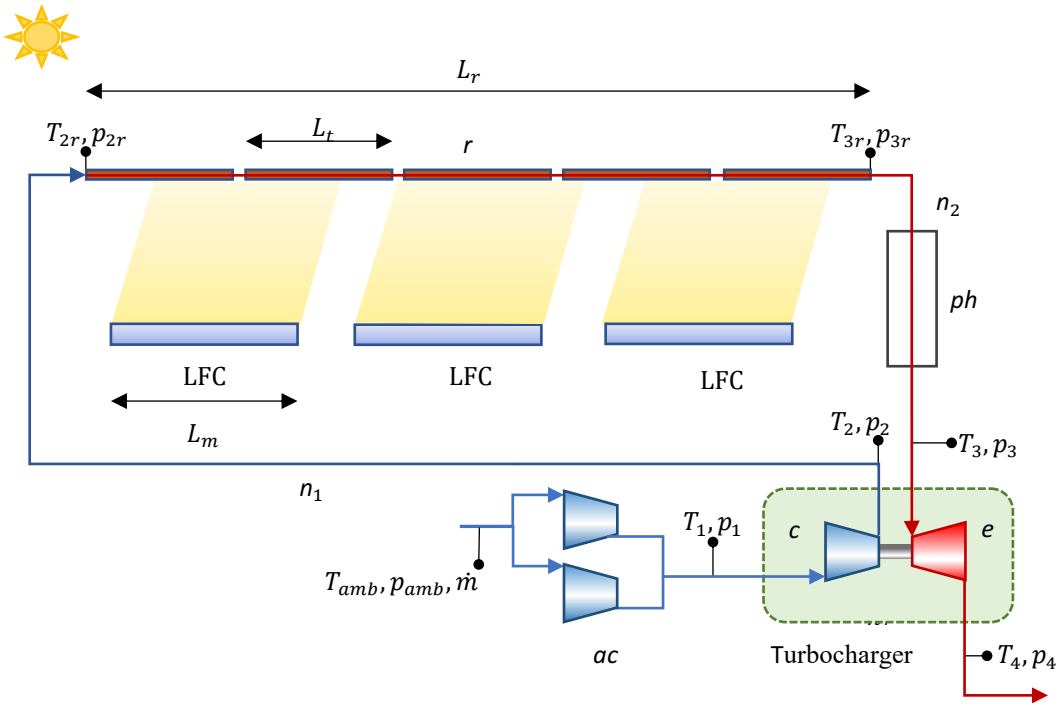

Fig. 4.1. Experimental setup scheme, Linear Fresnel *LFC* mirror field, receiver *r*, auxiliary compressor *ac*, experimental post-heating unit *ph*, turbocompressor *c*, turbine *e*. Sensors: temperature *T* and pressure *p*.

A turbocharger model is implemented, combining conventional and original techniques. It is based on the performance maps provided by the manufacturers, using them in a singular form. The maps have been digitized and a detailed fitting procedure has been applied to obtain the functional relation needed for effective modeling. The heat transfer occurring across the turbine and compressor has been analyzed. The analysis allows modifying the canonical turbocharger

model to account for the main effect of diabatic behavior. The developed modeling procedure has been applied to the turbocharger under study and holds general validity for its application to other devices.

4.1 Linear Fresnel Collector

An optical model of an LFC is needed to predict the incident heat flux on the receiver resulting from the incidence of the direct normal solar irradiance G_{bn} impacting on the aperture width W_a. The primary reflector, Fig. 4.2, is made of n_m mirrors with an individual lateral aperture w_m, thus the overall aperture results $W_a = n_m w_m$, Tab. 4.2.

Assuming an average circumferential distribution on the receiver perimeter P_{ex}, a concentrated solar heat flux $\dot{q}_s$, Eq. (4.1), impacts the illuminated receiver length.

$$\dot{q}_s = \eta_{op} G_{bn} \frac{W_a}{P_{ex}} \tag{4.1}$$

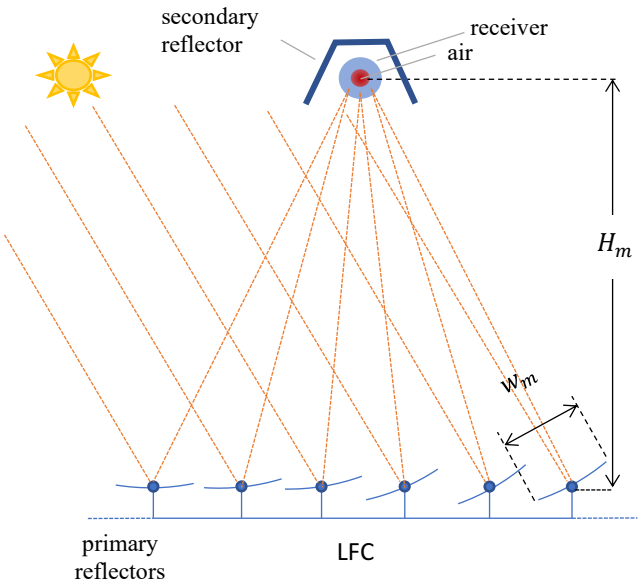

Fig. 4.2. Cross-section of the LFC primary and secondary reflectors.

The optical efficiency η_{op}, as a figure of merit by optics to capture the irradiance to the receiver, depends on the collector geometry and manufacturing accuracy, as well as on the sun position, collector orientation, and location, [24]. The sun incidence angle on the collector area can be expressed using two components, a longitudinal one θ_L and a transversal one θ_T, which are the projections of the solar ray on the vertical planes, respectively perpendicular and parallel to the receiver axis, Fig. 4.3. A longitudinal incidence angle θ_i is defined as the angle between the solar beam and its projection on the transversal plane. Several authors use θ_i instead of θ_L to characterize the longitudinal angle-dependent variables [81], Fig. 4.3. They can be obtained from

the collector azimuth angle γ_r and the sun position, i.e. sun azimuth γ_s and elevation α_s angles [82], and [23], Eqs. (4.2) to (4.4).

$$\theta_L = \tan^{-1}\left[\cos(\gamma_s - \gamma_r)\tan\left(\frac{\pi}{2} - \alpha_s\right)\right] \tag{4.2}$$

$$\theta_T = \tan^{-1}\left[|\sin(\gamma_s - \gamma_r)|\tan\left(\frac{\pi}{2} - \alpha_s\right)\right] \tag{4.3}$$

$$\theta_i = \sin^{-1}\left[\cos(\gamma_s - \gamma_r)\sin\left(\frac{\pi}{2} - \alpha_s\right)\right] \tag{4.4}$$

To use conventional nomenclature, in the following paragraph, it is assumed $\theta_L = \theta_i$, thus computed through Eq. (4.4).

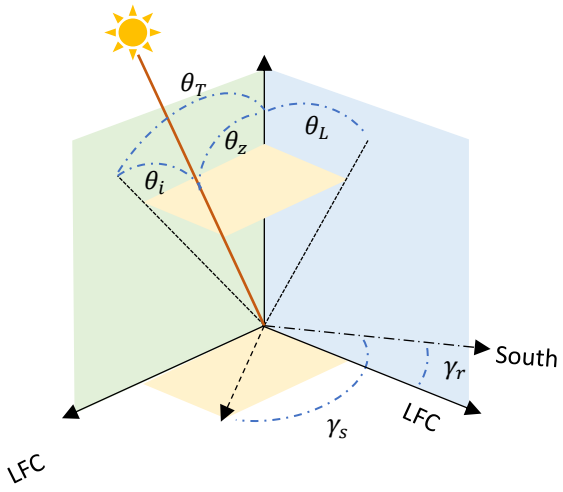

Fig. 4.3. LFC and sun mutual angles.

A common approach used to determine the effect of the incidence on the optical efficiency η_{op} involves the definition of a peak optical efficiency η_{op0} and an Incident Angle Modifier $IAM\langle\theta_L, \theta_T\rangle$, where $\langle\ \ \rangle$ herewith indicates functional dependence. η_{op0} is the optical efficiency at normal incidence, thus corresponding $\theta_L = \theta_T = 0$ deg. The IAM accounts for the reduction of η_{op} due to incidence angle: cosine effect, produced by a non-null incident angle of sun rays with respect to the reflecting surface normal direction, mutual shadowing, blocking, anisotropic mirrors properties variation, secondary optics optical efficiency variation, and its shadowing effect on the reflectors. Factorization is commonly accepted to express IAM as the product of the transversal and the longitudinal components $IAM\langle\theta_L, \theta_T\rangle = IAM_L\langle\theta_L\rangle IAM_T\langle\theta_T\rangle$. Thus, the optical efficiency η_{op} can be expressed as in Eq. (4.5).

$$\eta_{op} = \eta_{op0}\, IAM \cong \eta_{op0} IAM_T\langle\theta_T\rangle IAM_L\langle\theta_L\rangle \tag{4.5}$$

The manufacturer provided for our device the normal optical efficiency η_{op0}, Tab 4.2, as well as incidence angle modifier $IAM_T\langle\theta_T\rangle$ and $IAM_L\langle\theta_L\rangle$ obtained by the raytracing technique, Fig. 4.4. Since manufacturer's IAM_L included the length-dependent optical end losses effect, it has been replaced with $IAM_L\langle\theta_L\rangle = \cos\langle\theta_L\rangle$ to consider cosine effect only, Fig. 4.4.

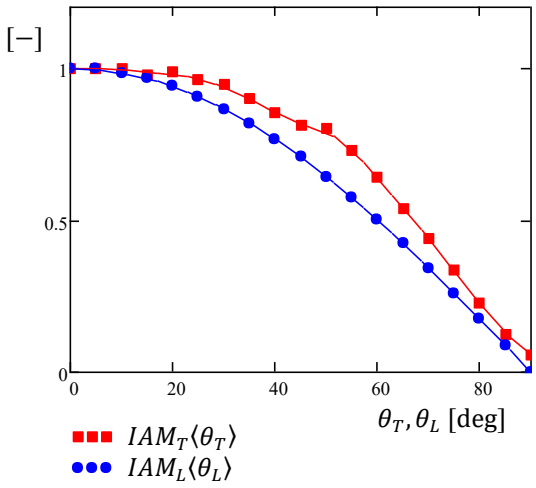

Fig. 4.4. IAM_T and IAM_L for the LFC under study.

In our case, the module mirror fields are not continuous due to a maintenance spacing between consecutive collectors L_{ex2} and L_{ex3} so that the irradiation of the receiver is broken by non-illuminated intervals of the same length, Fig. 4.5. In addition, the non-illuminated length can appear at one receiver extremity, while the opposite end can be fully or partially illuminated, according to longitudinal angle θ_L. Part of concentrated irradiance impacts out of the receiver for large θ_L, when $z_3 + L_t > L_r$, which is referred to as optical end loss. The distribution of $\dot{q}_s$ along the receiver length depends on the longitudinal incidence angle θ_L, the geometry of the collector row and receiver height, according to Fig. 4.5 and Eqs. (4.6) and (4.7).

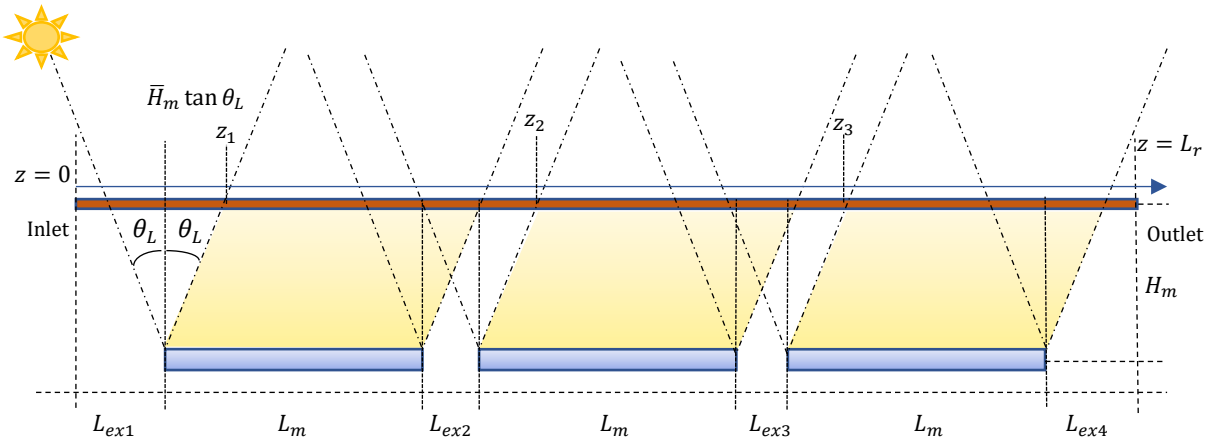

Fig. 4.5. Longitudinal view collector row of three modules.

$$\dot{q}_s\langle z\rangle = \begin{cases} \dot{q}_s \text{ for } z_k < z < z_k + L_m;\ k = 1,2,3 \\ 0 \text{ otherwise} \end{cases} \tag{4.6}$$

$$\begin{aligned} z_1 &= L_{ex1} + \bar{H}_m \tan\theta_L \\ z_2 &= z_1 + L_m + L_{ex2} \end{aligned} \tag{4.7}$$

$$z_3 = z_2 + L_m + L_{ex3}$$

An average distance from the tube to the reflector can be defined as $\bar{H}_m$ [81]:

$$\bar{H}_m = \sqrt{(W_a/4)^2 + H_m^2} \tag{4.8}$$

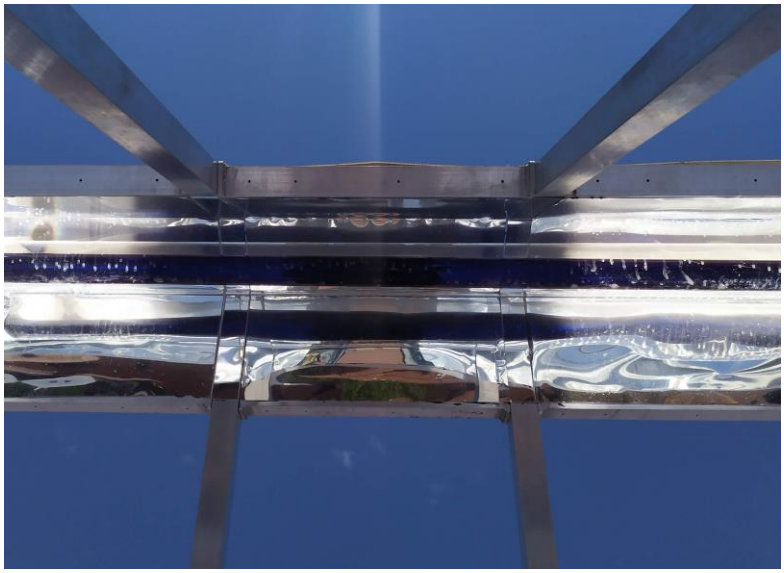

Fig. 4.6. Effect of collectors spacing L_{ex} on the receiver irradiation.

4.2 Sun position

Sun position in the sky for a given location and time of the year is required for computing the $IAMs$ and determining the axial heat flux on the receiver $\dot{q}_s\langle z\rangle$. Well-known equations from [66] are used for determining sun azimuth γ_s and elevation α_s angles. True Solar Time TST is obtained from Local standard time LST, Local time zone standard meridian longitude west $\lambda_{st} = -UTC \cdot \frac{2\pi}{24}$ and collector location longitude west λ_{loc}, through Eq. (4.9). The correction parameter E is estimated from the equation of time, Eq. 4.10. Solar declination δ, Eq. (4.11), and parameter B, Eq. (4.12), depends on the day of the year n_d. Solar hour angle ω_s results from Eq. (4.13). Eq. (4.14) gives the incident solar angle θ_z according to latitude north of the location Φ_{loc}, solar declination δ and solar hour angle ω_s. Elevation and azimuth results from Eqs. (4.15) and (4.16).

$$TST = 4(\lambda_{st} - \lambda_{loc}) + E + LST \tag{4.9}$$

$$E = 229.18(0.000075 + 0.001868\cos(B) - 0.032077\sin(B) - 0.014615\cos(2B) - 0.04089\sin(2B)) \tag{4.10}$$

$$\delta = 23.45\sin\left(\frac{2\pi}{365}\right)(284 + n_d) \tag{4.11}$$

$$B = \frac{(n_d - 1)2\pi}{365} \tag{4.12}$$

$$\omega_s = \frac{2\pi}{24}(\,TST - 12\text{ hr}\,) \tag{4.13}$$

$$\theta_z = \cos^{-1}[\cos(\Phi_{loc})\cos(\delta)\cos(\omega_s) + \sin(\Phi_{loc})\sin(\delta)] \tag{4.14}$$

$$\alpha_s = \frac{\pi}{2} - \theta_z \tag{4.15}$$

$$\gamma_s = \text{sign}(\omega_s)\left|\cos^{-1}\left(\frac{(\sin(\Phi_{loc})\cos(\theta_z) - \sin(\delta)}{\sin(\theta_z)\cos(\Phi_{loc})}\right)\right| \tag{4.16}$$

4.3 Receiver

Thermal modeling of an evacuated receiver tube was presented by several authors following different approaches, either for application to PTCs, [62], [83], [84] and LFCs, [85], [86], among others. Common techniques are reviewed by [87], including one-dimensional (1D) and three-dimensional (3D) approaches, either static or dynamic.

A 1D model is implemented here, since the hypothesis of average concentrated solar heat flux allows to consider a single receiver wall temperature at each cross-section, neglecting circumferential temperature gradients, either for static or dynamic formulation. While a static model is suitable for general prediction and design, a dynamic model can better fit the experimental results obtained from the prototype under the actual sun, for purposely designed transient tests, and optical efficiency experimental estimation.

4.3.1 Static model

The steady-state methodology recommended by [66] used in Chapter 2 to model the receiver is used here in a spatially discretized formulation. That approach relies on length-constant external and internal heat coefficients, U_L and h_a, constant heat flux $\dot{q}_s$, and fluid properties, along the considered discretized receiver length $L^* = \Delta L$, with $_t$ indicating stagnation properties. Useful heat power $\dot{Q}_u$ transferred to the airflow along a certain irradiated receiver length $L^* = \Delta L$, results from Eq. (4.17).

$$\dot{Q}_u = F_R L^* P_{ex}[\dot{q}_s - U_L(T_{in} - T_{amb})] = \dot{m}\left(c_{p,ou}T_{ou,t} - c_{p,in}T_{in,t}\right) \tag{4.17}$$

Eq. (4.18) gives the collector efficiency factor F', here including the extra feature of $P_{ex} > P$. The heat removal factor F_R is obtained integrating the temperature from the tube inlet $z = 0$ where $T = T_{in}$ to the outlet $z = L^*$ where $T = T_{ou}$, Eq. (4.19).

$$\begin{aligned} F' &= \frac{\dot{q}_s - U_L(T_w - T_{amb})}{\dot{q}_s - U_L(T - T_{amb})} = \frac{\dot{q}_s - U_L(T_w - T_{amb})}{\dot{q}_s - U_L(T_w - T_{amb}) + U_L\Delta T_w} \\ &= \frac{1}{1 + \dfrac{U_L\Delta T_w}{\dot{q}_s - U_L(T_w - T_{amb})}} = \frac{1}{1 + \dfrac{U_L P_{ex}}{h_a P}} \end{aligned} \tag{4.18}$$

$$F' P_{ex} \mathrm{d}z = \frac{\dot{m} c_p \mathrm{d}T_t}{\dot{q}_s - U_L (T - T_{amb})} \Longrightarrow F_R = \frac{\dot{m} c_p}{L^* P_{ex} U_L} \left[1 - \exp\left(- \frac{L^* F' P_{ex} U_L}{\dot{m} c_p} \right) \right] \qquad (4.19)$$

Values of U_L, h_a and fluid properties are temperature-dependent variables and can be estimated at the inlet, knowing T_{in}. $T_{w,in}$ is estimated iteratively through Eq. (4.20). The Gnielinski correlation [88] allows estimating the internal heat transfer coefficient, Eq. (4.21).

$$\dot{q}_s \ - U_L (T_w - T_{amb}) = \dot{q}_u = \frac{h_a P (T_w - T)}{P_{ex}} \qquad (4.20)$$

$$h_a = \frac{\frac{f}{8} (Re_D - 1000) Pr}{1 + 12.7 \left(\frac{f}{8} \right)^{0.5} \left(Pr^{\frac{2}{3}} - 1 \right)} \frac{k_a}{D} \ ; \quad f = (1.82 \log Re_D - 1.64)^{-2} \ ; \ Re_D = \frac{4\dot{m}}{\mu \pi D} \qquad (4.21)$$

The discretization of the tube length L_t into n_e elements allows an increased accuracy since the variable U_L, h_a, as well as the fluid properties, can be evaluated at the inlet of each element $\Delta L = \frac{L_t}{n_e}$. This is especially relevant for U_L which shows a noticeable dependency on wall temperature. On the other hand, the use of F' and F_R allows high accuracy using a small n_e, reducing the computational effort. It is worth mentioning that due to discontinuous distribution of heat flux along the receiver length, as from Eq. (4.6), $\dot{q}_s \langle z \rangle$ could results in being not constant in a given element length ΔL. For each element i the mean value of $\dot{q}_s$ along ΔL can be used in Eq. (4.17), being $\bar{\dot{q}}_{s,i} = \Delta L^{-1} \int_{z_{e,i}}^{z_{e,i} + \Delta L} \dot{q}_s \langle z \rangle$ and $z_{e,i}$ the coordinate of the starting edge of element i.

Combined heat transfer from the external tube surface to ambient through the coaxial glass tube of the evacuated receiver is considered through a global heat transfer coefficient U_L.

Previous analysis carried out in Chapter 2 was based on a constant value $U_L = 5 \ \mathrm{W\ m^{-2}\ K^{-1}}$, which allowed a simplified receiver modeling, suitable for a first screening of the direct air heating feasibility. A more accurate prediction of U_L is provided as follows. [62], among others, offers a physical model to predict U_L considering the numerous basic heat transfer mechanisms involved. Alternative and more convenient empirical expressions can be used. Here a polynomial expression for $U_L \langle T_w, T_{amb} \rangle$ is obtained from experimental thermal losses reported by [64] for a very similar evacuated tube receiver also having $D_{ex} = 0.070$ m, surrounded by an ambient temperature $T_{amb} = 23$ °C, Eq. (4.22). Coefficients are reported in Tab. 4.1. Fig. 4.7. depicts the resulting curve.

$$U_L \langle T_w, T_{amb} \rangle = c_{U3} (T_w - T_{amb})^3 + c_{U2} (T_w - T_{amb})^2 + c_{U1} (T_w - T_{amb}) + c_{U0} \qquad (4.22)$$

Table 4.1. Coefficients of the U_L correlation in Eq. (4.22).

U_L coefficients		
c_{U0}	$-5.075 \cdot 10^{-3}$	W m^{-2} K^{-1}
c_{U1}	0.011	W m^{-2} K^{-2}
c_{U2}	$-3.076 \cdot 10^{-5}$	W m^{-2} K^{-3}
c_{U3}	$7.645 \cdot 10^{-8}$	W m^{-2} K^{-4}

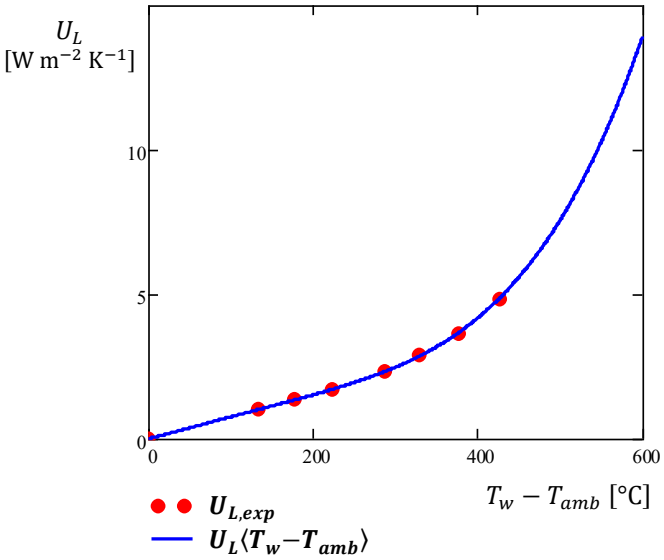

Fig. 4.7. Correlation for $U_L\langle T_w, T_{amb}\rangle$ fitting experimental data $U_{L,exp}$ by [64], according to Eq. (4.22).

Thermal losses for the junction length $_j$, Fig. 4.8, were estimated through a coefficient $U_{L,j}$, Eq. (4.23). The irradiation losses coefficient are indicated as h_{ir} , Eq. (4.24). The convection losses coefficient h_{co} is estimated from an expression developed by Churchill and Chu [67] for no wind case, Eq. (4.25) involving the Rayleigh number Ra. The supporting bracket thermal losses coefficient h_{bra} is estimated following [62], Eq. (4.26), where A_{bra} is the minimum cross-section of the bracket, and P_{bra} is the bracket perimeter.

$$U_{L,j} = h_{ir} + h_{co} + h_{bra} \tag{4.23}$$

$$h_{ir} = \frac{\sigma \varepsilon_j \left(T_{w,j}^4 - T_{amb}^4\right)}{T_{w,j} - T_{amb}} \tag{4.24}$$

$$h_{co} = \left(0.60 + \frac{0.387 Ra^{\frac{1}{6}}}{\left[1 + \left(\frac{0.559}{Pr} \right)^{\frac{9}{16}} \right]^{\frac{8}{27}}} \right)^2 \frac{k_a}{D_{ex}} \tag{4.25}$$

$$Ra = \frac{g \left(\frac{T_w + T_{amb}}{2} \right)^{-1} (T_w - T_{amb}) {D_{ex}}^3}{\nu \alpha}$$

$$h_{bra} = \frac{\sqrt{h_{co} P_{bra} k_w A_{bra}}}{P_{ex} L_j} \tag{4.26}$$

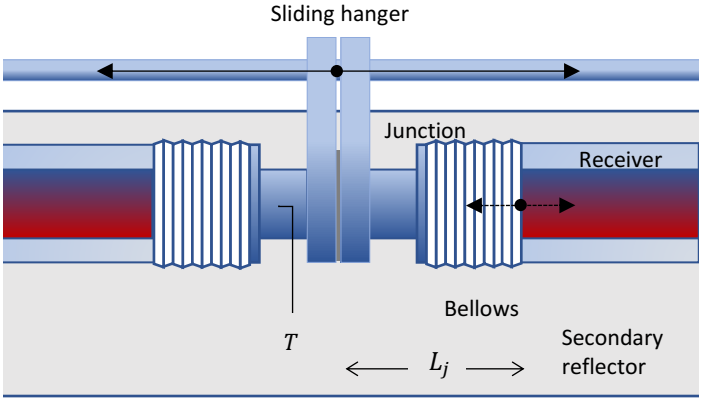

Fig. 4.8. Receiver tubes junction scheme, allowing thermal dilatation axial displacements.

4.3.2 Dynamic model

A dynamic model of the receiver tube is useful for estimating the system performance through a time marching scheme for achieving higher accuracy. While the static model is suitable for general prediction and prototype design, a dynamic one can provide a better fit with experimental results. This is of higher importance for receiver tube and collector characterization. The low heat capacity of air makes it sensitive to the thermal inertia effect of the receiver tube and piping.

An original receiver tube dynamic model has been developed, aiming at low computation cost and time, by modifying F', from Eq. (4.18) and F_R from Eq. (4.19) to include the thermal inertia effect.

The energy balance within an infinitesimal time interval $\mathrm{d}\tau$ on a receiver tube length $\mathrm{d}z$ can be formulated as in Eq. (4.27), being respectively C_w, A_w, ρ_w the thermal capacity, cross-section area, and density of the receiver tube. Assuming a finite-difference on the time variable τ, with $\mathrm{d}\tau \approx \Delta\tau$, it turns into Eq. (4.28).

$$\mathrm{d}T\dot{m}c_p = P_{ex}\dot{q}_s\mathrm{d}z - P_{ex}U_L(T_w - T_{amb})\mathrm{d}z - C_wA_w\rho_w dz\frac{\mathrm{d}T_w}{\mathrm{d}\tau} \tag{4.27}$$

$$\frac{\mathrm{d}T}{\mathrm{d}z}\dot{m}c_p = P_{ex}\left(\dot{q}_s - U_L(T_w - T_{amb}) - \frac{C_wA_w\rho_w}{P_{ex}}\frac{\left(T_w - T_w^{\tau-\Delta\tau}\right)}{\Delta\tau}\right) \tag{4.28}$$

Defining an equivalent "capacitive" heat transfer coefficient $U_C = \frac{C_wA_w\rho_w}{P_{ex}\Delta\tau}$, F' can be reformulated as follows, Eq. (4.29).

$$F' = \frac{\dot{q}_s - U_L(T_w - T_{amb}) - U_C\left(T_w - T_w^{\tau-\Delta\tau}\right)}{\dot{q}_s - U_L(T - T_{amb}) - U_C\left(T - T_w^{\tau-\Delta\tau}\right)} = \frac{1}{1 + (U_L + U_C)\frac{P_{ex}}{h_aP}} \tag{4.29}$$

F' allows substituting T_w with air temperature T in Eq. (4.28), obtaining Eq. (4.30). Integrating over z, Eq. (4.31) and solving for $T = T_{ou}$ and $z = L^*$ results in Eq. (4.32).

$$\frac{\mathrm{d}T}{\mathrm{d}z}\dot{m}c_p = PF'_s\left[\dot{q}_s - U_L(T - T_{amb}) - U_C\left(T - T_w^{\tau-\Delta\tau}\right)\right] \tag{4.30}$$

$$\frac{\dot{q}_s - U_L(T - T_{amb}) - U_C\left(T - T_w^{\tau-\Delta\tau}\right)}{\dot{q}_s - U_L(T_{in} - T_{amb}) - U_C\left(T_{in} - T_w^{\tau-\Delta\tau}\right)} = \exp\left(-\frac{zP_{ex}(U_L + U_C)}{\dot{m}c_p}\right) \tag{4.31}$$

$$\frac{\dot{q}_s - U_L(T_{ou} - T_{amb}) - U_C\left(T_{ou} - T_w^{\tau-\Delta\tau}\right)}{\dot{q}_s - U_L(T_{in} - T_{amb}) - U_C\left(T_{in} - T_w^{\tau-\Delta\tau}\right)} = \exp\left(-\frac{L^*P_{ex}(U_L + U_C)}{\dot{m}c_p}\right) \tag{4.32}$$

Introducing F_R, Eq. (4.33) gives the power gain by the airflow over a generic length L^* explicitly, Eq. (4.34).

$$\begin{aligned} F_R &= \frac{\dot{m}c_p(T_{ou} - T_{in})}{L^*P_{ex}\left[\dot{q}_s - U_L(T_{in} - T_{amb}) - U_C\left(T_{in} - T_w^{\tau-\Delta\tau}\right)\right]} \\ &= \frac{\dot{m}c_{p,m}}{P_{ex}L^*(U_L + U_C)}\left[1 - \exp\left(-\frac{F'P_{ex}(U_L + U_C)L^*}{\dot{m}c_{p,m}}\right)\right] \end{aligned} \tag{4.33}$$

$$\dot{Q}_u = F_RL^*P_{ex}[\dot{q}_s - U_L(T_{in} - T_{amb}) - U_C(T_{in} - T_w^{\tau-\Delta\tau})] = \dot{m}\left(c_{p,ou}T_{ou} - c_{p,in}T_{in}\right) \tag{4.34}$$

Eq. (4.34) allows calculating $\dot{Q}_u$ over a generic length L^*; actually, a discretized element length $\Delta L = \frac{L_t}{n_e}$ to increase the accuracy, as explained for the steady-state case. It is worth mentioning that here it is assumed $U_L\langle T_w, T_{amb}\rangle$ according to Eq. (4.22), neglecting the thermal inertia of the cover glass tube. The time-finite difference is assumed to equal the SCADA acquisition time interval $\Delta\tau = 30$ s. For this time interval a value of $U_C \cong 260\ \mathrm{W\,°C^{-1}\,m^{-2}}$ is found for the receiver tube.

The presented approach is extended to the junction length between the receiver tubes L_j using the corresponding $U_{C,j}$.

4.4 Piping

Thermally insulated connection pipes n_1 and n_2 in Fig. 4.1, needed for completing the air circuit, are modeled following the same equation of the receiver over the length L_n , Eqs. (4.17) to (4.19), using $\dot{q}_s = 0$ and a proper thermal losses coefficient U_{Ln}, as in Eq. (4.35) and (4.36).

$$\dot{Q}_u = -F_R L_n P_{ex} U_{Ln}(T_{in} - T_{amb}) = \dot{m}(h_{out} - h_{int}) \cong \dot{m}\left(c_{p,ou} T_{ou,t} - c_{p,in} T_{in,t}\right) \quad (4.35)$$

$$U_{Ln}^{-1} = \frac{\ln\left(\frac{D_{ins}}{D_{n,ex}}\right) D_{n,ex}}{2k_{ins}} + \frac{D_{n,ex}}{D_{ins}(h_{co} + h_{ir})} \quad (4.36)$$

h_{co} is estimated using Eq. (4.25) on the external insulation diameter D_{ins} and h_{ir} through Eq. (4.24) using insulation external layer emissivity of $\varepsilon_{ins} = 0.04$. Insulation thermal conductivity $k_{ins}\langle\bar{T}_{ins}\rangle$ comes from manufacturers data, expressed as a function of an average insulation temperature $\bar{T}_{ins}$ in Eq. (4.37).

$$k_{ins}\langle\bar{T}_{ins}\rangle = \left(0.031 - 6.285 \cdot 10^{-5} \frac{\bar{T}_{ins}}{\mathrm{K}} + 2.958 \cdot 10^{-7} \frac{\bar{T}_{ins}}{\mathrm{K}}^2\right) \frac{\mathrm{W}}{\mathrm{mK}} \quad (4.37)$$

Due to the modest spatial temperature variation expected, the length L_{n1} and L_{n2} are not spatially discretized. Where required, the dynamic formulation of Eqs. (4.27) to (4.34) can be applied for better accuracy on transient simulations, using a proper capacitive heat transfer coefficient $U_{C,ins}$.

Table 4.2. LFC solar field, receiver, and air piping parameters

LFC module active length $\boldsymbol{L_m}$	5.28 m
Mirrors per module $\boldsymbol{n_m}$	10
Mirror aperture width $\boldsymbol{w_m}$	0.50 m
LFC aperture width $\boldsymbol{W_a = w_m n_m}$	5.00 m
Height receiver $\boldsymbol{H_m}$	2.72 m
LFC active area $\boldsymbol{A_m = L_m W_a}$	26.40 m^2
Normal optical efficiency $\boldsymbol{\eta_{op0}}$	0.632
LFC in series $\boldsymbol{n_s}$	3
Overall active area $\boldsymbol{A_{tot} = n_s A_m}$	79.2 m^2
Overall receiver length $\boldsymbol{L_r}$	20.65 m
Receiver active length $\boldsymbol{L_t}$	3.902 m
Receiver internal diameter $\boldsymbol{D}$	0.066 m
Receiver external diameter $\boldsymbol{D_{ex}}$	0.070 m
Number of tubes $\boldsymbol{n_t}$	5
Selective coating maximum allowable temperature $\boldsymbol{T_{w,max}}$	600 °C
Junction length $\boldsymbol{L_j}$	0.115 m
Junction emissivity $\boldsymbol{\varepsilon_j}$	0.38
Extra length $\boldsymbol{L_{ex1}}$	1.05 m
Extra length $\boldsymbol{L_{ex2}}$	1.02 m
Extra length $\boldsymbol{L_{ex3}}$	1.02 m
Extra length $\boldsymbol{L_{ex4}}$	1.52 m
Concentration ratio $\boldsymbol{C = \frac{W_a}{D_{ex}\pi}}$	22.74
Connection pipe external diameter $\boldsymbol{D_{n,ex}}$	0.084m
Connection pipe internal diameter $\boldsymbol{D_n}$	0.08 m
Connection pipe n1 length $\boldsymbol{L_{n1}}$	26 m
Insulation diameter pipe $\boldsymbol{n_1}$ $\boldsymbol{D_{ins1}}$	0.280m
Connection pipe n2 length $\boldsymbol{L_{n2}}$	3 m
Insulation diameter pipe n2 $\boldsymbol{D_{ins1}}$	0.480 m
Solar field Orientation (0 = South) $\boldsymbol{\gamma_r}$	54.3 deg W
Solar field Latitude $\boldsymbol{\Phi_{loc}}$	40.165 deg N
Solar field Longitude $\boldsymbol{\lambda_{loc}}$	3.704 deg W

4.5 Turbocharger

In Chapter 2 a basic formulation for the turbocharger modeling was obtained, here reported for clarity, Eqs. (4.38) to (4.43). That model was based on constant values of η_c and η_e, assigned according to the recommendations in the open technical literature, thus not considering operation point excursions. Besides this, the pressure ratio π_c was an independent variable. That model is improved here to incorporate the relations between π_c, $\dot{m}_a$, T_{1t} and η_c for the compressor and π_e, $\dot{m}_a$, T_{3t} and η_e for the turbine, according to the characteristic performance

of the given turbocharger. This way, the functioning along a day or any other time period can be described.

Newton's second law of rotating systems, Eq. (4.38), turns into Eq. (4.39) under steady-state operation when the mechanical power provided by the turbine $\dot{W}_e$ drives the compressor, requiring power $\dot{W}_c$. A mechanical efficiency η_m accounts for the mechanical losses at the shaft, being J_T the turbocharger polar moment of inertia and n_T the rotational speed.

$$\left(\frac{\dot{W}_e\eta_m}{n_T}-\frac{\dot{W}_c}{n_T}\right)\frac{1}{J_T} = 2\pi\frac{\mathrm{d}n_T}{\mathrm{d}\tau} \tag{4.38}$$

$$\text{Freewheeling} \rightarrow \dot{W}_e\eta_m - \dot{W}_c = \dot{W}_{net} = 0 \tag{4.39}$$

The compressor and turbine power can be calculated using Eqs. (4.40) and (4.41), from empirical values of the isentropic total to total efficiencies η_c and η_e, pressure ratios $\pi_c = p_{2t}/p_{1t}$ and $\pi_e = p_{3t}/p_{4t}$, according to inlet stagnation temperatures T_{1t} and T_{3t} , being $\gamma = \frac{c_p}{c_v}$. The outlet temperature T_{2t} and T_{4t} results from Eqs. (4.42) and (4.43).

$$\dot{W}_c = \dot{m}_a c_{p,c} T_{1t}\left({\pi_c}^{(\gamma_c-1)/\gamma_c}-1\right)\eta_c^{-1} \tag{4.40}$$

$$\dot{W}_e = \dot{m}_a c_{p,e} T_{3t}\left[1-{\pi_e}^{-(\gamma_e-1)/\gamma_e}\right]\eta_e \tag{4.41}$$

$$T_{2t} = T_{1t}\left[1+\left(\pi_c^{(\gamma_c-1)/\gamma_c}-1\right)\eta_c^{-1}\right] \tag{4.42}$$

$$T_{4t} = T_{3t}\left[1-\eta_e\left(1-{\pi_e}^{-(\gamma_e-1)/\gamma_e}\right)\right] \tag{4.43}$$

In the layout of Fig. 4.1, the temperature T_{3t} results from air heating inside the receiver tube as well as across the experimental post-heating unit. The total pressure at the turbine inlet $p_{3t} = p_{2t} - \Delta p_t$ is affected by the stagnation pressure drop across the pressurized circuit, Δp_t. $\Delta p_t = \sum_i \Delta p_{t,i}$ can be estimated using Eq. (4.44), considering kinetic and frictional components $\Delta p_{k,t}, \Delta p_{f,t}$, for any portion i of the circuit across the length L_{n1}, L_r, L_{n2}. The localized pressure drops introduced by localized connections, elbows, and cross-section variation, are accounted for by K_i. $f_i = 0.316 {Re_D}^{-\frac{1}{4}}$ is the Darcy friction factor for element i.

$$\begin{aligned}\Delta p_{t,i} &= \overbrace{\frac{1}{2}\left(\rho_{ou,i}v_{ou,i}^2-\rho_{in,i}v_{in,i}^2\right)}^{\Delta p_{k,t}} + \overbrace{\frac{1}{2}\rho_{m,i}v^2\left(f_i\frac{L_i}{D_i}+\frac{K_i}{\rho_{m,i}}\right)}^{\Delta p_{f,t}} \\ &= \frac{1}{2}\left(\frac{4\dot{m}_a}{\pi D_i^2}\right)^2\left(\frac{1}{\rho_{ou,i}}-\frac{1}{\rho_{in,i}}+f_i\frac{L_i}{\rho_{m,i}D_i}+\frac{K_i}{\rho_{m,i}}\right)\end{aligned} \tag{4.44}$$

The absence of auxiliary compressors results in $T_{1t} = T_{0t}$ and $p_{1t} = p_{0t}$, with $T_0 = T_{amb}$ and $p_0 = p_{amb}$ neglecting the inlet nozzle head loss. Otherwise, the auxiliary compressor ratio $\pi_{ac} > 1$ leads to $p_{1t} = \pi_{ac}p_{0t}$, whereas T_{1t} results from Eq. (4.45).

$$T_{1t} = T_{0t}\left[1+\left(\pi_{ac}^{(\gamma_{ac}-1)/\gamma_{ac}}-1\right)\eta_{ac}^{-1}\right] \tag{4.45}$$

4.5.1 Compressor

According to [56] among others, the compressor performances are inter and extrapolated from the maps provided by the manufacturer. There are functional dependencies, $\pi_c = \pi_c\langle \dot{m}_c, T_{in}, n_T \rangle$ and $\eta_c = \eta_c\langle \dot{m}_c, T_{in}, n_T \rangle$, which are reported in terms of corrected mass flow rate $\dot{m}_{c,cor}$ and speed $n_{c,cor}$, according to reference values $T_{c,ref}$, $p_{c,ref}$ for the inlet variables $_{in}$, Eqs. (4.46) and (4.47), as in Fig. 4.9(a) for the turbocompressor.

$$\dot{m}_{c,cor} = \dot{m}_a \sqrt{\frac{T_{c,in} + \kappa}{T_{cref} + \kappa}} \frac{p_{c,ref}}{p_{c,in}} \tag{4.46}$$

$$n_{c,cor} = n_T \sqrt{\frac{T_{c,ref} + \kappa}{T_{c,in} + \kappa}} \tag{4.47}$$

4.5.1.1 Pressure ratio fitting function

Extrapolation of $\pi_c\langle \dot{m}_{c,cor}, n_{c,cor} \rangle$ is prepared using the methodology proposed in [89]. The non-dimensional flow rate parameter ϕ_c and the head parameter ψ_c are defined through the tip blade speed U_c and the compressor rotor diameter D_c. $c_p, T_a, \rho_a, \gamma_c$ are evaluated at the reference temperature $T_{c,ref}$, Eqs. (4.48), (4.49) and (4.50).

$$\phi_c = \frac{\dot{m}_{c,cor}}{\rho_a \frac{\pi}{4} D_c^2 U_c} \tag{4.48}$$

$$\psi_c = \frac{c_p T_a \left(\pi_c^{(\gamma_c - 1)/\gamma_c} - 1 \right)}{U_c^2/2} \tag{4.49}$$

$$U_c = n_{c,cor} \pi D_c \tag{4.50}$$

The fitting function $\psi_c\langle \phi_c\, , n_{c,cor} \rangle$, proposed by those authors, counts on six parameters k_{ij} and the inlet Mach number Ma. Here, it has been replaced with a third-order polynomial form for $k_i\langle Ma \rangle$, as proposed by [90], using nine parameters k_{ij}, Eq. (4.52). The function $\pi_c = \pi_c\langle \dot{m}_c, n_{c,cor} \rangle$ results as in Eq. (4.53). Fig. 4.9(a) reports $\pi_c\langle \dot{m}_{c,cor}, n_{c,cor} \rangle$ on the original compressor map, showing high accuracy.

$$Ma = U_c / \sqrt{\gamma_c R T_a} \tag{4.51}$$

$$\psi_c = \frac{k_1 + k_2 \phi_c}{k_3 - \phi_c}; \qquad k_i = k_{i1} + k_{i2} Ma + k_{i3} Ma^2 \tag{4.52}$$

$$\pi_c = \left[\frac{\frac{1}{2} \left(n_{c,cor} \pi D_c \right)^2 \psi_c\langle \phi_c \langle \dot{m}_{c,cor}, n_{c,cor} \rangle, n_{c,cor} \rangle}{c_p T_a} + 1 \right]^{\gamma_c/(\gamma_c - 1)} \tag{4.53}$$

4.5.1.2 Efficiency fitting function

The compressor map gives two alternative types of curves: a) iso-efficiency curves $\eta_c\langle \dot{m}_{c,cor}, \pi_c \rangle = \text{const.}$ or b) iso-speed efficiency curves $\eta_c\langle \dot{m}_{c,cor}, n_{c,cor} = \text{const.} \rangle$, Fig. 4.9(a). Although the technical literature offered both approaches, the second one gives better results

for the present case. An extrapolation method was presented by [89], analogous to the mass flow fitting, as well as by [90] and [91]. Galindo et al. [92] and [93] offered more complex procedures aiming at higher accuracy. An original method based on a local interpolation is developed here, keeping a low computational load. It relies on recognizing that on each side of the dorsal line of maximum efficiency $\eta_{c,max}$, Fig. 4.9(a), the compressor behaviour is different. On the left side the surge phenomenon appears while at the right side, sonic choke appears.

The iso-speed efficiency curves $\eta_c\langle \dot{m}_{c,cor}, n_{c,cor} = \text{const.} \rangle$ are locally interpolated aiming at high accuracy, keeping simplicity, and a low computational load. Each iso-speed efficiency data set have been normalized through the maximum efficiency value at such speed $\eta_{c,max}$, Eq. (4.54), and expressed as a function of a normalized non-dimensional mass flow rate $\phi_{c,norm}$, Eq. (4.55). The non-dimensional mass flow rate ϕ_c is defined in Eq. (4.48) and it is normalized using $\phi_{c,max}$, which corresponds to $\dot{m}_{c,cor}^{max}$, the abscissa of the here-called dorsal line, depicted in the map joining the $\eta_{c,max}$ points.

$$\eta_{c,norm} = \frac{\eta_c}{\eta_{c,max}} \tag{4.54}$$

$$\phi_{c,norm} = \frac{\phi_c}{\phi_{c,max}} \tag{4.55}$$

Then, each normalized iso-speed data set $\eta_{c,norm}\langle\phi_{c,norm}\rangle$ is approximated using second-order polynomial regression, separately for the two regions at both sides of the dorsal line $\phi_{c,norm} < 1$ and $\phi_{c,norm} > 1$ for increasing the accuracy as the behavior at both sides is different, Fig. 4.9(c), obtaining the functions $\eta_{c,norm} = \mathrm{f}_{n,i}\langle\phi_{c,norm}\rangle$. An interpolation ratio IR allows determining $\eta_{c,norm}$ for a generic $\phi_{c,norm}$ and speed $n_{c,corI} < n_{c,cor} < n_{c,corII}$, Eqs. (4.56) and (4.57).

$$\eta_{c,norm} = \mathrm{f}_{n,I}\langle\phi_{c,norm}\rangle(1 - IR) + \mathrm{f}_{n,II}\langle\phi_{c,norm}\rangle IR \tag{4.56}$$

$$IR = \frac{n_{c,cor} - n_{c,corI}}{n_{c,corII} - n_{c,corI}} \tag{4.57}$$

To ensure continuity between the left and the right region of the dorsal line, $\eta_{c,norm} = 1$ is imposed around $\phi_{c,norm} = 1$. Fig. 4.9(d) depicts the results. It is worth mentioning that the minimum corrected speed is considered to be $n_{c,cor}^{min} = 110$ krpm since not enough points are available on the map for extrapolating an accurate efficiency curve at 90 krpm.

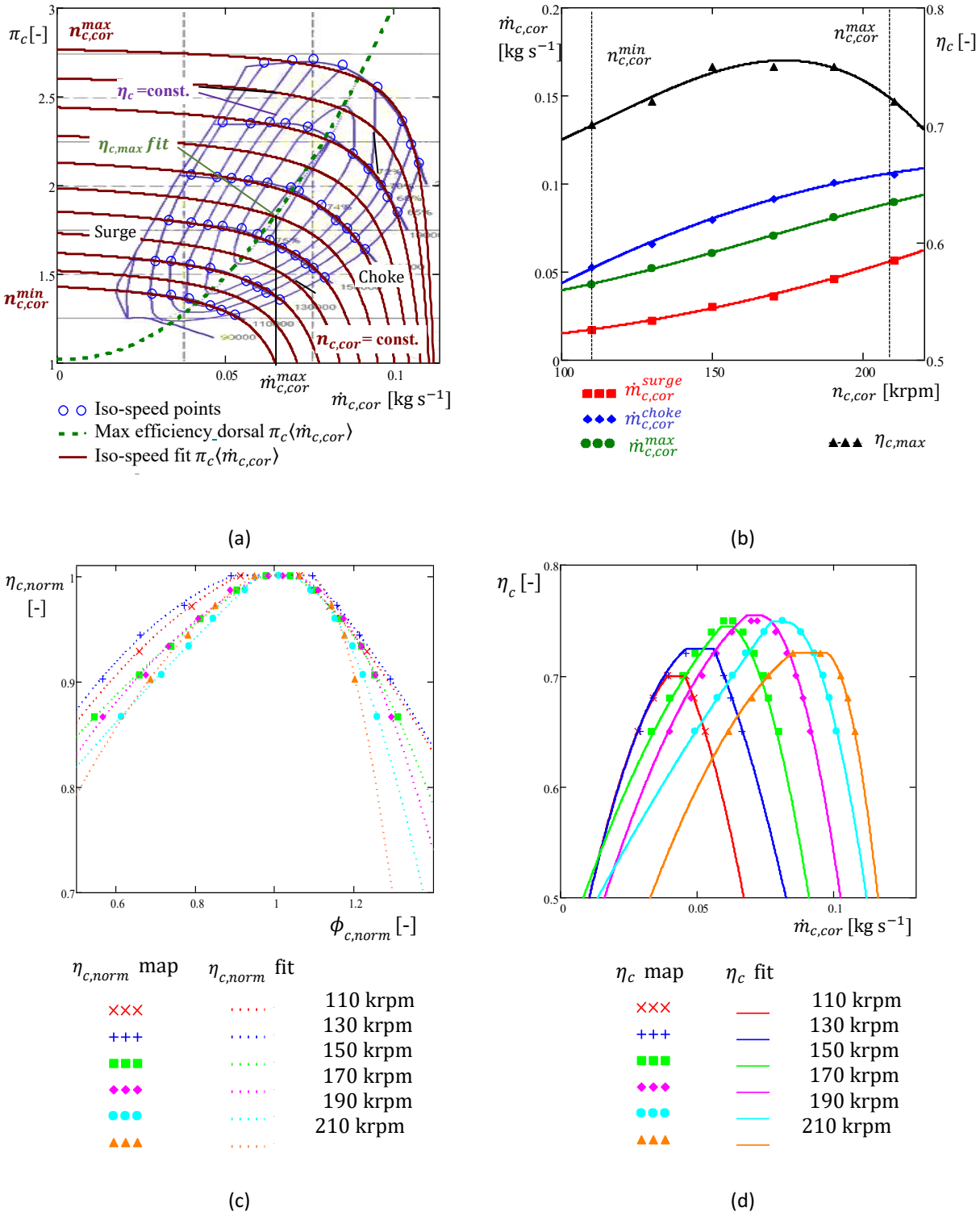

Fig. 4.9. Compressor map and derived points from the manufacturer data with the model fitted curves superimposed. (a) Compressor map $\pi_c\langle\dot{m}_{c,cor}\rangle$ for $n_{c,cor}$ = const. (dots) and dorsal line $\pi_c\langle\dot{m}_{c,cor}\rangle$ for $\eta_{c,max}$ (dash). (b) Choke and surge limits, dorsal-speed lines $\eta_{c,max}\langle n_{c,cor}\rangle$ and $\dot{m}_{c,max}\langle n_{c,cor}\rangle$. (c) Normalized iso-speed efficiency curves. (d) Iso-speed efficiency curves $\eta_c\langle\dot{m}_{c,cor}\rangle$. $T_{c,ref} = 29.45$ °C; $p_{c,ref} = 0.962$ bar.

4.5.2 Turbine

Several authors presented methodologies for turbine flow map extrapolation [94], [73], and [95], among others. They are applicable when the turbine map provided by the manufacturer

reports the function $\dot{m}_e\langle\pi_e, n_T\rangle$ at constant speed for several speed values. However, in most cases, only one curve is provided, approximating the iso-speed mass flow curves. Corrected values are customary, as for the compressor, Eqs. (4.58) and (4.59).

The relation $\dot{m}_{e,cor}\langle\pi_e\rangle$, is modeled according to [56] using Eq. (4.60), with c_e and k_e determined by curve fitting and using as reference $T_{e,ref}$ and $p_{e,ref}$, which are given by the manufacturer with $\kappa = 273.15\ °C$.

$$\dot{m}_{e,cor} = \frac{p_{e,ref}}{p_{e,in}} \sqrt{\frac{T_{e,in} + \kappa}{T_{e,ref} + \kappa}}\ \dot{m}_a \tag{4.58}$$

$$n_{e,cor} = n_T \sqrt{\frac{T_{e,ref} + \kappa}{T_{e,in} + \kappa}} \tag{4.59}$$

$$\dot{m}_{e,cor} = c_e \sqrt{1 - \pi_e^{k_e}} \tag{4.60}$$

Turbine efficiency prediction needs a model since many manufacturers only provide a value for the maximum efficiency $\eta_{e,max}$. Following [56], a blade speed ratio SR and a tip blade speed U_e are defined, using the turbine wheel diameter D_e, in order to express efficiency as in Eq. (4.63), according to an optimum $SR_{opt} = 0.7$, commonly accepted.

$$U_e = D_e \pi n_{e,cor} \tag{4.61}$$

$$SR\langle n_{e,corr}, \pi_e\rangle = U_e \Big/ \sqrt{2c_{p,3}T_3\left(1 - \pi_e^{-(\gamma_e - 1)/\gamma_e}\right)} \tag{4.62}$$

$$\eta_e\langle n_{e,cor}, \pi_e\rangle = \eta_{e,max}\left[\frac{2SR}{SR_{opt}} - \left(\frac{SR}{SR_{opt}}\right)^2\right] \tag{4.63}$$

Figure 4.10 depicts the curves of $\dot{m}_e\langle\pi_e\rangle$ and $\eta_e\langle n_{e,cor}, \pi_e\rangle$ according to this scheme. One can see in this figure that owing to an operating point mismatch the already low maximum efficiency of the very small automotive turbocharger can even be lower. As an example, $\eta_e \cong 0{,}4$ at $\pi_e = 1.4$ and $n_e = 100\ \mathrm{krpm}$, which is a common operating point with the off-the-shelf turbine chosen, obviously too large for our solar field. This negative circumstance can be improved very much by going to a larger size solar field to improve matching for the same turbine. Another improvement comes from an overall size increase that, as a generic tendency, improves the maximum turbomachine efficiency because of the larger Reynolds number benefit, larger machining accuracy, and smaller relative roughness. These larger sizes are reasonable for real-life applications. The operating point excursions away from the maximum efficiency region of the turbine can be alleviated by variable geometry nozzles, now a proven technology in turbocharging. Finally, the automotive turbochargers turbines are subject to intensive abuse in their original applications, because of engine exhaust pulses and frequent acceleration and deceleration, not forgetting the corrosive nature of exhaust gases. This implies a far tan optimal design that somewhat reduces maximum efficiency. A better design will be welcome. This happens in larger turbochargers, e. g. for Diesel industrial engines, or marine propulsion. They operate much more steadily, allowing higher turbocharger efficiencies concomitantly with the larger size.

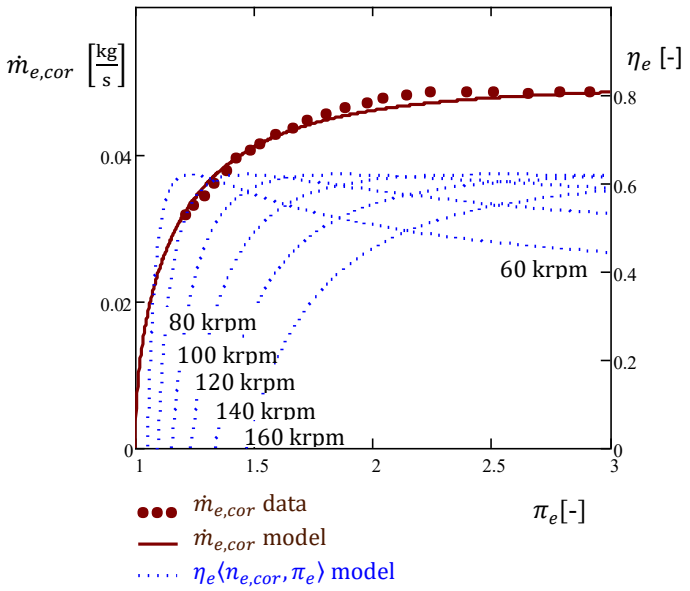

Fig. 4.10. Turbine manufacturer's data and model results for the turbine. $T_{e,ref} = 15.7$ °C; $p_{e,ref} = 1.013$ bar; $\eta_{e,max} = 0.62$.

4.6 Diabatic turbocharger

Heat transfer phenomena occurring between compressor, turbine, and the ambient can affect the turbocharger performances and consequently their prediction. Customarily, this is performed using an adiabatic numerical model that ignores them, like the one proposed in the previous sections. Several authors recently claimed their relevance to turbocharger performance. The standard approach uses turbine and compressor experimental maps, provided by the manufacturer through an experimental test bench, which can be "cold" or "hot" according to the temperature of gases during the test. According to [96], maps from the "hot" test include heat fluxes. Their usage leads to accurate predictions only when the operative temperature is the same as the gas reference temperatures used in the test bench. On the other hand, the use of "cold" maps leads to lower accuracy on the field use, especially for turbines. Testing of turbocompressors or turbines alone at near atmospheric conditions, thus "cold", approaches an adiabatic process very well. [96] stated that a heat fluxes model is needed in both cases if good predictions are demanded and reported several recent works on heat transfer phenomena in turbochargers. [97] recognized that in the low and medium rotating speed regimes, the specific work transfer is small, making heat transfer more relevant, being this attributed to low mass flow rates and pressure ratios.

Bohn and Heuer [98] and [99] developed a detailed 1D numerical model of heat fluxes besides evaluating them through an experimental analysis. A 1D heat transfer model was also proposed by [96] and [97]. [100] experimentally investigated the heat transfer in a turbocharger test bench. They proposed three simple methods for modifying a conventional adiabatic turbocharger model to account for heat fluxes.

Casey and Fesich [101] stated that using the isentropic process as a reference for the ideal work required by the compressor is not justified when the process is not anymore adiabatic. Instead, a polytropic efficiency accounting for the diabatic flows is more appropriate. The low compression ratio variations in the present study do not need such a paradigm, more appropriate for parametric studies.

According to [97] and [99], the isentropic efficiency can still be used combined with the heat transfer model, recognizing that an isobaric heat transfer process occurs before and after the compression/expansion as Fig. 4.11 indicates, reaching the same starting and ending points. Isobaric heat exchange by the compressor and turbine flow, respectively $\dot{Q}_c$ and $\dot{Q}_e$, can be split into two components, before and after, respectively $\dot{Q}_c = \dot{Q}_{c,be} + \dot{Q}_{c,af}$ and $\dot{Q}_e = \dot{Q}_{e,be} + \dot{Q}_{e,af}$. As a consequence, the inlet and outlet total temperatures of adiabatic processes $T_{1t}^{adi}, T_{2t}^{adi}, T_{3t}^{adi}, T_{4t}^{adi}$ do not coincide anymore with inlet and outlet diabatic total temperatures at compressor and turbine rotor inlet and outlet, respectively, $T_{1t},\ T_{2t},\ T_{3t},\ T_{4t}$.

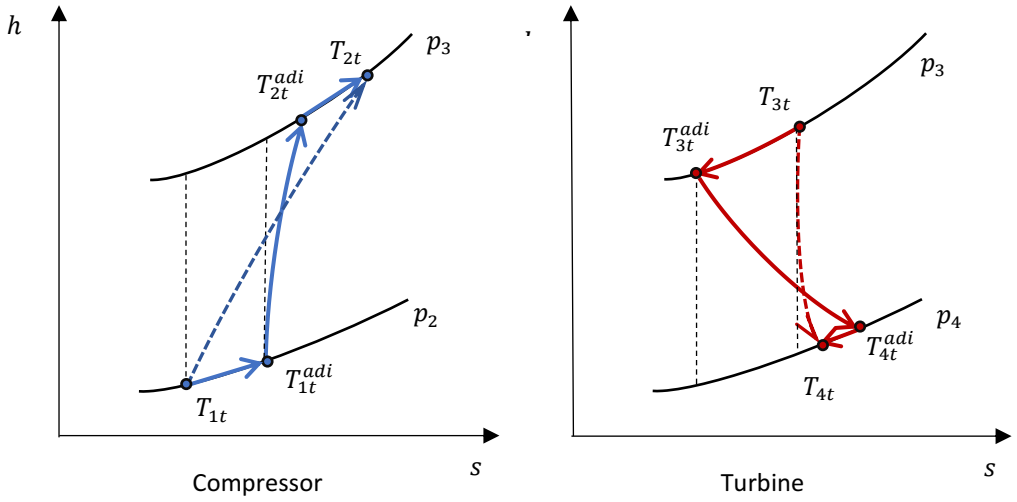

Fig. 4.11. Diabatic compression and expansion diagrams.

Several main heat fluxes can be identified considering a diabatic turbocharger. They slightly vary according to the level of accuracy of the thermal analysis. The simplified study performed in this section considers three relevant heat fluxes. Heat loss from the compressor flow to ambient $\dot{Q}_{c\to amb}$ occurs across the compressor case. According to Fig. 4.12, a heat transfer from the hot turbine flow to the attached lower temperature compressor $\dot{Q}_{e\to c}$ happens through the turbine case, the bearing housing, and the shaft, as well as through the compressor case portion consecutive to the bearing house, named the "backplate". Heat transfer to ambient from the turbine flow $\dot{Q}_{e\to amb}$ can include the thermal losses across the turbine case $\dot{Q}_{e\to amb}^{case}$, across the bearing housing $\dot{Q}_{e\to amb}^{bh}$, and heat transferred to the lubrication oil $\dot{Q}_{e\to amb}^{oil}$.

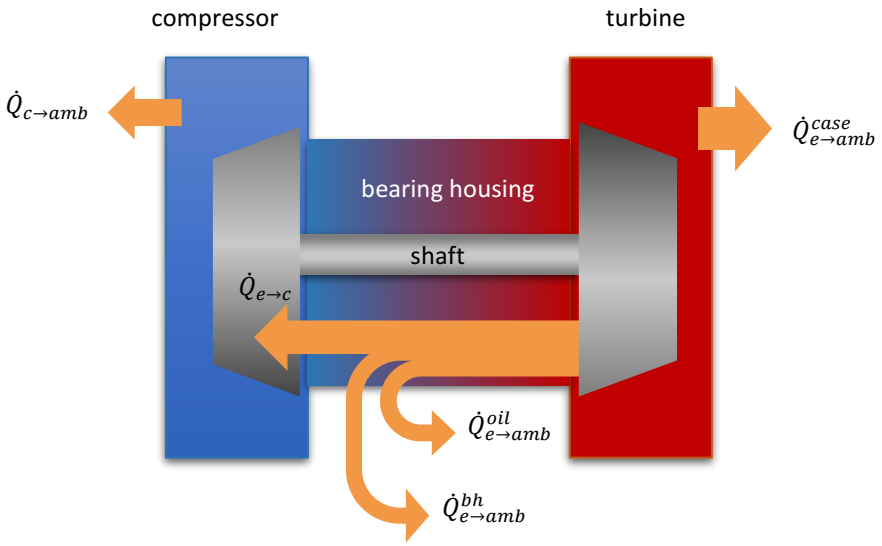

Fig. 4.12. Diabatic turbocharger heat paths.

According to [99], $\dot{Q}_{c,be}$ can be neglected in front of $\dot{Q}_{c,af}$ as a first approximation, since the inlet air flow only crosses a very short passage, the inducer inlet pipe, before compression, and its over-temperature is small. Extending this assumption to the turbine side, $\dot{Q}_{e,af}$ can be neglected in front of $\dot{Q}_{e,be}$ since the exit flow only goes through a short passage after expansion. These simplifying assumptions lead to $T_{1t}^{adi} \cong T_{1t}$ and $T_{4t}^{adi} \cong T_{4t}$.

Accordingly, compressor and turbine heat fluxes can be written as in Eq. (4.64) and Eq. (4.65).

$$\dot{Q}_c \cong \dot{Q}_{c,af} \cong \dot{Q}_{e\to c} - \dot{Q}_{c\to amb} \tag{4.64}$$

$$\dot{Q}_e \cong \dot{Q}_{e,be} \cong \dot{Q}^{case}_{e\to amb} + \dot{Q}^{bh}_{e\to amb} + \dot{Q}^{oil}_{e\to amb} + \dot{Q}_{e\to c} = \dot{Q}_{e\to amb} + \dot{Q}_{e\to c} \tag{4.65}$$

Estimation of heat fluxes is important to enhance the prediction accuracy of the adiabatic model provided in the previous section, which is based on “cold maps”. A semi-empirical quantification of heat fluxes $\dot{Q}_{e\to c}$, $\dot{Q}_{c\to amb}$ and $\dot{Q}_{e\to amb}$ is discussed in the following section.

From the previous analysis, it derives that Eqs. (4.38) to Eq. (4.40) keep their validity, whereas Eqs. (4.41) to (4.43) must be substituted by Eq. (4.66) to (4.68), respectively.

$$\dot{W}_e = \dot{m}_a c_{p,e} T_{3t}^{adi}\left[1 - \pi_e^{-(\gamma_e-1)/\gamma_e}\right]\eta_e = \dot{m}_a c_{p,e}\left(T_{3t} - \frac{\dot{Q}_e}{\dot{m}_a c_{p3}}\right)\left[1 - \pi_e^{-(\gamma_e-1)/\gamma_e}\right]\eta_e \tag{4.66}$$

$$T_{2t} = T_{2t}^{adi} + \frac{\dot{Q}_c}{\dot{m}_a c_{p2}} = T_{1t}\left[1 + \left(\pi_c^{(\gamma_c-1)/\gamma_c} - 1\right)\eta_c^{-1}\right] + \frac{\dot{Q}_c}{\dot{m}_a c_{p2}} \tag{4.67}$$

$$T_{4t} = T_{3t}^{adi}\left[1 - \eta_e\left(1 - \pi_e^{-(\gamma_e-1)/\gamma_e}\right)\right] = \left(T_{3t} - \frac{\dot{Q}_e}{\dot{m}_a c_{p3}}\right)\left[1 - \eta_e\left(1 - \pi_e^{-(\gamma_e-1)/\gamma_e}\right)\right] \tag{4.68}$$

5 EXPERIMENTAL CHARACTERIZATION OF T-SAH PROTOTYPE

This chapter carries out an experimental investigation on the installed T-SAH prototype, described in Chapter 3, Fig. 5.1. Purposely designed experiments are devised for the full characterization of the innovative T-SAH concept. The first section reports and analyzes several representative tests. The first one is conducted by running the prototype across a summer day with a clear sky. Solar air heating is performed in the best conditions to reach maximum solar power and air temperature at the receiver outlet, without the post-heating power aid. This allows studying the global behavior of the system, including the solar field, the turbocharger, and the auxiliary compressor. A second representative test, also performed during summer and clear sky conditions, is devised for the turbocharger characterization. The additional thermal power by electrical delivered by post-heating allows increasing the turbocharger testing range, due to higher inlet turbine temperature. A thermal losses test allows validating the thermal model of the receiver implemented in Chapter 4, both static and dynamic. A detailed characterization of the solar field is carried out by contrasting the experimental data of the first representative test with the opto - thermal model. Once validated, a dynamic receiver model has been used to obtain the experimental optical efficiency on transient operational data. The comparison of the experimental efficiency with the optical model allows defining an optical correction factor, accounting for optical errors and manufacturing imperfections, besides the sun tracking procedure accuracy.

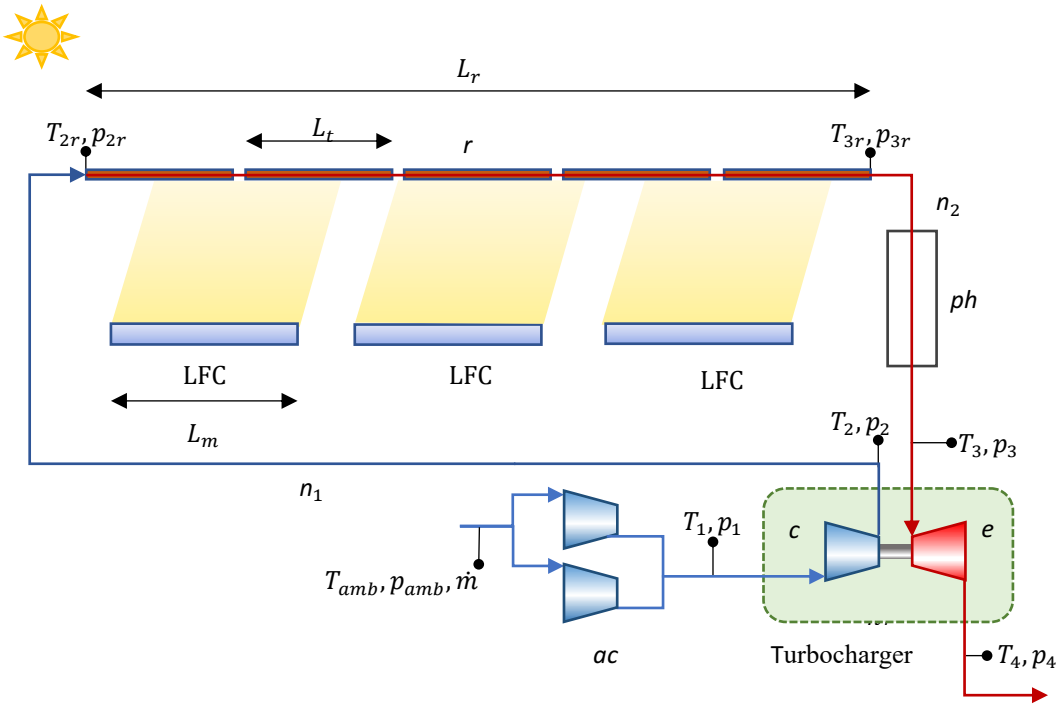

Fig. 5.1. Experimental setup scheme, Linear Fresnel *LFC* mirror field, receiver *r*, auxiliary compressor *ac*, experimental post-heating unit *ph*, turbocompressor *c*, turbine *e*. Sensors: temperature *T* and pressure *p*

The experimental campaign performed under different operating conditions of the representative tests allows accurately characterizing the turbocharger performances. Experimental data obtained allowed extending, verifying, and tunning the numerical model as well as quantifying the heat transfer phenomena affecting the diabatic turbocharger. A detailed discussion of the results highlights the improvements possible in scaling up the technology and streamlining the design for industrial applications. An experimental investigation of the Thermal Energy Storage (TES) unit is carried out and discussed.

5.1 Experiments overview

This section gives an overview of two representative experiments, both carried out during the summer season under an optimal local clear sky. The T-SAH operation without the experimental post-heating unit is presented first. Then, the T-SAH operation is enhanced with the experimental post-heating unit additional power, showing different working conditions for the setup.

5.1.1 T-SAH operation along a day

The prototype operated with the auxiliary compressor working in series with the turbocharger compressor at its inlet. The experimental post-heating unit was not activated. The three solar modules were in tracking mode during the considered time interval.

Fig. 5.2(a) reports temperature at the reference points of the circuit versus True Solar Time TST. While a substantially time-steady profile is obtained for the compressor static inlet temperature T_1. Following the ambient temperature, the compressor outlet temperature T_2 increases along TST following the time growth of compression ratio $\pi_c = \frac{p_{2\mathrm{t}}}{p_{1\mathrm{t}}}$. The receiver outlet temperature T_{3r} varies along TST according to the solar power received. A peak temperature T_{3r} above 500 °C is reached. A temperature drop from T_2 to $T_{2\mathrm{r}}$ and from $T_{3\mathrm{r}}$ to T_3, across the connection pipe lengths L_{n1} and L_{n2} can be observed. This is also due to the thermal inertia of the pipes n_1 and n_2, the experimental post-heating unit structure located within the n_2 length, and to a lesser extent the thermal insulation and the heat losses across it. After expansion, a peak air temperature at the turbine outlet $T_4 = 400$ °C is obtained.

Figure 5.2(b) shows the pressure in the main circuit points. Fig. 5.2(c) shows the mass flow rate and turbocharger speed. Following the inlet turbine temperature trend, the turbocharger speed reaches a peak of 110 krpm. This coincides with the higher pressure inside the receiver, surpassing 1.4 bar. The mass flow rate varies smoothly, increasing with speed and pressure.

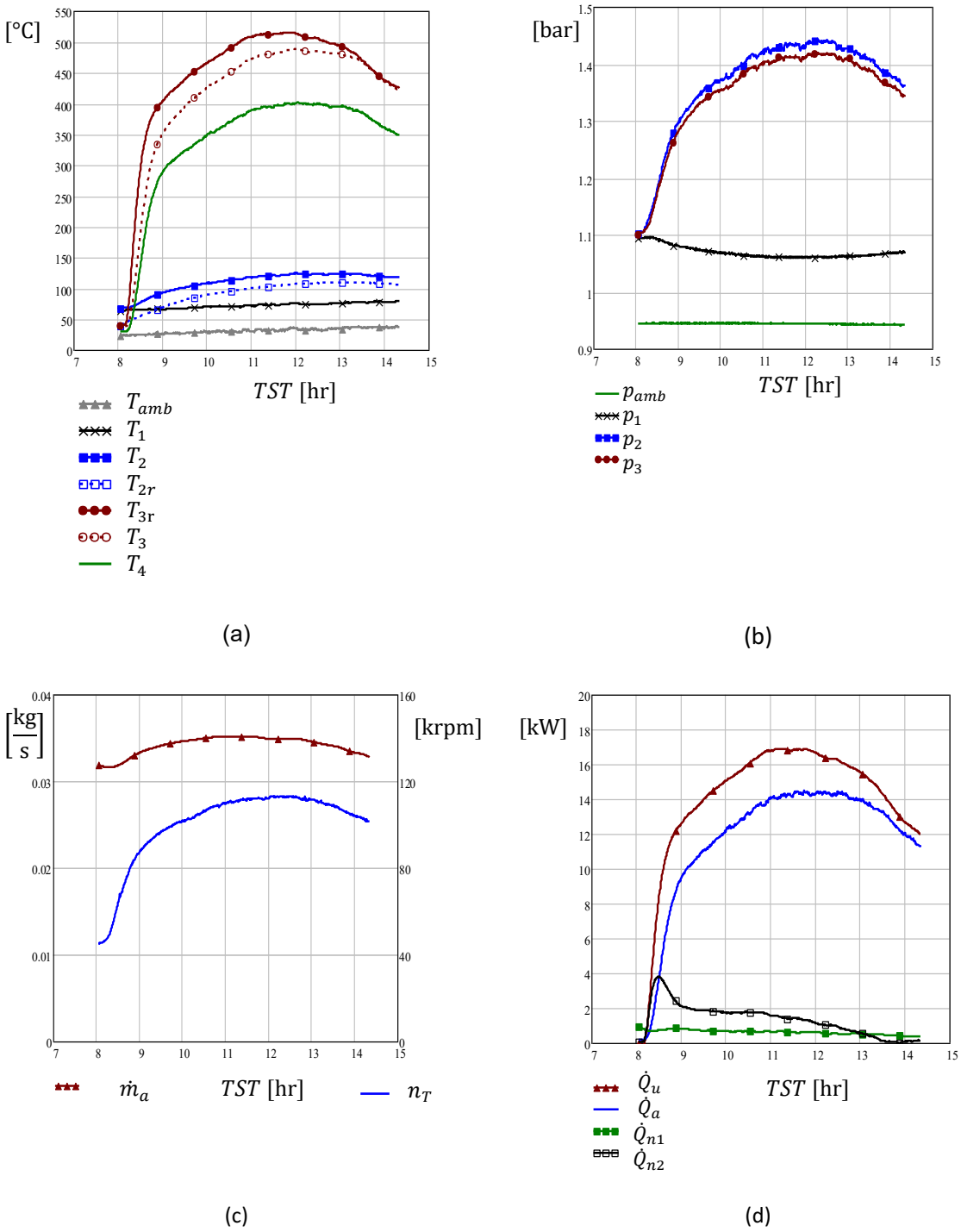

Fig. 5.2. Experimental results, T-SAH operation along a sunny summer day, experimental post-heating OFF, vs. true solar time. (a) Temperatures. (b) Pressures. (c) Mass flow rate and rotating speed. (d) Thermal powers.

Figure 5.2(d) shows the power gained by the air $\dot{Q}_u$ inside the receiver tube length vs. time, Eq. (5.1). With the temperature at the turbine outlet T_4, the power delivered to the outlet airflow is $\dot{Q}_a$, Eq. (5.2). Fig. 5.2(d) reports the thermal losses $\dot{Q}_{n1}$ occurring across the connection tube n_1, which were not negligible, as well as the losses $\dot{Q}_{n2}$, across the connection n_2, Eqs. (5.3) and (5.4). Indicating mainly the thermal inertia of the system, both $\dot{Q}_{n1}$ and $\dot{Q}_{n2}$ decrease over time.

Because of their thermal capacity, stainless steel connection tubes take between one and two hours to reach their operative temperature, heated by the airflow.

$$\dot{Q}_u = (T_{3r}c_{p3r} - T_{2r}c_{p2r})\,\dot{m}_a \tag{5.1}$$

$$\dot{Q}_a = (T_4c_{p4} - T_{amb}c_{pamb})\,\dot{m}_a \tag{5.2}$$

$$\dot{Q}_{n1} = (T_2c_{p2} - T_{2r}c_{p2r})\,\dot{m}_a \tag{5.3}$$

$$\dot{Q}_{n2} = (T_{3r}c_{p3r} - T_3c_{p3})\,\dot{m}_a \tag{5.4}$$

Some outcomes can be highlighted. This small-scale example of T-SAH demonstrated the viability of direct air heating inside a linear Fresnel collector up to 500 °C with a delivery temperature of 400 °C. Due to the low heat capacity of air, despite a relative short collector row, an outlet temperature T_{ou} slightly above 400 °C is reached after a transient of $\sim 1\mathrm{hr}$. A peak temperature of 500 °C is reached at solar noon. Thermal dilatation of the receiver tube occurs during heating, reaching an overall length extension up to ≈ 150 mm, confirming the suitability of the sliding hanger system and the flexible connections installed, described in Chapter 3. On the other hand, excessive receiver tube bending is recognized as a risk of glass cover breakage when the bending displacement of the tube makes it touch and press the cover glass tube. Tube bending seems due to non-uniform circumferential temperature, which originates a non-uniform peripheric wall dilatation, more substantial using air than using liquid HTF. Secondary reflectors are beneficial for distributing the solar heat flux across the receiver perimeter. In the present experiment, bending has been observed, especially during the starting transient when tubes still encompass circumferential temperature homogenization. Nevertheless, no damage to the cover glass occurred.

The turbocharger increased the air pressure into the T-SAH, recovering compressing power through the turbine. The auxiliary compressor was needed to sustain the turbocharger freewheeling under the operating conditions tested. This is due to two main reasons. On one side, the small turbocharger limits compressor and turbine efficiencies, which in this case have modest values owing to the small size. On the other side, the turbocharger does not operate under optimal conditions, it is large in size for the mass flow. A modest compressing ratio of 1.4 is reached, indicating that the compressor is working in the low region of the map. This is confirmed by the turbocharger speed, which does not overcome $110\ \mathrm{krpm}$. The compressor working point is determined by the turbine inlet temperature, which mainly controls the turbine power $\dot{W}_e$. An increase of $\dot{W}_e$ would accelerate the turbocharger, shifting its working point toward the map core, where efficiencies are higher, and the larger compression ratio would reduce the pressure drops. As a consequence, the mass flow rate would increase, resulting in a lower inlet turbine temperature for a given solar power available, thus again slowing down the turbocharger. This behavior highlights the importance of good matching between the turbocharger and solar field. Either a smaller turbocharger would be more appropriate for the available solar power of the three LFCs, or an LFC field designed for a higher mass flow rate and same outlet temperature would be advisable. Despite the limited performances of the

turbocharger, the overpressure imposed by *ac* decreases for increasing speed, as can be noted by observing p_{1t} in Fig. 5.2(b) showing a tendency to being not necessary.

5.1.2 T-SAH operation with the experimental post-heating ON

In this test, the three Fresnel modules were also in tracking mode throughout the experiment. The auxiliary compressor was active. The experimental post-heating unit was activated during the experiment with increasing electrical power. The use of an electrical post-heating unit downstream the solar tube allowed achieving a higher turbine inlet enthalpy, in this case by increasing temperature, without the risk of receiver tube overheating, hence extending the turbocharger testing range without a larger solar facility neither a smaller turbocharger, which would be less efficient. As explained in Chapter 3, the use of electrical post-heating is only for experimental purposes, extending the turbocharger testing range and would not be implemented in a real industrial plant, being not convenient to dissipate electricity into heat. The effect of the experimental post-heating unit can be seen after the first half-hour on temperature T_3, Fig. 5.3(a). A peak inlet turbine temperature of 570 °C was reached. T_{3r} was lower than in the previous case, for a bit lower solar power and a higher mass flow rate. The increased T_3 accelerated the turbocharger, up to $\approx 130\ \mathrm{krpm}$ increasing the mass flow rate, as required, Fig. 5.3(b). This also brought up the pressure in the receiver tube to 1.6 bar, Fig. 5.3(c). Fig. 5.3(d) plots the electrical power of the post-heating unit $\dot{Q}_{ph}$, as well as the net post-heating power delivered to the airflow $-\dot{Q}_{n2}$, together with other relevant power values, as for the previous case.

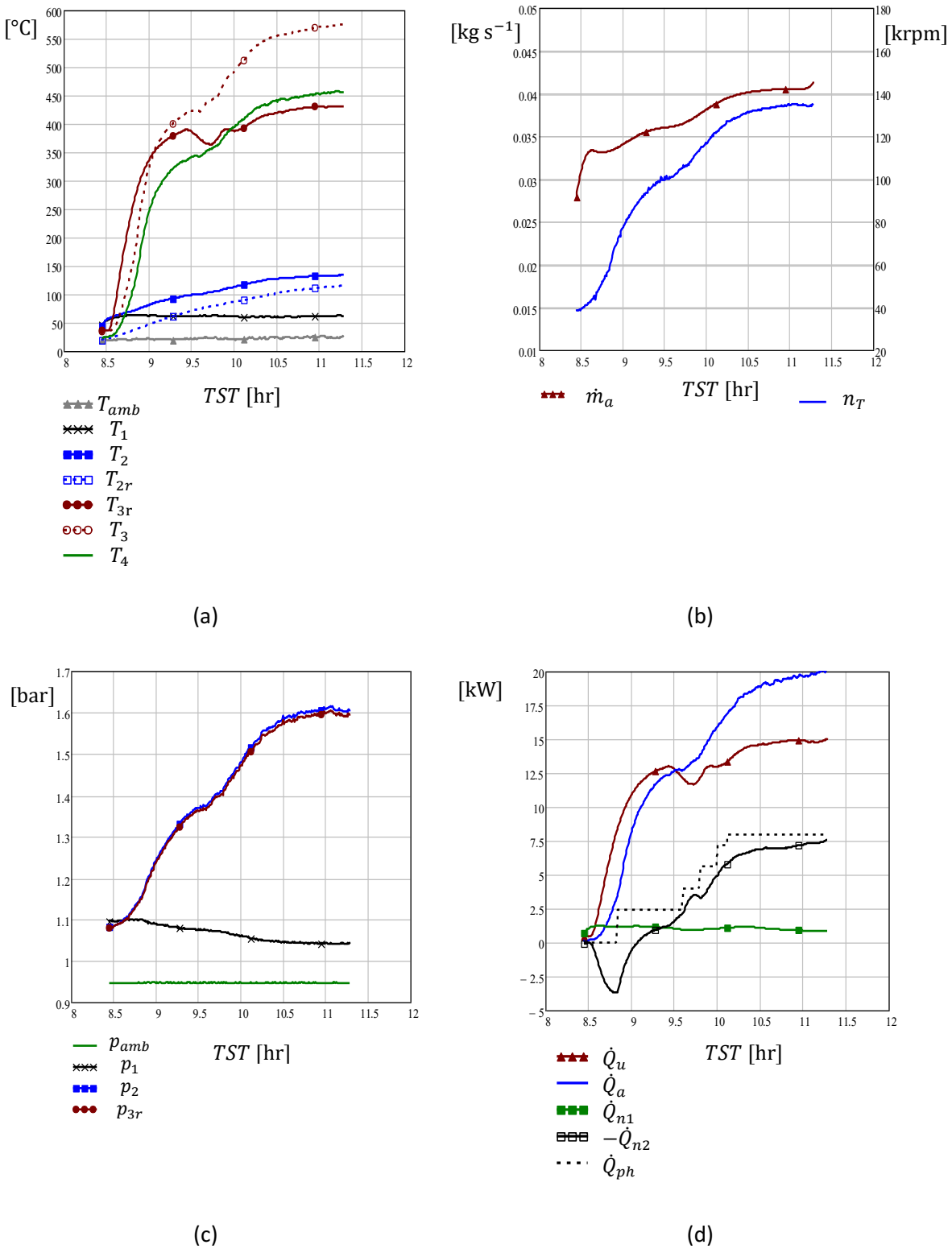

Fig. 5.3. Experimental results, T-SAH operation along a sunny summer day, experimental post-heating unit ON, vs. true solar time. (a) Temperatures. (b) Mass flow rate and speed. (c) Pressures. (d) Thermal powers.

The experimental post-heating unit allows reaching higher inlet turbine temperature, speed, pressure, and mass flow rate so that the compressor working point is shifted toward the map core, where slightly higher efficiencies are expected. Also, the increased air pressure should reduce the pressure drop across the circuit, or at least mitigate its growth as a consequence of

the increased mass flow rate. The beneficial effect of a higher pressure ratio can be noted by observing the very small mismatch between p_{2t} and p_{3t} in Fig.5.3(c), in comparison with Fig.5.2(b). The beneficial effect of higher T_3 on the turbocharger performance is proven by looking at the auxiliary compressor behavior. A drop of p_1 can be observed in Fig. 5.3(c), which is more relevant than in the previous test. The overpressure given by the auxiliary compressor drops, but it was still necessary to keep the turbocharger freewheeling.

5.2 Thermal losses model validation

An original specific test with the partial shut-off of the concentrated irradiance has been devised and carried out on the receiver tube to validate the discretized receiver model, either the static or the dynamic one. For this aim, only two of the downstream last tubes were considered for the validation, $L^* = L_L$, being permanently non-irradiated, as in Fig.5.4 and Fig.5.5, thus incorporating only heat losses in a transient test heating and cooling by the upstream tubes.

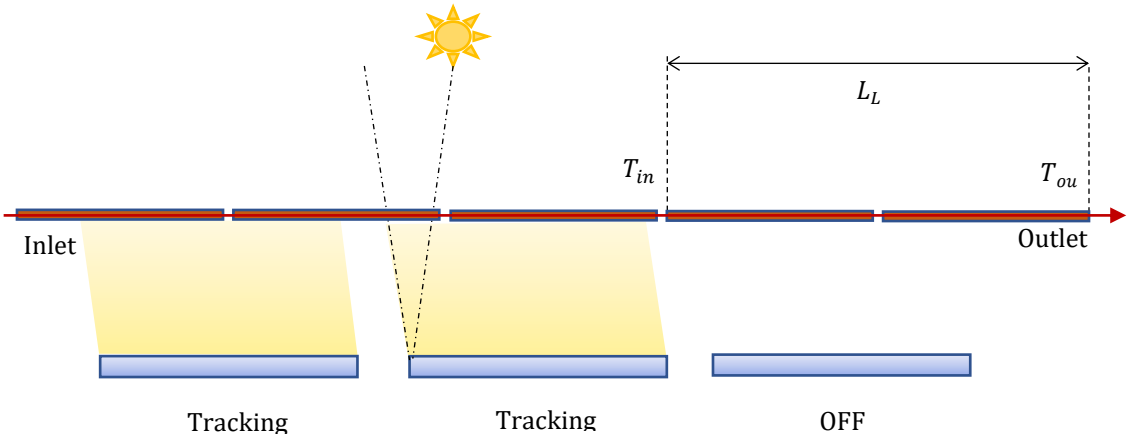

Fig. 5.4. Thermal losses test layout.

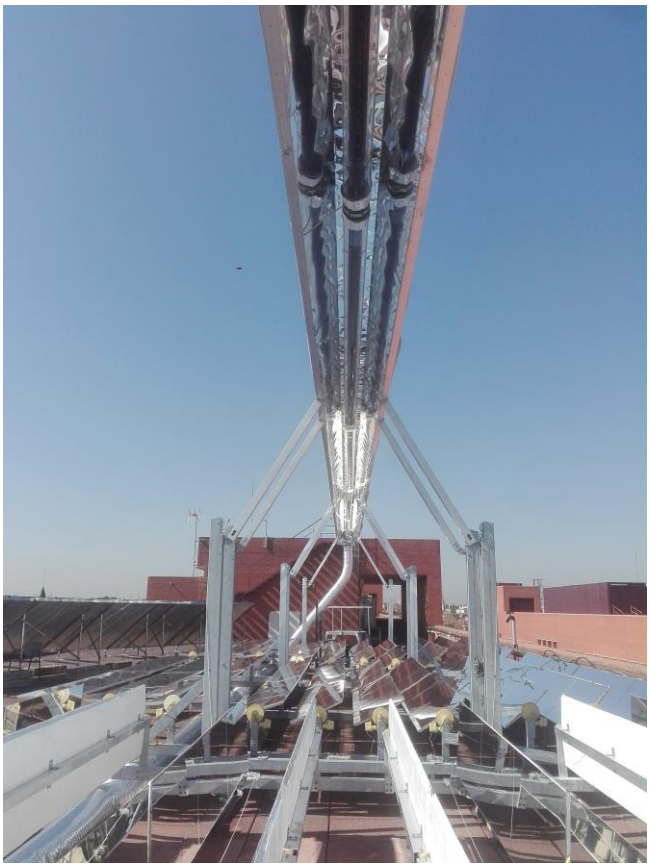

Fig. 5.5. Thermal losses test, the downstream receiver is partially irradiated.

Fig. 5.6 reports the experimental temperatures T_{in} and T_{ou}, during the thermal losses test, respectively at the inlet and outlet of the tested receiver length L_L as in Fig. 5.4. T_{in} was progressively increased using solar energy gathered by the irradiated upstream three tubes, up to 380 °C. Then they were defocused to perform the cooling transient. The static and the dynamic model were applied to compute the outlet temperature, T_{ou}^{st} and T_{ou}^{dy} respectively, over the length L_L, using measured T_{in} as input, together with mass flow rate, air pressure, ambient temperature, and null $\dot{q}_s$.

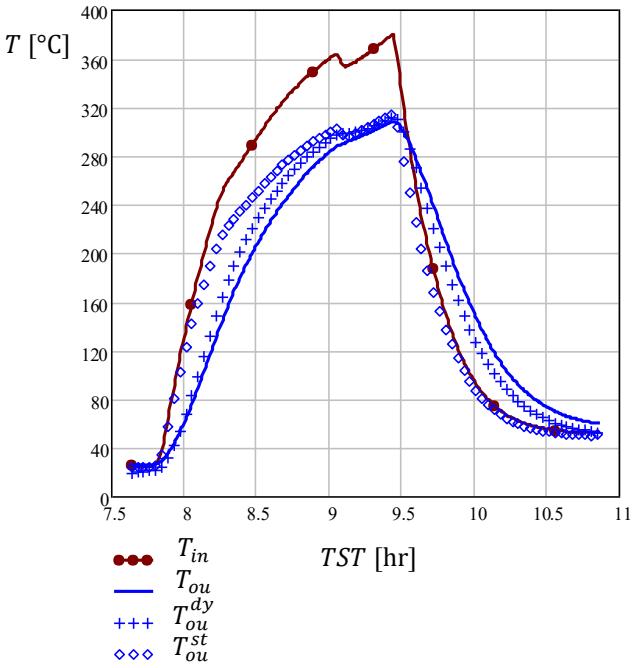

Fig. 5.6. Thermal losses test results. Temperatures at inlet and outlet of L_L.

T_{ou}^{st} diverges from T_{ou} during the transient heating and cooling, while is quite precise at the peak, 9:30 hr, when the time variation of T_{ou} is smoother and closer to steady-state conditions. As expected, the dynamic model can account for the receiver tube thermal inertia jointly with the correct thermal losses yielding a robust validation concerning the T_{ou}^{dy} values. As a result, the thermal losses account and the herewith proposed implementation of U_c seems correct, but still more features need validation.

5.3 Optical efficiency experimental quantification

The above-described experimental data of a typical summer day (post-heating OFF) has been used to validate the collector and receiver model. The collector and the solar field model of Chapter 4 allow determining the main parameters across true solar time TST for the duration of the test. The sun position is calculated according to [66], as reported in Chapter 4, yielding α_s, γ_s, and θ_z. The measured irradiances, G_{glo} for global, and G_d for diffuse on horizontal surfaces, shown in Fig. 5.7, are used to compute the direct normal irradiance is obtained as $G_{bn} = (G_{gl} - G_d)/\cos\theta_z$.

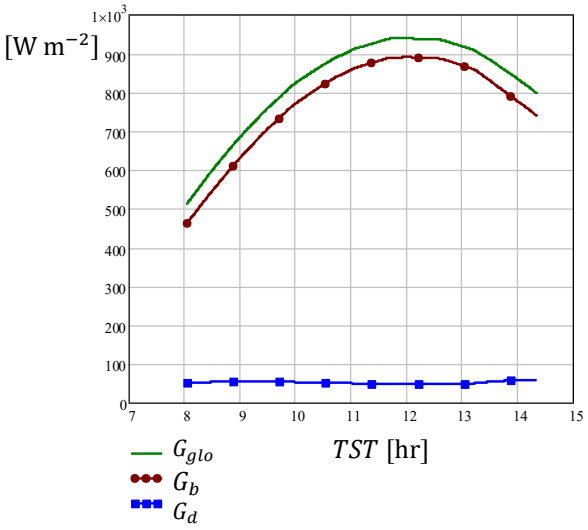

Fig. 5.7. Solar irradiance measurements during the clear summer day.

Fig. 5.8 shows the solar field parameters across the TST. The solar incidence angle longitudinal component θ_L and transversal component θ_T are obtained from Eqs. (4.3) and (4.4). The end losses factor is estimated as $f_{end} = (L_r - L_{irr,out})/L_r$, where $L_{irr,out}$ is the length of concentrated irradiance exceeding the receiver length from one or another extremity. It can be noticed as receiver extensions at the extremities L_{ex1} and L_{ex4} allow increasing the time interval with $f_{end} = 1$, thus with null end losses. The IAMs are obtained from the manufacturer data in Fig. 4.4, according to θ_T and θ_L. Eq. (4.5) gives the optical efficiency η_{op}, assuming $\eta_{op0} = 0.632$ provided by the manufacturer. Fig. 5.8(b) depicts the expected optical efficiency η_{op}, as well as the concentrated heat flux $\dot{q}_s$. Since in this facility, the initial focusing procedure is not instantaneous, a linear growth of $\dot{q}_s$ from null non-tracking value to full tracking value was assumed during the focusing transient interval, which lasted approximately 6 min.

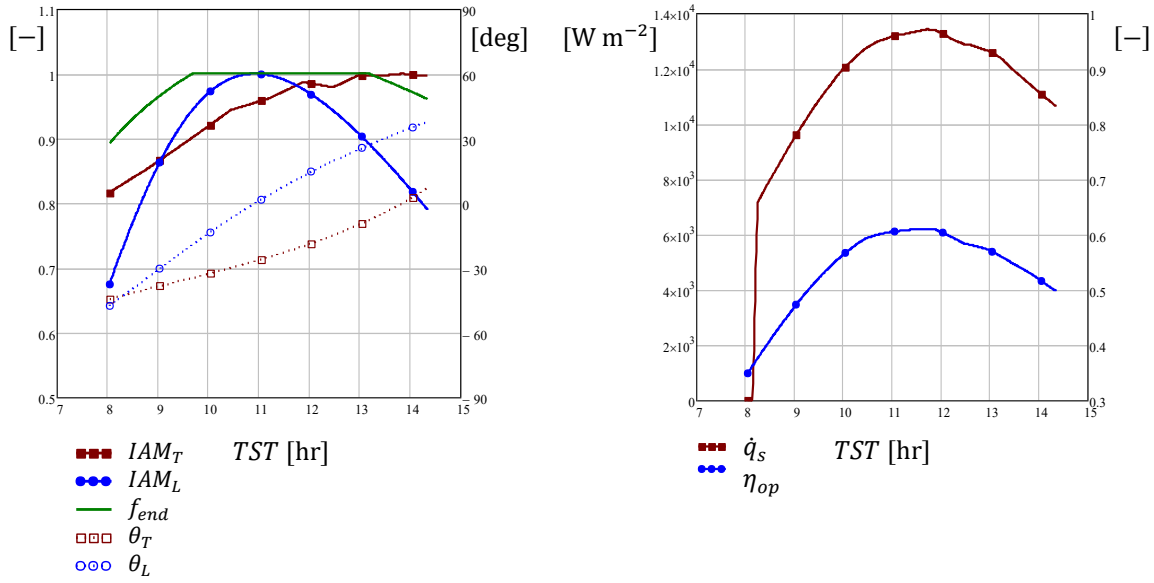

(a) (b)

Fig. 5.8. Collector model results. (a) LFC row solar angles, $IAMs$ and f_{end}. (b) Concentrated heat flux and experimental optical efficiency.

Knowing $\dot{q}_s$ and its axial distribution along the receiver length $\dot{q}_s\langle z\rangle$ from Eqs. (4.7) and (4.8) the receiver thermal model can be solved at each time step, either in the static or dynamic formulation, assuming the experimental air conditions at the receiver inlet $T_{in} = T_{2r}, p_{in} = p_{2r}$, mass flow rate $\dot{m}$, ambient conditions p_{amb}, T_{amb}, according to Fig.5.2. The main outputs are the estimated outlet temperature T_{ou}^{st} and T_{ou}^{dy}, the thermal power to the airflow $\dot{Q}_u = (T_{ou}cp_{ou} - T_{in}cp_{in})\dot{m}_a$, hence $\dot{Q}_u^{st}$ and $\dot{Q}_u^{dy}$, respectively for the static and dynamic model. Temperature and power are plotted in Fig.5.9(a) and Fig. 5.9(b) respectively v.s. TST.

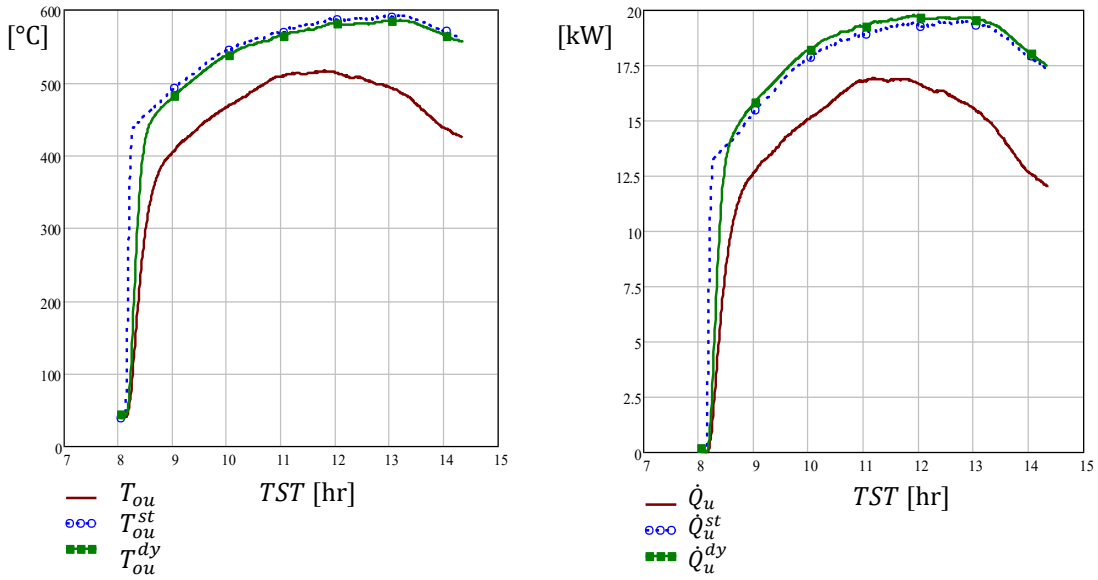

(a) (b)

Fig. 5.9. Comparison of the model results using the manufacturer η_{op} with the experimental results. (a) Air outlet temperature. (b) Useful power to the airflow.

The results show that the model overestimates both the outlet temperature and power gain. The deviation increases after the peak power is reached. Further simulations confirmed that the results were not very sensitive to the heat loss coefficients nor the thermal inertia, respectively U_L and U_C. Furthermore, the results were much more affected by the concentrated solar heat flux. This suggests that the actual optical collector efficiency can be lower than the value delivered by the manufacturer. This can be due to several imperfections affecting the real system available, not properly accounted for by η_{op}, Eq.(4.5). Common optical errors in concentrating systems are reviewed in [102]. Imperfectly manufactured reflectors, deformations due to aging, tracking errors, reflectors displacement due to wind, among others, are potential causes of loss of optical efficiency. An empirical optical efficiency η_{op}^{exp} can be estimated from experimental performances and real sun data, using the dynamic receiver model for thermal losses estimation. At each time step η_{op}^{exp} is the optical efficiency that the collectors must hold to give at the collector outlet the same temperature T_{ou}^{dy} as the experimental value T_{ou}, thus giving a negligible deviation $\left|\dot{Q}_u^{dy} - \dot{Q}_u\right|$. An iterative calculation scheme allows to obtain η_{op}^{exp} satisfying Eq. (5.5) for each time step, where the thermal power to air of each receiver element $\dot{Q}_{u,i}^{dy}$ is obtained according to Eqs. (4.33) and (4.34), using a concentrating heat flux $\dot{q}_s = \eta_{op}^{exp} G_{bn} W_a P_{ex}^{-1}$ in Eq. (4.6).

$$\dot{Q}_u^{dy} = \sum_{i=1}^{n_e} \dot{Q}_{u,i}^{dy} = \dot{m}\left(c_{p,ou} T_{ou} - c_{p,in} T_{in}\right) \tag{5.5}$$

Fig. 5.10(a) shows that η_{op}^{exp} is lower than the expected theoretical $\eta_{op} = \eta_{op0} IAM_T\langle\theta_T\rangle IAM_L\langle\theta_L\rangle$, so that an empirical efficiency correction term η_{cor} can be defined and evaluated, Eq. (5.6).

$$\eta_{cor} = \frac{\eta_{op}^{exp}}{\eta_{op}} \tag{5.6}$$

As reported in Fig. 5.10(a), $\eta_{cor} < 1$ was found. Its value varied across a mean value during the first hours of experimentation and started to drop in the afternoon hours. This suggests exploring the relationship between the correction efficiency η_{cor} and operating parameters.

A clear dependence of η_{cor} on solar angles θ_T or θ_L has not been observed; instead, a drop with $\mathrm{d}\theta_T/\mathrm{d}\tau$ was found. This suggests that a tracking error arises when $\mathrm{d}\theta_T/\mathrm{d}\tau$ increases, due to loss of focus within the interval of time separating two consecutive tracking angle adjustments. Tracking error in concentrating systems, including LFC applications, has been studied by several authors [103], [104], [105], among others. They point out that power loss increases with tracking angle deviation according to the geometry of the concentrator. Due to the large focal distance, LFCs are very sensitive to tracking accuracy, for which they need a precise tracking system as well as secondary optics to recover part of concentrated irradiance missing the receiver tube. Among other causes, it is well known that time lag between consecutive tracking angle adjustment can induce a focusing error. In the present setup, the tracking system checks continuously one by one the mirrors of a module, taking approximately 20 s for each of the 10 mirrors. Each mirror is refocused any $\tau_{tr} \approx 200$ s so that the tracking error due to lag between two consecutive adjustments is $\sigma_{tr} = (\mathrm{d}\theta_T/\mathrm{d}\tau)\tau_{tr}$. At each instant, each mirror has a different tracking error, being theoretically null for the last checked mirror and growing to σ_{tr} for the next one in the checking loop routine. η_{cor} is plotted against σ_{tr} in Fig. 5.10(b). It can be noticed that from a certain angle deviation σ_{tr} the effect of tracking lag is remarkable over other possible errors. A reasonable assumption is considering $\eta_{cor} = \eta_{st}\eta_{tr}$ where a static term η_{st} accounts for static imperfections (mirrors and receiver cleanness, manufacturing errors, bending, slope, imperfect reflectivity) and a term η_{tr} accounts for the tracking lag error. As a threshold for η_{tr} to take place noticeably, $\sigma_{tr}^* = 7$ mrad can be assumed according to Fig. 5.10(b). For $\sigma_{tr} < \sigma_{tr}^*$ the tracking error effect is neglected and $\eta_{tr} = 1$, so that $\eta_{cor} = \eta_{st}$. An average value of $\bar{\eta}_{st} = 0.69$ was found for $\sigma_{tr} < \sigma_{tr}^*$.

For $\sigma_{tr} > \sigma_{tr}^*$ part of reflected irradiance is supposed to go out of the receiver diameter during a certain portion of the tracking time interval τ_{tr}. Although the trapezoidal secondary reflector can recover part of the irradiance missing the receiver tube, an optical efficiency drop is reasonably expected and accounted for by $\eta_{tr} = \eta_{cor}/\bar{\eta}_{st}$, which Fig. 5.10(b) shows. In fact, among the available non-imaging secondary optics, the trapezoidal shape offers lower performances compared to adaptative geometries, CPC, or segmented parabolic-shaped secondary optics [106], [24] among others.

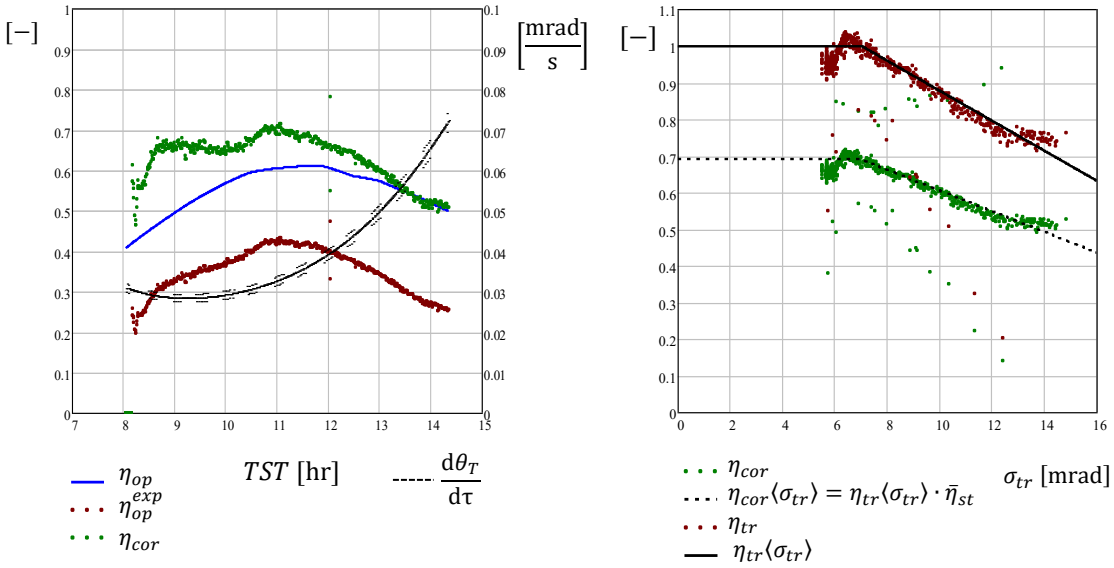

(a) (b)

Fig. 5.10. Empirical correction for optical efficiency. (a) Experimental and theoretical optical efficiencies, η_{op}^{exp} and η_{op} respectively. (b) η_{cor} and η_{tr} versus σ_{tr}.

For the range of σ_{tr} corresponding to the present dataset, the tracking efficiency can be approximated as a linear function of σ_{tr} as follows, with $c_{tr} = -40.9\ \text{rad}^{-1}$

$$\eta_{tr}\langle\sigma_{tr}\rangle = 1 - c_{tr}(\sigma_{tr} - \sigma_{tr}^{*}) \tag{5.7}$$

$$\eta_{cor}\langle\sigma_{tr}\rangle = \eta_{tr}\langle\sigma_{tr}\rangle \cdot \bar{\eta}_{st} \tag{5.8}$$

The modeled correction for optical efficiency, Eq. (5.8), can be used for running the dynamic and static models to verify their effect on the main outputs T_{ou} and $\dot{Q}_u$. For that, $\eta_{op,cor} = \eta_{op0} IAM_T IAM_L \eta_{cor}\langle\sigma_{tr}\rangle$ was used instead of $\eta_{op} = \eta_{op0} IAM_T IAM_L$ delivering good results, as reported in Fig. 5.11, with an RMS deviation of 10 °C on T_{ou} and 450 W on $\dot{Q}_{ou}$ for the dynamic model and 48 °C on T_{ou} and 1,760 W on $\dot{Q}_{ou}$ for the less accurate static model.

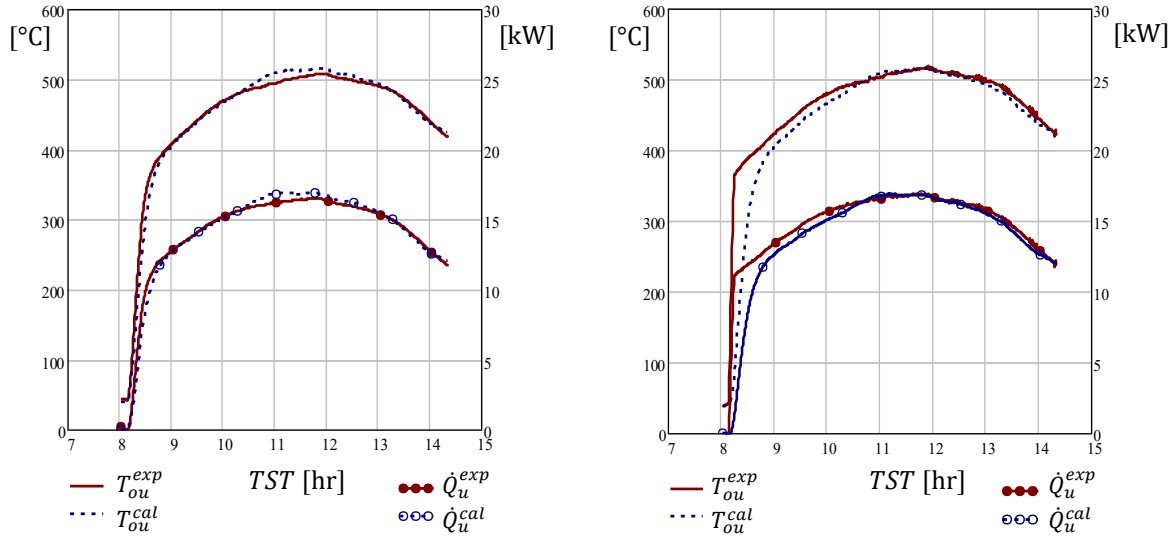

Figure 5.11. Validation of the corrected optical efficiency. (a) Dynamic model. (b) Static model.

The calculation for η_{tr} and the estimation of η_{st} was repeated for another experimental test obtained on a typical spring day. Despite the slightly different testing conditions (mirrors tracking calibration, mirrors and receiver cleanness, wind, etc.) $\bar{\eta}_{st} = 0.72$ was found, close to the previous summer value. η_{tr} had a similar trend of the previous summer case, confirming the validity of the assumption made. Besides, due to the larger test duration along the day, higher angles σ_{tr} were reached during the test, comparing with the previous summer one, and the effect of tracking angle error can be observed over a larger range. For larger σ_{tr}, η_{tr} is still dropping with σ_{tr} but at a lower rate. For small σ_{tr} a linear approximation seems acceptable. A better approximation over a larger σ_{tr} range was obtained using a potential function as follows, with $c_{tr1} = 1.754\ \text{rad}^{-1}$and $c_{tr2} = 0.488$, Eq. (5.9), Fig. 5.12.

$$\eta_{tr}\langle\sigma_{tr}\rangle = 1 - c_{tr1}(\sigma_{tr} - \sigma_{tr}^{*})^{c_{tr2}} \tag{5.9}$$

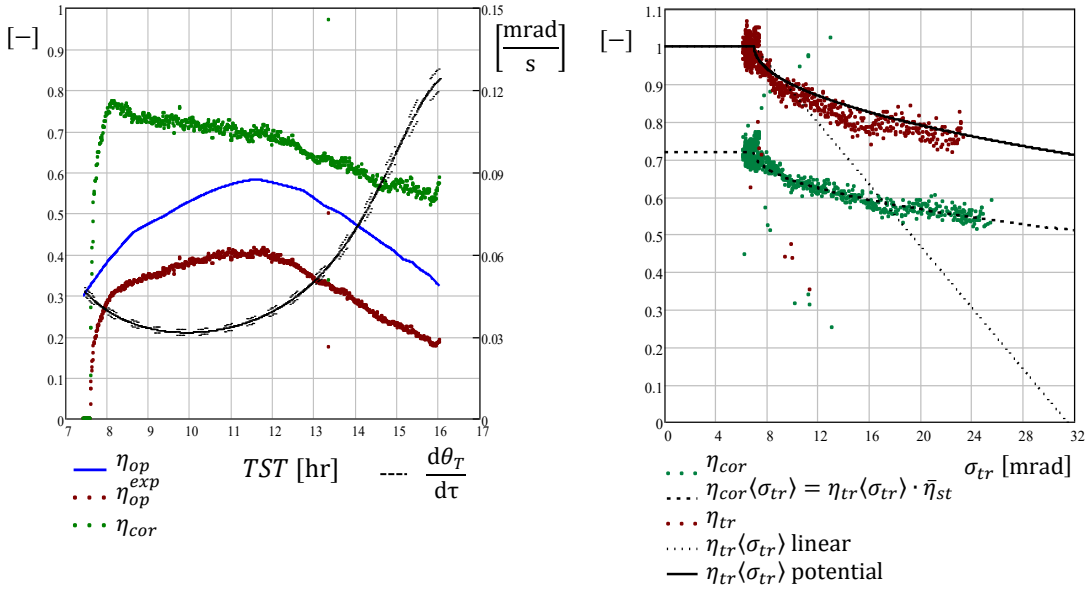

(a) (b)

Fig. 5.11. Empirical corrections for optical efficiency (spring clear day). (a) Experimental and theoretical optical efficiencies, η_{op}^{exp} and η_{op} respectively. (b) η_{cor} and η_{tr} versus σ_{tr}.

The static and the dynamic model were solved using $\eta_{op,cor} = \eta_{op0} IAM_T IAM_L \eta_{cor}\langle\sigma_{tr}\rangle$ with the potential approximation for $\eta_{cor}\langle\sigma_{tr}\rangle$. The results show a low RMS deviation of 32 °C on T_{ou} and 1,210 W on $\dot{Q}_{ou}$ for the static model and 5 °C on T_{ou} and 250 W on $\dot{Q}_{ou}$ for the dynamic model, a substantial improvement. Fig. 5.13 shows the high coherence with experimental data obtained for the time evolution.

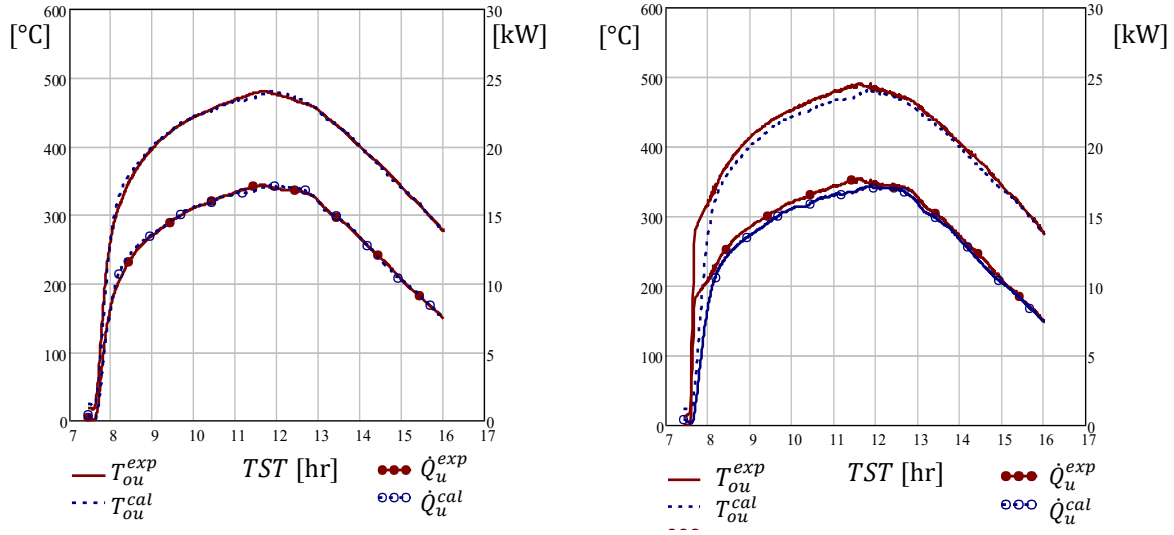

Fig. 5.12. Validation of the corrected optical efficiency for a spring day test. (a) Dynamic model. (b) Static model.

Although a complete optical efficiency characterization requires a deep analysis of errors, supported by raytracing techniques and extended measurement and testing campaigns, besides needing a higher level of measurement techniques, the limited experimental analysis carried out allows improving the predictions by the numerical model for the specific collector used in the facility under study at a reasonable expenditure of time and cost. This kind of experimental quantification could be part of the commissioning process of more conventional facilities.

Even though the dynamic model is required to predict rapid transients, the static model can give acceptable results during quasi-steady operations, such as on the central hours of the day.

5.4 Receiver thermal features

Additional features can be observed solving the model at the power peak of the tested summer day. Fig. 5.13(a) plots the air temperature profile along the tube length $T_{ou,i}^{cal}$ calculated from the dynamic model and corrected optical efficiency $\eta_{op,cor}$, allowing a comparison with the measured air temperature at each tube outlet T_{ou}^{exp}, showing good agreement. A low discretization element number $n_e = 10$ has been used. The wall temperature T_w is also depicted. It increased along z despite the discontinuity induced by the junctions between tubes.

As expected, due to low internal heat transfer, the overtemperature $\Delta T_w = T_w - T_a$ is remarkable on the irradiated single tube length. ΔT_w is ≈ 200 °C at the tube entrance and decreases down to ~ 50 °C toward the outlet. This is coherent with Eq. (4.20): for a given $\dot{q}_s$, the increase of T_w consequent to higher T, translates into higher U_L and lower $\dot{q}_u = \dot{q}_s - U_L(T_w - T_{amb})$, hence lower $\Delta T_w = \dot{q}_u P_{ex}/(h_a P)$, being h_a mainly dependent on the Reynolds number. The drop of $\dot{q}_u$ with z can be observed in Fig. 5.13(b). The receiver tube thermal limit of 600 °C is not overcome, avoiding the receiver damage. Fig. 5.13(a) plots the variation of U_L, showing an increase with T_w up to a value of $10\ \mathrm{W\ m^{-2}\ K^{-1}}$ for the receiver tube, while for

uncovered stainless steel junction elements between two tubes increased up to $U_{L,j} \approx 20\ \mathrm{W\,m^{-2}\,K^{-1}}$. This indicates the necessity of reducing this parameter and/or the reduction of the extension length.

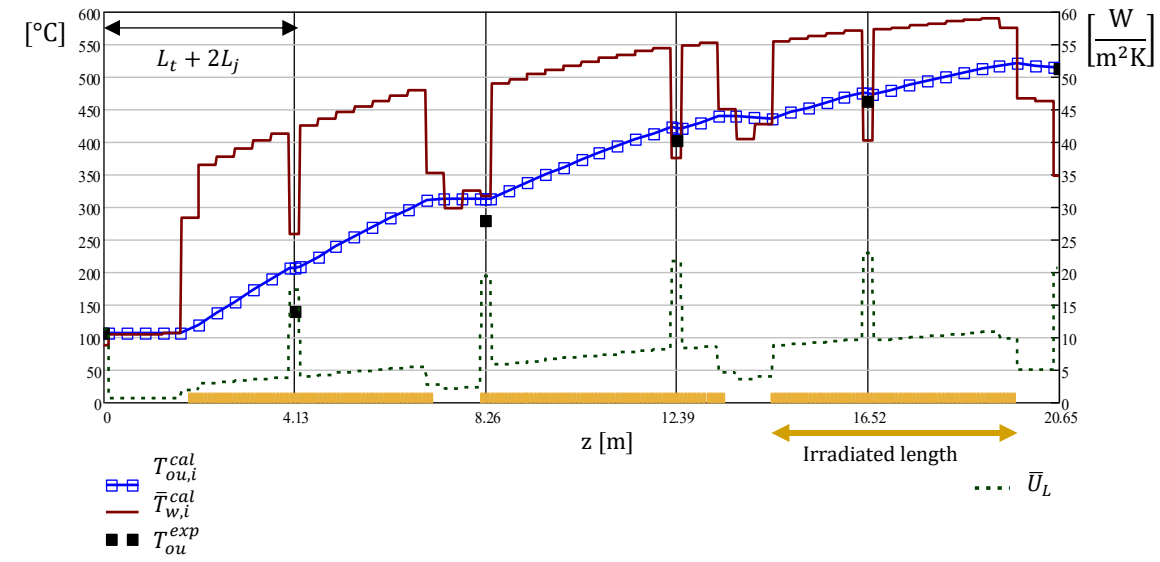

(a)

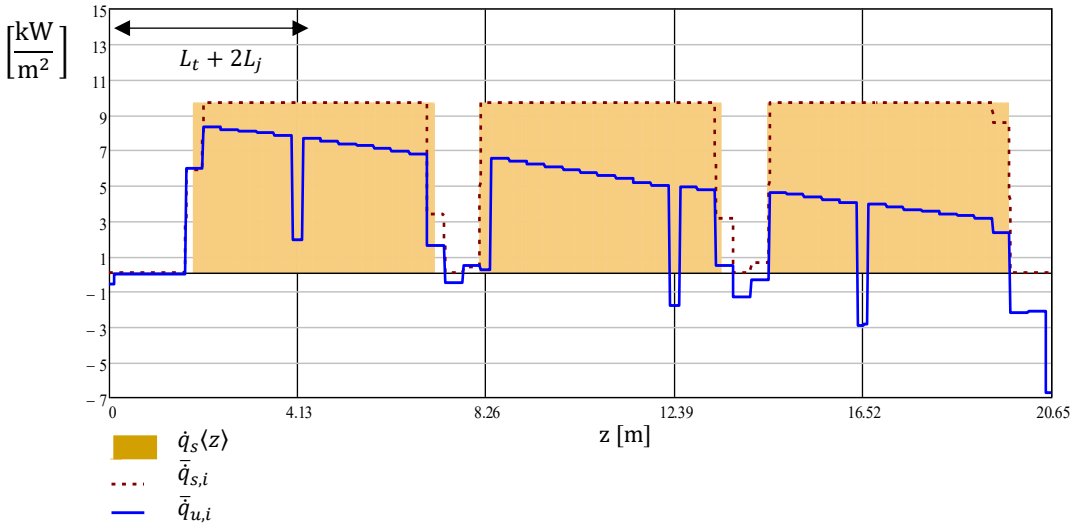

(b)

Fig. 5.13. Receiver thermal distributions at power peak. (a). Air and receiver wall temperatures and heat losses coefficient. (b) Concentrated heat fluxes.

Fig. 5.13(b) plots the concentrated heat flux on the receiver $\dot{q}_s = \eta_{op,cor} G_{bn} W_a P_{ex}^{-1}$. Its distribution on the receiver length $\dot{q}_s\langle z\rangle$, according to Eq. (4.6), can be observed as well as its discretized approximation $\bar{\dot{q}}_{s,i}$, constant along each discretization element i. Heat flux to ambient $\dot{q}_s - \dot{q}_u = U_L(T_w - T_{amb})$ increased with wall temperature T_w. Non-irradiated length

due to spacing between LFCs and end effect can both be observed. Fig. 5.13 shows the detailed information that can be obtained from the models herewith proposed. Among other issues, they quantify the improvements possible by reducing the important losses in tube junctions and additional spacing, L_{ex2}, L_{ex3} and the increased L_j.

5.5 Diabatic turbocharger analysis

This section performs an in-depth analysis of the turbocharger performances under the two experimental tests reported above. According to the diabatic turbocharger behavior introduced in Chapter 4, the main heat transfer contributions are estimated as follows, through a semi-empirical analysis, carried out combining the adiabatic turbocharger model from "cold" maps with experimental data (temperature and pressure, speed, and mass flow rate).

T_{2t}^{adi} can be estimated using the modeled compressor efficiency $\eta_c\langle T_{1t}, \dot{m}, n_T\rangle$ and the experimental π_c, from Eq. (5.10).

$$T_{2t}^{adi} = \frac{\left(\pi_c{}^{(\gamma_c-1)/\gamma_c} - 1\right)T_{1t}}{\eta_c\langle T_{1t}, \dot{m}_a, n_T\rangle} + T_{1t} \tag{5.10}$$

Again, using the turbine efficiency model, the adiabatic turbine inlet temperature T_{3t}^{adi} can be estimated from experimental π_e. $\eta_e\langle \dot{m}, T_{3t}^{adi}, \pi_e\rangle$ is dependent on T_{3t}^{adi} so that an iterative procedure is needed for solving Eq. (5.11).

$$\eta_e\langle \dot{m}_a, T_{3t}^{adi}, \pi_e\rangle = \frac{T_{3t}^{adi}c_{p3} - T_{4t}c_{p4}}{\left(1 - \pi_e{}^{-(\gamma_c-1)/\gamma_c}\right)T_{3t}^{adi}c_{p,e}.} \tag{5.11}$$

The adiabatic compressor and turbine power result from Eq. (5.12) and Eq. (5.13).

$$\dot{W}_c = \left(T_{2t}^{adi}c_{p2} - T_{1t}c_{p1}\right)\ \dot{m}_a \tag{5.12}$$

$$\dot{W}_e = \left(T_{3t}^{adi}c_{p3} - T_{4t}c_{p4}\right)\dot{m}_a \tag{5.13}$$

The diabatic compressor and turbine power come from experimental data, Eq. (5.14) and Eq. (5.15).

$$\dot{W}_c^{dia} = \left(T_{2t}c_{p2} - T_{1t}c_{p1}\right)\ \dot{m}_a \tag{5.14}$$

$$\dot{W}_e^{dia} = \left(T_{3t}c_{p3} - T_{4t}c_{p4}\right)\ \dot{m}_a \tag{5.15}$$

Estimation of the heat fluxes $\dot{Q}_{c\to amb}$, $\dot{Q}_{e\to c}$, and $\dot{Q}_{e\to amb}$ can be carried out as follows.

$\dot{Q}_{c\to amb}$ can be estimated modeling the compressor outlet spiral casing as a tube with an internal diameter $D_c = \frac{D_{c,in}+D_{c.ou}}{2}$ and a length $L_c = \pi D_c^{case}$. The internal heat transfer coefficient for convection $h_{c,int}$ and external heat transfer coefficient $U_{L,case} = h_c^{con} + h_c^{rad}$ include convection and radiation, neglecting conduction temperature loss across the wall.

Modeling $\dot{Q}_{e\to c}$ would be complex due to several heat transfer phenomena occurring on the turbine side, inside the bearing housing, oil lubrication system, and finally inside the compressor case. Instead, it is possible to estimate it from Eq. (5.16), being $\dot{Q}_{c,af} \cong \dot{Q}_c = \dot{Q}_{e\to c} - \dot{Q}_{c\to amb}$.

$$\dot{Q}_{e\to c} = \dot{W}_c^{dia} - \dot{W}_c + \dot{Q}_{c\to amb} \tag{5.16}$$

On the turbine side $\dot{Q}_{e,af} \cong \dot{Q}_e = \dot{Q}_{e\to amb} + \dot{Q}_{e\to c}$ so that $\dot{Q}_e$ and $\dot{Q}_{e\to amb}$ can be then obtained from the experimental $\dot{W}_e^{dia}$ as Eq. (5.17) indicates.

$$\dot{Q}_{e\to amb} = \dot{Q}_e - \dot{Q}_{e\to c} = \dot{W}_e^{dia} - \dot{W}_e - \dot{Q}_{e\to c} \tag{5.17}$$

This methodology was applied to experimental data from the T-SAH operation with post-heating (second representative test, Fig.5.3), where the higher turbocharger speeds were reached and the turbocharger operated inside the map with $n_{c,cor} > n_{c,cor}^{min}$, allowing evaluation of adiabatic compressor efficiency, as required in Eq. (5.10).

$\dot{Q}_{e\to c}$ was obtained for $n_{c,cor} > n_{c,cor}^{min}$ and is reported Fig. 5.14(a). For $n_{c,cor}^{min} > n_{c,cor}$, $\dot{Q}_{e\to c}$ can be approximated with a fitting function $\dot{Q}_{e\to c}\langle T_3 - T_2\rangle$, as Fig. 5.14(a) shows, with the form $\dot{Q}_{e\to c}\langle T_3 - T_2\rangle = c_{ec1}(T_3 - T_2)^{c_{ec2}}$ resulting in $c_{ec1} = 1.86 \cdot 10^{-11}$ W °C^{-1}, and $c_{ec2} = 5.11$. Using this approximation, $\dot{Q}_{e\to c}$ can be drawn across the full experimental time interval as Fig. 5.14(b) reports. $\dot{Q}_{c\to amb}$ and $\dot{Q}_c = \dot{Q}_{e\to c} - \dot{Q}_{c\to amb}$ are also reported. $\dot{Q}_{e\to c}$ resulted to be much higher than $\dot{Q}_{c\to amb}$, as expected due to the temperature differences $T_3 - T_2 > T_2 - T_{amb}$ and the contribution of conduction of the bearing housing.

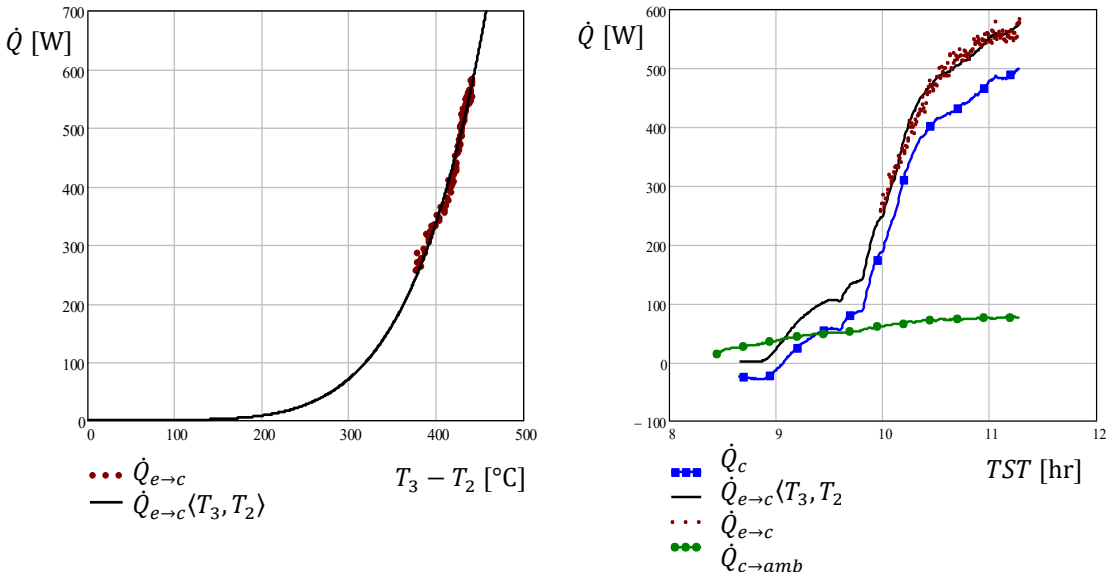

(a) (b)

Fig. 5.14. Compressor heat transfer. (a) Fitting of $\dot{Q}_{e\to c}$. (b) $\dot{Q}_c$, $\dot{Q}_{e\to c}$, $\dot{Q}_{c\to amb}$ vs. true solar time.

Figure 5.15(a) shows the turbine heat transfer rate. As expected, $\dot{Q}_{e\to amb}$ was the main thermal loss, reaching ~2.4 kW although an insulating mineral wood layer of ~5 cm covered the turbine case, although not in a perfect fit. This is due to the high temperature difference $T_3 - T_{amb}$ as well as the large heat transfer surface, which includes the turbine inlet, case, and bearing

housing. This term also includes the thermal losses to the lubrication oil, which can be relevant due to the continuous and substantial oil flow, needed by journal bearings. $\dot{Q}_e$ is addressed before expansion, as explained, and it translates into a remarkable drop of adiabatic turbine inlet temperature, $T_3^{adi} < T_3$, which causes lower turbocharger performances. Due to the relevance of $\dot{Q}_e$, it is worth extracting an expression for its prediction. $\dot{Q}_e = \dot{Q}_{e\to amb} + \dot{Q}_{e\to c}$. $\dot{Q}_{e\to amb}$ can be approximated as $\dot{Q}_{e\to amb} = (UA)_{eamb}(T_3 - T_{amb})$, with the empirical value $(UA)_{eamb} = 4.5$ W °C^{-1} as Fig. 5.15(b) shows, giving a good fit for the temperatures of interest.

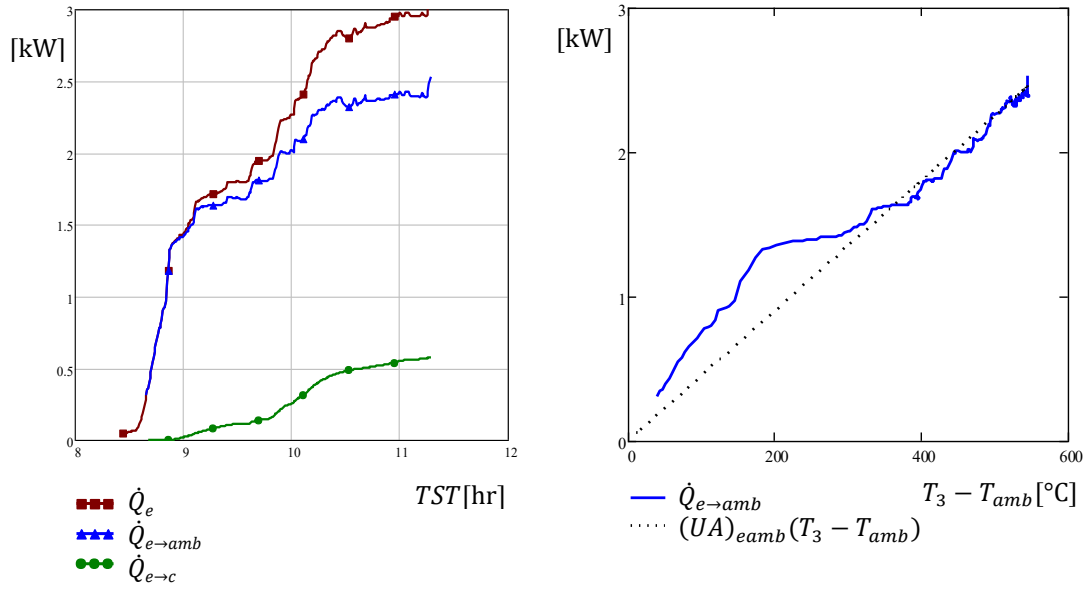

(a) (b)

Fig. 5.15. Turbine heat transfer during the experimental test. (a) $\dot{Q}_e$, $\dot{Q}_{e\to amb}$, $\dot{Q}_{e\to c}$ vs true solar time. (b) $\dot{Q}_{e\to amb}$ linear approximation vs. experimental data.

Fig. 5.16 (a) compares the modeled adiabatic and diabatic compressor outlet temperatures, as well as the adiabatic and diabatic turbine inlet temperatures obtained. It can be observed that the main effect of the diabatic turbocharger behavior is cooling the inlet air before the work extraction process. Air heating at the compressor outlet does not affect the compressor power $\dot{W}_c$, and it is not relevant due to the modest figure of $\dot{Q}_c$. Fig. 5.16 (b) plots the compressor and turbine power variation along with the test. The power provided by the turbine $\dot{W}_e$ delivered to the turbocharger shaft is estimated according to Eq. (5.13). It reaches 2.8 kW at the end of the test with maximum T_3. The compressor power $\dot{W}_c$ is slightly lower than $\dot{W}_e$ due to the mechanical efficiency of the shaft $\eta_m < 1$. The isoentropic turbine power $\dot{W}_{es} = \left(1 - \pi_e^{-(\gamma_c - 1)/\gamma_c}\right) T_{3t}^{adi} c_{p,e} \dot{m}$, which would be provided by an ideal turbine having inlet air temperature T_3^{adi} is plotted for comparison. The thermal power $\dot{W}_e^{dia}$ extracted from the airflow across the diabatic turbocharger reaches up to 5.8 kW and the maximum T_3. It confirms that reducing $\dot{Q}_e = \dot{W}_e^{dia} - \dot{W}_e$ would be of great importance for improving the performance of the turbocharger. The isoentropic compressor power $\dot{W}_{cs}$ and diabatic compressor power $\dot{W}_c^{dia}$ are also reported.

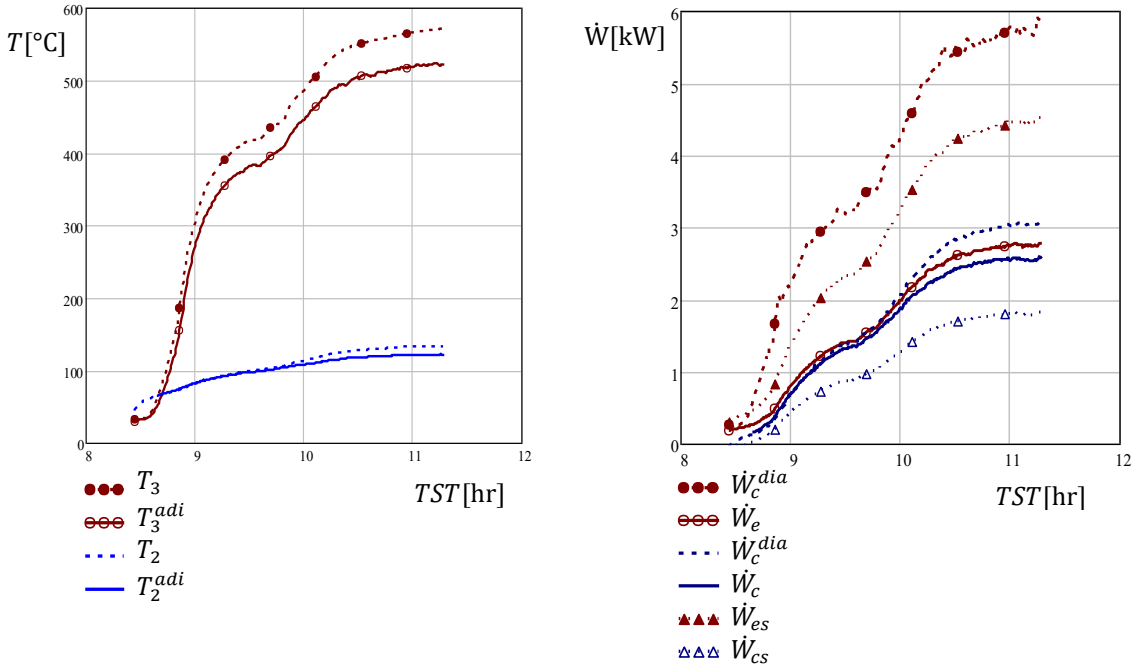

(a) (b)

Fig. 5.16. Diabatic and adiabatic turbocharger. (a) Diabatic and adiabatic temperatures compared vs. true solar time; (b) Turbine and compressor powers.

Figure 5.17 shows the compressor and turbine adiabatic efficiencies, plotted against the turbocharger speed n_T. Fig. 5.17 also reports the global adiabatic turbine efficiency, including the overall expansion mechanical efficiency $\eta_{em} = \eta_e \eta_m$, Eq. (5.18).

$$\eta_{em} = \eta_e \eta_m = \frac{\dot{W}_c}{\dot{W}_{es}} = \frac{\dot{W}_c^{dia} - \dot{Q}_c}{\dot{m}\, c_{p,e} T_{3t}^{adi} [1 - \pi_e{}^{-(\gamma_e - 1)/\gamma_e}]} \tag{5.18}$$

The values of η_{em} are slightly lower than η_e as expected due to $\eta_m < 1$. Then, the mechanical efficiency can be estimated as $\eta_m = \frac{\eta_{em}}{\eta_e}$, as reported in the same plot. η_m reached a mean value close to 0.92 at high speeds and decreased for lower speeds down to 0.6. This behavior is reasonable according to the open literature, e.g., [107], among others. As expected, both the compressor and the turbine efficiencies were modest, as typical in small-scale turbochargers, but the low value of η_e seems easily improved as the harsh environment of the pulsed flow of piston engines is not present. Ball bearings would increase η_m. Transformation from journal bearings is always posible.

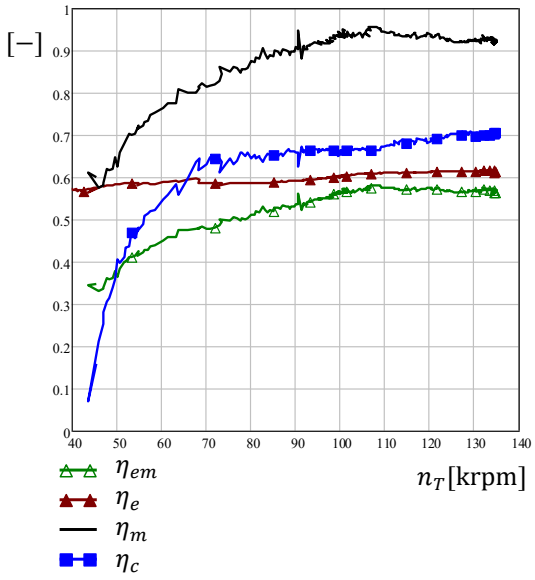

Fig. 5.17. Compressor, turbine, and mechanical efficiencies vs. rotating speed.

Figure 5.18 reports the operative compressor points on the corresponding map for the performed tests, respectively without post-heating (a) and with post-heating (b). In Fig. 5.18(a) it can be observed that the compressor worked below the minimum speed $n_{c,cor}^{min} = 110$ krpm and $\pi_c^{exp} < 1.4$. In Fig. 5.18(b) higher speeds were reached thanks to higher inlet turbine temperatures enabled by the experimental post-heating unit, allowing the compressor to work inside the top efficiency map core. In both cases, it can be noted that the compressor did not operate near the dorsal line, which corresponds to maximum efficiency for a given π_c. Instead, the working points appeared on the leftward region, at lower mass flow rates than on the dorsal line. This behavior, not beneficial for the turbocharger mechanical balance, could be induced by the auxiliary compressor characteristic, shown in the following section.

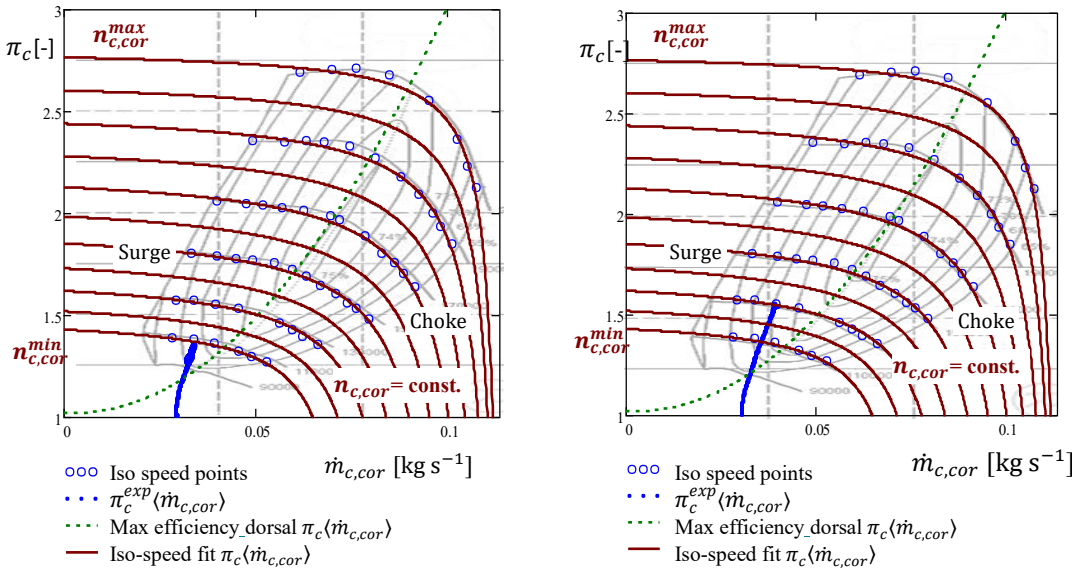

(a) (b)

Fig. 5.18. Compressor operative path on the performance map with experimental post-heating (a) OFF; (b) ON.

According to the compressor model presented in the previous section, the compressor pressure ratio can be calculated as $\pi_c^{cal} = \pi_c\langle\dot{m}_{c,cor}, n_{c,cor}\rangle$ using Eq. (4.53), and experimental inputs $\dot{m}_a, T_1$ and n_T. Fig. 5.19 shows π_c^{cal} for the performed tests against the experimental value $\pi_c^{exp} = \frac{p_{2t}}{p_{1t}}$. The comparison reveals the excellent accuracy of the model, being the maximum relative error width of +/-5%.

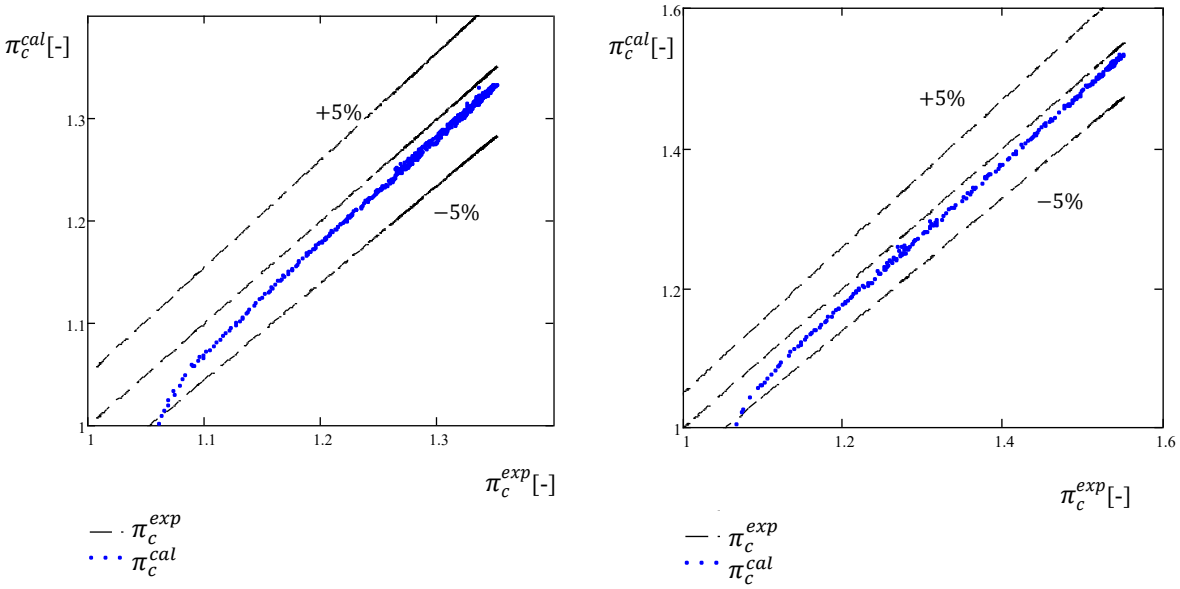

Fig. 5.19. Compressor ratio fitting results. Calculated pressure ratios vs. experimental ones. Experimental post-heating (a) OFF. (b) ON.

Figure 5.20 depicts the experimental corrected turbine mass flow rate $\dot{m}_{e,cor}^{exp}$ obtained from $\dot{m}_a$ and T_3^{adi}, plotted against pressure ratio $\pi_e^{exp} = p_{3t}/p_{4t}$. The calculated values using the model $\dot{m}_{e,cor}^{cal}\langle\pi_e^{exp}\rangle$ are also reported, showing good agreement with experimental results. Due to the higher inlet temperatures allowed by the experimental post-heating unit, higher π_e^{exp} are reached, Fig. 5.20(b).

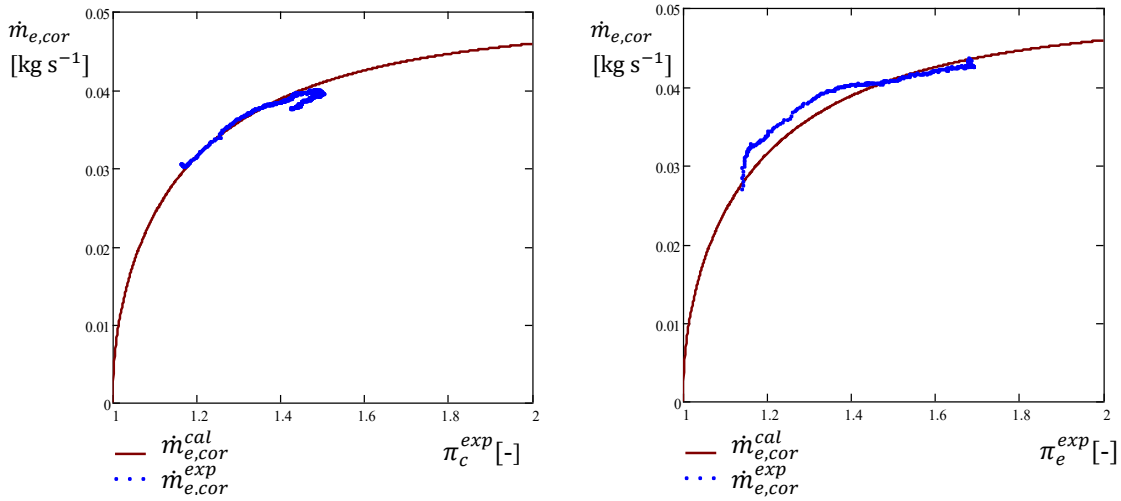

Fig. 5.20. Turbine single line mass flow rate line vs. experimental data. Experimental post-heating (a) OFF; (b) ON.

5.6 Auxiliary compressor

This section analyses the auxiliary compressor behavior. Two electrical driven low-pressure compressors (blowers), arranged in parallel, form the single auxiliary compressor unit, Fig. 5.1. A dedicated electrical inverter feeds them constantly with a maximum frequency $FQ = 80$ Hz, three-phase AC. They work with equal mass flow rates $\frac{\dot{m}_a}{2}$, globally providing a $\Delta p_{ac,t}\langle \dot{m}_a, FQ\rangle$, according to the manufacturer map of performances and feeding frequency, as Fig. 5.21(a) reports. As can be seen in Fig. 5.21(a), the pressure drops across the *ac* inlet and outlet piping are not negligible. This is due to the high velocity reached in the small section of the connection pipes and localized losses due to tees and elbows. They are estimated as Δp_{0t} at the auxiliary compressor inlet and Δp_{1t} at its outlet, respectively, according to Eq. (4.44).

Due to Δp_{0t} and Δp_{1t}, the pressure ratio produced by the blower π_{ac}^* results larger than the measured $\pi_{ac} = p_{1t}/p_{0t}$, Fig. 5.21(b).

$$\pi_{ac}^* = \frac{p_{1t} + \Delta p_{t1}}{p_{0t} - \Delta p_{0t}} = \frac{p_{0t} - \Delta p_{0t} + \Delta p_{ac,t}\langle \dot{m}, FQ\rangle}{p_{0t} - \Delta p_{0t}} \tag{5.19}$$

$\Delta p_{ac,t} = p_{1t} + \Delta p_{t1} - (p_{0t} - \Delta p_{0t})$ can be obtained from measured p_{1t} and p_{0t} and estimated Δp_{1t} and Δp_{0t}, as reported in Fig. 5.21(a), revealing the working point of the auxiliary compressor on the map. Parasitic pressure drops induced by inlet and outlet piping $\Delta p_{1t} + \Delta p_{0t}$ are in the same order of magnitude of the overpressure required to sustain the turbocharger

$p_{1t} - p_{0t}$. Moreover $\Delta p_{1t} + \Delta p_{0t}$ grows with mass flow rate up to half the overpressure imposed by the auxiliary compressors $\Delta p_{ac,t}$.

The efficiency map is not given by the manufacturer. A rough estimation can be performed on experimental data, now considering the real pressure ratio drops π^*_{ac}.

$$\eta^*_{ac} = \frac{\dot{W}^*_{acs}}{\dot{W}_{ac}} = \frac{\left(\pi^{*\,(\gamma_{ac}-1)/\gamma_{ac}}_{ac} - 1\right) T_{0t}\,\overline{c_{pac}}}{T_{1t}c_{p1} - T_{0t}c_{p0}} \tag{5.20}$$

Figure 5.21(b) depicts results from experimental data, an average value of $\eta^*_{ac} \cong 0.45$ was found, in accordance with similar side-channel blowers models.

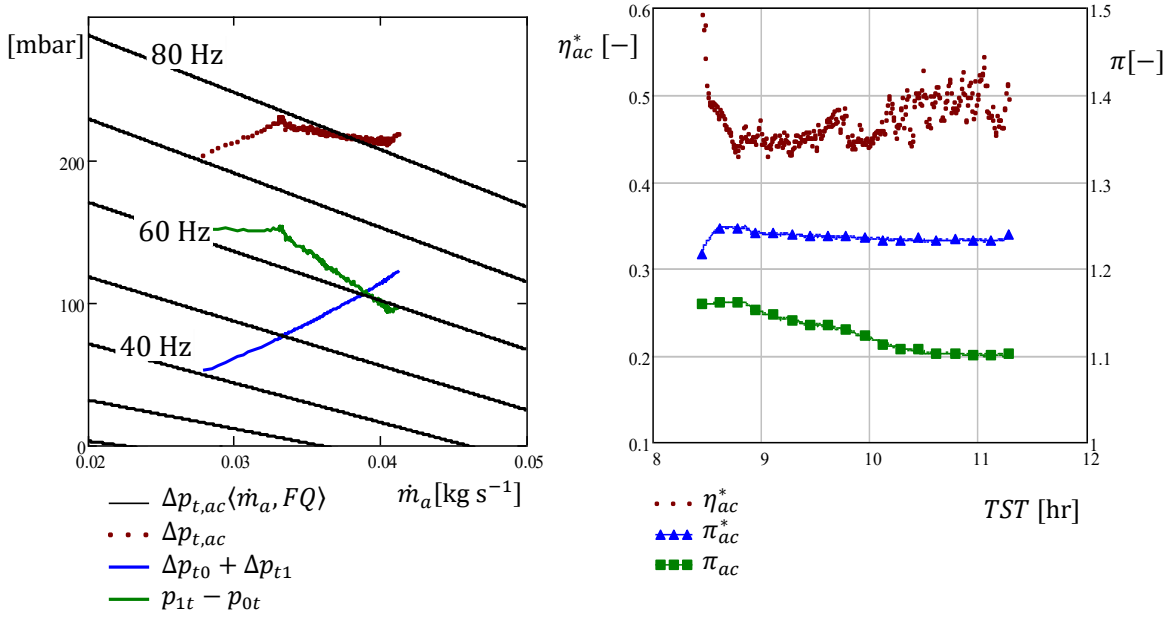

(a) (b)

Fig. 5.21. Auxiliary compressor. Map (a); pressure ratios and efficiency (b).

The auxiliary compressors offer the main effect of increasing p_{1t}, the inlet pressure at the turbocharger, providing the auxiliary mechanical power required by the turbocharger to keep freewheeling. As discussed in the following section, the aid of auxiliary compressor would be avoided using turbochargers with higher efficiency corresponding to higher size, both in the turbine and compressor side, minimizing thermal losses across them, better external matching, and increasing η_m with ball bearings.

In the present setup, the overpressure $p_{1t} - p_{0t}$ is needed to sustain the turbocharger freewheeling. Moreover, a decreasing value pressure p_1 is detected as shown in Fig.5.3(b), resulting in a decreasing π_{ac} in Fig.5.21(b). The corresponding isoentropic mechanical power required $\dot{W}_{acs}$ results from Eq. (5.21).

$$\dot{W}_{acs} = \dot{m}\left(\pi_{ac}^{(\gamma_{ac}-1)/\gamma_{ac}} - 1\right) T_{0t}\overline{c_{pac}} \tag{5.21}$$

As reported in Fig. 5.22 the isoentropic mechanical power $\dot{W}_{acs}$ decrease during the test, as long as the turbocharger accelerates toward the optimal working range according to higher inlet turbine temperature. Due to parasitic pressure drops in the inlet and outlet auxiliary compressor piping $\Delta p_{1t} + \Delta p_{0t}$, and the modest efficiency, the auxiliary compressor power consumption is higher $\dot{W}_{ac} > \dot{W}_{acs}$ as shown in Fig. 5.22. Moreover, $\dot{W}_{ac}$ shows a slightly growing trend, due to increasing parasitic pressure drops $\Delta p_{1t} + \Delta p_{0t}$ with mass flow rate. Observing specific powers, respectively $\dot{w}_{acs} = \frac{\dot{W}_{acs}}{\dot{m}}$ and $w_{ac} = \frac{\dot{W}_{ac}}{\dot{m}}$, it can be proven as both have a decreasing trend as a consequence of turbocharger acceleration. $\dot{w}_{acs}$ drops from 12 W g^{-1} at the beginning of the test with turbocharger at less than 50 krpm, down to 8 Wg^{-1} at its maximum speed of 140 krpm; a relative drop of 33%.

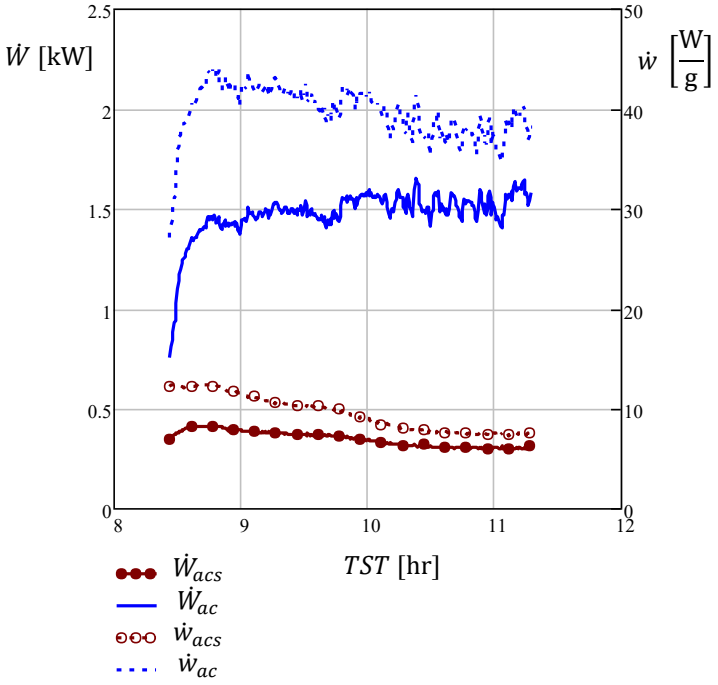

Fig. 5.22. Auxiliary compressor powers and specific powers (experimental post-heating ON).

Besides electrical power consumption, the drawback of using an auxiliary compressor is the increased temperature T_1, which reduces the turbocharger compressor performance. The non-negligible pressure drops and the low efficiency increase this adverse effect, since $\pi_{ac}^{*} > \pi_{ac}$ leads to a T_1 increase, as can be seen in Fig. 5.2(a) and 5.3(a), where it ranges between 60 °C and 80 °C.

As Fig. 5.23 reports, $\dot{W}_{ac}$ represents around 18% of thermal power delivered to the air, $\dot{Q}_a$, at the beginning of the test, decreasing down to 8%, although the $\dot{W}_{acs}$ is much lower in relative terms. Other main power contributions are shown in relative terms over $\dot{Q}_a$. The turbine power $\dot{W}_e$ is around 10 to 15% of $\dot{Q}_a$, while the overall thermal power that is taken from the heated airflow $\dot{W}_e^{dia}$ is twice, up to 30%. As discussed above, thermal losses from the turbine housing,

bearing housing, and through the lubrication oil to the ambient $\dot{Q}_{e\to amb}$ are relevant, up to 15% of $\dot{Q}_a$. Fig. 5.23 also reports a thermal efficiency parameter, estimated as $\frac{\eta_{th}=\dot{Q}_a}{\dot{Q}_u+\dot{Q}_{ph}+\dot{W}_{ac}}$. It does not take into account the thermal efficiency of the solar receiver tubes neither the optical efficiency of the solar collector but only accounts for the thermal losses across insulated piping and the turbocharger. It can be seen that η_{th} grows during the test, while the transient heating effect due to their thermal inertia disappears, reaching $\eta_{th} = 0.84$. $\dot{Q}_{e\to amb}$ is the main cause of thermal efficiency drop, whose reduction is of great importance for the optimal scaling up of the system T-SAH herewith proposed as optimal.

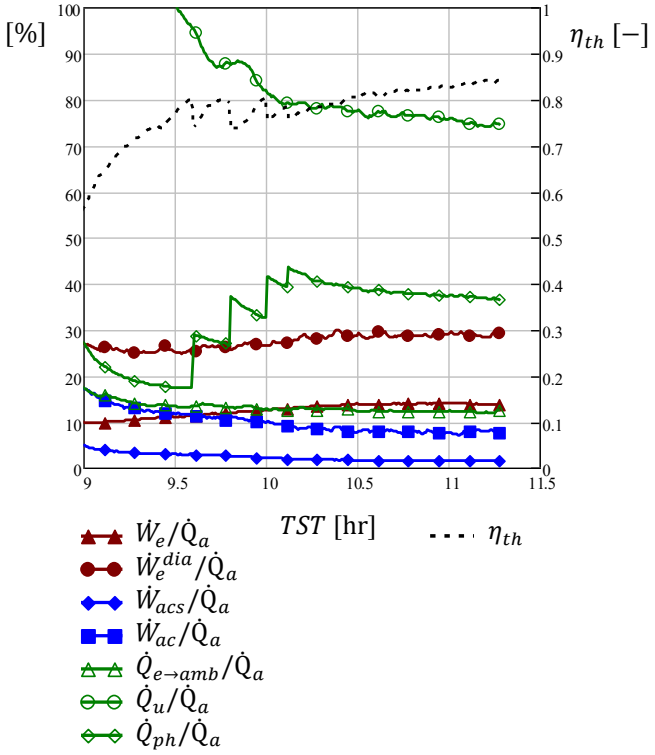

Fig. 5.23. Main mechanical and thermal power over the delivered thermal power $\dot{Q}_a$ and thermal efficiency vs. time (experimental post-heating ON).

5.7 Turbocharger freewheeling issues

Minimizing the energy consumed by the auxiliary compressor is one of the main goals for the T-SAH development, and if possible, to deliver some power. The correct T-SAH operating conditions would be achieved when the turbine provides at least enough power for driving the compressor, allowing turbocharger freewheeling without the auxiliary compressor aid, and eventually leaving surplus pressure for head losses down to the consumption point. The auxiliary compressor would be needed only for some transients, such as starting, incidental failures, or temporary drops of solar power.

Using the developed numerical model, it is possible to estimate under which conditions the auxiliary compressor aid can be avoided. The mechanical balance on the turbocharger shaft can

be expressed as in Eq. (5.22), using Eq. (4.39), (4.40), and (4.66). Eqs. (5.22) and (5.23) allow the calculation of the inlet turbine (adiabatic) temperature required for providing enough turbine power to drive the compressor.

$$\dot{m}c_{p,e}T_{3t}^{adi}\left[1-{\pi_e}^{-(\gamma_e-1)/\gamma_e}\right]\eta_e\eta_m-\dot{m}c_{p,c}T_{1t}\left({\pi_c}^{(\gamma_c-1)/\gamma_c}-1\right)\eta_c^{-1}=\dot{W}_{net}=0 \qquad (5.22)$$

$$T_{3t}^{adi}=\frac{T_{1t}}{\eta_e\eta_m\eta_c}\frac{c_{p,c}}{c_{p,e}}\frac{{\pi_c}^{(\gamma_c-1)/\gamma_c}-1}{1-{\pi_e}^{-(\gamma_e-1)/\gamma_e}} \qquad (5.23)$$

The turbine expansion ratio $\pi_e=p_{3t}/p_{amb}=(p_{2t}-\Delta p_t)/p_{amb}$ is affected by the stagnation pressure drop. Pressure drops Δp_t, as well as pressure ratios π_c,π_e and efficiencies η_c,η_e depend on the mass flow rate $\dot{m}_a$. For each considered turbocharger speed, the mass flow rate results from matching turbine and compressor maps, Eq. (4.53) and Eq. (4.60). T_{3t}^{adi} is the independent variable iteratively adjusted to obtain $\dot{W}_{net}=0$. Considering a diabatic turbocharger, the inlet temperature T_{3t} would be larger due to the cooling effect of turbine thermal losses $\dot{Q}_e$.

Considering the setup experienced, the turbine temperature required for freewheeling without the auxiliary compressor aid, at any turbocharger speed in the range of compressor map, was estimated according to Eq. (5.22). For this purpose, the turbocharger model developed and tuned above has been used. A value of mechanical efficiency $\eta_m=0.92$ was used. The main thermal losses of the diabatic turbocharger at the turbine inlet were taken into account. The stagnation pressure drops across the air circuit were estimated according to Eq. (4.44). Solar power gain across the solar collector was assumed $\dot{Q}_u=17$ kW heating the airflow up to T_{3rt}, whereas an adjustable post-heating power $\dot{Q}_{ph}=\dot{m}\left(T_{3t}c_{p3}-T_{3rt}c_{p3r}\right)$ heats the air up to $T_{3t.}$ Inlet diabatic turbine temperature is $T_{3t}=T_{3t}^{adi}+\frac{\dot{Q}_e}{\dot{m}c_{p,e}}$, where $\dot{Q}_e=\dot{Q}_{e\to amb}+\dot{Q}_{e\to c}=c_{ec1}(T_3-T_2)^{c_{ec2}}+(UA)_{eamb}(T_3-T_{amb})$.

Figure 5.24 shows the results. T_{3t}^{adi} varies remarkably with speed, as a consequence of several combined effects, Fig. 5.24(a). As a general trend, the equations show that T_{3t}^{adi} is mainly affected by the turbocharger overall efficiency $\eta_T=\eta_c\eta_e\eta_m$, which varies according to turbocharger speed. When the turbocharger works in the core of the compressor map $130\text{ krpm}<n_T<170\text{ krpm}$, η_c and hence η_T reach their maximum, $\eta_c\cong0.69$ and $\eta_T\cong0.39$, respectively, allowing lower inlet turbine temperatures, according to Eq. (5.23), as reported in Fig. 5.24(d). Besides, the stagnation pressure drop across the pressurized circuit Δp_t has an impact on T_{3t}^{adi}. As speed increases the operating mass flow rate increases, Fig. 5.24(b), according to the compressor and turbine flow maps. Higher mass flow rate leads to higher stagnation pressure drops Δp_t, reducing the turbine pressure ratio π_e. This effect is appreciable, although the increased compression ratio in Fig. 5.24. (b) mitigates the growth of Δp_t, by reducing air velocity inside the pressurized circuit. These combined effects give that the lowest inlet turbine (adiabatic) temperature of freewheeling would be $T_{3t}^{adi}=620$ °C, for $n_T=130$ krpm, with $\dot{m}_a=0.035\text{ kg s}^{-1}$, and $\pi_c=1.6$.

The diabatic inlet turbine temperature is above T_{3t}^{adi} due to heat losses $\dot{Q}_{e\to amb}$ and $\dot{Q}_{e\to c}$. Both of these losses are not negligible and increase with T_{3t}^{adi}, as in Fig. 5.24(c), being in the same

order of magnitude of $\dot{W}_e$. Fig.5.24 (a) gives the outlet receiver temperature resulting from the heating effect of $\dot{Q}_u$. The outlet turbine temperature goes up in the range of 550 to 600 °C.

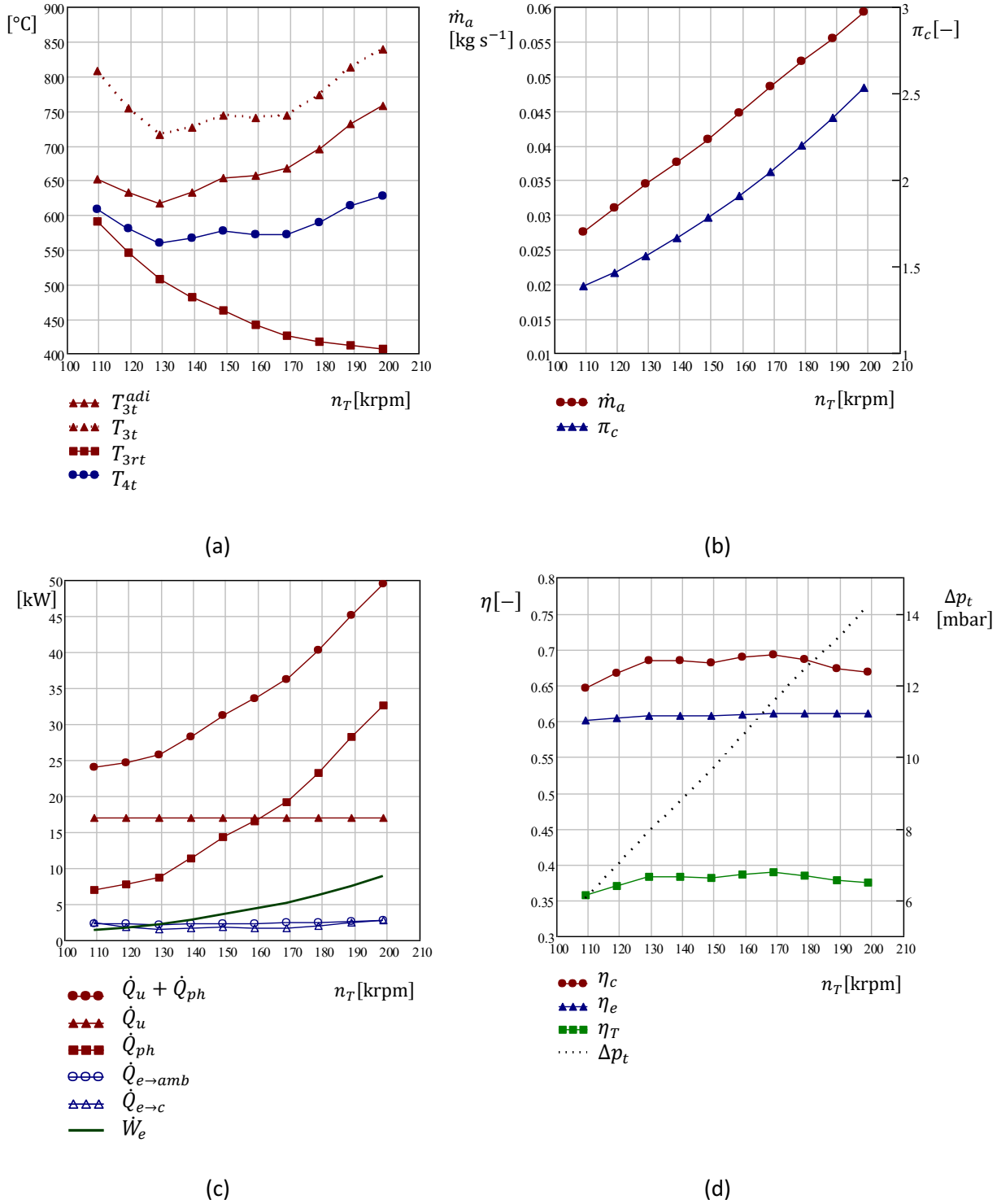

Fig. 5.24. Freewheeling conditions. (a) Temperatures. (b) Pressure ratios and mass flow rates. (c) Thermal powers and losses. (d) Efficiencies and total pressure drop.

As Fig. 5.24 clarifies, turbocharger freewheeling without the auxiliary compressor aid requires inlet adiabatic turbine temperature T_{3t}^{adi}> 600 °C which wasn't reached during the experiments carried out. Although turbocharger freewheeling is foreseen to be achieved with null auxiliary

energy consumption in a well-designed and/or large installation, reaching it in a small size installation, as the prototype here studied, is challenging, due to low turbocharger efficiency, especially notable the one of the turbine, which is lower than the one of the compressor, and it could be higher. Moreover, the diabatic behavior of the turbocharger, especially the thermal losses occurring from the turbine to ambient and the compressor, presumably driven by the low specific work of the present operating conditions, makes it difficult to achieve the required turbine power production.

Nevertheless, a decrease in the overpressure imposed by the auxiliary compressor can be noticed from the reported data, either in the case of the collector heating alone or in the case of the post-heating experimental operation. The progressive drop of the auxiliary compressor overpressure p_{1t} as well as the auxiliary isoentropic specific power $\dot{w}_{acs}$ needed for air pumping underpins what would occur in a more performing installation. After a starting transient, during which the auxiliary compressor is used for accelerating the turbocharger, the inlet compressor pressure would progressively decrease down to ambient pressure, as soon as the inlet turbine temperature reaches the freewheeling theoretical temperature, Eq. (5.23). At that point, the auxiliary compressor can be either kept working with negligible power consumption, ready for action, or either bypassed and switched off.

5.8 Advantages of scaling up

The analysis carried out on the experimental setup combining experimental and numerical results allows pointing out several considerations dealing with the foreseeable scaling up the turbo-assisted solar air heater concept T-SAH for an industrial application.

The turbocharger efficiency is of great importance for the viability of the system aiming at the elimination of auxiliary energy consumption for air pumping. The temperature required at the turbine inlet for enabling turbocharger freewheeling without auxiliary compressor aid is higher as lower is the turbocharger efficiency $\eta_T = \eta_c \eta_e \eta_m$, according to Eq. (48). Larger installation than the presented setup would offer a better match with larger size turbochargers which have higher efficiency, up to $\eta_T \cong 0.6$, according to datasheets of the models available on the market, for Reynolds number and relative roughness considerations in turbomachines scale-up, e.g. [69], [78] or [77]. Optimized variants for continuous flow rate or one-stage axial variants can reach adiabatic efficiencies as high as 0.8. In that case, turbocharger autonomous freewheeling could be achieved at a lower T_{3t}, with the obvious no need for a post-heating unit, according to the original layout of T-SAH. Using a large size and high-performing turbocharger, parallel collector rows can be considered for scale-up. Attention must be paid to collector length since this affects the pressure drop inside the pressurized circuit which plays against the turbocharger mechanical balance. Pressure losses should be kept to a minimum.

It is worth mentioning that the temperature drop across the expansion process is modest, 100 to 150 °C, allowing a temperature of delivery to the user in the range of 300 to 400 °C when the inlet turbine does not surpass 500 to 550 °C, which is achievable inside the receiver, considering current thermal limits.

The analysis of undesired heat losses to ambient suggests paying attention to a good turbine thermal insulation as well as to a proper lubrication system that minimizes the work dissipation, e.g. ball or air bearings.

Moreover, specific speed considerations call for a turbocharger trimmed or optimized for moderate π_c and π_e, typically lower than current values in automotive turbocharging from $\pi \cong 2 - 4$. The necessity of an auxiliary compressor and its deleterious effect suggest its avoidance and aims at an electrically boosted turbocharger, now emerging in the turbochargers industry.

5.9 Thermal Energy Storage

An experimental investigation on the installed TES has been carried out aiming at its first characterization. The TES unit, described in Chapter 3, is integrated into the existing T-SAH prototype as shown in Fig. 5.25. A switching valve allows bypassing the TES if required.

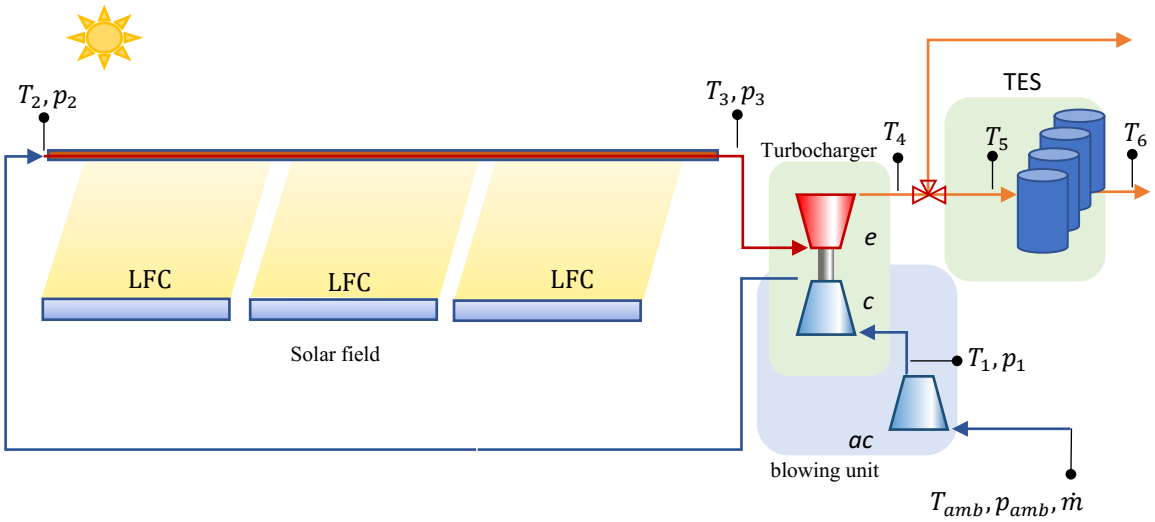

Fig. 5.25. Experimental setup scheme with TES, Linear Fresnel Collector LFC, auxiliary compressor ac, turbocompressor c, turbine e, thermal storage unit TES.

Each of the four cylinders is initially filled with 2.6 kg of commercial $LiNO_3$ in a granular state, initially occupying 100% of the internal volume of 2.18 L, thus with an average density of 1,190 kg/m^3. The weight of an empty finned cylinder is 8.9 kg. The density of solid salt at room temperature is higher, although in the literature the exact value diverges from one source to another, between 1,780 kg/m^3 [108] to 2,380/ kg/m^3 [109]. For that reason, a first melting and solidifying cycle has been carried out, before inspecting inside the cylinders, as reported in Fig. 5.26. It shows as the solidified salt fills around 60% of cylinder volume, having a density of 1,990 kg/m^3 at room temperature.

(a) (b)

Fig. 5.26. Finned cylinder inspection after first melting/solidifying cycle. (a) Partially filled volume, (b) empty height.

An additional amount of salt of 0.770 kg is filled in each cylinder, reaching a total amount of 3.37 kg of salt per cylinder and 13.48 kg for the whole TES. A melting and solidifying cycle has been repeated before checking again the status of the salt, reported in Fig. 5.27.

The filled volume with solid salt is now 77% of the total height. The air gap in the upper part of the cylinder allows the volume to increase from a solid to a liquid state. Considering a liquid density at $300\ °C$ of $1{,}753\ kg\ m^{-3}$, the salt volume at the liquid state is expected to reach 90% of the internal cylinder volume, avoiding the risk of leakage from the upper flange or its rupture. In Fig. 5.27(a) it can be noticed that during the solidification process the contracting salt can originate an empty region in the center of the material block similar to a hole. This is caused by the inner progression of the solidification front and the fall of the inner liquid fraction.

(a) (b)

Fig. 5.27. Finned cylinder inspection after the second melting/solidifying cycle with increased salt content. (a) Non-uniform salt block, (b) Empty height showing the thermocouple brackets.

Two representative tests were devised for qualitative characterization of the TES unit. The first one allows to obtain the charging and discharging curves and features. The second test reveals the effect of the TES unit on the delivery air temperature of the combined T-SAH and TES prototypes.

Charging and discharging test results are reported in Fig. 5.28. The TES is initially disconnected from the T-SAH. During more than one hour the T-SAH is run alone, with the solar field in tracking mode. When the exit turbine temperature T_4, higher than 300°C, is reached, then the TES unit is connected and the hot airflow starts to heat the finned cylinders. Air temperature at the TES inlet T_5 is reported in Fig.5.28 (a). Due to T-SAH features and sun availability, T_5 is not constant during the charging period, but varies between 300 °C and 350 °C. The temperature of the salt T_s measured at three points of the medium-height transversal cross-section according to Fig. 5.29(b) is reported in Fig. 5.28(a). A sensible solid heating period of 65-70 min with a rapid temperature rise proceeds the melting process, which lasts approximatively 70 min. Once the salt is completely molten the temperature starts to rise again during sensible liquid heating, going up to 280 °C. Air at TES outlet holds the temperature T_6, also reported in Fig.5.28 (a), which shows a smoother time profile than the salt temperature T_s.

Before running the discharging test, the solar field is defocused, and TES is disconnected from T-SAH for a short time. Meanwhile, the air flowing into the T-SAH cools progressively the components of the air circuit (pipes, receiver, turbocharger). When the air temperature at the turbine outlet T_4 drops below the salt temperature ($\sim$200 °C) the TES is connected again to the T-SAH, and the airflow starts to cool the cylinders. The solidification process lasts around 75 min, with inlet air temperature T_5 dropping from $\sim$200 °C to $\sim$80 °C. A sensible solid cooling time interval follows. As a consequence of the TES discharge, the outlet temperature T_6 has a slower drop with respect to T_5.

Air mass flow rate through the TES $\dot{m}_{TES}$ is shown in Fig. 5.28(b), together with thermal powers $\dot{Q}_{a5}$, $\dot{Q}_{a6}$, $\dot{Q}_{TES}$, Eqs. (5.24) to (5.26).

$$\dot{Q}_{a5} = \left(T_5 c_{p5} - T_{amb} c_{p,amb}\right)\dot{m}_{TES} \tag{5.24}$$

$$\dot{Q}_{a6} = \left(T_6 c_{p6} - T_{amb} c_{p,amb}\right)\dot{m}_{TES} \tag{5.25}$$

$$\dot{Q}_{TES} = \dot{Q}_{a6} - \dot{Q}_{a5} \tag{5.26}$$

The power exchanged between the airflow and the TES has a peak of 6 kW and ranges between 2 kW and 4 kW during latent heating and cooling, depending on the operating conditions.

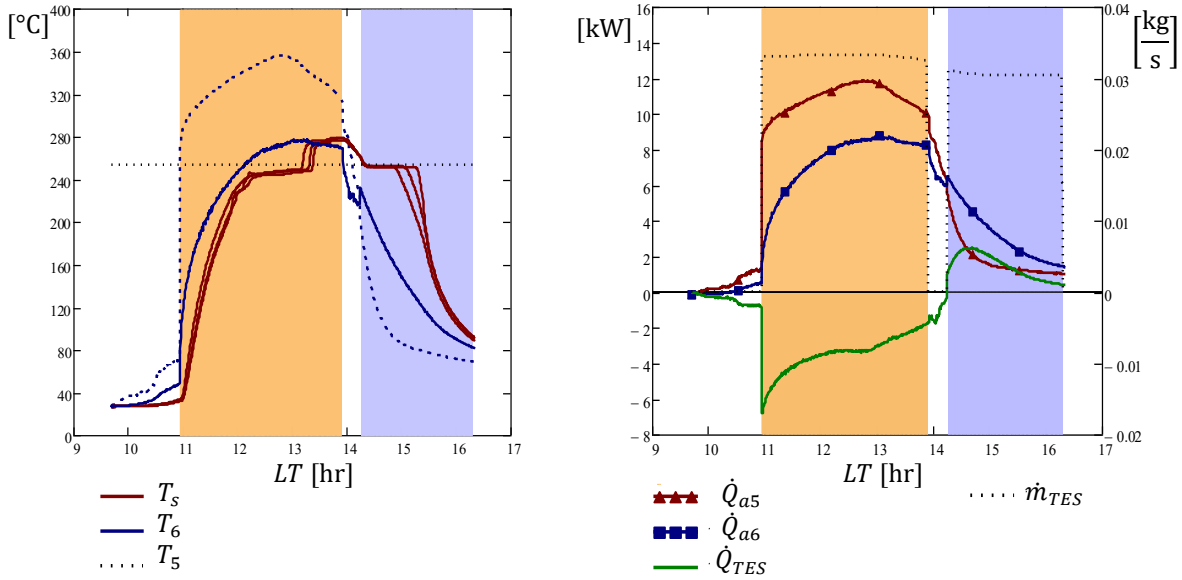

(a) (b)

Fig. 5.28. Charging and discharging test. (a) Main temperatures and melting temperature, (b) Thermal power and mass flow rate vs. Local Time LT.

Sensible and latent heat stored during the charging process can be estimated from thermophysical properties of the salt and its container. During sensible heating at solid-state from ambient temperature (30 °C) to salt melting temperature (254 °C), the overall amount of salt can store $Q_{salt}^{sol} = 1.25$ kW hr of heat, considering an average specific heat capacity of 0.414 W hr kg^{-1} K^{-1}, (1.49 kJ kg^{-1}K^{-1}). Considering the specific latent heat of 0.1 kW hr kg^{-1} (360 kJ kg^{-1}), the latent heat stored during complete melting results $Q_{salt}^{mel} = 1.348$ kW hr. The amount of heat stored in the salt during charging, up to complete melting is $Q_{salt} = Q_{salt}^{sol} + Q_{salt}^{melt} = 2.6$ kW hr.

The sensible heating of the finned tubes containing the salts is not negligible. The mass of the stainless-steel tube is 3.37 kg, in addition to the 5.7 kg of carbon steel fins. Considering an average specific heat of 0.5 kJ/kg K, the four finned tubes stores $Q_{cyl} = 1.108$ kW hr of heat when heated from ambient to salt melting temperature, corresponding to 30% of the amount of heat stored in the salt and finned tube container $Q_{TES,ch}^{cal} = Q_{salt} + Q_{cyl} = 3.7$ kW hr.

An experimental estimation of $Q_{TES,ch}^{exp}$ can be obtained by integrating over the charging time τ (excluding liquid heating) the $\dot{Q}_{TES}$ of Eq.5.26, reported in Fig.5.28(b).

$$Q_{TES,ch}^{exp} = \int_{\tau_0}^{\tau_m} \dot{Q}_{TES}\langle\tau\rangle \, d\tau \tag{5.27}$$

A value of $Q_{TES,ch}^{exp} = 9.14$ kW hr is found between the time of charging start τ_0 and the time of complete salt melting τ_m. The much higher value of $Q_{TES,ch}^{exp}$ than $Q_{TES,ch}^{cal}$ is due to heat exchange between airflow and the TES external case. Although the losses to ambient are minimized by the

mineral wool thermal insulation, either the square air channel walls or the insulation itself increase their temperature during the charging period, storing a non-negligible amount of heat.

Additional features of melting and solidifying processes can be observed in Fig. 5.29 (a). It reports, besides three internal salt temperatures $T_{s,up}, T_{s,c}, T_{s,do}$, the temperature of the salt layer adjacent to the wall $T_{w,up}, T_{w,do}$ as in Fig. 5.29(b).

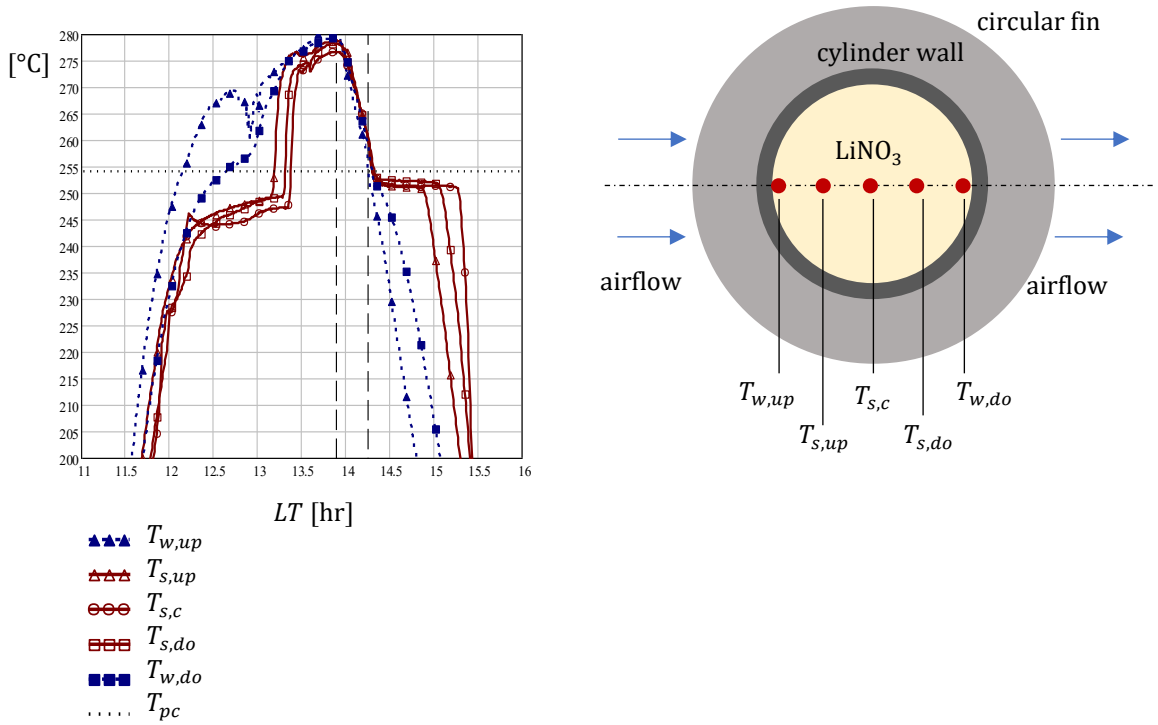

(a) (b)

Fig. 5.29. The salt temperature during melting and solidification. (a) Temperatures vs Local Time LT, (b) sensors position.

As expected, the salt temperature adjacent to the upstream wall $T_{w,up}$ reaches the melting point at first, followed by the salt temperature at the opposite site $T_{w,do}$. The salt starts to melt from the external layer adjacent to the hot wall of the cylinder, while the core of the salt block is still a few degrees below the melting point. The limited thermal conductivity of the solid salt $k_{salt}^{sol} = 1.348\ \mathrm{W\ K^{-1}\ m^{-1}}$ controls the heat transfer to the salt core and the melting front speed from the outer surface to the inner core.

The core temperatures $T_{s,up}, T_{s,c}, T_{s,do}$ grow smoothly during the melting process, below the theoretical melting temperature $T_{pc} = 254$ °C. The center temperature $T_{s,c}$ is the lowest and the last which start to raise again for liquid sensible heating. A similar trend is observed during the solidifying process. The wall temperatures $T_{w,up}$ and $T_{w,do}$ drops as first. Then, internal temperatures keep steady around 252 - 253 °C. They are much closer between them than in the melting case, depicting a more homogeneous process. This can be an effect of the higher liquid salt thermal conductivity with respect to solid, $k_{salt}^{liq} = 2.96\ \mathrm{W\ K^{-1}\ m^{-1}}$. Moreover, solidification progresses from the outer surface to the inner core. The subcooling phenomenon,

a typical effect that delays the solidification of some phase change materials, is not observed in our case.

The second test performed considers the joint behavior of T-SAH and the TES. The TES is connected permanently in series with the T-SAH as in Fig.5.25. From the time when the solar field begins to track the sun, either the T-SAH and the TES undergo a heating transient, which brings up the air temperature at the TES inlet (turbine outlet) T_5 as in Fig. 5.30(a). The outlet TES temperature T_6 grows slower and below T_5. After sensible heating of about 2 hr, the salt starts melting. Liquid sensible heating takes place as the final step of the charging process, up to 290 °C of salt temperature. Then, the solar field is defocused to simulate a short sun power interruption, as during the appearance of clouds.

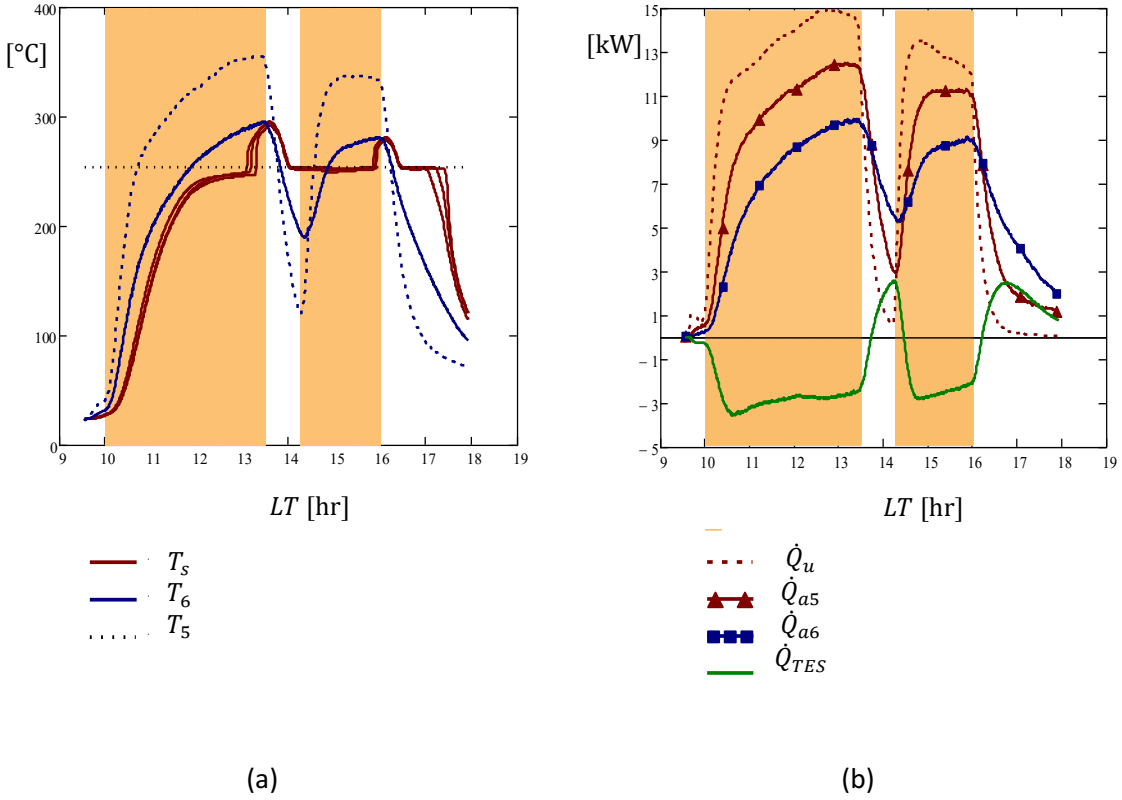

(a) (b)

Fig. 5.30. Effect of TES on delivery hot airflow. (a) Temperature. (b) Thermal power vs Local Time LT.

Due to the thermal inertia of T-SAH components (pipes, receiver tubes, turbocharger) the temperature drops at the TES inlet T_5 is not instantaneous and the airflow keeps heating the TES for a few minutes. Then it starts to discharge the TES, which begins to solidify. Its effect on the outlet temperature T_6 can be noticed, which remain above 180 °C during a sun power shortage of 45 min, while T_5 drops down to 120 °C.

Subsequently, the sun tracking is restored. The salt keeps solidifying for a few minutes before it starts to melt again, then heated as a liquid. The last part of the experiment is again a full TES discharge. Globally, the effect of the TES charging and discharging thermal capacity is smoothing the variation of outlet air temperature T_6 with respect to T_5, which would be the delivery in the

absence of TES. Fig.5.30 (b) reports the exchanged power $\dot{Q}_{TES}$ as well as the solar power gain across the solar field $\dot{Q}_u$ and the power $\dot{Q}_{a5}$ and $\dot{Q}_{a6}$.

The results obtained during the first experimental tests carried out on the TES unit indicate the viability Lithium Nitrate as phase change material for the range of temperatures typical of T-SAH. The shall-and-tube configuration selected for the heat exchanger design, seems a suitable solution, aiming at compactness, simplicity and low-cost, by using commercial finned tubes and air conducts. The experiments indicate that more than one row of vertical tubes would be needed for increasing the storage capacity and the beneficial effect of TES on T-SAH outputs.

An extensive thermal analysis would be convenient for characterizing the heat transfer phenomena taking place, through the development of a comprehensive numerical model. The experimental data provided would represent a useful information for the numerical model tuning and validation.

6 FEASIBILITY STUDY OF INDUSTRIAL T-SAH

The following study focuses on scaling up the concept of T-SAH to a medium-scale solar facility for hot air production in a generic industry. The large variety of industrial processes requiring hot air in the low-to-medium temperature range $T < 400$ °C have been reviewed in Chapter 1. Although the thermal energy needs of an industrial facility can be huge, the space available for solar field installation is limited in most cases. This fact, together with the relevant investment cost of a solar heating facility, orients the feasibility study of T-SAH toward installations having less than 1,000m^2 of solar field surface, here referred to as "medium-size plant". Moreover, this approach suggests that an industrial T-SAH can integrate the existing air heating facility rather than replacing it completely. This means that at any time of the year, the T-SAH delivers all the provided thermal energy to the industrial process according to solar availability without any heat storage excepting its thermal inertia. This seems the current practice aiming at a decrease in carbon emissions and increasing the use of local renewable energies. The solar heat delivery modulation with the industrial thermal load is not an issue at this stage, assuming that the existing facility provides the remaining thermal power required to fit the industrial load profile, or the overall thermal power required during the night or cloudy time. In addition, the T-SAH design is oriented to modularity, hence pointing at the possibility of progressive replacement of conventional heating power. Finally, the medium-scale option meets two main technical requirements: the proper size of the turbocharger and the collector row length limitation imposed by stagnation pressure drops, as will be clarified in the following paragraphs.

On the other hand, a very small-scale T-SAH facility would not be technically convenient. As highlighted in the previous experimental analysis of Chapter 5, the turbocharger with a very small size yields low performances in terms of compressor and turbine efficiencies, which difficult to achieve efficient operating conditions that eliminate the pumping power and even produces some mechanical work. Moreover, for a very small size solar field, according to the analysis of Chapter 2, the direct air heating can be performed using concentrating collectors without the use of the turbocharger, in simpler SAH configuration, Fig. 2.1, being the pumping power relatively low, affordable using an electrically driven blower only. SAH feasibility depends on the concentration ratio but is limited to a small range of sizes since the pumping power grows rapidly with collector row length. According to Fig. 2.4, heating air directly (without the turbocharger) up to 350 °C using an LFCs solar field with 5 m of lateral aperture, concentrating a direct normal solar irradiance of 1,000 W m^{-2} with an optical efficiency of $\sim$ 0.5 on the external perimeter of a standard vacuum receiver tube of 0.07 m diameter, thus with a concentration ratio of 22.7 and a resultant heat flux $\sim$ 12 kW m^{-2}, requires an isoentropic pumping power in the order of $\sim$10% of net solar power gain for a collector length of 30 m, growing to $\sim$ 20% for a collector length of 40 m. This amounts to more than $\sim$ 50% for a length of 50 m, for what the T-SAH configuration is now required.

In the following section, numerical models developed in the previous Chapters are used and adjusted to the case, as they already incorporate the technical features of commercial LFCs and turbochargers. In addition, the Typical Meteorological Year TMY of the studied location is required to model the solar irradiance, as well as ambient temperature and pressure.

First, a procedure for setting the solar field size and configuration is implemented, enabling a correct and optimized match with the turbocharger. Once the main design parameters of T-SAH

are defined, the evaluation of its time performances under variable solar resources on a daily and yearly basis is carried out. The methodology developed for the feasibility study is first carried out on a 633.6 m^2 solar field and later it is applied to several cases of slightly different sizes and configurations.

6.1 Solar field

The Turbo-assisted Solar Air Heater T-SAH admits a variety of configurations, combining several LFC modules in series and parallel layouts, connected to a single turbocharger to reach the required temperature and mass flow rate. At least two approaches are possible:

a) implementing a number n_p of U-loops, each incorporating a series of n_s LFC modules of length L_m and aperture W_a, forming two parallel collector rows of equal length $L_{row} = \frac{L_m n_s}{2}$, as in Fig. 6.1(a).

b) implementing n_p straight rows of $L_{row} = n_s L_m$, using a common sending pipe, as in Fig. 6.1(b).

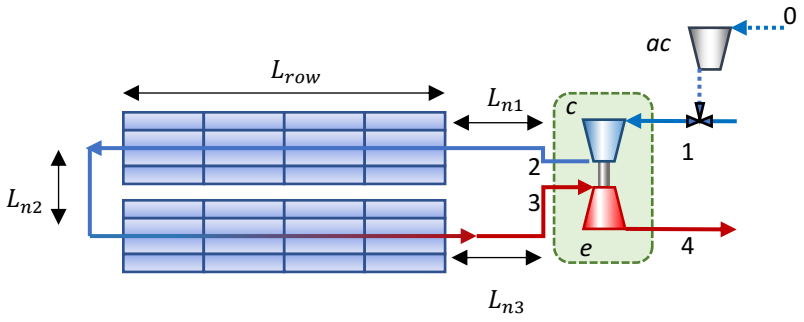

(a)

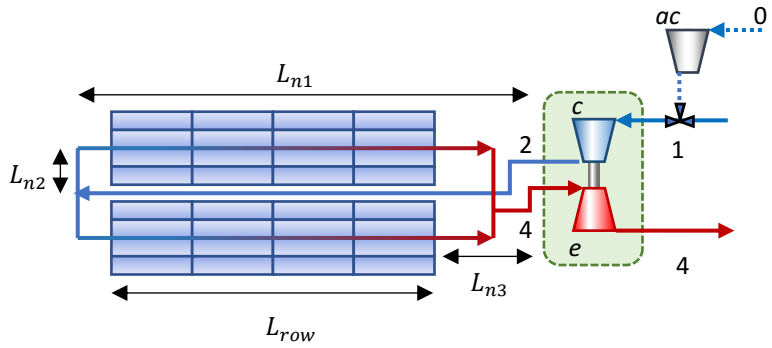

(b)

Fig. 6.1. Turbo-assisted solar air heater T–SAH layout with LFC. a) U-loop scheme with $n_s = 8$ and $n_p = 1$. b) straight row scheme with $n_s = 4$ and $n_p = 2$.

For case a) thermally isolated piping elements connect the two rows to the turbocharger unit and between them, with length L_{n1}, L_{n2} and L_{n3}. The flow leaving the compressor, point (2),

enters the U-loop to be heated before entering the turbine (3). n_p U-loops are connected in parallel to the turbocharger unit, reaching an overall solar field area of $A_{tot} = L_m W_a n_s n_p$. The mass flow rate $\dot{m}_a$ flowing through the turbocharger is equally split into n_p flows.

For case b) a common sending pipe, of diameter D_{n1} and length L_{n1}, thermally insulated, host the overall airflow $\dot{m}_a$, then equally splits into n_p flows; through L_{n2}, the receiver L_{row} and L_{n3} exhausting to the turbine inlet.

6.2 Linear Fresnel collector

The LFC model detailed in Chapter 4, is used for the present analysis, incorporating the feature of the specific collector manufactured by Solatom™ (geometry, efficiency, and $IAMs$). The experimental optical efficiency drop with respect to the modelled one, observed in the experimental analysis of Chapter 5 where is accounted by an additional correction term $\eta_{cor} < 1$, Eq. (5.6), has not be considered in the following feasibility analysis. In fact, most of the causes determining a $\eta_{cor} < 1$ in the prototype, as manufacturing imperfections, mirror axes deformation due to aging and tracking errors among others, are supposed to be mitigated or negligible in a commercial stage collector. The estimation of $\dot{q}_s$ can be obtained through Eq. (6.1).

$$\dot{q}_s = G_{bn} IAM_T\langle\theta_T\rangle IAM_L\langle\theta_L\rangle \eta_{op0} \frac{W_a}{P_{ex}} \tag{6.1}$$

Some simplifications are introduced concerning the model of Chapter 4: a) the solar field is not interrupted by the spacing between consecutive collectors; b) the receiver length coincides with the collector row length below it, hence no extension at the row extremities are considered. This allows simplifying the spatial axial distribution of $\dot{q}_s$ concerning the case of the prototype. The row length $L_{row} = L_{irr} + L_{no,irr}$ is separated into two portions, one L_{irr} being irradiated by $\dot{q}_s$, and the other $L_{no,irr}$ not irradiated, having $\dot{q}_s = 0$, due to end losses effect, according to θ_L and the mean receiver height $\overline{H}_m$, Eq. (6.2) and Eq. (6.3).

For non-null longitudinal incidence angles, the concentrated solar irradiance lost over $L_{no,irr}$ impacts away from the tube end. Being another angle-dependent optical loss, some authors include end losses into IAM, [58]. Here it is evaluated separately, accounted by a factor f_{end}, Eq. (6.4) which is useful for estimating the end loss impact on the LFC performances, which is especially critical for relatively short rows, common in small and medium scale installations, [110].

$$L_{no,irr} = \overline{H}_m \tan|\theta_L| \tag{6.2}$$

$$\overline{H}_m = \sqrt{\left(\frac{W_a}{4}\right)^2 + H_m^2} \tag{6.3}$$

$$f_{end} = \frac{L_{row} - L_{no,irr}}{L_{row}} = 1 - \frac{\overline{H}_m \tan|\theta_L|}{L_{row}} \tag{6.4}$$

It is worth mentioning that longitudinal incidence angle θ_i Eq. (4.4) is used instead of the longitudinal component θ_L, as recommended by [110], hence $\theta_L = \theta_i$ is assumed to keep the conventional nomenclature.

Depending on the orientation of the rows, N-S, E-W, or arbitrary, end losses may differ. Here, N-S orientation is adopted, although a latitude North shift in the receiver tubes has not been explicitly adopted, neither a length mismatch between solar receiver tubes length with row length, although both are possible solutions for reducing the optical end losses.

6.3 Receiver and air pipes

The static model of the receiver tube developed in Chapter 4 is suitable for the feasibility study performed here since quasi-steady-state conditions are assumed. Due to considerable temperature variation expected along with the receiver, the row length illuminated L_{irr} is discretized into n_e elements, thus reducing the error associated with constant U_L, h_a and fluid properties assumption. Eqs. (4.17) to (4.21) are applied on consecutive elements using $L = \frac{L_{irr}}{n_e}$.

A few discretization elements $n_e = n_s \frac{}{2}$ are considered enough for the simulation so that $L \leq L_m$. Non-irradiated receiver tail $L_{no,irr}$ has null $\dot{q}_s$ but still heat losses to ambient. The methodology indicated by Eqs. (4.17) to (4.21) is then applied to $L_{no,irr}$ considering $\dot{q}_s = 0$. Due to the modest temperature variation expected across the non-irradiated length, it is not discretized.

Insulated supply piping thermal losses are considered according to Eq. (4.35) and (4.36). Pressure drops across any portion of the air circuit are computed according to Eq. (4.44).

Tab. 6.1 summarizes the main LFC and receiver parameters used for the study. Tab. 6.2 Reports further solar field parameters.

Table 6.1. LFC and receiver

Module length	L_m	5.28 m
Aperture width	W_a	5.00 m
Height above mirrors	H_m	2.72 m
Module active area	A_m	26.40 m^2
Peak optical efficiency	η_{op0}	0.632
Number of mirrors per module	n_m	10
Mirror aperture	w_a	0.50 m
Inner receiver diameter	D	0.066 m
Outer receiver diameter	D_{ex}	0.07 m

Table 6.2. Solar field parameters

Layout		U-loop	Straight row
Row length	L_{row}	$\frac{L_m n_s}{2}$	$L_m n_s$
Connection pipe length	L_{n1}	$W_a \frac{3}{2} + H_m$	$H_m + L_{row}$
	L_{n2}	W_a	$\frac{(n_p - 1)W_a}{2}$
	L_{n3}	$\frac{W_a}{2} + H_m$	$H_m + \frac{(n_p - 1)W_a}{2}$
Connection pipe diameter	D_{n1}	0.1 m	0.25 m
	D_{n2}	0.1 m	0.1 m
	D_{n3}	0.1 m	0.1 m
Total Active area	A_{tot}	$A_m n_s n_p$	$A_m n_s n_p$
Orientation N-S	γ_r	0°	0°

6.4 Turbocharger

The methodology implemented in Chapter 4 for modeling the turbocharger based on commercial compressor and turbine maps is applied here to the selected turbochargers. Diabatic behavior of the turbochargers is not considered in the feasibility study as a first approximation. In fact, the main diabatic effect detected in the experimental analysis, the thermal losses at turbine entrance $\dot{Q}_{e\to a}$, is assumed to be minimized thanks to three main reasons: a) the turbine is thermally well insulated; b) the turbochargers used are equipped with ball bearings instead of journal bearings as in the prototype, hence requiring a minimum amount of lubricating oil, which was recognized as an important cause of thermal losses; c) the bigger size and good match of the turbocharger make the thermal losses lower in relatives terms over the overall external surface and turbine power.

It is worth mentioning that in the case of a larger installation, two or more turbochargers can be used in parallel. This has the advantage of closing one of them in case of a low mass flow rate. Thus, no upper limit is foreseen for the total capacity of the T-SAH technology.

Here, aiming at simplicity, a fixed geometry turbocharger has been chosen. Variable Nozzle turbine VNT would increase efficiency a low mass flow rates “off-design” conditions, at the expense of a slight decrease of the maximum values obtained, as a consequence of the larger wetted internal surfaces.

For the present analysis, the Garrett™ turbocharger model GT5533R is chosen. It is a ball bearings turbocharger. It is one of the larger-size models on the market for automotive applications. According to the methodology developed in Chapter 4, the performances of the GT5533R are reported in Fig. 6.2 for the compressor and Fig. 6.3 for the turbine. It is worth

mentioning that this turbocharger is available either with turbine $\frac{A}{R} = 1.00$, Fig.6.3(a) or with turbine $\frac{A}{R} = 1.24$, Fig. 6.3(b).

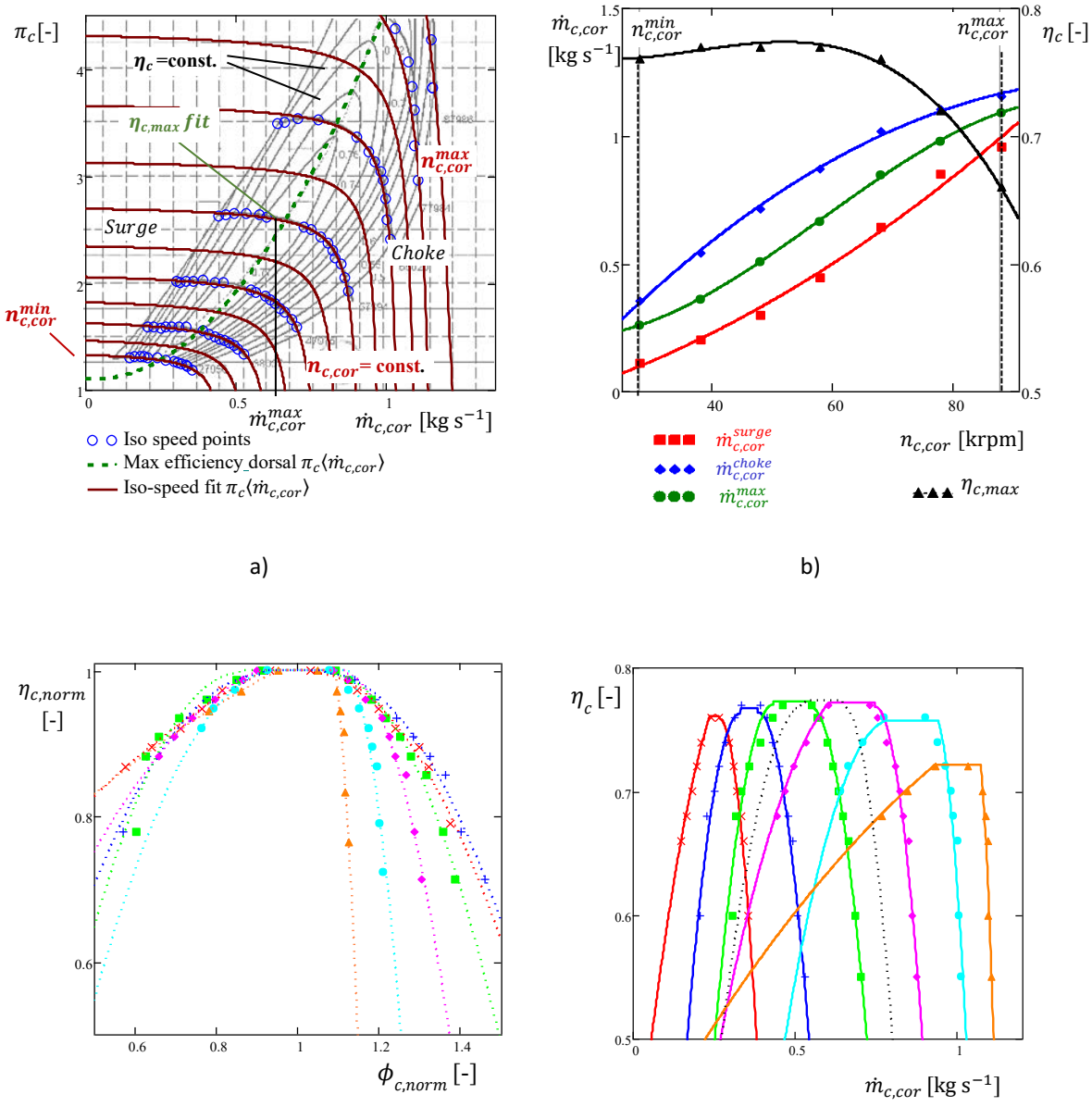

Fig. 6.2. Compressor model results superimposed to data dots. a) Compressor map with superposed $\pi_c\langle\dot{m}_{c,cor}\rangle$ for $n_{c,cor}$ = const. (blue circle dots and brown line) and dorsal line $\pi_c\langle\dot{m}_{c,cor}\rangle$ for $\eta_{c,max}$ (green dash), b) Choke and surge limits, dorsal-speed lines $\eta_{c,max}\langle n_{c,cor}\rangle$ and $\dot{m}_{c,max}\langle n_{c,cor}\rangle$. c) normalized iso- speed efficiency curves. d) iso-speed efficiency $\eta_c\langle\dot{m}_{c,cor}\rangle$. $T_{c,ref}$ = 302.6 K; $p_{c,ref}$ = 0.962 bar; D_c = 133 mm.

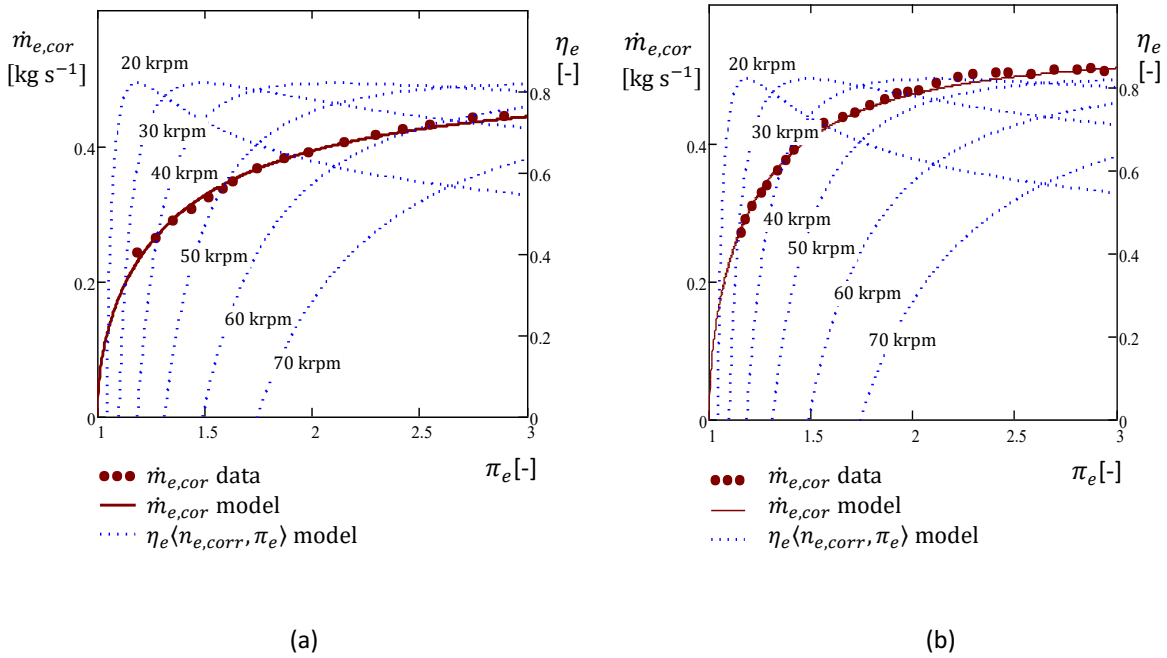

Fig. 6.3. Turbine data with model superimposed and efficiency map estimation for the fixed geometry turbine. $T_{e,ref} = 288.8$ K; $p_{e,ref} = 1.013$ bar; $D_e = 111.5$ mm; $\eta_{e,max} = 0.82$. (a) A/R=1.00; (b) A/R=1.24.

6.5 Typical Meteorological Year

To evaluate the availability of a T-SAH plant under off-design performances, realistic ambient and solar inputs are needed. According to common practice in solar engineering, [111], a typical meteorological year TMY is used to model G_{bn}, T_{amb}, p_{amb} for the specific location selected. A TMY is built from solar and ambient data measured during several years at a specified location and merged into a single year. The data are reported with a time interval of one hour. Sun azimuth and elevation, γ_s, α_s, for the corresponding hour of the year are computed using the relations in Chapter 4.

6.6 Turbocharger-solar field matching procedure

According to the proposed concept, a few physical constraints define the domain of working conditions for the T-SAH: I) turbocharger working range, II) the thermal limit of the solar receiver tube and III) the turbocharger freewheeling operation. They are explained as follows.

I) The mass flow rate $\dot{m}_a = \dot{m}_c = \dot{m}_e$ and rotating speed n_T must be within the turbocharger working limits. The allowed range in n_T is defined by its minimum and maximum $n_{c,cor}$ values, indicated by the compressor map. A range for $\dot{m}_a$ is defined for any speed n_T by the compressor surge and choke limits, indicated on the map.

$$n_{c,cor}^{min} < n_{c,cor} < n_{c,cor}^{max} \tag{6.5}$$

$$\dot{m}_{c,cor}^{surge}\langle n_{c,cor}\rangle < \dot{m}_{c,cor}\langle n_{c,cor}\rangle < \dot{m}_{c,cor}^{choke}\langle n_{c,cor}\rangle \tag{6.6}$$

II) The receiver thermal limit, Eq. (6.7), imposes the second constraint. The highest wall temperature takes place at the U-loop outlet (3) in Fig. 6.1, T_{w3}, which must be lower than $T_{w,max}$. T_{w3} is affected by $\dot{q}_s$ and U-loop outlet air temperature T_3, as well as by $\dot{m}_a$, which determines h_a. Eq. (4.21) can be rewritten and iteratively solved to compute T_{w3} as in Eq. (6.7), where $U_L\langle T_w - T_{amb}\rangle$ is a temperature-dependent variable.

$$T_{w3} = \frac{\dot{q}_s D_{ex} + T_3 D h_a + T_{amb} D_{ex} U_L}{D h_a + D_{ex} U_L} \leq T_{w,max} \tag{6.7}$$

III) When Eq. (6.8) of the turbocharger mechanical balance is verified, the turbine fully drives the compressor and the turbocharger is freewheeling at constant rotational speed, enabling the T-SAH to deliver hot air without any external auxiliary pumping power consumption.

$$\dot{W}_e \eta_m - \dot{W}_c = \dot{W}_{net} = 0 \tag{6.8}$$

According to these three constraints, a suitable turbocharger can be selected considering the solar field parameters and the expected solar and ambient inputs for the specific location, or conversely, for a given turbocharger the right solar field configuration can be set. In practice, a few iterations can be required to obtain a good matching between a turbocharger and the solar field for a given location.

To carry out easily the matching procedure, for a given turbocharger and solar field, the simultaneous fulfillment of constraints I, II, and III can be predicted by building a matching map. With this aim, the broad range of working conditions corresponding to variable solar and ambient inputs, $G_{bn}, \gamma_s, \alpha_s, T_{amb}, p_{amb}$, is approximated considering a concentrated solar irradiance $\dot{q}_s$ variation in the range $0 < \dot{q}_s < \dot{q}_{s,peak}$ and assuming $f_{end} = 1$, setting an average constant T_{amb} and p_{amb} for simplicity. $\dot{q}_{s,peak}$ is the maximum concentrated irradiance expected during the typical year for the selected location. The T-SAH model described above is then solved for several compressor corrected speed values $n_{c,cor}$ within the range of expected concentrated solar irradiance $0 < \dot{q}_s < \dot{q}_{s,peak}$. A matching map is obtained reporting the theoretical turbocharger excess power $\dot{W}_{net}$, for the T-SAH operating at a constant speed $n_{c,cor}$, fulfilling conditions I and II. The range of $\dot{q}_s$ for which the $\dot{W}_{net}\langle n_{c,cor}\rangle$ curves cross $\dot{W}_{net} = 0$, gives the range of possible freewheeling (condition III). This is clarified in the following paragraph.

6.7 Industrial T-SAH: example I

As a result of the matching procedure applied to a large-size turbocharger GT5533R (turbine $\frac{A}{R} = 1.00$) and medium-scale solar field, one possible configuration is obtained following the U-loop scheme. It is set according to Fig. 6.4(a) and the parameters of Tab. 6.1 and Tab. 6.2. $n_p = 4$ U-loops with $n_s = 6$ LFC are implemented, reaching an overall capturing surface of $A_{tot} = 633.6\ \mathrm{m}^2$. U-loop full length reaches 52.2 m, including two rows of L_{row}=15.8 m and piping. The row orientation chosen is North-South. Fig. 6.4(a) shows the T-SAH layout and a 3D view of the solar field is reported in Fig. 6.4(b).

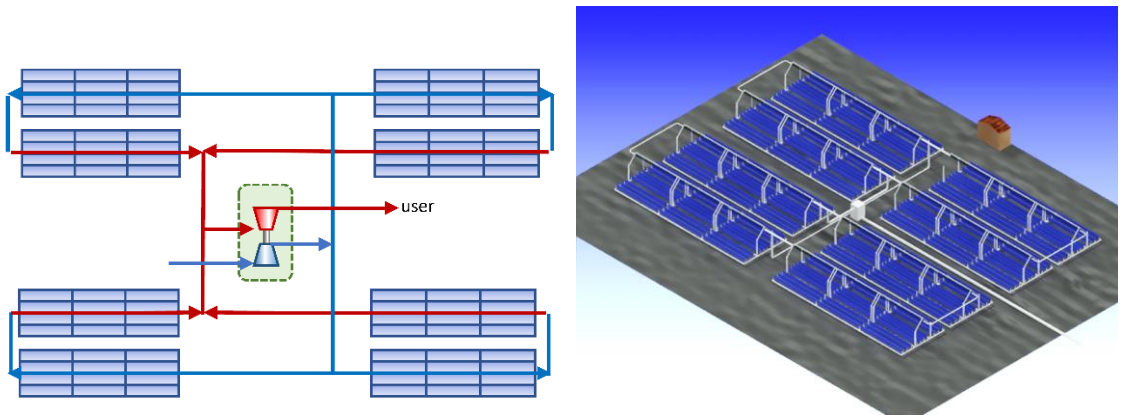

(a) (b)

Fig. 6.4. Industrial T-SAH layout (a) and 3D view (b), $n_p = 4$ U-loops with $n_s = 6$ LFC, $A_{tot} = 633.6\ m^2$.

Fig. 6.5 reports the matching map obtained with that settings. Results are reported in relative terms. $\dot{W}_{net}$ is reported as a percentage of solar power $\dot{Q}_s = \dot{q}_s P_{ex} L_m n_s n_p$ against a load factor $LF = \frac{\dot{q}_s}{\dot{q}_{s,peak}}$. For the selected location of Madrid, Spain (40° 24' 59'' N, 3° 42' 9'' W), whose TMY is obtained from [112], according to the collector efficiency and N-S orientation, the maximum heat flux expected during the year is $\dot{q}_{s,peak} = 13.5\ \mathrm{kW\ m^{-2}}$.

In a broad range of LF, $\dot{W}_{net}$ can be null choosing a proper turbocharger speed for a given $\dot{q}_s$. This indicates that steady-state freewheeling can be obtained across a large portion of the expected concentrated irradiance range, around 70%, excluding very low irradiances. An approximated minimum threshold for the load factor is identified LF_{th}, defining the low power working limit for the T-SAH to operate correctly. At low irradiances $LF < LF_{th}$, to reach a high enough inlet temperature at the turbine which can then provide the required power, the T-SAH would require a mass flow rate lower than the minimum value allowed by turbocharger constraint I. The turbocharger allows reducing the mass flow rate by decreasing the speed or shifting its working point toward surge, respectively limited by the minimum speed $n_{c,cor}^{min}$ and the surge limit $\dot{m}_{c,cor}^{surge}$, Fig. 6.3(a-b). In addition, at low speed, the turbocharger efficiencies are lower, impeding to achieve freewheeling. For these reasons, when $LF < LF_{th}$, the T-SAH should be shut down or bypassed. Alternative solutions can be studied to ensure hot air production at marginal load. A simple solution proposed here is to use the system in SAH configuration, Fig. 2.1, for low irradiance $LF < LF_{th}$, and T-SAH configuration for $LF > LF_{th}$, as explained below.

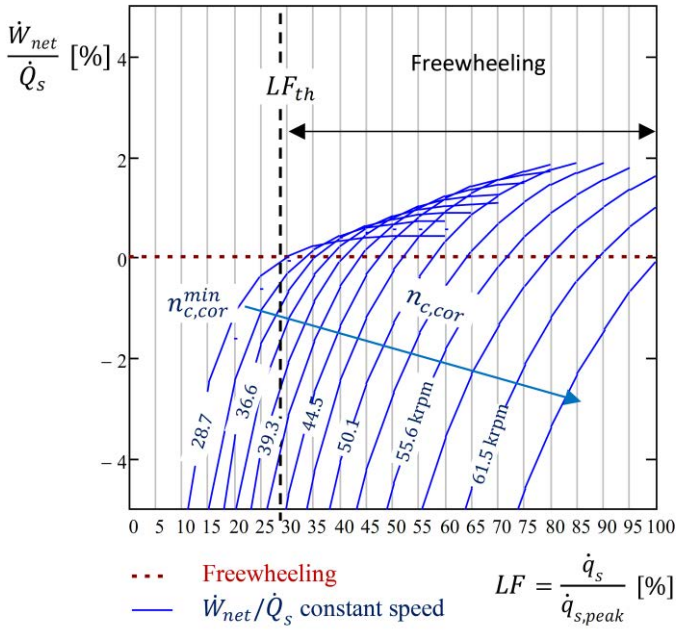

Fig. 6.5. Matching map. $\frac{\dot{W}_{net}}{\dot{Q}_s}$ vs. *LF* for operating points fulfilling conditions I and II, in Madrid (Spain).

In the following paragraph, the above-described T-SAH model is run with the setting of Tab. 6.1 and the layout of Fig. 6.4, thus using four parallel U-loops with six LFC in series, connected to turbocharger GT3355R ($\frac{A}{R} = 1.00$). The main T-SAH operating parameters are evaluated at any hour of the TMY.

First performances and operating conditions are reported and discussed for representative summer, spring, and winter days. Then, the global results over the whole TMY are shown considering the system operating only when the turbocharger freewheeling is achieved, according to the physical constraints detailed above. Finally the integration with SAH mode for low irradiance condition with $LF < LF_{th}$ is considered to increase annual operating hours and thermal energy yield.

6.7.1 Representative days

Fig. 6.6 reports the instantaneous results of a representative summer clear day, as a function of the true solar time TST. The direct normal irradiance G_{bn}, together with IAMs and end losses factor f_{end} are shown in Fig. 6.6(a). Despite the relatively short collector length, $f_{end} > 0.9$ is obtained, according to θ_L. Fig. 6.6(b) shows the daily variation of thermal power available, lost, and delivered to the user. The hot air delivered at the turbine outlet, holding $T_a = T_{4t}$, corresponds to an outlet power $\dot{Q}_a$, Eq. (6.8). The solar power $\dot{Q}_{bn}$ available on a surface normal to sunrays equivalent to the overall capturing surface $A_{tot} = A_m n_s n_p$ is evaluated as a reference, Eq. (6.9). The solar power concentrated on the receiver focal line $\dot{Q}_s$ varies according to G_{bn}, optical efficiency and $IAMs$, Eq. (6.10). $\dot{Q}_s$ is not entirely available for the receiver since a portion $\dot{Q}_{fend} = \dot{Q}_s - \dot{Q}_r$ is lost due to optical end losses, which is relatively low, corresponding to less than 10% of the delivered thermal power $\dot{Q}_a$. $\dot{Q}_r$ represents the solar

power that effectively reaches the receiver tube, Eq. (6.11). Due to thermal losses to the ambient from the receiver surface, as well as from insulated piping, part of the power $\dot{Q}_r$ is lost. Thermal losses $\dot{Q}_L = \dot{Q}_r - \dot{Q}_a$ corresponds to around 30% of the delivered thermal power $\dot{Q}_a$.

$$\dot{Q}_a = (T_a c_{p,a} - T_{amb} c_{p,amb}) \dot{m}_a \tag{6.8}$$

$$\dot{Q}_{bn} = G_{bn} A_m n_s n_p \tag{6.9}$$

$$\dot{Q}_s = G_{bn} \eta_{op0} IAM_T IAM_L A_m n_s n_p \tag{6.10}$$

$$\dot{Q}_r = G_{bn} \eta_{op0} IAM_T IAM_L f_{end} A_m n_s n_p \tag{6.11}$$

The operating conditions of the turbocharger and its effect on the airflow and solar receiver tube can be analyzed considering Fig. 6.6(c) - (d). Fig. 6.6(c) depicts the air temperature in the main points of the circuit, according to Fig. 6.1. At the compressor outlet, T_2 varies between 100 °C and 150 °C because of π_c, according to Eq. (4.42). T_3 reaches a peak of 500 °C at midday, whereas the temperature difference $\Delta T = T_3 - T_2$ across the solar field is quite steady around 350 °C, since the mass flow rate $\dot{m}_a$, also reported in Fig. 9(c), increases in concert to the solar power. The increase in Δp_{tn_i} induced by the higher $\dot{m}_a$ when at power peak is moderate thanks to the higher π_c, which leads to higher air densities and lower airflow velocities. Besides, the moderate increase fo Δp_{tn_i} is more than compensated by the higher turbine inlet temperature, resulting in a turbine power increase. This beneficial effect of self-regulation comes from the turbocharger performance map and the good matching of the turbocharger chosen with the solar field. Although the working conditions vary remarkably with solar power, the delivered air temperature $T_a = T_{4t}$ shows a flat time profile, varying between 350 °C and 380 °C. This is an outstanding, and ab-initio, non-expected good result.

Concerning the receiver thermal limit, the maximum wall temperature reached by the receiver tube is $T_{w3} < T_{w,max} = 600$ °C, confirming that the constraint II) formulated above is respected, Fig. 6.6(c). The turbocharger performance can be deduced from the main parameter plotted in Fig. 6.6(d). It works at high compressor and turbine efficiencies $\eta_c \approx 0.78$ and $\eta_e \approx 0.80$ almost constantly during the operating hours, while π_c, as well as π_e, varies according to the mass flow rate and irradiance. The corrected compressor speed $n_{c,cor}$ varies within the allowed limits, from 40% to 70% of its maximum $n_{c,cor}^{max}$.

The simulation demonstrated that the T-SAH operates almost during all daylight time, confirming the excellent turbocharger matching with the solar field performance and the feasibility of the proposed layout on a summer clear day. Only in the early morning and late afternoon hours, turbocharger freewheeling is not achievable and the T-SAH stops (OFF), as of being the $LF < LF_{th}$, Fig. 6.6(b), confirming the prediction from the matching map. The T-SAH operates for 10 hours, over the 14 hours of daylight when $G_{bn} > 0$. Fig. 6.6 highlights the hours of freewheeling operation.

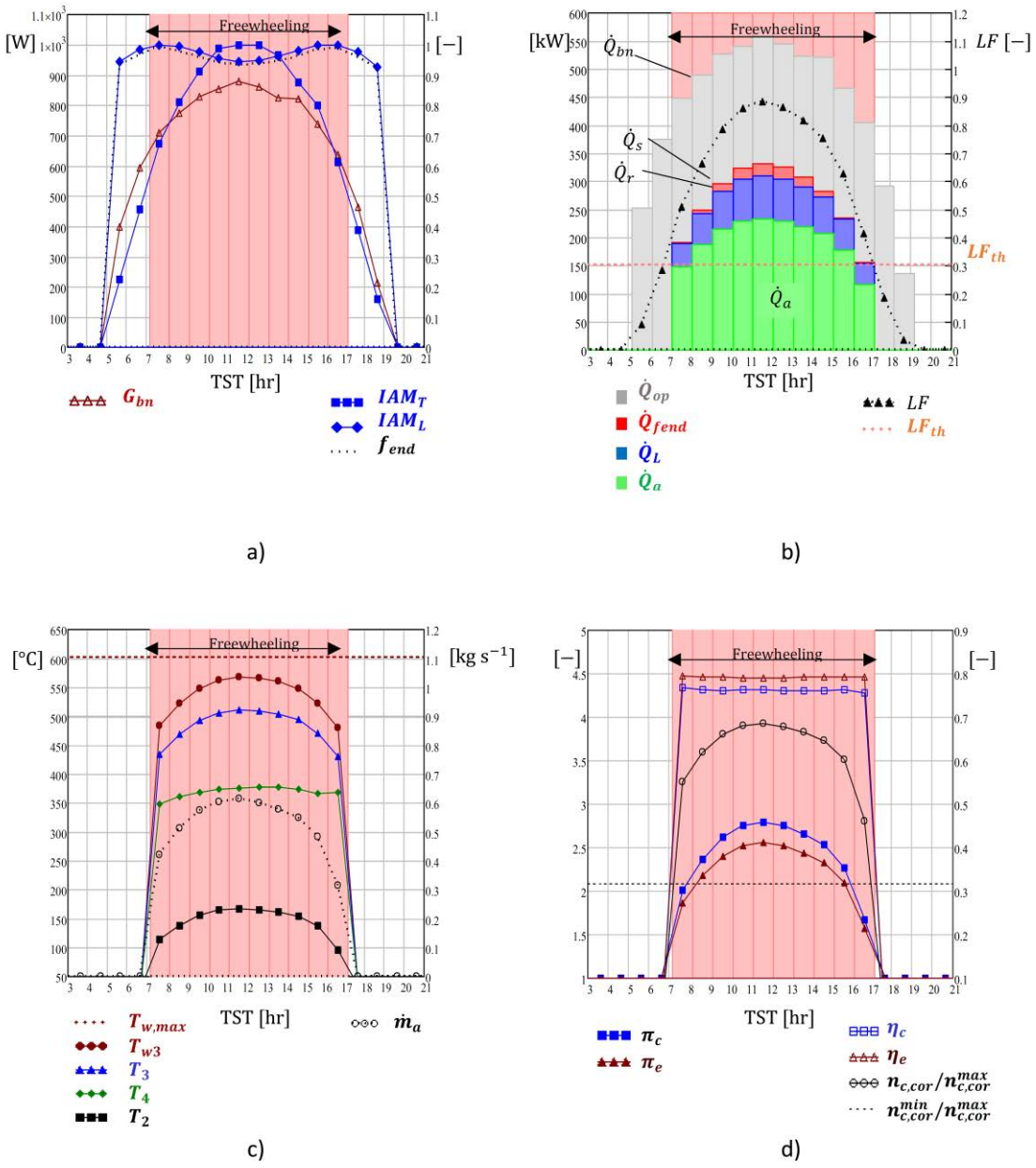

Fig. 6.6. T-SAH performances vs. true solar time TST during a clear summer day, Madrid (Spain).

The simulation was repeated on a representative spring day with a clear sky from the TMY. Performances during a typical day with a clear sky in March are representative of the intermediate seasons, Fig. 6.7. The lower sun elevation results in lower optical efficiency, being the incident angle modifier lower than in the summer case. End losses are also more significant. The load factor, Fig. 6.7(b) is lower than LF_{th} either in the morning and afternoon. Operative hours are reduced with respect to the summer case, but the system can produce hot air in the central hours of the day. On the other hand, the output air temperature remains higher than 300 °C, fulfilling the scope of medium-temperature heat production, Fig. 6.7(c).

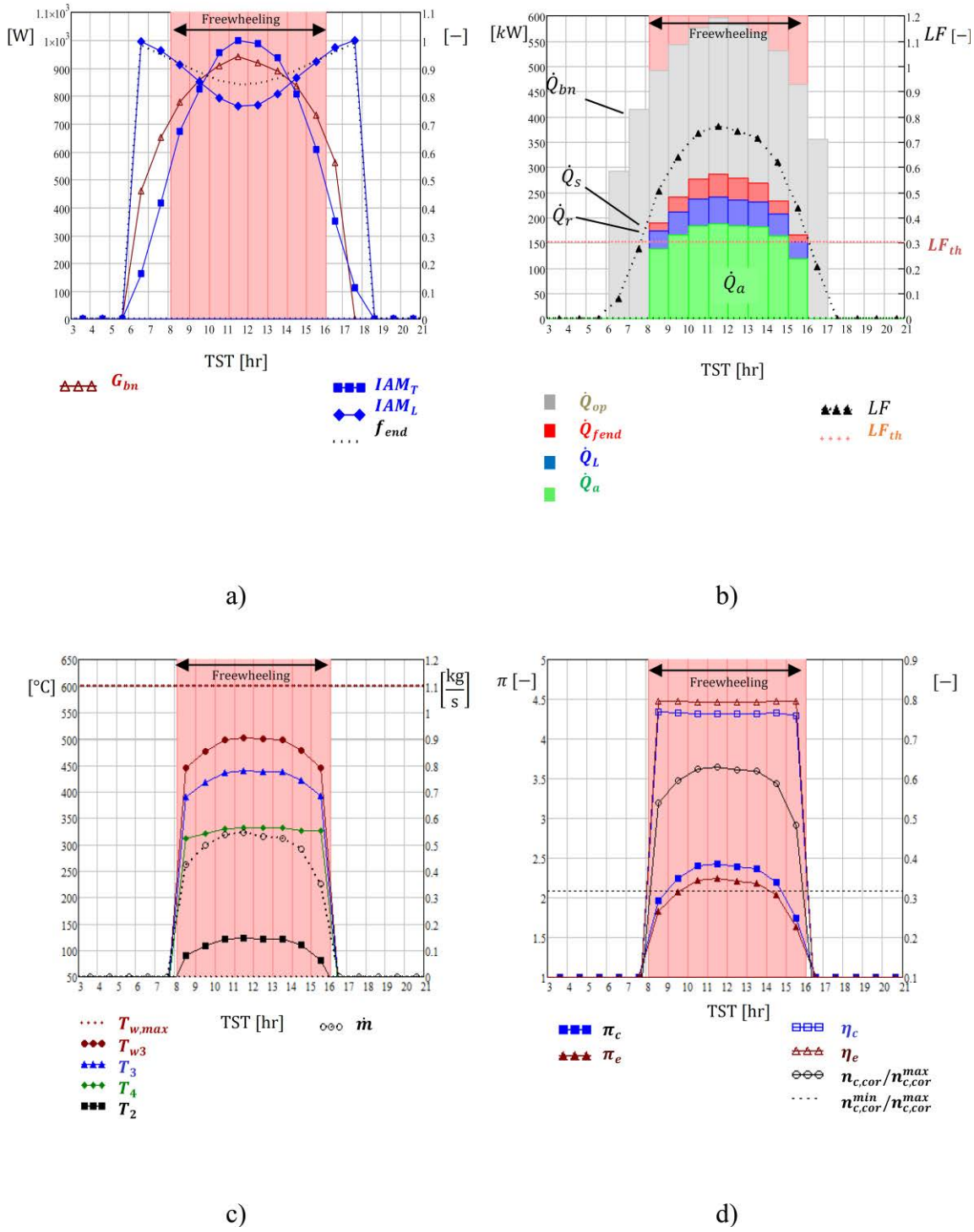

Fig. 6.7. T-SAH performances vs. true solar time TST during a clear spring day, Madrid (Spain).

Fig. 6.8 shows the main results obtained on a representative winter day. When comparing them with the results from the summer day-case discussed above, the optical collector efficiency is lower on the winter day due to a lower IAM_L because of the higher θ_L. This has also a remarkable impact on f_{end}, which dropped to 0.6 at midday. Optical end losses are relatively higher than is summer day-case, being around 30% of the delivered power $\dot{Q}_a$. Higher optical losses translate into an also lower concentrated solar power $\dot{Q}_s$ and $\dot{Q}_r$. In contrast, the thermal losses are reduced from summer to winter, as can be seen in Fig. 6.7(b), due to the lower mean

wall temperature reached. On the winter day, the thermal power delivered to the user drops below $100\ \mathrm{kW}$. The operating hours are reduced according to the shorter winter daylight, whereas the low irradiance cut-off $LF_{th} \cong 0.3$ is still valid. Fig. 6.8(c) - (d) confirms that the turbocharger is operating with a lower mass flow rate in winter than in summer, as well as with a lower π_c. Nevertheless, the self-regulation of the turbocharger allows delivering hot air at a fairly steady temperature around $330\ °\mathrm{C}$.

It is worth mentioning that an axial displacement of the receiver tube toward North beyond the latitude angle will reduce the end losses in winter more than in summer, smoothing the difference in production from winter to summer. A receiver tube larger than the mirror length is another issue worth investigating.

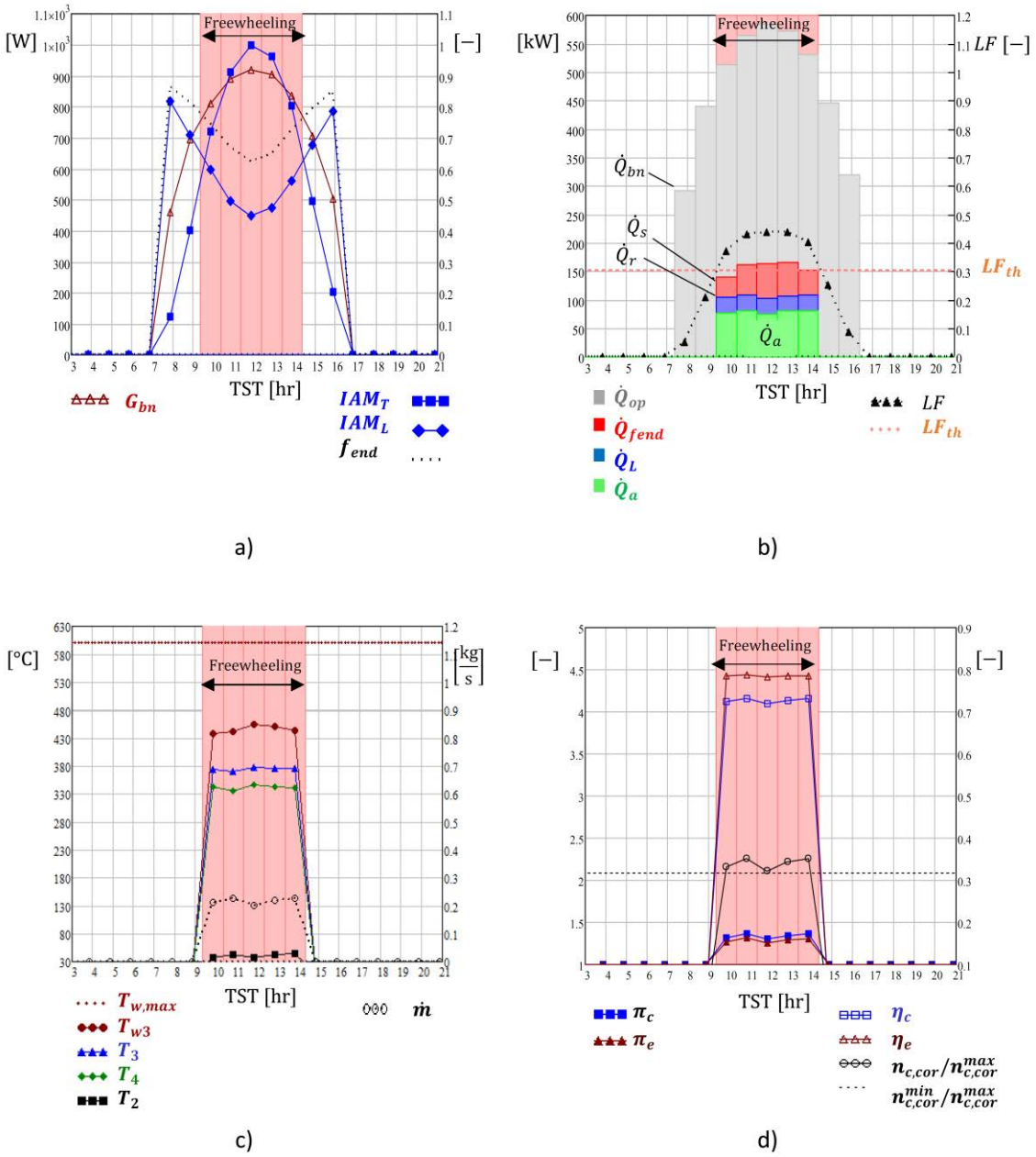

Fig. 6.8. T-SAH performances vs. true solar time TST during a clear winter day, Madrid (Spain).

6.7.2 Typical year

Extending the simulation all over the TMY allows a complete availability profile, whose results Fig. 6.9 depicts. As mentioned, turbocharger freewheeling can be achieved across a large portion of the concentrated solar irradiance range expected during the year, excluding low solar irradiance conditions. This issue is evident in Fig. 6.9(a) that displays the load factor $LF = \dot{q}_s \dot{q}_{s,peak}^{-1}$ for each hour of the year across a TMY and the corresponding state of the T-SAH, either freewheeling (ON), or shut down (OFF) if freewheeling is not achievable. The approximate threshold $LF_{th} \cong 0.3$, predicted using the matching map as a low power cut-off, seems confirmed across the whole year. Its effect on monthly working hours varies remarkably, as is evident in Fig. 6.9(b), where monthly ON and OFF daylight hours are reported. The operative hours (ON) over the total monthly daylight hours drop in the winter season due to lower irradiance. During the OFF hours the solar power available at the receiver $\dot{Q}_r$, Eq. (6.11), is relatively low, and therefore the energy not exploited by the T-SAH $Q_{r,OFF}$ in the whole TMY is around 14% of the overall amount of energy available $Q_{r,TOT} = Q_{r,ON} + Q_{r,OFF}$. Fig. 6.9(c) reports $Q_{r,ON}$ and $Q_{r,OFF}$ on a monthly basis. The T-SAH could operate for 2,060 hr per year, corresponding to 52 % of daylight yearly hours and 72 % of yearly hours with appreciable irradiance, thus, higher than 10% of $\dot{q}_{s,peak}$.

Fig. 6.9(d) reports the T-SAH performances in terms of monthly energy contributions. Thermal energy delivered to the airflow sums the hourly energy contributions from the first to the last i hour of the month where T-SAH is ON, $Q_a = \sum \dot{Q}_{a_i}\,\mathrm{hr}$. Thermal losses $Q_L = \sum \dot{Q}_{L_i}\,\mathrm{hr}$, as well as optical end losses $Q_{fend} = \sum \dot{Q}_{fend_i}\,\mathrm{hr}$ were evaluated. Normal direct (beam) solar energy available is computed considering the operating hours of T-SAH, $Q_{bn} = \sum \dot{Q}_{bn_i}\,\mathrm{hr}$. Both concentrated energy on the focal line, $Q_s = \sum \dot{Q}_{s_i}\,\mathrm{hr}$, and on the receiver $Q_r = Q_s - Q_{fend}$ are indicated, as well as optical losses $Q_{op} = Q_{bn} - Q_s$. Along the year, the T-SAH delivered $330\ \mathrm{MW\,hr}$ of thermal energy.

Fig. 6.9(e) depicts a more detailed screening of the T-SAH output, in terms of $\dot{m}_a$ against the corresponding air delivery temperature $T_a = T_4$. As expected, the delivery temperature varies in the range of $300\ °\mathrm{C} < T_a < 400\ °\mathrm{C}$ according to the aim of the technology proposed. The mass flow rate varies in a range of $0.2\ \mathrm{kg\,s^{-1}} < \dot{m}_a < 0.7\ \mathrm{kg\,s^{-1}}$.

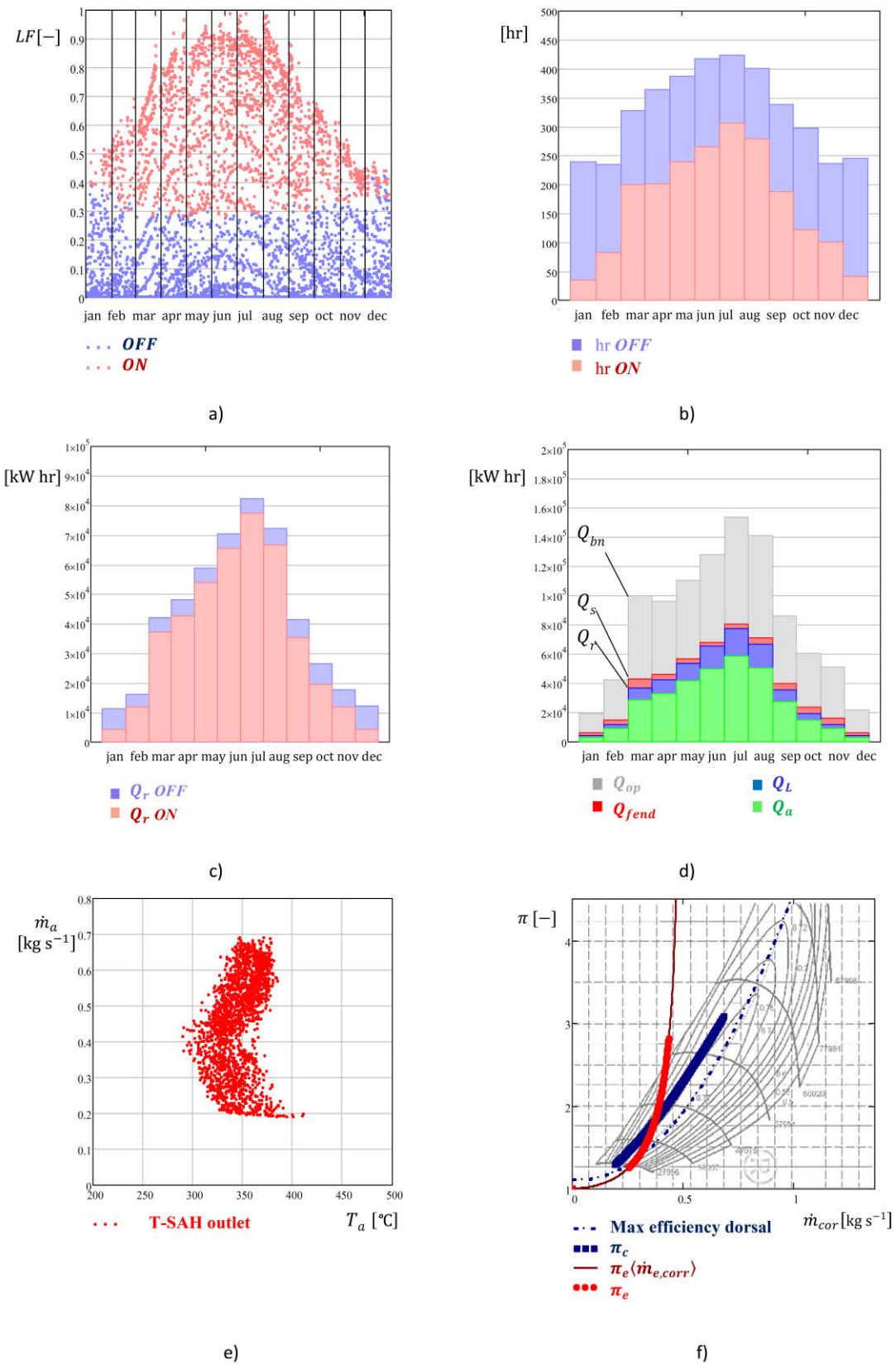

Fig. 6.9. T-SAH simulation results all over the year. a) concentrating solar irradiance range. b) operating hours per month. c) Energy delivered and not delivered per month. d) Energy contributions. e) T-SAH output. f) turbocharger operating parameters.

Fig. 6.9(f) displays the compressor and turbine working points on their maps for the whole TMY. The compressor works within the allowed speed range, and the mass flow rate does not exceed the surge and choke limits, besides operating near the highest-efficiency dorsal line. It was estimated that only 15% of working hours $T_{w3} > 550$ °C, giving a significant safety margin to the thermal limit. During peaks of power, T_{w3} do not overcome $T_{w,max} = 600$ °C.

6.7.3 Integration with SAH

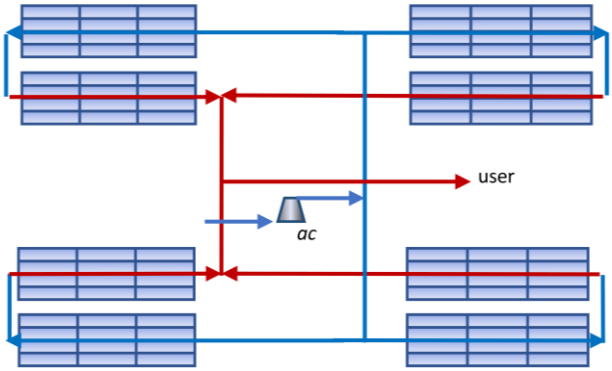

Fig. 6.10. Solar Air Heater SAH configuration, excluding the turbocharger.

As discussed above, the T-SAH is not able to operate correctly at low solar power input, as seen for the present case roughly for $LF < 0.3$, mainly occurring during winter months. A possibility to increase the annual hot air production exploiting the solar field also in T-SAH OFF conditions arises by modifying the layout of Fig. 6.4(a) into a simple SAH configuration, Fig. 6.10. This means temporarily bypassing the turbocharger from the circuit and pumping the airflow through the solar field using the auxiliary compressor *ac*. Air exits the U-loop and it is directly delivered to the user at the temperature $T_3 = T_a$ and atmospheric pressure. The low concentrated irradiance requires a relatively low mass flow rate to control the outlet temperature, Eq. (4.17). As a consequence, the total pressure loss across the U-loop $\Delta p_{nr,t}$ is low, requiring a modest pumping power $\dot{W}_{ac}$ to the auxiliary compressor/fan, Eq. (6.12), $\pi_{ac} = 1 + \Delta p_{nr,t}/p_{0t}$. Inlet receiver temperature and pressure are T_{1t}, Eq. (6.13) and $p_{1t} = p_{0t}\pi_{ac}$

$$\dot{W}_{ac} = \dot{m}_c c_{p,c} T_{0t} \left(\pi_{ac}^{\frac{\gamma_{ac}-1}{\gamma_{ac}}} - 1 \right) \eta_{ac}^{-1} \tag{6.12}$$

$$T_{1t} = T_{0t} \left[1 + \left(\pi_{ac}^{\frac{\gamma_{ac}-1}{\gamma_{ac}}} - 1 \right) \eta_{ac}^{-1} \right] \tag{6.13}$$

Assuming that the electrical driven auxiliary compressor/fan is capable of continuous mass flow rate control, the desired temperature outlet $T_a = 300$ °C can be achieved in the range of low irradiance conditions, where T-SAH is not able to operate $LF < \sim 0.3$. Below $LF < 0.1$, solar power is assumed to be too low to run the concentrating solar plant, so that SAHs is OFF.

Integrating the T-SAH operation with the SAH mode for low irradiance conditions results in a higher number of working hours per month, as reported in Fig. 6.11(a), showing thermal performances in terms of monthly energy contribution. Energy consumed by the auxiliary

compressor for air pumping in SAH mode W_{ac} is moderate, corresponding to the very low percentage of solar energy gain by air in the corresponding month Q_a, Fig. 6.11(b). For the 72 % of exploitable sunny hours with $LF > 0.1$, the system works as T-SAH and the rest of the time as SAH. The annual energy delivered increases by 13.3% thanks to the SAH integration, reaching 374 MW hr, and the annual working hours grow 38% with respect to the only T-SAH mode. The combination of the two modes allows exploiting the 97 % of annual energy available at the receiver tube $Q_{r,TOT}$.

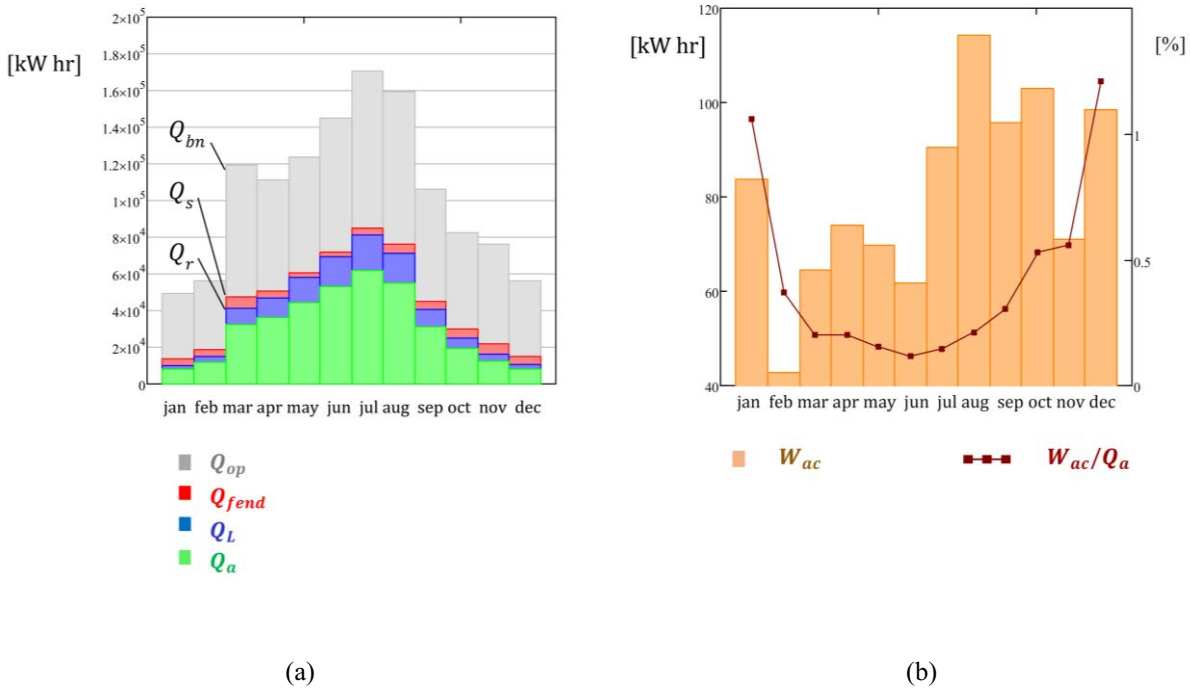

(a) (b)

Fig. 6.11. T-SAH integrated with SAH for low solar power: (a) monthly energy contributions; (b) auxiliary compressor consumption.

6.7.4 Remarks on industrial scale T-SAH

A 633.6 m^2 solar field of LFCs was coupled to an off-the-shelf turbocharger unit to achieve the best matching for the considered location of Madrid (Spain). The T-SAH performances were simulated for typical days in summer and winter, as well as along the typical meteorological year.

The results showed that the T-SAH can deliver 330 MW hr per year of thermal power, supplying hot air in the range of 300 °C - 400 °C without any external energy consumption for air pumping during 2,060 hours of the year with no storage. This is possible due to the beneficial self-adjusting operation of the turbocharger.

Only for very low solar irradiance, the T-SAH is not able to fulfill the turbocharger freewheeling operation, which occurred during winter months as well as in the early morning and late afternoon hours every day. Under this condition, using the system in SAH mode would increase the annual energy yield up to 374 MW hr. Other options can be considered in further research, including external heat source backup, either from biofuel or renewable electricity, as well as from any thermal storage unit. Moreover, for better matching, further work can consider in-

parallel switchable turbochargers and/or variable geometry turbines to cope with lower sun irradiances. No overspeeding of the turbocharger has been detected.

Several performance parameters on yearly basis are summarized in Tab. 6.3. The solar field average optical efficiency over the yearly working hours $\bar{\eta}_{op} = Q_s/Q_{bn}$ together with yearly optical end losses factor $\bar{f}_{end} = Q_r/Q_s$, determine the global optical efficiency $\bar{\eta}_{opg} = \bar{\eta}_{op}\bar{f}_{end} = Q_r/Q_{bn}$. Yearly averaged thermal efficiency is defined as $\bar{\eta}_{th} = Q_a/Q_r$ and accounts for thermal losses from the collector tubes and piping. The global efficiency of solar air heating results $\bar{\eta}_a = \frac{Q_a}{Q_{bn}} = \bar{\eta}_{opg}\bar{\eta}_{th}$. They are estimated for T-SAH as well as for the T-SAH integrated with SAH (T-SAH*) over the respective operating yearly hours. For the T-SAH* $\bar{\eta}_{op} = 0.427$ and $\bar{f}_{end} = 0.902$ gives a global optical efficiency of $\bar{\eta}_{opg} = 0.386$. Thermal efficiency results $\bar{\eta}_{th} = 0.772$, giving an air heating efficiency of $\bar{\eta}_a = 0.298$. These figures are close to the ones attained by similar solar technologies which use conventional HTFs. Although the usage of the turbocharger and the air as HTF difficult the comparison with similar plants, the optical and thermal efficiency obtained results following other linear Fresnel facilities reported in the literature. [82] simulated using commercial code a linear Fresnel field of 268.6 m^2 (36.1 deg N latitude), obtaining an average yearly optical efficiency of 0.379 and thermal efficiency of 0.858, which corresponds to a global efficiency of 0.325. [113] obtained a yearly global efficiency of 0.39 simulating a large LFC solar field of 6,602 m^2 (38.1 deg N latitude) at moderate temperatures.

Table 6.3. Yearly performance parameter for T-SAH and T-SAH* (T-SAH integrated with SAH)

Yearly Value	Unit	T-SAH	T-SAH*
$\boldsymbol{hr\ ON}$	hr	2060	2858
$\boldsymbol{Q_a}$	MW hr y^{-1}	330	374
$\boldsymbol{Q_a/A_{tot}}$	kW hr y^{-1}m^{-2}	521.6	590.5
$\boldsymbol{Q_{bn}}$	MW hr y^{1}	1012	1256
$\boldsymbol{\bar{\eta}_{op} = Q_s/Q_{bn}}$	-	0.468	0.427
$\boldsymbol{\bar{f}_{end} = Q_r/Q_s}$	-	0.909	0.902
$\boldsymbol{\bar{\eta}_{opg} = \bar{\eta}_{op}\bar{f}_{end}}$	-	0.426	0.386
$\boldsymbol{\bar{\eta}_{th} = Q_a/Q_r}$	-	0.767	0.772
$\boldsymbol{\bar{\eta}_a = Q_a/Q_{bn}}$	-	0.327	0.298

6.8 Industrial T-SAH: example II

A further T-SAH example is analyzed in the following paragraph. Straight collector rows instead of two branches as in the U-loop scheme are used, as in Fig. 6.12. A single sending pipe is used to bring airflow from the compressor outlet to the receiver inlet. Moreover, the larger turbine ($A/R = 1.24$) is used.

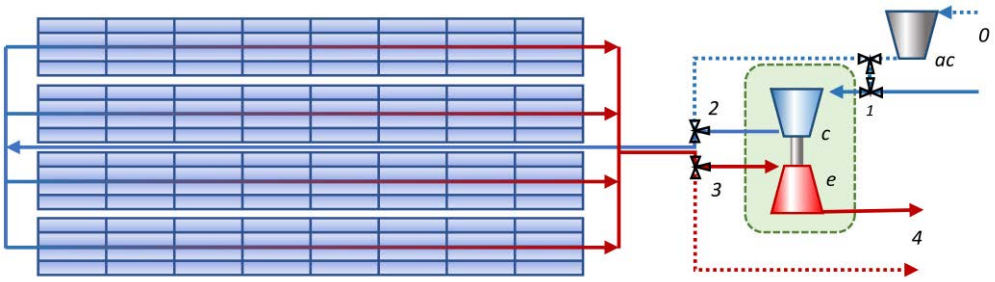

Fig. 6.12. Industrial T-SAH example II, straight row scheme. Air circuit in T-SAH mode (solid line) and SAH mode (dashed line).

The matching map for this configuration has been computed and reported in Fig. 6.13. It evidences as for very low heat flux $\dot{q}_s < 0.27\dot{q}_{s,max} = 3.63\ \mathrm{kWm^{-2}}$ with $\dot{q}_{s,max} = 13.5\mathrm{kWm^{-2}}$, the turbocharger does not reach freewheeling. In this condition, the turbocharger can be excluded from the circuit and the auxiliary compressor blow air through the solar field in SAH mode. For $\dot{q}_s > 0.27\dot{q}_{s,max}$ the system operates as T-SAH.

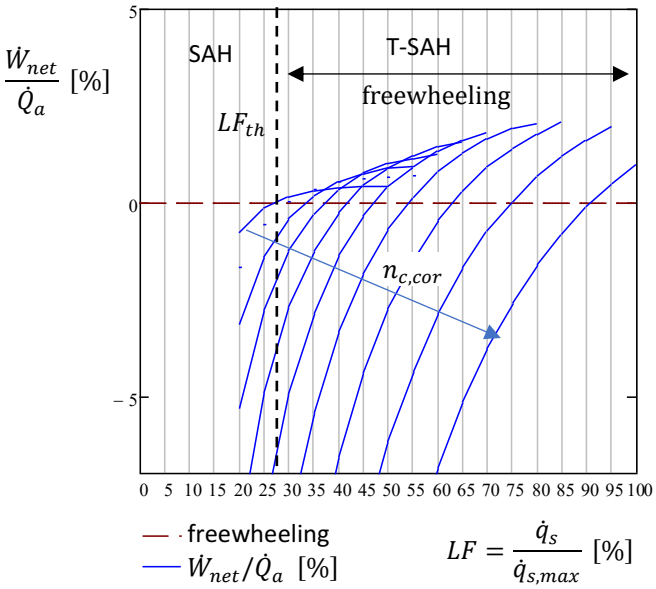

Fig. 6.13. Matching map of turbocharger GT5533R (A/R=1.24) with straight row solar field, $n_s = 8, n_p = 4$.

As done for the previous Example I, the performances of T-SAH are simulated along representative days in the summer and winter seasons. Results are reported in Fig. 6.14.

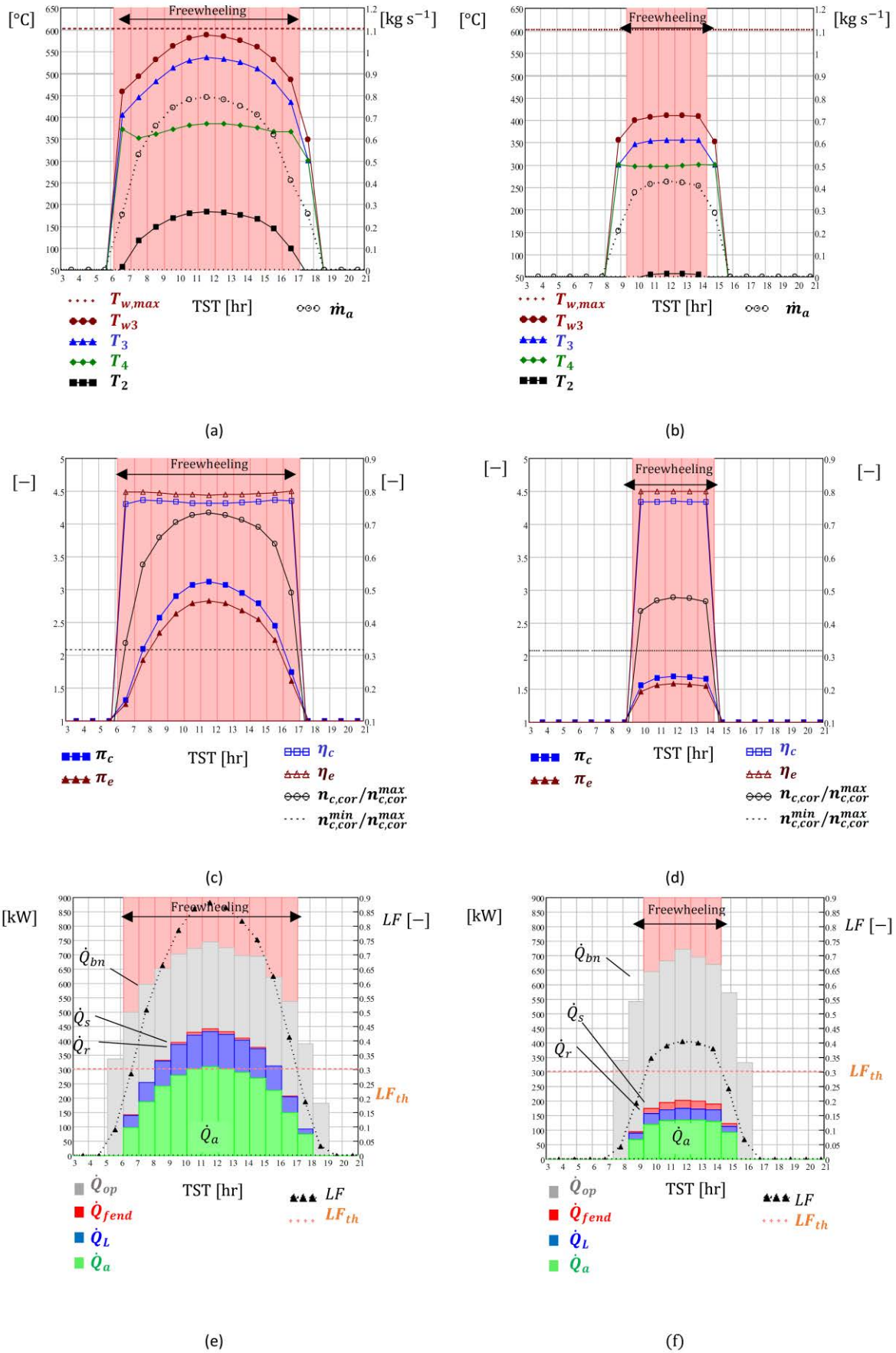

Fig. 6.14. T-SAH performances vs. true solar time TST during a clear summer day (a)-(c)-(e) and winter day (b)-(d)-(e) in Madrid (Spain).

Fig. 6.15 and Tab. 6.5 summarize the main yearly performances.

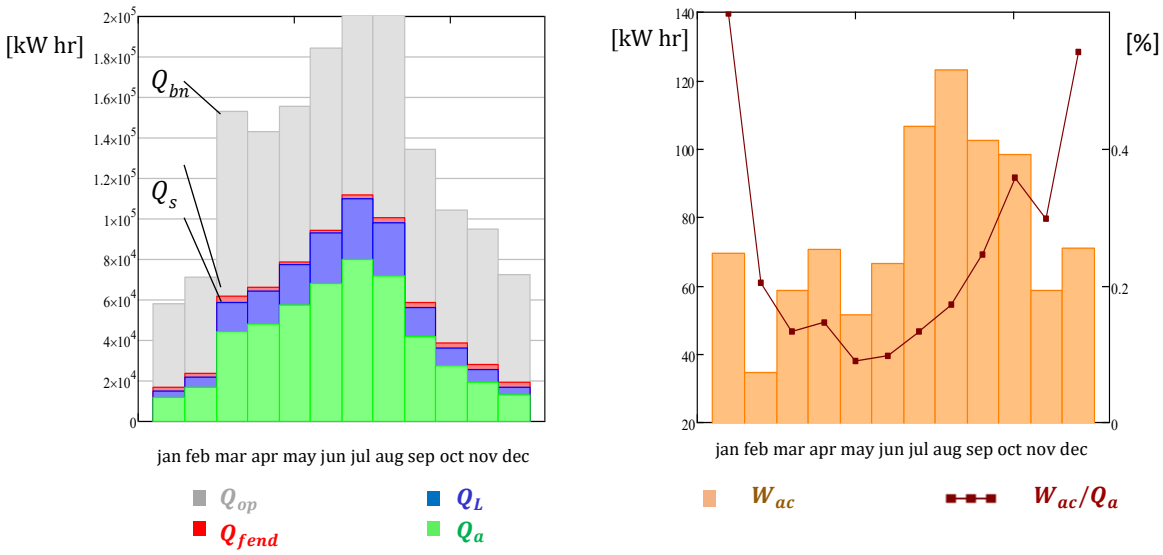

(a) (b)

Fig. 6.15. T-SAH integrated with SAH for low solar power: (a) monthly energy contributions; (b) auxiliary compressor consumption.

Table 6.4. Yearly T-SAH performances

Yearly Value	Unit	T-SAH	T-SAH*
A_{tot}	m^2	845	845
$hr\ ON$	hr	2251	2629
Q_a	MW hr y^{-1}	469.5	500
Q_a/A_{tot}	kW hr $y^{-1}m^{-2}$	555.8	592.1
Q_{bn}	MW hr y^1	1,448	1,602
$\bar{\eta}_{op} = Q_s/Q_{bn}$	-	0.456	0.437
$\bar{f}_{end} = Q_r/Q_s$	-	0.964	0.964
$\bar{\eta}_{opg} = \bar{\eta}_{op}\bar{f}_{end}$	-	0.44	0.421
$\bar{\eta}_{th} = Q_a/Q_r$	-	0.737	0.741
$\bar{\eta}_a = Q_a/Q_{bn}$	-	0.324	0.312

6.9 Further analysis

The simulation across representative days and TMY is a good methodology to scrutinize the behavior of the system under real operating conditions. An alternative compact representation of its performances can be obtained by solving the system for any value of concentrated heat flux $\dot{q}_s$. Assuming an end losses factor $f_{end} = 1$, constant ambient temperature and pressure, it

is possible to obtain the main system variables in the expected range of $0 < \dot{q}_s < \dot{q}_{s,max}$, with low computational cost. This methodology has been applied to the T-SAH, Example II, and the results are reported in Fig. 6.16. As explained above, the system works in SAH mode for $\dot{q}_s < 0.27\ \dot{q}_{s,max}$ and in T-SAH mode for $\dot{q}_s > 0.27\ \dot{q}_{s,max}$.

Fig. 6.16(a) shows the pumping power required by the system. In SAH mode $\dot{W}_p$ done by the auxiliary compressor does not overcome 5 kW before to be eliminated, thanks to turbocharger effect when entering in T-SAH mode. The dashed line shows the $\dot{W}_p$ which would be required by the system if SAH mode would be extended to higher heat fluxes. On the left axis, the same parameter is reported in relative terms $\dot{W}_p/\dot{Q}_a$. It does not exceed 4%. Fig. 6.16 shows air temperature and pressure. Maximum receiver temperature T_{w3} is also reported. Although the variation of $\dot{q}_s$, output temperature T_4 is quite steady, thanks to the stabilizing effect of the turbocharger. Inlet and outlet air temperatures T_2 and T_3 and wall temperature T_{w3} increase with $\dot{q}_s$. The increased pressure imposed by the turbocharger moderates the pressure stagnation drops which would be induced by the greater mass flow rate, Fig. 6.16(c). The inlet turbine temperature required to provide enough power for compressing and pumping has a negative impact on the thermal efficiency η_{th}, reported in Fig. 6.16(d). In fact, the receiver average temperature grows with $\dot{q}_s$, as well as heat losses to the ambient. In SAH operating mode, where the maximum T_{w3} does not exceed 350 °C, η_{th} is higher than in T-SAH mode.

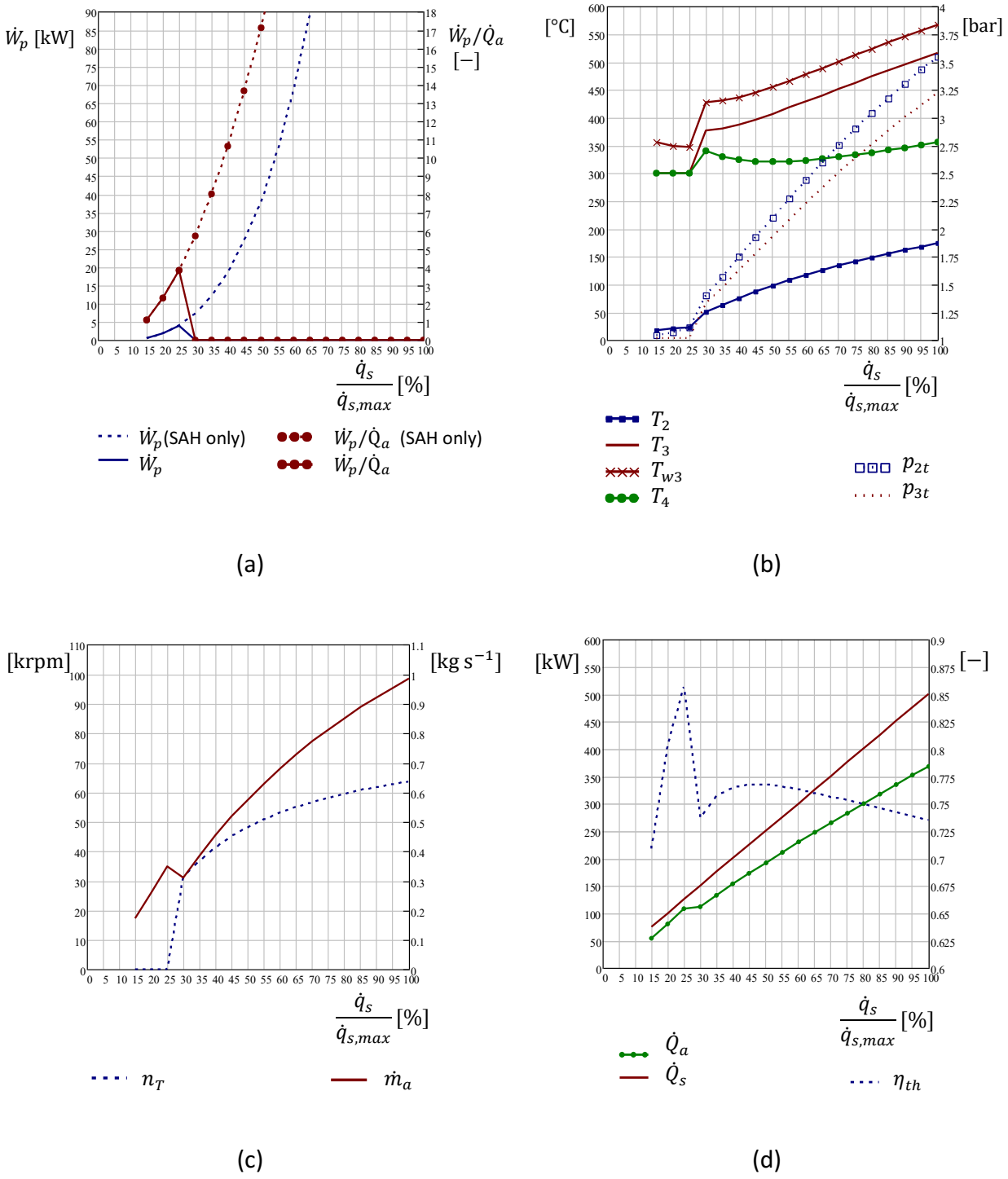

Fig. 6.16. Performances of T-SAH integrated with SAH at low irradiances vs. concentrated relative irradiance.

6.9.1 T-SAH with auxiliary compressor aid

According to the original T-SAH configuration, the auxiliary compressor *ac* is used only during starting transient, providing the required mechanical power to accelerate the turbocharger before the system reaches steady-state operation. Nevertheless, it could be activated in some cases to improve the performance of T-SAH, hence in series with the turbocharger. Under the right conditions, it could provide a limited overpressure at the turbocharger inlet, thus helping

the turbocharger to reach mechanical balance, with lower turbine power. This can translate into slightly lower inlet turbine temperature improving the thermal efficiency η_{th} and/or reducing the risk of receiver overheating.

The power $\dot{W}_{ac}$ consumed by the *ac* to assist the turbocharger must be limited to a few percent of the overall power $\dot{Q}_a$; otherwise, this solution would not be convenient. Fig. 6.17 gives some quantitative information. Fig. 6.17(a) compares the relative auxiliary compressor power $\dot{W}_{ac}/\dot{Q}_a$ and the thermal efficiency η_{th} for the T-SAH without *ac*, with T-SAH and *ac* aid with different pressure ratios π_{ac}. It can be noticed as the thermal efficiency η_{th} grows slightly when passing from $\pi_{ac} = 1$ (no *ac* aid) to $\pi_{ac} = 1.1$. This is due to the lower inlet turbine temperature T_3 required for turbocharger freewheeling and the lower (maximum) receiver wall temperature T_{w3}, as confirmed by Fig. 6.17(b). It also reports the temperature T_4 at the turbine outlet, which slightly decreases according to lower T_3. The external power required to obtain the pressure ratios $\pi_{ac} > 1$ is reported in Fig. 6.17(b). Although not negligible, it is limited to less than 5% of $\dot{Q}_a$.

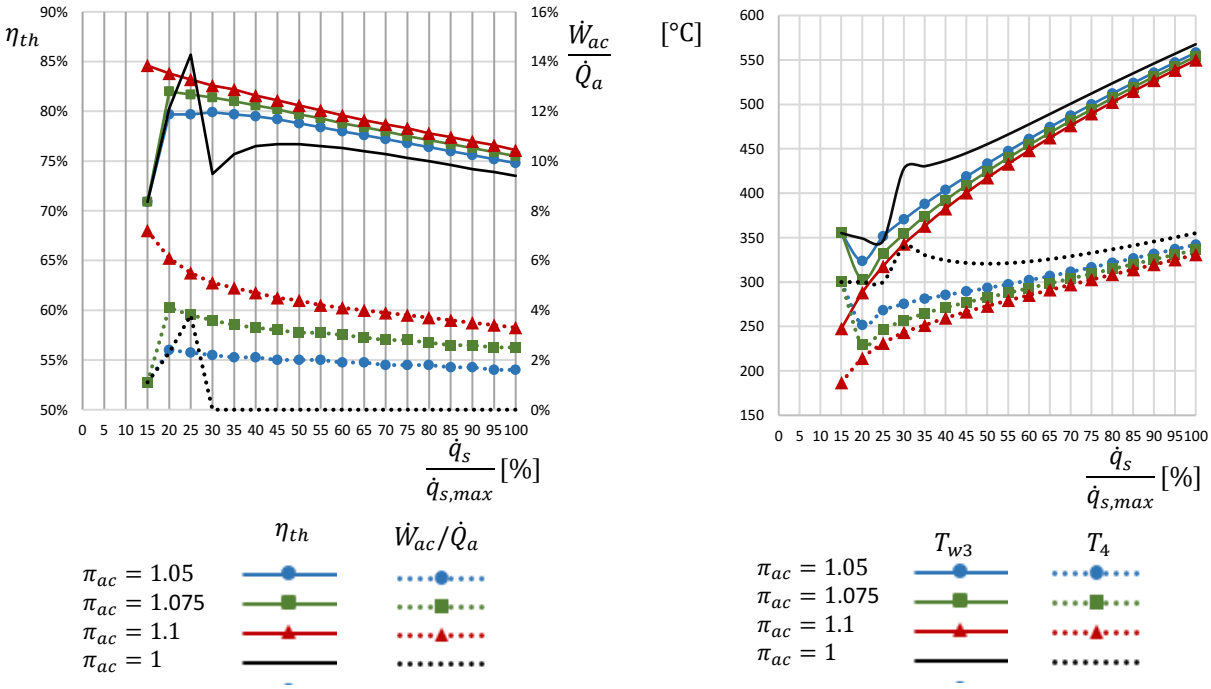

Fig. 6.17. T-SAH operating with auxiliary compressor working in series with the turbocharger, which different pressure ratios vs. concentrated relative irradiance. (a) Thermal efficiency and relative auxiliary power consumption; (b) temperatures.

The advantage of using a limited amount of $\dot{W}_{ac}$ to reduce the receiver temperature depends on the auxiliary pressure ratio π_{ac} imposed and the other variables of the system (heat flux, mass flow rate, turbocharger speed, etc.). The limited increase in η_{th} achieved seems not justifying the electrical power consumption of the auxiliary compressor during a continuous operation. Nevertheless, T-SAH operation with auxiliary compressor aid can be applied to short time intervals for control purposes. This approach can be considered for reducing the maximum receiver temperature during high irradiance conditions when the maximum receiver

temperature is very close to its thermal limits, reducing the risk of overheating and increase receiver lifetime.

6.9.2 Optimization

Besides the two T-SAH examples studied above, other configurations of solar field can match the turbocharger GT5533R. Considering the LFC in Tab. 6.1 as a basic module, the number of series modules n_s and parallel modules n_p can be varied, either assuming a "U-loop" or "straight row" scheme, to achieve an optimal design.

First, the matching map is obtained for each of the possible solar field configurations. Considering the turbine $A/R = 1.00$ and the turbine $A/R = 1.24$, some possible configurations are reported in Tab. 6.5. The range of $\dot{q}_s$ where the system can work as T-SAH is reported also, as a result of the matching procedure. It includes the previous Example I and II (bold typed).

Table 6.5. Further solar field configuration matching the turbocharger GT5533R.

Turbine	Scheme	n_s	n_p	$n_s n_p$	A_{tot} [m^2]	Range $\dot{q}_s$ T-SAH [% of $\dot{q}_{s,max}$]
A/R=1.00	U-loop	6	4	24	633.6	30-100
A/R=1.00	Straight rows	6	4	24	633.6	30-100
A/R=1.00	Straight rows	8	3	24	633.6	35-100
A/R=1.24	U-loop	8	4	32	844.8	30-100
A/R=1.24	Straight rows	8	4	32	844.8	30-100
A/R=1.24	Straight rows	6	5	30	792	30-100
A/R=1.24	Straight rows	9	3	27	712	35-100
A/R=1.24	Straight rows	7	4	28	739.2	30-100

A few selected configurations are then considered for the numerical simulation. Their performance is evaluated in the range of expected heat flux $\dot{q}_s$, as in the previous paragraphs. Fig. 6.18 shows the result for a comparative analysis of five solar field configurations coupled with turbocharger GT5533R and turbine $A/R = 1.24$. The facilities work in SAH mode for low irradiances where turbocharger freewheeling is not achievable. It can be noticed that the minimum $\dot{q}_s$ allowing T-SAH mode operation varies slightly from one to another configuration. Fig. 6.18(a) reports the thermal efficiency η_{th} as well as the relative pumping power $\dot{W}_p/\dot{Q}_a$ in SAH mode (null in T-SAH mode). Fig. 6.18(b) shows the maximum wall temperature T_{w3} and the delivery temperature T_4. "S" indicates straight row configuration, "U" indicates U-loop configuration.

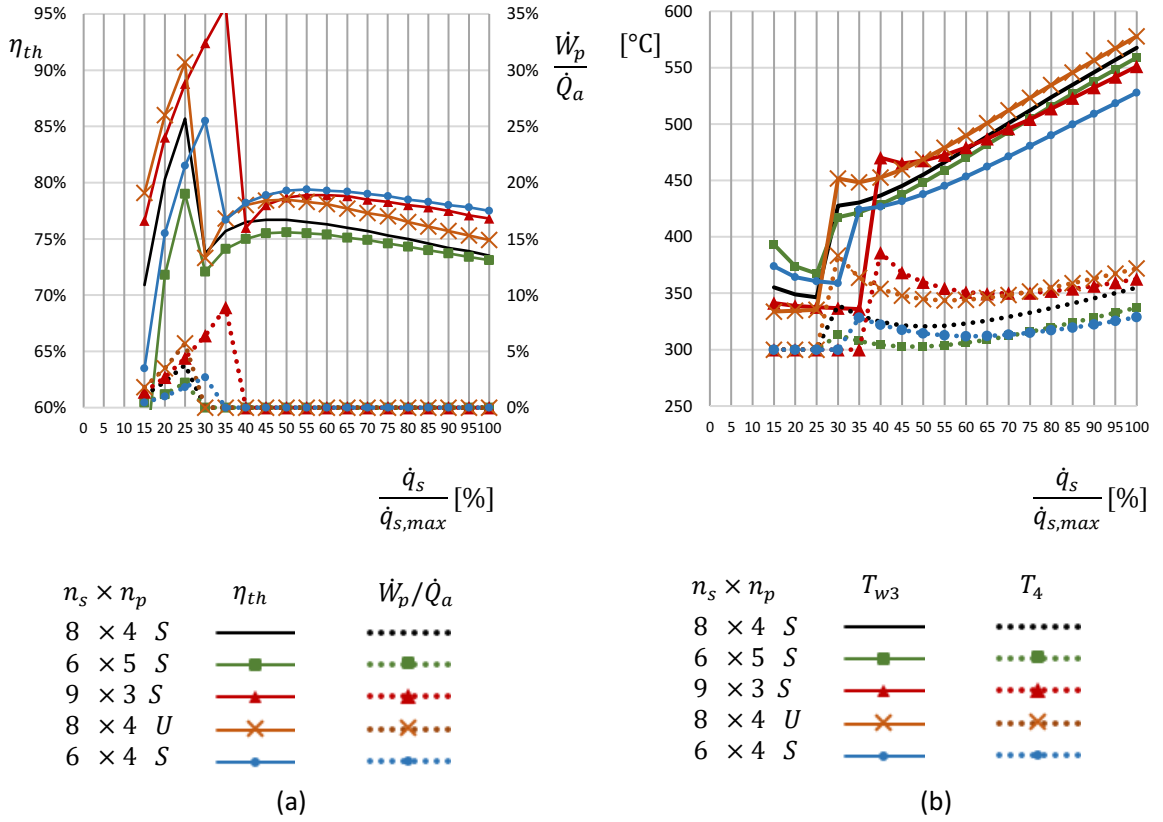

Fig. 6.18. Performance of selected solar field configurations. (a) Thermal efficiency and pumping power vs. concentrated relative irradiance; (b) Temperatures.

All the selected configurations show thermal efficiency values ranging between 75 to 80%. The output temperature varies between 300 - 370 °C. The smallest size plant $6 \times 4\ S$ presents better performance than the others, probably due to shorter air paths across the solar field inducing lower pressure drops and/or a better fit with turbocharger characteristics. In fact, it seems working with lower maximum temperature T_{w3} and also lower T_4. The auxiliary power consumption in SAH mode is higher as lower the T-SAH operating range is, although it falls in all cases below 10% of $\dot{Q}_a$.

Further information is obtained simulating across a typical year TMY as done for Example I and II. Tab. 6.6 reports the annual performances of the selected plants in Madrid. For each of them, the operation mode with T-SAH only and with T-SAH combined with SAH at low irradiances (T-SAH*) are simulated.

The information provided offers the possibility of optimizing the design of the solar field according to the different objectives and the land layout. Maximizing the energy delivered Q_a leads to select the 8 x 4 S example as the most performing one, with $Q_a = 500\ \mathrm{MW\ hr\ y^{-1}}$. Instead, considering specific energy per unit of area, the best results are obtained with the smaller solar field 6 x 4 S, with $Q_a = 609.7\ \mathrm{kW\ hr\ y^{-1} m^{-2}}$.

The overall efficiency $\bar{\eta}_a$ includes both the optical efficiency $\bar{\eta}_{opg}$ and the thermal one $\bar{\eta}_{th}$. The optical efficiency is affected by the end losses factor $\bar{f}_{end}$. Although it is in all cases greater than 0.9, this factor varies from one configuration to another being dependent on the collector row length. The configuration with a longer collector row, the 9 x 3 S example, have a higher $\bar{f}_{end} =$

0.968. As expected, the worst case is the U loop configuration, 8 x 4 U, with $\bar{f}_{end} = 0.928$ where the collector rows are shorter, being the series of n_s modules split into two branches. The higher optical efficiency $\bar{\eta}_{opg}$ is then achieved for a long straight collector row configuration, 9 x 3 S, which reaches $\bar{\eta}_{opg} = 0.429$. The average thermal efficiency is determined by the working point of the turbocharger and its matching with the solar field, as well as by the operating T-SAH and SAH range.

Table 6.6. Annual performances of several solar fields applied to GT5533R (turbine A/R=1.24) for the TMY of Madrid (Spain).

Solar Field	Mode	hr ON	Q_a	Q_a/A_{tot}	$\bar{\eta}_{op}$	$\bar{f}_{end}$	$\bar{\eta}_{opg}$	$\bar{\eta}_{th}$	$\bar{\eta}_a$	W_p
					$\frac{Q_s}{Q_{bn}}$	$\frac{Q_r}{Q_s}$	$\bar{\eta}_{op}\bar{f}_{end}$	$\frac{Q_a}{Q_r}$	$\frac{Q_a}{Q_{bn}}$	
$n_s \times n_p$		hr	$\frac{\text{MW hr}}{y}$	$\frac{\text{kW hr}}{\text{y m}^2}$	-	-	-	-	-	$\frac{\text{MW hr}}{y}$
8 x 4 S	T-SAH	2,251	469.5	555.8	0.456	0.964	0.44	0.737	0.324	0
	T-SAH*	2,629	500	592	0.437	0.964	0.421	0.741	0.312	0.911
8 x 4 U	T-SAH	2,120	448	530	0.463	0.93	0.431	0.751	0.324	0
	T-SAH*	2,601	492.6	583	0.438	0.928	0.407	0.761	0.309	2.265
6 x 5 S	T-SAH	2,214	426.5	538.6	0.458	0.953	0.437	0.729	0.318	0
	T-SAH*	2,620	454.6	574	0.437	0.952	0.416	0.729	0.303	0.485
9 x 3 S	T-SAH	1,944	381.9	535	0.472	0.968	0.457	0.762	0.349	0
	T-SAH*	2,632	445	625	0.437	0.968	0.423	0.779	0.329	3.784
6 x 4 S	T-SAH	2,038	347	547.7	0.468	0.953	0.446	0.771	0.344	0
	T-SAH*	2,620	386.3	609.7	0.437	0.952	0.416	0.774	0.321	0.784

As a result of the combination of these factors, the 9 x 3 S plant holds the higher annual average efficiency $\bar{\eta}_a = 0.329$. The energy consumed for pumping during the SAH mode operating hours is also a critical parameter. According to Fig. 6.18(a) the examples where the minimum heat flux for T-SAH operation is greater presents the higher pumping power consumption. This is coherent with Tab. 6.6 which reports as the higher W_p is consumed by 9 x 3 S and 8 x 4 U.

The comparative analysis shows as all the considered examples of solar field configuration give very similar performances. This ensures good accommodation to different shapes of the space

available. Moreover, the relatively small variation of the different evaluating parameters indicates the possibility of optimization and clarifies the effect of the solar field design parameters on the final outputs.

7 CONCLUSION AND FURTHER WORKS

7.1 Main contributions

7.1.1 Previous works

The bibliographic survey highlights the importance of solar thermal energy for decarbonizing and greening industrial processes that consume heat. Among them, the review identifies several high-energy demanding processes requiring hot air as heat and moisture carrier in the low and medium temperature range (< 400 °C). Drying is one widely used technique requiring hot air, common to different industrial sectors, including food and beverage, wastewater treatment, mining, manufacturing, agroindustry, among others. Despite the high potential, solar thermal energy is rarely used for hot air production in the industry. The analysis of the state-of-art of solar thermal technologies for hot air production highlights that solar air collectors are the most common solution but are limited to low-temperature applications (< 150 °C), also referred to as Solar Air Heaters. In a few cases linear concentrating solar collectors, such as LFC and PTC types are used to provide hot air at higher temperature, with oil or water as HTF and an HTF/air heat exchanger. Directly heating atmospheric air to medium temperatures (150 - 400 °C) inside LFCs and PTCs, has not been a common practice, although simpler, cheaper, and lighter solar facilities are possible avoiding liquid HTFs and HTF/air heat exchanger, at the same time avoiding dangerous leakages and expenses for its replacement.

7.1.2 Analysis

In this thesis an innovative Concentrating Solar Air Heater is proposed and extensively investigated, enabling direct air heating inside standard evacuated receivers using linear concentrating collectors.

An initial screening of the Concentrating Solar Air Heater carried out on a 1D numerical model establishes the framework of the technical viability and identifies the critical aspects. The air can be supplied to the user in the range of 300 °C to 450 °C with specific collector layouts. In fact, the procedure requires relatively high external pumping power, with a large consumption for long rows of collectors and wide apertures. The thermal limit of commercial receiver tubes (600 °C) is another limitation. The modest heat transfer rate between the receiver and the internal airflow leads to relevant receiver over-temperature. This translates into a minimum row length limit, besides inducing high thermal losses.

7.1.3 Proposal and first results

Based on the theoretical analysis, the Turbo-assisted Concentrating Solar Air Heater is proposed to overcome the limitation of direct air heating in linear concentrating collectors. The numerical results obtained indicate the viability of T-SAH concept under a wide range of design parameters and operating conditions. The original Brayton cycle configuration, implemented through a turbocharger, allows supplying the user with hot air up to 400 °C eliminating the need for external pumping power under suitable working conditions, which can be achieved in a wide range of collectors sizes. The maximum allowable temperature of standard evacuated receiver tubes limits the inlet turbine temperature to 500-550 °C making unviable the production of an excess of mechanical power at the shaft. Instead, it allows providing the pumping power

required for air circulation inside the solar field. For the turbocharger efficiency to be high enough, the T-SAH concept can supply the user process with hot air at a slight pressure over the atmosphere for coping with the process pressure losses.

7.1.4 Design of an industrialized prototype

An original prototype is designed and installed. Linear Fresnel collectors equipped with standard evacuated tubes have been selected for the solar field, reaching 79.2 m^2 of reflecting surface. An automotive commercial turbocharger is coupled with the air circuit. Several technical aspects required special attention, as sizing the solar field and the turbocharger for a good matching, dealing with thermal dilatation of receiver tubes, building an optimized air circuit, minimizing pressure drops and thermal losses, providing the required auxiliary equipment as the auxiliary compressor, the turbocharger lubrication, preparing the instrumentation and control system.

7.1.5 Proof of concept

An extensive experimental investigation is carried out on the first small-scale T-SAH prototype. The results demonstrate the feasibility of the direct air heating inside the evacuated tube in a Linear Fresnel collector with modest air pressure, which was less than 1.5 bar. During typical clear summer days in Madrid (Spain) air temperature at the receiver tube outlet up to 500 °C has been reached without overcoming the receiver wall temperature limit. Although tube bending has been observed, no cover tube damage has been detected. Owing to the short length of the solar field and its unavoidable orientation because of the allowable roof space, optical end losses were high during the early morning and afternoon hours.

7.1.6 Advanced analysis and results

1D static and dynamic numerical models for the receiver tube have been implemented and validated on the performed tests. The discretized receiver model takes into account the non-continuous solar field, as well as the junction elements connecting consecutive receiver tubes. The receiver tube static model has been improved in a straightforward way incorporating a thermal inertia coefficient U_C complementing the overall heat losses coefficient U_L, by modifying the efficiency and heat removal factors, $F´$ and F_R respectively, commonly used in canonical models.

7.1.7 Transient analysis and experiments

The purposely designed transient heating and cooling tests with partial solar irradiance allowed validating the dynamic model. Its use seems unavoidable for high accuracy, owing to the low heat capacity of air in comparison to tube thermal inertia. The experimental data obtained corroborate this assumption.

During the performed tests, the solar power gain was lower than expected from the specifications due to transient tracking errors besides manufacturing imperfections. The theoretical optical efficiency obtained using the given IAMs and the normal incidence optical efficiency η_{op0} did not provide accurate results, especially when the tracking angle has to change fast. Of especial importance is a tracking error that arises between the serial alignment of each mirror that takes a long time. Using experimental data and the dynamic model an experimental optical efficiency has been estimated allowing the definition of a correction term for the optical efficiency. The correction term takes into account both static errors and tracking errors. As a

result, the model can anticipate accurately instantaneous performances and underpin improvements to the solar collector understudy and similar ones.

7.1.8 Turbomachine modeling and results

The experimental campaign allowed characterizing the thermal and mechanical behavior of the turbocharger, besides tuning and validating the numerical model implemented. Emphasis is put on the turbocharger characterization as this component plays a crucial role in eliminating the blowing electrical power and even expand to a higher than atmospheric pressure, leaving blowing power for the user's needs.

A low-capacity high-production automotive turbocharger has been modeled and experimentally characterized under non-standard operating conditions using the advanced diabatic approach. A detailed model of the turbocharger is developed integrating the conventional approach based on the compressor and turbine cold maps provided by the manufacturer with a semi-empirical characterization of heat transfer phenomena affecting its performance, the diabatic turbocharger. The model has been verified and tuned using experimental data directly obtained in the facility constructed, thus offering ways of fast and low-cost commissioning of similar facilities.

The small-scale facility did not allow to reach optimum operating conditions in the implementation here considered, due to low turbocharger efficiency, typical of small size turbochargers. Nevertheless, the analysis carried out indicates the relevant features of the system when scaled up to typical sizes.

7.1.9 Industrial application

The experimental results corroborate the practical possibility of an industrial-scale application of the T-SAH concept. Medium-scale industrial applications of T-SAH offer great potential for hot air production, reducing cost, weight, bulk, complexity, and environmental impact over more conventional approaches.

A comprehensive mathematical model is implemented for detailed performance analysis of a medium-scale T-SAH facility for industrial applications using off-the-shelf components and real meteorological data. A methodology for obtaining a good matching between the solar field and the turbocharger is implemented.

7.1.10 Test cases

Two case studies are studied in detail, revealing the features of two different solar field configurations, obtained using parallel “U-loops” and “straight rows” of Linear Fresnel collectors, with a collecting area of $633.6\ \mathrm{m}^2$ and $845\ \mathrm{m}^2$ respectively. In both cases, the solar field of LFCs is coupled to an off-the-shelf turbocharger unit to achieve the best matching for the considered location of Madrid (Spain). The T-SAH performances are simulated for typical days in summer and winter, as well as along the typical meteorological year. The results show that the T-SAH can deliver 330 MW hr and 470 MW hr per year of thermal power, respectively for two cases, supplying hot air in the range of 300 °C - 400 °C without any external energy consumption for air pumping during more than 2000 hours of the year with no storage. This is possible due to the beneficial self-adjusting operation of the turbocharger. Only for very low solar irradiance, the T-SAH is not able to fulfil the turbocharger freewheeling operation, which

occurred during winter months as well as in the early morning and late afternoon hours every day. Under this condition, the turbocharger can be excluded from the circuit and a simpler direct air heating at atmospheric pressure is possible with modest pumping power consumption. The sola facilities simulated operates with an average annual global efficiency of 0.30 - 0.31 respectively for the two example analysed. The average annual global optical efficiency range around 0.38 - 0.40, determined by the Linear Fresnel module features (normal optical efficiency and IAMs) as well as by length-dependent end losses factor. Although the modest row length, typical in medium-size solar fields, the annual average end losses factor is still high, 0.9 - 0.96. Thermal efficiency determined by the thermal losses from the receiver tubes and the rest of the air circuit result 0.77 - 0.76. The medium-size T-SAH simulated can deliver 590 - 580 kW hr m^{-2} per year.

7.1.11 Solar field optimization

The feasibility analysis is extended to other solar field configurations. They are simulated across the typical meteorological year. The results show a small variation of the relevant parameters as thermal and optical efficiency, end losses, thermal power output among others. The comparative analysis allows identifying the main parameters affecting the T-SAH performances, aiming at an optimum design.

7.2 Future works

The extensive research carried out in this thesis allowed to identify several aspects that require further investigation. Same relevant remarks are indicated as possible field of research which can significantly contribute to the industrial development of the direct solar air heating in concentrating collector and the related technical and scientific issues.

High concentrated solar heat flux impacting the receiver combined with high temperature can induce excessive mechanical stress on the evacuated receiver tube. Moreover, heat flux inhomogeneous circumferential distribution on the receiver surface combined with low internal heat transfer to airflow can induce tube bending with the risk of glass cover breakdown or selective coating wear. The effect of the heat flux distribution on the circumferential temperature distribution of the receiver can be analyzed by combining raytracing techniques with a detailed receiver thermal receiver model. This way an estimation of tube bending and its minimization can be obtained and considered as an additional design constraint. The optimization of secondary optics is foreseen as a promising technique for heat flux homogenization, improving the feasibility of direct air heating either using Linear Fresnel or Parabolic through collectors.

Although in the present thesis Linear Fresnel collector is preferred for direct air heating, the theoretical analysis suggested that parabolic through collectors are also suitable for the purpose. Based on the methodology developed, commercial PTC can be considered for a detailed feasibility study.

The turbocharger is a key component for effective T-SAH operation. Although the fixed geometry turbocharger considered in this thesis gives good performances, Variable Nozzle turbine VNT can be considered for further research, especially for increasing efficiency at “off-

design" conditions. The use of two or more turbochargers in parallel can be considered for very large installations aiming at flexible operation and modularity. Electric turbochargers are an emerging technology for improving automotive engines performances. They can be considered for the application with T-SAH, avoiding the need for an auxiliary compressor for starting transient and control purposes.

7.2.1 Thermal energy storage

Thermal Energy Storage can extend the operating hours of the solar facility beyond the direct solar availability. Latent heat storage has huge potential for application with T-SAH. The preliminary experimental results obtained in this thesis using Lithium Nitrate as phase change material confirms its suitability and encourages further research. The development of an accurate numerical model, able to account for the heat transfer phenomena involved, would be a useful tool for designing an optimized energy storage unit either at a prototypal or industrial scale. Sensible heat storage using low-cost and/or recycled waste materials is another relevant issue that is worth investigating.

7.2.2 Main industrial outcome

An industrial-scale demonstrator is viable according to the feasibility study discussed in this thesis. It will demonstrate the technological readiness and reliability of T-SAH. It will be the first among the SHIP (Solar Heat for Industrial Processes) technologies that is capable of directly solar-heating air up to 300ºC without any need of heat-carrying fluids HTFs (water/glycol, oils, etc.), thus aiming at lower cost respect to other SHIP technologies, either using concentrating and non-concentrating technologies. Moreover, thanks to the use of a turbocharger the auxiliary energy consumption for air blowing is minimized. The solution will be energetically and ecologically sustainable, safe, mechanically simple, with minimal area requirements, and with a reasonable payback period. It is modular, small, lightweight, and can be placed on rooftops. The innovative T-SAH, eventually combined with thermal storage, has disruptive potential in the industrial heat market as it can be used in any industrial sector requiring pre/heating/drying operations, including seawater desalination, distillation, cooking, evaporating, pasteurizing, sterilizing, bleaching, coloring, fixing, compressing, pyrolysis, curing, etc, increasing the possibilities for industrial decarbonization towards an environmentally sustainable future.

7.2.3 Other results

The methodology developed, the experimental testing campaign and its information combine to allow analyzing and developing other innovative applications of the thermal solar energy using compressed gases.

BIBLIOGRAPHY

[1] A. Famiglietti, A. Lecuona-Neumann, J. Nogueira, M. Rahjoo, Direct solar production of medium temperature hot air for industrial applications in linear concentrating solar collectors using an open Brayton cycle. Viability analysis, Appl. Therm. Eng. 169 (2020). https://doi.org/10.1016/j.applthermaleng.2020.114914.

[2] A. Famiglietti, A. Lecuona, Direct solar air heating inside small-scale linear Fresnel collector assisted by a turbocharger : Experimental characterization, Appl. Therm. Eng. 196 (2021). https://doi.org/10.1016/j.applthermaleng.2021.117323.

[3] A. Famiglietti, A. Lecuona, Small-scale linear Fresnel collector using air as heat transfer fl uid : Experimental characterization, 176 (2021).

[4] A. Famiglietti, A. Lecuona, M. Ibarra, J. Roa, Turbo-assisted direct solar air heater for medium temperature industrial processes using Linear Fresnel Collectors . Assessment on daily and yearly basis, 223 (2021). https://doi.org/10.1016/j.energy.2021.120011.

[5] World Energy Outlook 2019, Paris, n.d. https://www.iea.org/reports/world-energy-outlook-2019.

[6] F.T. Princiotta, D.H. Loughlin, Global climate change: The quantifiable sustainability challenge, J. Air Waste Manag. Assoc. 64 (2014) 979–994. https://doi.org/10.1080/10962247.2014.923351.

[7] IEA Solar Heating & Cooling Programme, (n.d.). https://www.iea-shc.org/.

[8] Z.X. and T.G. R. Wang, Introduction to solar heating and cooling systems, in: Adv. Sol. Heat. Cool., Woodhead Publishing, 2017: pp. 3–12.

[9] T.M. Razykov, C.S. Ferekides, D. Morel, E. Stefanakos, H.S. Ullal, H.M. Upadhyaya, Solar photovoltaic electricity: Current status and future prospects, Sol. Energy. 85 (2011) 1580–1608. https://doi.org/10.1016/j.solener.2010.12.002.

[10] Heating and Cooling, (n.d.). https://ec.europa.eu/energy/topics/energy-efficiency/heating-and-cooling_en.

[11] International Energy Agency, KEY WORLD ENERGY STATISTICS 2019, 2018.

[12] IEA, World Energy Statistics 2016, n.d. www.iea.org/statistics/.

[13] International Renewable Energy Agency (IRENA), (n.d.). www.irena.org.

[14] Heat Roadmap Europe, HEATING AND COOLING FACTS AND FIGURES, 2017. www.heatroadmap.eu.

[15] A.K. Sharma, C. Sharma, S.C. Mullick, T.C. Kandpal, Solar industrial process heating: A review, Renew. Sustain. Energy Rev. 78 (2017) 124–137. https://doi.org/10.1016/j.rser.2017.04.079.

[16] S.H. Farjana, N. Huda, M.A.P. Mahmud, R. Saidur, Solar process heat in industrial systems – A global review, Renew. Sustain. Energy Rev. 82 (2018) 2270–2286. https://doi.org/10.1016/j.rser.2017.08.065.

[17] S. Mekhilef, R. Saidur, A. Safari, A review on solar energy use in industries, Renew. Sustain. Energy Rev. 15 (2011) 1777–1790. https://doi.org/10.1016/j.rser.2010.12.018.

[18] L. Kumar, M. Hasanuzzaman, N.A. Rahim, Global advancement of solar thermal energy

technologies for industrial process heat and its future prospects: A review, Energy Convers. Manag. 195 (2019) 885–908. https://doi.org/10.1016/j.enconman.2019.05.081.

[19] C. Brunner, B. Muster, Technology Position Paper Solar Heat Integrations in Industrial Processes, IEA SHC Technol. Collab. Program. (SHC TCP). (2020).

[20] SHIP Database, (n.d.). http://ship-plants.info/.

[21] W. Fuqiang, C. Ziming, T. Jianyu, Y. Yuan, S. Yong, L. Linhua, Progress in concentrated solar power technology with parabolic trough collector system: A comprehensive review, Renew. Sustain. Energy Rev. 79 (2017) 1314–1328. https://doi.org/10.1016/j.rser.2017.05.174.

[22] A. Bilal Awan, M.N. Khan, M. Zubair, E. Bellos, Commercial parabolic trough CSP plants: Research trends and technological advancements, Sol. Energy. 211 (2020) 1422–1458. https://doi.org/10.1016/j.solener.2020.09.072.

[23] S. Karathanasis, Linear Fresnel Reflector Systems for Solar Radiation Concentration, 2019. https://doi.org/10.1007/978-3-030-05279-9.

[24] E. Bellos, Progress in the design and the applications of linear Fresnel reflectors – A critical review, Therm. Sci. Eng. Prog. 10 (2019) 112–137. https://doi.org/10.1016/j.tsep.2019.01.014.

[25] I. Dincer, On energetic, exergetic and environmental aspects of drying systems, Int. J. Energy Res. 26 (2002) 717–727. https://doi.org/10.1002/er.792.

[26] V. Belessiotis, E. Delyannis, Solar drying, Sol. Energy. 85 (2011) 1665–1691. https://doi.org/10.1016/j.solener.2009.10.001.

[27] G. Pirasteh, R. Saidur, S.M.A. Rahman, N.A. Rahim, A review on development of solar drying applications, Renew. Sustain. Energy Rev. 31 (2014) 133–148. https://doi.org/10.1016/j.rser.2013.11.052.

[28] Z.H. Wu, Y.J. Hu, D.J. Lee, A.S. Mujumdar, Z.Y. Li, Dewatering and drying in mineral processing industry: Potential for innovation, Dry. Technol. 28 (2010) 834–842. https://doi.org/10.1080/07373937.2010.490485.

[29] P.P. Lewicki, Design of hot air drying for better foods, Trends Food Sci. Technol. 17 (2006) 153–163. https://doi.org/10.1016/j.tifs.2005.10.012.

[30] C. Ratti, Hot air and freeze-drying of high-value foods: A review, J. Food Eng. 49 (2001) 311–319. https://doi.org/10.1016/S0260-8774(00)00228-4.

[31] S. Mekhilef, S.Z. Faramarzi, R. Saidur, Z. Salam, The application of solar technologies for sustainable development of agricultural sector, Renew. Sustain. Energy Rev. 18 (2013) 583–594. https://doi.org/10.1016/j.rser.2012.10.049.

[32] H. Schnitzer, C. Brunner, G. Gwehenberger, Minimizing greenhouse gas emissions through the application of solar thermal energy in industrial processes, J. Clean. Prod. 15 (2007) 1271–1286. https://doi.org/10.1016/j.jclepro.2006.07.023.

[33] A.E. Kabeel, M.H. Hamed, Z.M. Omara, A.W. Kandeal, Solar air heaters: Design configurations, improvement methods and applications – A detailed review, Renew. Sustain. Energy Rev. 70 (2017) 1189–1206. https://doi.org/10.1016/j.rser.2016.12.021.

[34] A. Saxena, Varun, A.A. El-Sebaii, A thermodynamic review of solar air heaters, Renew.

Sustain. Energy Rev. 43 (2015) 863–890. https://doi.org/10.1016/j.rser.2014.11.059.

[35] M. Kumar, S.K. Sansaniwal, P. Khatak, Progress in solar dryers for drying various commodities, Renew. Sustain. Energy Rev. 55 (2016) 346–360. https://doi.org/10.1016/j.rser.2015.10.158.

[36] S. Rehman, A. Ahmad, L.M. Alhems, M.M. Rafique, Experimental evaluation of solar thermal performance of linear Fresnel reflector, J. Mech. Sci. Technol. 33 (2019) 4555–4562. https://doi.org/10.1007/s12206-019-0852-6.

[37] D. Pietruschka, I. Ben Hassine, M. Cotrado, R. Fedrizzi, M. Cozzini, Large Scale Solar Process Heat Systems -planning, Realization and System Operation, Energy Procedia. 91 (2016) 638–649. https://doi.org/10.1016/j.egypro.2016.06.223.

[38] G. Zhu, T. Wendelin, M.J. Wagner, C. Kutscher, History, current state, and future of linear Fresnel concentrating solar collectors, Sol. Energy. 103 (2014) 639–652. https://doi.org/10.1016/j.solener.2013.05.021.

[39] Archimede Solar Energy, (n.d.). http://www.archimedesolarenergy.it/.

[40] J. Muñoz-Anton, M. Biencinto, E. Zarza, L.E. Díez, Theoretical basis and experimental facility for parabolic trough collectors at high temperature using gas as heat transfer fluid, Appl. Energy. 135 (2014) 373–381. https://doi.org/10.1016/j.apenergy.2014.08.099.

[41] F. Xuening, C. Lei, D. Yuman, J. Min, F. Jinping, CFD modeling and analysis of brine spray evaporation system integrated with solar collector, Desalination. 366 (2015) 139–145. https://doi.org/10.1016/j.desal.2015.02.027.

[42] E. Bellos, C. Tzivanidis, K.A. Antonopoulos, A detailed working fluid investigation for solar parabolic trough collectors, Appl. Therm. Eng. 114 (2017) 374–386. https://doi.org/10.1016/j.applthermaleng.2016.11.201.

[43] E. Bellos, C. Tzivanidis, K.A. Antonopoulos, I. Daniil, The use of gas working fluids in parabolic trough collectors – An energetic and exergetic analysis, Appl. Therm. Eng. 109 (2016) 1–14. https://doi.org/10.1016/j.applthermaleng.2016.08.043.

[44] M.I. Roldán, L. Valenzuela, E. Zarza, Thermal analysis of solar receiver pipes with superheated steam, Appl. Energy. 103 (2013) 73–84. https://doi.org/10.1016/j.apenergy.2012.10.021.

[45] E. Bellos, C. Tzivanidis, Parametric investigation of supercritical carbon dioxide utilization in parabolic trough collectors, Appl. Therm. Eng. 127 (2017) 736–747. https://doi.org/10.1016/j.applthermaleng.2017.08.032.

[46] E. Bellos, C. Tzivanidis, I. Daniil, K.A. Antonopoulos, The impact of internal longitudinal fins in parabolic trough collectors operating with gases, Energy Convers. Manag. 135 (2017) 35–54. https://doi.org/10.1016/j.enconman.2016.12.057.

[47] J. Kasperski, M. Nemś, Investigation of thermo-hydraulic performance of concentrated solar air-heater with internal multiple-fin array, Appl. Therm. Eng. 58 (2013) 411–419. https://doi.org/10.1016/j.applthermaleng.2013.04.018.

[48] P. Good, G. Ambrosetti, A. Pedretti, A. Steinfeld, An array of coiled absorber tubes for solar trough concentrators operating with air at 600°C and above, Sol. Energy. 111 (2015) 378–395. https://doi.org/10.1016/j.solener.2014.09.016.

[49] R. Bader, A. Pedretti, M. Barbato, A. Steinfeld, An air-based corrugated cavity-receiver for solar parabolic trough concentrators, Appl. Energy. 138 (2015) 337–345.

https://doi.org/10.1016/j.apenergy.2014.10.050.

[50] M.H. Ahmadi, M. Alhuyi Nazari, R. Ghasempour, F. Pourfayaz, M. Rahimzadeh, T. Ming, A review on solar-assisted gas turbines, Energy Sci. Eng. 6 (2018) 658–674. https://doi.org/10.1002/ese3.238.

[51] O. Behar, Solar thermal power plants - A review of configurations and performance comparison, Renew. Sustain. Energy Rev. 92 (2018) 608–627. https://doi.org/10.1016/j.rser.2018.04.102.

[52] M. Amelio, V. Ferraro, V. Marinelli, A. Summaria, An evaluation of the performance of an integrated solar combined cycle plant provided with air-linear parabolic collectors, Energy. 69 (2014) 742–748. https://doi.org/10.1016/j.energy.2014.03.068.

[53] E. Bellos, C. Tzivanidis, K.A. Antonopoulos, Parametric analysis and optimization of a solar assisted gas turbine, Energy Convers. Manag. 139 (2017) 151–165. https://doi.org/10.1016/j.enconman.2017.02.042.

[54] V. Ferraro, V. Marinelli, An evaluation of thermodynamic solar plants with cylindrical parabolic collectors and air turbine engines with open Joule-Brayton cycle, Energy. 44 (2012) 862–869. https://doi.org/10.1016/j.energy.2012.05.005.

[55] A. Cinocca, R. Cipollone, R. Cipollone, R. Carapellucci, V. Iampieri, M. Rivo, CSP-PT gas plant using air as Heat Transfer Fluid with a packed-bed storage section., in: 73rd Conf. Ital. Therm. Mach. Eng. Assoc. (ATI 2018), 12-14 Sept. 2018, Pisa,Italy, 2018. https://doi.org/10.1016/j.egypro.2018.08.110.

[56] L. Guzzella, C.H. Onder, Introduction to modeling and control of internal combustion engine systems, 2010. https://doi.org/10.1007/978-3-642-10775-7.

[57] A. Crespo, C. Barreneche, M. Ibarra, W. Platzer, Latent thermal energy storage for solar process heat applications at medium-high temperatures – A review, Sol. Energy. (2018) 1–32. https://doi.org/10.1016/j.solener.2018.06.101.

[58] M. Eck, T. Hirsch, J.F. Feldhoff, D. Kretschmann, J. Dersch, A. Gavilan Morales, L. Gonzalez-Martinez, C. Bachelier, W. Platzer, K.J. Riffelmann, M. Wagner, Guidelines for CSP yield analysis - Optical losses of line focusing systems; definitions, sensitivity analysis and modeling approaches, Energy Procedia. 49 (2014) 1318–1327. https://doi.org/10.1016/j.egypro.2014.03.141.

[59] SCHOTT SOLAR, (n.d.). https://www.us.schott.com/csp/english/schott-solar-receivers.html.

[60] J. Sun, Z. Zhang, L. Wang, Z. Zhang, J. Wei, Comprehensive Review of Line-Focus Concentrating Solar Thermal Technologies: Parabolic Trough Collector (PTC) vs Linear Fresnel Reflector (LFR), J. Therm. Sci. 29 (2020) 1097–1124. https://doi.org/10.1007/s11630-020-1365-4.

[61] Y.L. He, K. Wang, Y. Qiu, B.C. Du, Q. Liang, S. Du, Review of the solar flux distribution in concentrated solar power: Non-uniform features, challenges, and solutions, Appl. Therm. Eng. 149 (2019) 448–474. https://doi.org/10.1016/j.applthermaleng.2018.12.006.

[62] R. Forristall, Heat Transfer Analysis and Modeling of a Parabolic Trough Solar Receiver Implemented in Engineering Equation Solver, (2003) 164. https://doi.org/NREL/TP-550-34169.

[63] F. Burkholder, M. Brandemuehl, H. Price, J. Netter, C. Kutscher, E. Wolfrum, Parabolic

trough receiver thermal testing, Proc. Energy Sustain. Conf. 2007. (2007) 961–970. https://doi.org/10.1115/ES2007-36129.

[64] F. Burkholder, C. Kutscher, Heat-Loss Testing of Solel's UVAC3 Parabolic Trough Receiver, NREL Tech. Rep. TP-550-423 (2008) 19.

[65] F. Burkholder, C.F. Kutscher, Heat loss testing of Schott's 2008 PTR70 parabolic trough receiver, NREL Tech. Rep. (2009) 58. http://www.nrel.gov/docs/fy09osti/45633.pdf.

[66] J.A. Duffie, W.A. Beckman, J. McGowan, Solar Engineering of Thermal Processes , 1985. https://doi.org/10.1119/1.14178.

[67] F.P. Incropera, D.P. DeWitt, Fundamentals of Heat and Mass Transfer, (1996) 890. https://doi.org/10.1016/j.applthermaleng.2011.03.022.

[68] A. Lecuona-Neumann, Secadero solar, P201630068, 2016.

[69] O.E. Balje, Turbomachines, John Wiley, New York, 1981.

[70] J.B. Heywood, Internal Combustion Engine Fundamentals., New York, 1988.

[71] J. El Hadef, G. Colin, V. Talon, Y. Chamaillard, J. El Hadef, G. Colin, V. Talon, Y. Chamaillard, N.P. Turbocharger, J. El Hadef, G. Colin, V. Talon, Y. Chamaillard, New Physics-Based Turbocharger Data-Maps Extrapolation Algorithms : Validation on a Spark-Ignited Engine, (2013).

[72] et al. Stricker, K., Turbocharger Map Reduction for Control-Oriented Modeling., Ournal Dyn. Syst. Meas. Control. 136 (2014).

[73] S. Zhu, K. Deng, S. Liu, Modeling and extrapolating mass flow characteristics of a radial turbocharger turbine, Energy. 87 (2015) 628–637. https://doi.org/10.1016/j.energy.2015.05.032.

[74] C.L. Weigel, C. and Ball, Reynolds Number Effect on Overall Performance pf a 10.8 centimeter (4.25 inch) Sweptback Bladed Centrifugal Compressor. ., 1972.

[75] R. Capata, E. Sciubba, Use of modified balje maps in the design of low reynolds number turbocompressors, ASME Int. Mech. Eng. Congr. Expo. Proc. 7 (2012) 835–841. https://doi.org/10.1115/IMECE2012-85582.

[76] R. Capata, E. Sciubba, Experimental fitting of the re-scaled Balje maps for low-reynolds radial turbomachinery, Energies. 8 (2015) 7986–8000. https://doi.org/10.3390/en8087986.

[77] S.L. Dixon, Fluid Mechanics and Thermodynamics of Turbomachinery. 4, Butterworth-Heinemann, 1998.

[78] D.G. Wilson, T. Korakianitis., The design of high-efficiency turbomachinery and gas turbines., 2nd ed., MIT Press, Cambridge, Massachusetts, 1998.

[79] Garrett Advancing Motion, (n.d.). https://www.garrettmotion.com/.

[80] Solatom, SOLAR STEAM FOR INDUSTRIAL PROCESSES, (n.d.). http://www.solatom.com/.

[81] A. Heimsath, G. Bern, D. Van Rooyen, P. Nitz, Quantifying optical loss factors of small linear concentrating collectors for process heat application, Energy Procedia. 48 (2014) 77–86. https://doi.org/10.1016/j.egypro.2014.02.010.

[82] A. Giostri, M. Binotti, P. Silva, E. Macchi, G. Manzolini, Comparison of Two Linear

Collectors in Solar Thermal Plants: Parabolic Trough Vs Fresnel, Proc. ASME 2011 Int. Conf. Energy Sustain. (2011).

[83] R.V. Padilla, G. Demirkaya, D.Y. Goswami, E. Stefanakos, M.M. Rahman, Heat transfer analysis of parabolic trough solar receiver, Appl. Energy. 88 (2011) 5097–5110. https://doi.org/10.1016/j.apenergy.2011.07.012.

[84] G. Zhu, T.T. Chow, K.F. Fong, C.K. Lee, Comparative study on humidified gas turbine cycles with different air saturator designs, Appl. Energy. 254 (2019) 113592. https://doi.org/10.1016/j.apenergy.2019.113592.

[85] M.J. Montes, R. Barbero, R. Abbas, A. Rovira, Performance model and thermal comparison of different alternatives for the Fresnel single-tube receiver, Appl. Therm. Eng. 104 (2016) 162–175. https://doi.org/10.1016/j.applthermaleng.2016.05.015.

[86] Y. Qiu, Y.L. He, Z.D. Cheng, K. Wang, Study on optical and thermal performance of a linear Fresnel solar reflector using molten salt as HTF with MCRT and FVM methods, Appl. Energy. 146 (2015) 162–173. https://doi.org/10.1016/j.apenergy.2015.01.135.

[87] L. Salgado Conrado, A. Rodriguez-Pulido, G. Calderón, Thermal perfomance of parabolic trough solar collectors, Renew. Sustain. Energy Rev. 67 (2017) 1345–1359. https://doi.org/10.1016/j.rser.2016.09.071.

[88] V. Gnielinski, New Equations for Heat and Mass Transfer in Turbulent Pipe and Channel Flow, Int Chem Eng 2. n. 16 (1976) 359–68.

[89] J.P. Jensen, A.F. Kristensen, S.C. Sorenson, N. Houbak, E. Hendricks, Mean value modeling of a small turbocharged diesel engine, SAE Tech. Pap. (1991). https://doi.org/10.4271/910070.

[90] L. Eriksson, Modeling and Control of TC SI and DI enignes, Oil Gas Sci. Technol. 63 (2008) 9–19. https://doi.org/10.2516/ogst.

[91] S.C. Sorenson, E. Hendricks, S. Magnusson, A. Bertelsen, Compact and accurate turbocharger modelling for engine control, SAE Tech. Pap. 2005 (2005). https://doi.org/10.4271/2005-01-1942.

[92] J. Galindo, A. Tiseira, R. Navarro, D. Tarí, H. Tartoussi, S. Guilain, Compressor Efficiency Extrapolation for 0D-1D Engine Simulations, SAE Tech. Pap. (2016). https://doi.org/10.4271/2016-01-0554.

[93] M. Casey, C. Robinson, A Method to Estimate the Performance Map of a Centrifugal Compressor Stage, J. Turbomach. 135 (2012) 1–10. https://doi.org/10.1115/1.4006590.

[94] F. Payri, J.R. Serrano, P. Fajardo, M.A. Reyes-Belmonte, R. Gozalbo-Belles, A physically based methodology to extrapolate performance maps of radial turbines, Energy Convers. Manag. 55 (2012) 149–163. https://doi.org/10.1016/j.enconman.2011.11.003.

[95] X. Fang, Q. Dai, Y. Yin, Y. Xu, A compact and accurate empirical model for turbine mass flow characteristics, Energy. 35 (2010) 4819–4823. https://doi.org/10.1016/j.energy.2010.09.006.

[96] A. Dombrovsky, Synthesis of the 1D modelling of turbochargers and its effects on engine performance prediction, (2016) 1–238. https://doi.org/10.4995/Thesis/10251/82307.

[97] M. Schinnerl, J. Seume, J. Ehrhard, M. Bogner, Heat Transfer Correction Methods for Turbocharger Performance Measurements, J. Eng. Gas Turbines Power. 139 (2017) 1–9. https://doi.org/10.1115/1.4034234.

[98] D. Bohn, T. Heuer, K. Kusterer, Conjugate flow and heat transfer investigation of a turbo charger, J. Eng. Gas Turbines Power. 127 (2005) 663–669. https://doi.org/10.1115/1.1839919.

[99] A. Romagnoli, R. Martinez-Botas, Heat transfer analysis in a turbocharger turbine: An experimental and computational evaluation, Appl. Therm. Eng. 38 (2012) 58–77. https://doi.org/10.1016/j.applthermaleng.2011.12.022.

[100] M. Cormerais, J.F. Hetet, P. Chesse, A. Maiboom, Heat Transfer Analysis in a Turbocharger Compressor : Modeling and Experiments, 2006 (2019).

[101] M. V. Casey, T.M. Fesich, The efficiency of turbocharger compressors with diabatic flows, J. Eng. Gas Turbines Power. 132 (2010) 1–13. https://doi.org/10.1115/1.4000300.

[102] M. El Ydrissi, H. Ghennioui, E.G. Bennouna, A. Farid, A review of optical errors and available applications of deflectometry technique in solar thermal power applications, Renew. Sustain. Energy Rev. 116 (2019). https://doi.org/10.1016/j.rser.2019.109438.

[103] F. Sallaberry, R. Pujol, B. Perers, Optical Losses Due to Tracking Misaligment on Linear Concentrating Solar Thermal Collectors, (2017) 1–12. https://doi.org/10.18086/eurosun.2016.07.10.

[104] J. Zheng, J. Yan, J. Pei, G. Liu, Solar tracking error analysis of fresnel reflector, Sci. World J. 2014 (2014). https://doi.org/10.1155/2014/834392.

[105] A. Barbón, C. Bayón-Cueli, L. Bayón, P.F. Ayuso, Influence of solar tracking error on the performance of a small-scale linear Fresnel reflector, Renew. Energy. 162 (2020) 43–54. https://doi.org/10.1016/j.renene.2020.07.132.

[106] G.S. Chaitanya Prasad, K.S. Reddy, T. Sundararajan, Optimization of solar linear Fresnel reflector system with secondary concentrator for uniform flux distribution over absorber tube, Sol. Energy. 150 (2017) 1–12. https://doi.org/10.1016/j.solener.2017.04.026.

[107] G. Salameh, P. Chesse, D. Chalet, Different Measurement Techniques for Wider Small Radial Turbine Performance Maps, Exp. Tech. 40 (2016) 1511–1525. https://doi.org/10.1007/s40799-016-0107-8.

[108] W.D. Tamme, R.; Bauer, T.; Buschle, J.; Laing, D.; Müller-Steinhagen, H.; Steinmann, Latent heat storage above 120 C for applications in the industrial process heat sector and solar power generation., Int. J. Energy Res. 32(3) (2008) 264–271. https://doi.org/10.1002/er.

[109] www.chemicalbook.com, (n.d.). https://www.chemicalbook.com/ChemicalProductProperty_EN_CB7400757.htm.

[110] M. Hongn, S.F. Larsen, M. Gea, M. Altamirano, Least square based method for the estimation of the optical end loss of linear Fresnel concentrators, Sol. Energy. 111 (2015) 264–276. https://doi.org/10.1016/j.solener.2014.10.042.

[111] A. Habte, T. Stoffel, R. Perez, D. Myers, C. Gueymard, P. Blanc, S. Wilbert, Best Practices Handbook for the Collection and Use of Solar Resource Data for Solar Energy Applications: Second Edition, Nrel. (2017) 2.1-2.22. www.nrel.gov/publications.

[112] EU SCIENCE HUB, PVGIS, (n.d.). https://ec.europa.eu/jrc/en/pvgis.

[113] A. Buscemi, D. Panno, G. Ciulla, M. Beccali, V. Lo Brano, Concrete thermal energy storage for linear Fresnel collectors: Exploiting the South Mediterranean's solar potential for agri-food processes, Energy Convers. Manag. 166 (2018) 719–734.

https://doi.org/10.1016/j.enconman.2018.04.075.